

# **LIGHT EXTRACTION FROM MICROCAVITY LIGHT EMITTING DIODES: OPTIMIZATION AND CHARACTERIZATION OF HIGH-BRIGHTNESS AlGaInP-BASED DEVICES**

THÈSE N° 2216 (2000)

PRÉSENTÉE AU DÉPARTEMENT DE PHYSIQUE

ÉCOLE POLYTECHNIQUE FÉDÉRALE DE LAUSANNE

POUR L'OBTENTION DU GRADE DE DOCTEUR ÈS SCIENCES

PAR

**Paul ROYO**

Ingénieur électricien diplômé EPF  
de nationalité française

acceptée sur proposition du jury:

Prof. M. Illegems, directeur de thèse  
Prof. R. Baets, rapporteur  
Dr M. Moser, rapporteur  
Dr R. Stanley, rapporteur  
Dr K. Streubel, rapporteur  
Prof. L. Zuppiroli, rapporteur

Lausanne, EPFL  
2000



# Contents

<b>Version abrégée</b>	<b>v</b>
<b>Abstract</b>	<b>ix</b>
<b>1 Introduction</b>	<b>1</b>
1.1 Extraction of light from semiconductors . . . . .	1
1.2 Thesis layout . . . . .	6
<b>2 Optics of dielectric multilayers</b>	<b>9</b>
2.1 Transfer matrix formalism . . . . .	9
2.2 Periodic structures and the Distributed Bragg Reflector (DBR) . . . . .	15
2.3 Study of the Fabry-Pérot resonator . . . . .	28
<b>3 Description of quantum well spontaneous emission by a distribution of oscillating dipoles</b>	<b>35</b>
3.1 Dipole emission in a multilayer structure (discrete dipoles) . . . . .	35
3.2 Dipole emission in a multilayer structure (3D distribution of dipoles) . . . . .	40
<b>4 Top-emitting MCLEDs with two DBRs: analytical formalism and design rules</b>	<b>45</b>
4.1 Extraction efficiency of top-emitting MCLEDs: exact formula . . . . .	45
4.2 Extraction efficiency of top-emitting MCLEDs: analytical approximations . . . . .	50
4.3 Optimization of the extraction efficiency . . . . .	56
4.4 Guided modes, Purcell effect and photon recycling . . . . .	67
<b>5 Effect of the detuning on the extraction: theory and experiments</b>	<b>73</b>
5.1 Controlled detuning in MCLEDs . . . . .	73
5.2 Description of the growth system used . . . . .	77
5.3 Description of the processing . . . . .	81
5.4 Description of the mask . . . . .	83
5.5 Characterization of the MCLED structure . . . . .	86
<b>6 Emission properties of red MCLEDs</b>	<b>91</b>
6.1 Angle resolved spectral measurements . . . . .	93
6.2 Angular emission profiles of LEDs and MCLEDs: comparison . . . . .	102
6.3 Current density dependence of the intrinsic spontaneous emission spectrum . . . . .	109
<b>7 Study of the external quantum efficiency of red MCLEDs</b>	<b>115</b>
7.1 Factors determining the external quantum efficiency . . . . .	115
7.2 Determination of the internal quantum efficiency . . . . .	120
7.3 Effect of the current spreading on the external quantum efficiency . . . . .	124
7.4 Effect of the device size on the external quantum efficiency . . . . .	135
7.5 Conclusions . . . . .	143
<b>8 Conclusion</b>	<b>145</b>
<b>A Analytical approximations on DBR complex reflectivity.</b>	<b>147</b>

<b>B Material Parameters</b>	<b>155</b>
B.1 Indices of refraction . . . . .	155
B.2 Lattice constants . . . . .	157
B.3 Bandgap energy and band discontinuity . . . . .	157
B.4 Effective masses . . . . .	159
<b>Bibliography</b>	<b>173</b>
<b>Curriculum vitae</b>	<b>175</b>
<b>Acknowledgments</b>	<b>177</b>

*A mes parents*



# Version abrégée

Les diodes électroluminescentes visibles offrent un vaste champ d'applications qui vont des panneaux d'affichage à haute brillance, aux signaux lumineux de contrôle en passant par les télécommunications (interconnexions optiques).

Un des problèmes fondamentaux des diodes électroluminescentes n'est pas l'émission de lumière par le semiconducteur, mais son extraction hors de celui-ci. En effet, un photon émis dans un semiconducteur standard n'est émis dans l'air qu'avec une probabilité de 2% du fait de la réflexion totale interne. Différentes approches existent pour contourner cette limitation physique. Parmi celles-ci figure l'utilisation des microcavités. L'idée est de faire entrer en résonance la lumière émise à l'aide d'une cavité optique dont la dimension est de l'ordre de grandeur de la longueur d'onde des photons émis. En accordant de façon appropriée les propriétés intrinsèques de la source de photons aux propriétés de la cavité, il est possible d'augmenter d'un ordre de grandeur le coefficient d'extraction de lumière.

Le but de ce travail a été d'appliquer ce concept aux longueurs d'ondes visibles en utilisant le système de matériau quaternaire  $(Al_xGa_{1-x})_{0.5}In_{0.5}P$  en accord de maille avec le GaAs pour la conception de la zone active. Les substrats de GaAs utilisés étant absorbants à la longueur d'onde souhaitée (650 nm), il a été nécessaire d'intégrer à la structure des miroirs de Bragg diélectriques à base d' $Al_{0.5}Ga_{0.5}As$  et d'AlAs, afin d'avoir un contraste d'indices de réfraction suffisant et une faible absorption.

La première étape de ce projet a été d'étudier l'influence des paramètres de la structure (réflectivités des deux miroirs, épaisseur de la cavité et propriétés spectrales de l'émission spontanée des puits quantiques) sur le rendement d'extraction. A cet effet, un modèle numérique a été utilisé pour déterminer les valeurs optimales de ces paramètres maximisant le rendement d'extraction de ce type de structure. Dans ce modèle, l'émission d'un puits quantique est calculée en décomposant le rayonnement d'une distribution de dipôles oscillants sous forme d'ondes planes et d'ondes évanescentes. La propagation de ces ondes dans une structure planaire multicouche est calculée en utilisant le formalisme des matrices de transfert. Des approximations analytiques de ce modèle ont été dérivées et ont permis d'exprimer simplement le rendement d'extraction. Il a été démontré que le rendement d'extraction maximal pouvant être atteint par ce type de structure était inversement proportionnel à l'ordre de la cavité physique corrigée d'un coefficient dépendant de la variation angulaire de la phase des coefficients complexes de réflectivité des miroirs diélectriques. De ces calculs il est également apparu que le principe de base de la microcavité (en régime de couplage faible) était une redistribution angulaire du rayonnement de la source par la cavité. L'effet du "detuning" (défini comme la différence entre la longueur d'onde

d'émission des puits quantiques et celle du mode de la cavité défini à incidence normale) sur la forme du diagramme de rayonnement et sur le rendement d'extraction a été étudié.

Une vérification expérimentale de ces résultats théoriques a été effectuée en épitaxiant des couches à microcavité à partir desquelles des dispositifs ont été fabriqués en salle blanche. En modifiant de façon contrôlée les flux de gaz dans le réacteur chimique utilisé pour l'épitaxie (de type MOCVD), il a été possible d'obtenir des gradients d'épaisseur et par conséquent une variation continue et connue du detuning. Les prédictions théoriques ont été confirmées et il a été possible d'estimer à 56% le rendement quantique interne de ces structures.

Afin d'étudier en détail les propriétés d'émission des diodes à microcavités, des mesures spectrales résolues en angles ont été faites à partir desquelles le spectre d'émission spontané des puits quantiques a été obtenu par un procédé de déconvolution. Des mesures similaires sur des diodes électroluminescentes sans cavité ont permis de confirmer l'exactitude de ces calculs. Le spectre d'émission intrinsèque étant connu, il a été possible de calculer précisément le rendement d'extraction des diodes. Une valeur de 11%, approximativement indépendante de la densité de courant injectée, a été déterminée. Il a été démontré que pour cette structure les effets d'élargissement spectral étaient compensés par le décalage spectral vers le rouge de la longueur d'onde d'émission des puits quantiques (lié à des effets de chauffage).

Ces calculs ont permis de calculer le rendement quantique interne de la diode à microcavité en fonction de la densité de courant injectée. Une valeur de 40% a été déterminée à une densité de  $50 [A/cm^2]$  pour une diode ayant un mesa carré large de  $262 [\mu m]$ .

Les différents facteurs physiques contribuant au rendement quantique interne ont été étudiés. Il a été montré que le rendement quantique externe pouvait s'exprimer comme le produit: d'un rendement d'extraction lié à la structure microcavité, d'un rendement d'extraction lié à la géométrie de la grille de contact, d'un rendement d'injection et d'un rendement radiatif.

La fin de ce travail a été consacrée à l'étude de chacun de ces facteurs. Le rendement d'extraction lié à la structure microcavité ayant été étudié en détail au début de ce travail, il a été possible d'évaluer l'effet de la géométrie de la grille de contact sur le rendement en comparant des diodes de même taille mais ayant des géométries différentes pour leurs contacts. Il a été montré que la géométrie optimale était un compromis entre une forte interconnexion des lignes de contacts (permettant un bon étalement du courant sur la surface active) et une distance suffisante entre celles-ci pour minimiser le masquage de la surface émettrice du dispositif. Un rendement quantique externe de 5.1% a été obtenu à une densité de courant de  $40 [A/cm^2]$  pour une diode large de  $262 [\mu m]$  ayant une grille de géométrie optimisée.

La dépendance en courant du rendement radiatif a été étudiée à l'aide d'un modèle simple tenant compte de la taille de la zone active. Un modèle empirique a été proposé pour expliquer l'effet du rendement d'injection. Ces modèles faisant apparaître la taille de la zone active comme paramètre, il a été possible de vérifier expérimentalement cette dépendance. Un mauvais confinement des électrons dans la zone active a pu être mis en évidence et expliquer les faibles valeurs de rendement quantique interne mesurées.



# Abstract

Visible light-emitting diodes (LED's) offer a wide range of applications like high brightness displays, indicator lights or optical interconnects. The fundamental problem of light-emitting diodes is not the emission of light but its extraction from the semiconductor. Indeed, for one photon emitted inside a standard semiconductor diode, the probability of escape is only 2% because of total internal reflection. Several approaches exist to overcome this physical limitation, and among these ones, the microcavities. The idea is to embed the active layer in a small cavity with dimensions of the order of the wavelength of the emitted light. By appropriately matching the intrinsic spectrum properties to the cavity properties, it is possible to enhance the extraction efficiency by an order of magnitude. The purpose of this work was to apply this concept to visible wavelengths, using for the active region,  $(Al_xGa_{1-x})_{0.5}In_{0.5}P$  quaternary compounds which are lattice-matched to GaAs. Since the GaAs substrates are absorbant at the desired wavelength of emission (650 nm), it was necessary to integrate to the structure two dielectric mirrors (Distributed Bragg Reflectors) based on periodic sequence of  $Al_{0.5}Ga_{0.5}As/AlAs$  layers so as to get reasonable refraction index contrasts and small absorption.

The first step of this project was to study the effect of structure parameters (mirror reflectivity, cavity thickness and spectral properties of the quantum wells) on the extraction efficiency. For that purpose, a numerical model was used to determine the optimal structure so as to maximize the extraction efficiency. In this model, the quantum well emission is calculated by using a plane and evanescent wave decomposition of the radiation which is described by a distribution of oscillating electric dipoles. Propagation of plane waves inside a planar multilayer structure is calculated by using the transfer matrix formalism. Some approximations of this model are proposed in this work, allowing one to analytically express the extraction efficiency. It was shown that the highest extraction efficiency which could be obtained from this kind of structure was inversely proportional to the physical cavity order, corrected by a factor which depends on the angular variation of the phase of the mirror reflectivity. In these calculations, it also appeared that the basic principle of operation of microcavity light-emitting diodes (in the weak coupling regime) was the angular redirection of the source emission due to the cavity. The wavelength detuning between the quantum well electroluminescence and the cavity mode defined at normal incidence was shown to influence strongly the extraction efficiency and the pattern of emission.

An experimental verification of these results was performed by growth and processing of MOCVD AlGaInP LED's. By modifying carefully the gas fluxes in the reactor, it was possible to get controlled

gradient of thicknesses and hence continuous and controlled variation of the detuning. Measurement on the devices confirmed theoretical predictions and allowed one to estimate at 56% their internal quantum efficiency.

Angle-resolved spectral measurements were performed in order to investigate the optical emission properties of the microcavity light-emitting diodes. The intrinsic spontaneous emission spectrum of the quantum wells could be deconvolved from comparison between these measurements and numerical simulations. Similar measurements were done on conventional light-emitting diodes (without cavity) so as to confirm the accuracy of this method. The intrinsic emission spectrum being known, it was possible to accurately calculate the extraction efficiency of these diodes, which was found to be of 11% and approximately independent of the injected current density. It was shown that in these structures, the spectral broadening was counterbalanced by the red-shift of the quantum well emission wavelength due to heating effects. This results enabled calculation of the internal quantum efficiency with respect to the injected current density. A maximum of 40% was found at  $50 [A/cm^2]$  for a large size diode (squared mesa of  $262 [\mu m]$ ).

The different physical mechanisms responsible for the variation of the internal quantum efficiency with the current were identified and studied. It was shown that the external quantum efficiency could be expressed as the product of four terms: the extraction efficiency related to the optical design of the structure, the shadowing efficiency related to the geometry of the grid contact, the injection and the radiative efficiencies.

The final part of this work was devoted to the study of each of these factors. The shadowing efficiency was studied by comparing devices having same sizes but different grid contact geometries. It was shown that the optimal geometry was a trade-off between strong interconnection of the contact stripes (allowing a good current spreading), and a large distance between each of them (so as to minimize the masking of the emitting surface). An external quantum efficiency of 5.1% was found at  $50 [A/cm^2]$  for a large size diode (squared mesa of  $262 [\mu m]$ ) having an optimized contact geometry.

The current dependence of the radiative efficiency was studied by using a model taking into account the size of the emitting region. An empirical model was proposed to describe the effect of injection efficiency on the internal quantum efficiency. The effect of the device size on the external quantum efficiency was experimentally studied and confirmed the general trends predicted by the simple models. These measurements show that the low injection efficiency is due to a poor confinement of the electrons in the active region.

# Chapter 1

## Introduction

The main topic of this thesis is the fabrication and the investigation of the optical and electrical properties of red microcavity light-emitting diodes (MCLEDs). This project was carried out in collaboration with the Zurich laboratories of the Centre Suisse d'Electronique et de Microtechnique (CSEM), formerly Paul Scherrer Institut (PSIZ). Experimental work (growth and characterization of the wafers, clean-room processing and electrical measurements) was done in Zurich whereas theoretical studies and optical measurements were performed in Lausanne. Part of the work presented here was performed in the framework of the ESPRIT-SMILED european project. We received from one of the participant (Mitel Semiconductors) some wafers which were processed in Zurich and characterized in Lausanne.

Section 1.1 presents a general survey of the existing methods used to extract light from semiconductor LEDs. Basic principles of MCLEDs are presented and their advantages compared to other structures are discussed. Section 1.2 gives the general layout of this thesis.

### 1.1 Extraction of light from semiconductors

Light-emitting diodes (LEDs) are solid-state semiconductor devices that convert electrical energy directly into light. The basic structure consists of a semiconductor p-n junction: when it is forward biased, light is emitted due to radiative recombination processes occurring inside a sequence of semiconductor layers called the active region. The energy of the emitted photons, which determines the color, is approximately equal to the energy gap of the semiconductor material in the active region of the LED [32]. Most of the materials used for visible and infrared LEDs are compounds of elements from columns III and V of the periodic chart, also called III-V compounds [77].

The efficiency of the electrical to optical energy conversion is an important factor of merit for LEDs. Two coefficients are defined for that purpose. The wall-plug efficiency  $\eta_{wp}$  is defined as the ratio between the optical output power  $P_{opt}$  and the injected electrical power  $P_{el}$ :

$$\eta_{wp} = \frac{P_{opt}}{P_{el}} \quad (1.1)$$

corresponding to a power conversion efficiency.

The second coefficient, the external quantum efficiency  $\eta_{ext}$  is defined as the ratio of the externally produced photon flux to the injected electron flux:

$$\eta_{ex} = \frac{\Phi_{opt}}{\Phi_{el}} = \frac{e}{h\nu} \frac{P_{opt}}{i} \quad (1.2)$$

where  $h\nu$  is the energy of emitted photons,  $e$  the electron charge,  $i$  the injected current and  $P_{opt}$  the optical output power [130].

Since  $P_{el}$  includes electrical power dissipated as heat in the device through its series resistance, the two efficiencies are different ( $\eta_{wp}$  is normally greater than  $\eta_{ex}$ ).

The emission properties of LEDs are governed by the recombination processes of excess carriers injected in the active layer. The external quantum efficiency is the product of the internal quantum efficiency  $\eta_{int}$  and the extraction efficiency  $\bar{\eta}$ . Optimizing these two parameters involves different approaches. The internal quantum efficiency describes the conversion efficiency of electron-hole pairs to photons inside the semiconductor. Its optimization is a material purity as well as a bandgap engineering problem (for the design of the active zone). When optimizing  $\eta_{int}$ , several problems have to be addressed such as the efficiency of carrier injection into the active zone, the capture efficiency by quantum wells, material quality and all competing non-radiative mechanisms. The evolution of LED technology has followed the development of  $\eta_{int}$  and  $\bar{\eta}$ . The first visible LEDs were based on indirect gap GaP materials with isoelectronic impurities. A simple cube geometry gives  $\bar{\eta} \approx 10 - 15\%$ , while  $\eta_{int}$  was in the low percents. The advance of direct bandgap quaternary meant that  $\eta_{int}$  of the order of unity could be easily achieved (the penalty was absorbing substrate reducing the extraction efficiency for cube geometry). The emphasis thus rest with changing  $\bar{\eta}$ .

The extraction efficiency is defined as the fraction of the light generated inside the semiconductor which is extracted out of the device. It depends on the optical properties of the structure and of its microscopic (layer sequence) and macroscopic (device size and shape) geometries. This parameter is strongly dependent upon the difference in index of refraction between the LED chip ( $n_{semiconductor} \approx 3.5$ ) and the surrounding medium which is usually air ( $n_{air} = 1$ ) or epoxy ( $n_{epoxy} = 1.5$ ). Because of Snell's law, light emitted outside the escape cone (defined by its half angle  $\theta_c = \text{asin}(n_{outside}/n_{inside})$ ) suffers from total internal reflection and can not escape to the outside medium. Assuming that the spontaneous emission is isotropic in the semiconductor (which is usually the case when electrons and holes recombine in bulk material), only a fraction  $\bar{\eta}$  of the total  $4\pi$  solid angle can be emitted [31] with

$$\bar{\eta} = \frac{1}{2} (1 - \cos(\theta_c)). \quad (1.3)$$

Hence about 4% (2%) of the light which impacts the chip surface escapes into epoxy (air): even if the internal quantum efficiency is close to unity, 96% (98%) of the photons are lost.

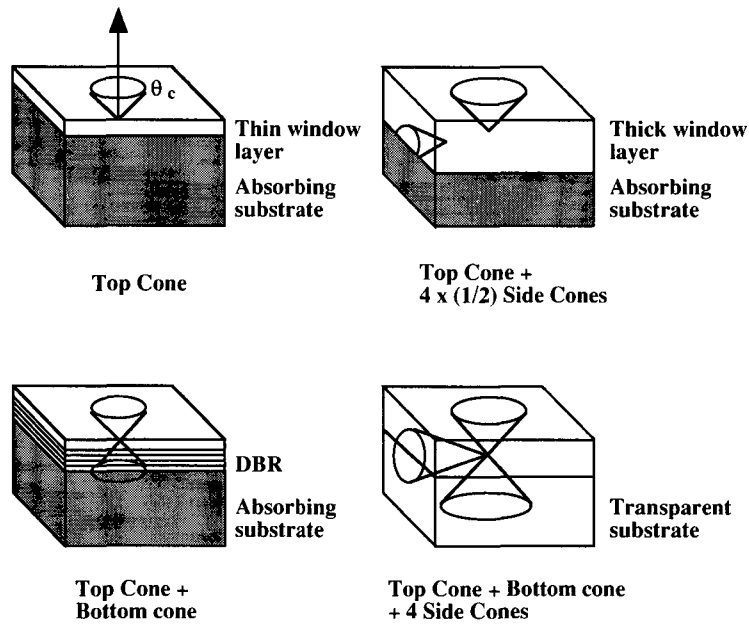


Figure 1.1: Simplified schematic illustration of light extraction from various LED structures: photons emitted the escape cones with critical angle  $\theta_c$  are trapped inside the chip, due to total internal reflection and can not be extracted.

Several structures were proposed to overcome this severe limitation and to improve the LED extraction efficiency.

A first simple solution is to increase the number of extraction cones [151], [32]: the extraction efficiency per side is not changed but the light is collected from several facets (see figure 1.1). Growing a thick transparent window layer above the emission layers can be used to improve the extraction efficiency, by a factor of three (one cone plus four half side cones) if the substrate is absorbant [61]. A factor of six can be obtained provided the substrate is transparent to the emitted light: wafer bonding techniques were successfully used for that purpose [44], [47], [57], [79], [151].

Another method to reach high efficiency is to use geometrically deformed chips. The geometry displayed on figure 1.2 improves light extraction by redirecting totally internally reflected photons from the sidewall interfaces towards the top surface of the chip near normal incidence, allowing them to escape. Photons that are totally internally reflected at the top surface are redirected for escape through the beveled sidewalls [92], [91]. Truncated-inverted-pyramid structures based on this principle leads to measured external quantum efficiency higher than 50% [84].

Another mechanism (which can be exploited so as to increase the extraction efficiency) is to use surface textured thin-film LEDs. This solution consists of roughening one LED surface and using a back mirror. Light which is not coupled outside of the structure is internally reflected at the top surface, scattered at the rough surface and thus changes its angle of propagation. After reflection at

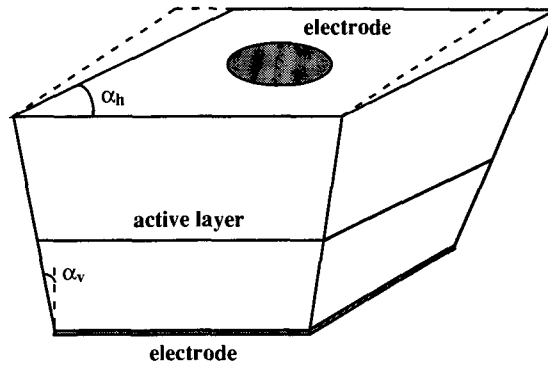


Figure 1.2: Geometrically deformed chip: photon trajectories are randomized and this can be controlled by chip deformation angles  $\alpha_h$  and  $\alpha_v$ .

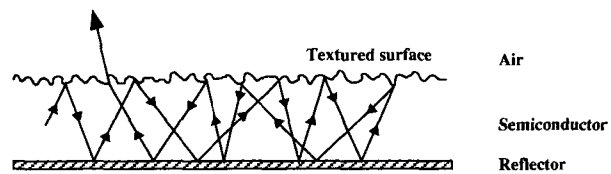


Figure 1.3: In the textured film, angular randomization is achieved by strong surface scattering.

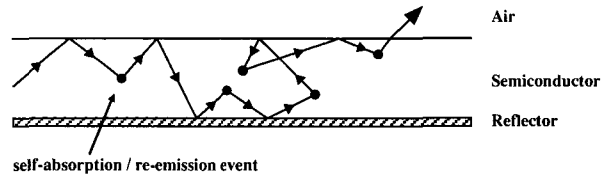


Figure 1.4: Photons' trajectories are randomized by self-absorption / re-emission events represented by dots.

the back mirror, it gets a second chance to escape from the semiconductor. This technique lead to efficiencies as high as 30% [135], [156], [155]. Note that randomization is also present in the structure displayed on figure 1.1 which increases its extraction. As mentioned in reference [31], the extraction obtained from a transparent substrate LED encapsulated in epoxy is about 30%, which suggests that randomization at the sawed chip edges is significant.

Another way to reach high extraction efficiency is to recycle the photons which are internally reflected in the structure. The idea is to make them undergo as many reabsorptions and reemissions as necessary (in the active layer) until a favorable angle is found. It was demonstrated in reference [136] that in a very high-quality semiconductor, this mechanism (known as photon recycling), could lead to a dramatic increase of the extraction efficiency (72 %) in spite of the modest (2 %) bare extraction efficiency (the device was optically pumped). This result corresponds to around twenty five or more reincarnations of the photons which demands a large internal radiative efficiency (the reincarnated photons has twenty five or more times the possibility to recombine non-radiatively), and negligible optical losses in the structure. As mentioned in reference [135] angular randomization by photon recycling is not a practical approach for electrically injected devices since this mechanism is vulnerable to the slightest deterioration of material or mirror quality, to parasitic losses or to non-radiative defects. As indicated in reference [12] however, MCLED structures are better suited to exploit photon recycling compared to conventional LEDs because of their intrinsic high extraction efficiency. There is some evidence that photon recycling is significant in large size MCLEDs [114] and in single mirror LEDs [36].

For some devices single facet emission is preferred (high-brightness applications and planar technology for instance). In this case, macroscopic solutions like cubes or pyramids are no help. One way of improving single-facet extraction efficiency is to use interference effects. For example, placing the active region in front of a mirror allows multiple interference effects between light emitted from the active region and light reflected by the mirror. Depending on the distance between the active region and the mirror, a factor of two (far-mirror case) or four (close-mirror case) can be achieved [13]. Top-emitting LEDs based on single dielectric mirrors (Distributed Bragg Reflector) can be found in the literature [42], [41], [59] as well as single-mirror bottom-emitting LEDs [36]. In the latter

case, the emission reflected by the top-side (metallic) mirror interferes constructively with the emission through the substrate, giving a fourfold increase in power per facet. Theory shows that it is possible to go one step further in the extraction efficiency improvement by adding a second mirror [13]. This structure corresponds to the resonant cavity LED (RCLED) also called microcavity LED (MCLED) [137], [138]. The basic idea is to modify the spontaneous emission by placing the source inside a microcavity, so as to redirect the emission into the escape cone. Besides high extraction efficiency and high brightness, MCLEDs offer a number of advantages over conventional LEDs such as improved directionality and higher spectral purity. They can compete with VCSELs for short and medium distance ( $< 5\text{ km}$ ), medium bit-rate ( $< 1\text{ Gb/s}$ ) optical fiber communication systems [137] because of their higher reliability, lower cost and simplicity of fabrication. They moreover do not suffer from any threshold behavior. The first MCLEDs studied were based on InGaAs/AlGaAs materials emitting in the infrared. Different designs are reported in the references [67], [18], [114], [113], [22], [65], [153]. Fabrication of red-visible (650 nm) MCLEDs was pursued by several groups [97], [98], [71], [70], [146], [127]. These devices have potential applications in local area networks based on polymer optical fibers (POF) [40], [115], [146] with a minimum attenuation at 650 nm and a wide core diameter (0.75-1 mm) [81]. Furthermore these devices have potential applications in printing or fabrication of densely packed two-dimensional arrays for monochromatic display applications which require high brightness capabilities. The purpose of this thesis is to better understand the emission properties of these devices.

## 1.2 Thesis layout

The target of this thesis is to study top-emitting MCLEDs. The structures we studied consist of two dielectric mirrors (Distributed Bragg Reflectors, DBRs) surrounding a cavity in which the active material is placed. The basic building block of a top-emitting microcavity is the DBR mirror which is a complex dielectric multilayer. Describing its behavior is fundamental so as to understand the optics of microcavities. For that purpose, chapter 2 reviews some fundamental optical properties of dielectric multilayers and presents new analytical approximations for the calculation of DBR properties.

Chapter 3 describes how to model the spontaneous emission of a quantum well by a distribution of classical dipoles. This formalism allowed numerical simulations of the optical properties of complex one-dimensional multilayers to be performed.

Combining results of preceding two chapters, chapter 4 presents analytical approximations for the calculation of the MCLED extraction efficiency. Results obtained are compared with exact numerical simulations and design rules are given so as to optimize the MCLED extraction efficiency.

Chapter 5 presents the experimental characterization of red MCLEDs. By using a sophisticated growth procedure, it was possible to produce diodes with different optical performance on the same wafer. After explaining the processing steps performed, we explain how emission pattern measurements combined with numerical simulations can validate the theoretical predictions of previous chapters. We



also show that an estimate of the internal quantum efficiency is possible with this method.

Chapter 6 is devoted to extensive characterization of top-emission red MCLEDs that we compare with those of a conventional p-i-n LED. We show that angle-resolved spectral measurements bring a wealth of information on the diode emission properties. By a deconvolution procedure we demonstrate that it is possible to deconvolve the intrinsic spontaneous emission spectrum of the MCLED, which is an important and difficult parameter to measure. The effect of the current injection on the intrinsic emission spectrum is also investigated. Moreover, thermal heating effects are discussed.

Chapter 7 focuses on the study of the external quantum efficiency in MCLEDs. We discuss the effects of device size, grid contact geometry and internal quantum efficiency on the roll-over which is observed in the measurements of the MCLEDs external quantum efficiency.

Finally, chapter 8 presents the conclusions of this work and an outlook for further development.



## Chapter 2

# Optics of dielectric multilayers

The target of this thesis is to study top-emitting microcavity light-emitting diodes (MCLEDs). The structures we will study consist of two dielectric mirrors (Distributed Bragg Reflectors, DBRs) surrounding a cavity in which the active material is placed. The purpose of the first three chapters is to understand how to optimize the extraction efficiency of MCLEDs, and hence will be mainly concerned with the calculation of the optical properties of the structure. The basic building block of a top-emitting microcavity is the DBR mirror which is a complex dielectric multilayer. Understanding its behavior is fundamental to study the optics of microcavity. For that purpose, section 2.1 recalls some basics of plane wave propagation in one dimensional multilayer dielectric stacks and section 2.2 reviews the optical properties of the DBRs. Some new analytical approximations are also proposed and will be used for a full analytical calculation of the MCLEDs light efficiency in chapter 4. Finally, section 2.3 presents the basic properties of the Fabry-Pérot resonator which is the base of the MCLED structures.

### 2.1 Transfer matrix formalism

The method we used to calculate the spontaneous emission of a quantum well embedded inside a planar multilayer structure is based on the plane wave expansion of electric dipole emission [14]. To describe the propagation of plane waves inside such a structure, it is very convenient to use the transfer matrix formalism [80], [93]. The purpose of this section is to recall the basics of this formalism. Since we will use explicitly this formalism in the following chapters, it is important to clearly define the transfer matrix expressions which are defined in a lot of different ways in the literature [80], [93], [29], [19], [51], [26]. We will define a plane wave by its complex vector phasor  $\vec{E} = \vec{E}_0 e^{i(\vec{k} \cdot \vec{r} - \omega t)}$  where  $\vec{k}$  is the propagation vector of the plane wave which can be complex. The frequency of the plane wave is given by  $\nu = \omega/2\pi$ . The electric field  $\vec{\mathcal{E}}$  is simply given by the real part of the vector phasor:  $\vec{\mathcal{E}} = \text{Re}(\vec{E})$ . With these definitions, the Maxwell equations reduce to the following expressions for the vector phasors of the plane wave:

$$\vec{\nabla} \wedge \vec{E} = i\omega \vec{B} \quad (2.1)$$

$$\vec{\nabla} \wedge \vec{H} = \vec{J} - i\omega \vec{D} \quad (2.2)$$

$$\vec{\nabla} \cdot \vec{D} = \rho \quad (2.3)$$

$$\vec{\nabla} \cdot \vec{B} = 0 \quad (2.4)$$

where  $\vec{J}$  is a current density,  $\rho$  a density of charge,  $\vec{E}$  is the electric field,  $\vec{H}$  is the magnetic field,  $\vec{D}$  is the electric displacement and  $\vec{B}$  is the magnetic flux density. The general boundary conditions at the interface between two media labelled 1 and 2 are given by the following expressions:

$$\vec{n}_{12} \wedge (\vec{E}_2 - \vec{E}_1) = 0 \quad (2.5)$$

$$\vec{n}_{12} \wedge (\vec{H}_2 - \vec{H}_1) = \vec{J}_s \quad (2.6)$$

$$\vec{n}_{12} \cdot (\vec{D}_2 - \vec{D}_1) = \rho_s \quad (2.7)$$

$$\vec{n}_{12} \cdot (\vec{B}_2 - \vec{B}_1) = 0 \quad (2.8)$$

where  $\vec{J}_s$  and  $\rho_s$  are surface densities of current and charge respectively [141], and  $\vec{n}_{12}$  is a unit vector pointing from region 1 to region 2. These equations are local. If one wants to describe macroscopic material as it will be the case in this work, then the Maxwell equations can be simplified, expressing  $\vec{D}$  and  $\vec{B}$  with respect to  $\vec{E}$  and  $\vec{H}$  via constitutive relations  $\vec{D} = f(\vec{E}, \vec{H})$  and  $\vec{B} = g(\vec{E}, \vec{H})$  where  $f$  and  $g$  are suitable functionals depending on the considered medium [82], [128]. The structures investigated in this work are based on semiconductor materials. These media are generally linear, homogeneous and dispersive. In some particular cases it is possible to find anisotropic semiconductors, like in ordered GaInP for instance [158]. If we assume that the media are homogeneous and isotropic then the constitutive relations reduce to

$$\vec{D} = \epsilon(\omega) \vec{E} \quad (2.9)$$

$$\vec{B} = \mu_0 \vec{H} \quad (2.10)$$

where  $\epsilon = \epsilon_1 + i\epsilon_2$  is the complex permittivity and  $\mu_0$  the vacuum permeability. If there are no source terms, the electric vector phasor satisfy the Helmholtz equation [46]:

$$\vec{\nabla}^2 \vec{E} + \omega^2 \mu_0 \epsilon \vec{E} = 0. \quad (2.11)$$

Introducing  $\vec{E} = \vec{E}_0 e^{i(\vec{k} \cdot \vec{r} - \omega t)}$  in this last equation we find that  $\vec{k} \cdot \vec{k} = \omega^2 \mu_0 \epsilon$  where the propagation vector  $\vec{k}$  can be complex:  $\vec{k} = \vec{k}_r + i\vec{k}_i$ ,  $\vec{k}_r$  and  $\vec{k}_i$  being real vectors. It follows from the last equality that  $\vec{k}_r$  and  $\vec{k}_i$  are not necessarily parallel: these waves are called inhomogeneous or non-uniform plane

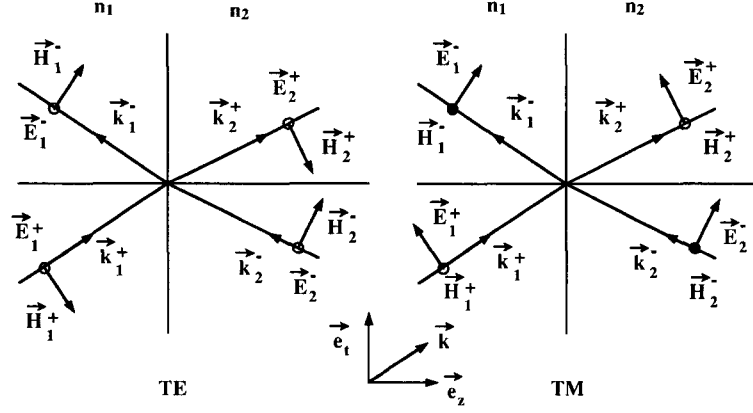


Figure 2.1: Reflection and refraction at the boundary between two dielectric media.

waves [39], [38] because the equiphase and equiamplitude planes are not the same. Uniform plane waves correspond to the case where  $\vec{k}_r$  and  $\vec{k}_i$  are parallel. If the medium is lossless ( $\epsilon_2 = 0$ ), then the plane waves are uniform (same equiamplitude and equiphase planes) but great care must be taken when dealing with absorbing media.

In the MCLEDs structures studied here, the index of refraction is piecewise constant. It is then necessary to describe the propagation of a plane wave inside a homogeneous layer and at the interface between two such layers.

Since we consider plane waves with arbitrary orientation, it is necessary to take into account the polarization of light. For monochromatic light, the three components of the electric field vary sinusoidally with time, with amplitudes and phases that are generally different: at each position of space the electric field vector moves in a plane and its endpoint traces an ellipse. The wave is said elliptically polarized. When the ellipse degenerates into a straight line, the wave is said to be linearly polarized. It is always possible to decompose any elliptically polarized wave as the sum of two linearly polarized waves with orthogonal polarization [130]. The choice of the direction of these two linear polarizations is arbitrary, but in layered structures it is convenient to make the choice of two well-defined polarizations known as TE and TM polarizations. In the TE case, the electric field is parallel to the interface plane and for the TM polarization this is the case for the magnetic field (see figure 2.1). This decomposition is very convenient since the TE and TM polarizations are conserved upon refraction or reflection at a planar interface, which means that it is possible to analyze the propagation of any plane wave in any multilayer structure by solving two uncoupled systems corresponding to the TE and respectively TM polarizations [9].

From the continuity relations and the Maxwell equations, it is possible to relate the fields amplitudes of the medium 1 with the ones of the medium 2, using the definitions given in figure 2.1 where we have considered that the axis  $e_z$  was perpendicular to the planes of interface of the optical structure.

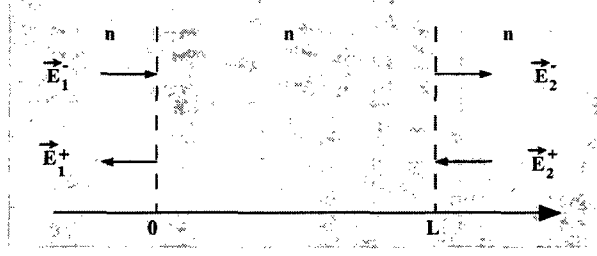


Figure 2.2: Propagation inside an homogeneous medium.

$$\begin{bmatrix} E_2^+ \\ E_2^- \end{bmatrix} = [I_{12}^s] \cdot \begin{bmatrix} E_1^+ \\ E_1^- \end{bmatrix} \quad (2.12)$$

with

$$[I_{12}^s] = \frac{1}{2k_{z2}} \begin{bmatrix} k_{z2} + k_{z1} & k_{z2} - k_{z1} \\ k_{z2} - k_{z1} & k_{z2} + k_{z1} \end{bmatrix} \quad (2.13)$$

for TE polarization and

$$\begin{bmatrix} E_2^+ \\ E_2^- \end{bmatrix} = [I_{12}^p] \cdot \begin{bmatrix} E_1^+ \\ E_1^- \end{bmatrix} \quad (2.14)$$

with

$$[I_{12}^p] = \frac{1}{2k_{z2}} \begin{bmatrix} \left(\frac{n_2}{n_1}\right) k_{z1} + \left(\frac{n_1}{n_2}\right) k_{z2} & \left(\frac{n_2}{n_1}\right) k_{z1} - \left(\frac{n_1}{n_2}\right) k_{z2} \\ \left(\frac{n_2}{n_1}\right) k_{z1} - \left(\frac{n_1}{n_2}\right) k_{z2} & \left(\frac{n_2}{n_1}\right) k_{z1} + \left(\frac{n_1}{n_2}\right) k_{z2} \end{bmatrix} \quad (2.15)$$

for the TM polarization. The indexes of refraction  $n_1$  and  $n_2$  are indicated on figure 2.1, and  $k_{z1}$ ,  $k_{z2}$  are the z components of the complex propagation vector  $\vec{k}_{1,2}$ .

Note that with this formalism,  $E_{1,2}^\pm$  correspond to the complex amplitudes of their vectors phasors:  $\vec{E}_{1,2}^\pm = E_{1,2}^\pm \vec{e}$  where  $\vec{e}$  is a normalized vector describing the orientation of the field ( $|\vec{e}| = 1$ ). Great care must be taken so as to use the right signs in the expressions of the matrix given above: the fields directions must coincide at normal incidence. Many different definitions can be found in the literature for the  $[I_{12}^{s,p}]$  matrixes expressions. The definition we choose has the following property:  $\text{Det}[I_{12}^s] = \text{Det}[I_{12}^p] = k_{z1}/k_{z2}$  where  $\text{Det}[A]$  is the determinant of the  $[A]$  matrix. This is very convenient since it will allow us to get formally the same matrix expressions for TE and for TM polarizations.

The matrix of propagation between two planes spaced by a distance  $L$  (see figure 2.2) is independent of the polarization and given by the following relation:

$$\begin{bmatrix} E_2^+ \\ E_2^- \end{bmatrix} = \begin{bmatrix} e^{ik_z L} & 0 \\ 0 & e^{-ik_z L} \end{bmatrix} \begin{bmatrix} E_1^+ \\ E_1^- \end{bmatrix} = [P_n] \cdot \begin{bmatrix} E_1^+ \\ E_1^- \end{bmatrix}. \quad (2.16)$$

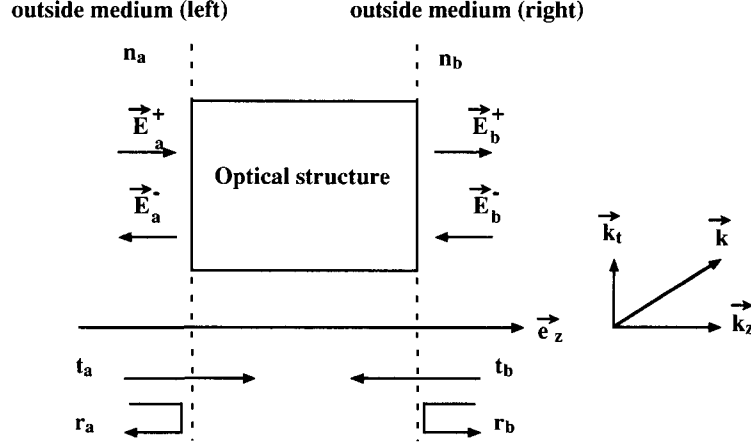


Figure 2.3: Definitions of the complex reflection and transmission coefficients for an arbitrary optical structure.

Using the transfer matrix formalism, it is then possible to express the matrix of an arbitrary structure by the product of interface  $[I_{ij}^{s,p}]$  and propagation  $[P_i]$  matrices [93], [80]. The matrix elements of  $[I_{12}^s]$ ,  $[I_{12}^p]$  and  $[P_n]$  depend on the projection of the wave vectors  $\vec{k}_1$  and  $\vec{k}_2$  onto the axis  $\vec{e}_z$ :  $k_{z1} = \vec{k}_1 \cdot \vec{e}_z$ ,  $k_{z2} = \vec{k}_2 \cdot \vec{e}_z$  with  $|\vec{k}_1| = 2\pi n_1/\lambda$  and  $|\vec{k}_2| = 2\pi n_2/\lambda$ . It is possible to relate  $k_{z1}$  and  $k_{z12}$  by using the Snell's law:

$$\vec{k}_1 \cdot \vec{e}_t = \vec{k}_2 \cdot \vec{e}_t \Leftrightarrow k_{t1} = k_{t2} \quad (2.17)$$

where

$$\begin{cases} |k_1|^2 = |k_{t1}|^2 + |k_{z1}|^2 \\ |k_2|^2 = |k_{t2}|^2 + |k_{z2}|^2. \end{cases} \quad (2.18)$$

Note that (2.17) is a generalized Snell's law and that matrices given in (2.12), (2.14) and (2.16) are equally valid for evanescent and propagating plane waves [93]. Since we can calculate the global transfer matrix  $[m]$  of an arbitrary multilayer structure (by multiplying interface and propagation matrices, for both polarizations), it is possible to define some complex reflection and transmission coefficients and to relate them to the matrix elements of  $[m]$ . In this work we will assume that the optical structure is limited by two semi-infinite lossless dielectric media with indexes of refraction  $n_a$  (left side) and  $n_b$  (right side). This structure is described on figure 2.3, where the arrows indicate whether the wave is a propagating ( $k_z > 0$ ) or a contrapropagating one ( $k_z < 0$ ). The direction of the  $\vec{k}$  vector is arbitrary and its amplitude can be complex.

The optical structure is made of an arbitrary sequence of dielectric layers whose index of refraction can be complex  $\tilde{n} = n + i\kappa$  with  $\kappa = \alpha \lambda / 4\pi$  where  $\alpha$ , in units of  $[cm^{-1}]$ , corresponds to the absorption coefficient if  $\alpha > 0$  or to the gain if  $\alpha < 0$ , and  $\lambda$  is the wavelength of the plane wave. The layers are assumed to be infinite in the planes perpendicular to  $\vec{e}_z$ .

The phasors of the plane waves propagating in each outside media are related by the matrix expression:

$$\begin{bmatrix} E_b^+ \\ E_b^- \end{bmatrix} = \begin{bmatrix} m_{11} & m_{12} \\ m_{21} & m_{22} \end{bmatrix} \begin{bmatrix} E_a^+ \\ E_a^- \end{bmatrix}. \quad (2.19)$$

It can be verified [131] that:

$$\text{Det}[m] = m_{11} m_{22} - m_{12} m_{21} = \frac{k_{za}}{k_{zb}} = \Delta \quad (2.20)$$

where  $k_{za} = \vec{k}_a \cdot \vec{e}_z$  and  $k_a = 2\pi n_a/\lambda$ . From the relation (2.19), we can define and express the transmission and reflection coefficients for the vector phasors:

$$r_a = \left. \frac{E_a^-}{E_a^+} \right|_{E_b^- = 0} = -\frac{m_{21}}{m_{22}} \quad (2.21)$$

$$t_a = \left. \frac{E_b^+}{E_a^+} \right|_{E_b^- = 0} = \frac{\Delta}{m_{22}} \quad (2.22)$$

$$r_b = \left. \frac{E_b^+}{E_b^-} \right|_{E_a^+ = 0} = \frac{m_{12}}{m_{22}} \quad (2.23)$$

$$t_b = \left. \frac{E_a^-}{E_b^-} \right|_{E_a^+ = 0} = \frac{1}{m_{22}}. \quad (2.24)$$

It is then possible to rewrite (2.19) using the reflection and transmission coefficients:

$$\begin{bmatrix} E_b^+ \\ E_b^- \end{bmatrix} = \frac{1}{t_b} \begin{bmatrix} t_a t_b - r_a r_b & r_b \\ -r_a & 1 \end{bmatrix} \begin{bmatrix} E_a^+ \\ E_a^- \end{bmatrix}. \quad (2.25)$$

Since we are interested in calculating the optical power of the fields propagating in the structure, we need to introduce the complex Poynting vector  $\vec{S}_c = \frac{1}{2} \vec{E} \wedge \vec{H}^*$  where  $\vec{E}$  and  $\vec{H}$  are the electric and respectively magnetic complex vector phasors. It can be demonstrated [141] that the real part of the complex Poynting vector is the time average over one period of oscillation  $T = 2\pi/\omega$  of the Poynting vector  $\vec{S} = \vec{E} \wedge \vec{H}$ :

$$\text{Re}(\vec{S}_c) = \langle \vec{S} \rangle = \frac{1}{T} \int_0^T \vec{S} dt. \quad (2.26)$$

Taking the real part of the complex Poynting theorem one get :



$$\iint_S \operatorname{Re}(\vec{S}_c) \cdot d\vec{S} + \iiint_V \frac{1}{2} \frac{|\vec{J}_c|^2}{\sigma} dV + \iiint_V \operatorname{Re} \left( \frac{1}{2} \vec{E} \cdot \vec{J}_i^* \right) dV = 0 \quad (2.27)$$

where  $\vec{J}_c$  is a conduction current (null in our case) and  $\vec{J}_i$  is an impressed current (related to a dipole emission for instance). The volume of integration is  $V$  and is delimited by the closed surface  $S$ . If we apply (2.27) to a box enclosing the interface between two lossless dielectrics without any sources, an expression representing the energy conservation is found, from which it is possible to define reflection and transmission coefficients for the power carried by the plane wave. These coefficients are generally defined as the reflectance  $R$  and the transmittance  $T$  [29]. Generalization of this result to any arbitrary optical structure is straightforward and gives:

$$R_a = |r_a|^2 \quad (2.28)$$

$$R_b = |r_b|^2 \quad (2.29)$$

$$T_a = \frac{1}{\Delta} |t_a|^2 \quad (2.30)$$

$$T_b = \Delta |t_b|^2 \quad (2.31)$$

and we see that  $T_a = T_b$  which means that the transmittance of the structure does not depend on the direction in which it is considered. This property is very general and only requires that the structure is reciprocal [29]. This is no longer true for reflectance:  $R_a = R_b$  is true for lossless media only. In lossy media, we have  $R_a + T_a + A_a = R_b + T_b + A_b = 1$  where  $A_a$  and  $A_b$  are the absorption coefficients.

## 2.2 Periodic structures and the Distributed Bragg Reflector (DBR)

For the optoelectronic devices we want to simulate, we will have to calculate the optical properties of distributed Bragg reflectors (DBRs) made of periodic sequence of layers. We present here a way to analytically express the transfer matrices of such periodic structures. The structure we first consider consists of  $N$  times a given and arbitrary multilayer structure which is described by its transfer matrix  $[m]$ . The outside medium is assumed to be the same on both sides of the structure (see figure 2.4).

We have then

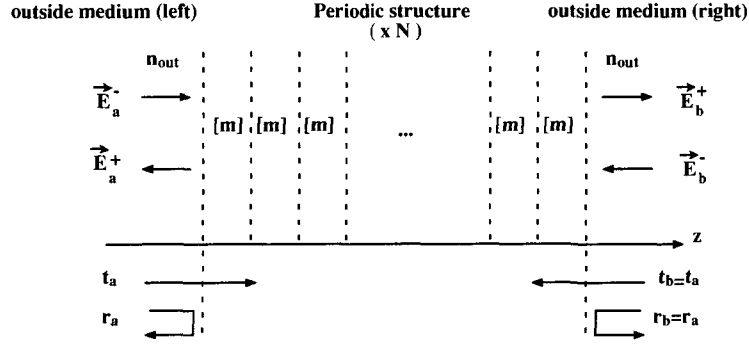


Figure 2.4: Periodic multilayer structure: definitions.

$$\begin{bmatrix} E_b^+ \\ E_b^- \end{bmatrix} = [m]^N \begin{bmatrix} E_a^+ \\ E_a^- \end{bmatrix} \quad (2.32)$$

where  $N$  is the number of periods in the structure and  $[m]$  is the transfer matrix of one period. Our purpose is to convert the product of the  $N$  matrices  $[m]^N$  into one single matrix  $[\tilde{m}]$ . The method we use here is discussed in [29] and [129]. The idea is to find the eigenvalues and eigenvectors of the matrix  $[m]$  and then to decompose the input vector on the eigenvectors basis. We define:

$$\begin{bmatrix} m_{11} & m_{12} \\ m_{21} & m_{22} \end{bmatrix} \begin{bmatrix} r_{1,2} \\ 1 \end{bmatrix} = \zeta_{1,2} \begin{bmatrix} r_{1,2} \\ 1 \end{bmatrix} \quad (2.33)$$

where  $\zeta_{1,2}$  are the eigenvalues of the matrix  $[m]$  and  $\begin{bmatrix} r_{1,2} \\ 1 \end{bmatrix}$  its eigenvectors. After simple manipulations, we find:

$$\zeta_{1,2} = \frac{1}{2} \text{Tr}[m] \pm \sqrt{\frac{1}{4} (\text{Tr}[m])^2 - \text{Det}[m]} \quad (2.34)$$

where  $\text{Det}[m]$  is the determinant of  $[m]$  and  $\text{Tr}[m]$  its trace. In the structure we consider here, the outside media are the same on the left and right hand sides. Using (2.20), the last expression can be simplified by setting  $\text{Det}[m] = 1$ .

It is simple to show that we also have:

$$r_{1,2} = \frac{m_{12}}{\zeta_{1,2} - m_{11}} \quad (2.35)$$

and that

$$\zeta_1 \cdot \zeta_2 = 1. \quad (2.36)$$

We can now decompose the input vector on the eigenvectors basis:

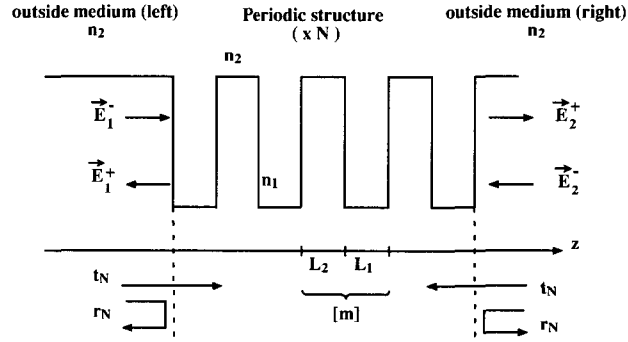


Figure 2.5: Symmetrical Distributed Bragg Reflector: definitions.

$$\begin{bmatrix} E_a^+ \\ E_a^- \end{bmatrix} = p \begin{bmatrix} r_1 \\ 1 \end{bmatrix} + q \begin{bmatrix} r_2 \\ 1 \end{bmatrix} \quad (2.37)$$

where  $p$  and  $q$  are given by:

$$\begin{cases} p = \frac{r_2 E_a^- - E_a^+}{r_2 - r_1} \\ q = \frac{E_a^+ - r_1 E_a^-}{r_2 - r_1} \end{cases} \quad (2.38)$$

After simple manipulations we get finally:

$$[m]^N = \underbrace{[m] \cdots [m]}_N = [\tilde{m}] = \begin{bmatrix} \tilde{m}_{11} & \tilde{m}_{12} \\ \tilde{m}_{21} & \tilde{m}_{22} \end{bmatrix} \quad (2.39)$$

with

$$[\tilde{m}] = \frac{1}{r_2 - r_1} \begin{bmatrix} r_2 \zeta_2^N - r_1 \zeta_1^N & r_1 r_2 (\zeta_1^N - \zeta_2^N) \\ (\zeta_2^N - \zeta_1^N) & r_2 \zeta_1^N - r_1 \zeta_2^N \end{bmatrix}. \quad (2.40)$$

Note that this matrix is very general: it is possible to utilize it to calculate the transfer matrix of a lossy structure at any wavelength and any angle. The only condition is that the medium is reciprocal, which is the case for the media we consider.

We can utilize these results to calculate the complex reflection and transmission coefficients ( $r_N$  and  $t_N$ ) of the layer sequence presented on figure 2.5.

This structure is referred to as a Distributed Bragg Reflector (DBR). It is a stack of semiconductor layers with two alternating indices of refraction that we call  $n_1$  and  $n_2$  with  $n_2 > n_1$ ,  $N$  being the number of layers of index  $n_1$ . We define the layers thicknesses as  $L_1$  and  $L_2$  and we assume that the whole structure is lossless ( $n_1$  and  $n_2$  are real). Let us consider an incoming plane wave of wavelength  $\lambda_0$  with a wave vector  $\vec{k}_0$ . As the plane wave propagates into the structure, it undergoes

multiple reflections. The multiple interferences (at normal incidence) will be constructive if the phase shift corresponding to one period is a multiple of  $2\pi$ :  $\frac{2\pi}{\lambda_0} n_1 L_1 + \frac{2\pi}{\lambda_0} n_2 L_2 = 2\pi m$  where  $m$  is an integer [9]. This is equivalent to write the Bragg condition for diffraction in periodic structures:  $\vec{k}_{diffracted} = \vec{k}_{incident} + m\vec{q}$  where  $\vec{q}$  is oriented along the direction of periodicity (axis  $\vec{e}_z$ ). It is possible to show that the highest reflectivity is obtained when the high and the low refractive index layers are each a quarter wavelength thick [93], thus:  $L_1 = \lambda_0/4n_1$  and  $L_2 = \lambda_0/4n_2$ . If the number of pairs is high enough, this result is valid for a range of wavelengths different from the Bragg wavelength  $\lambda_0$ , which defines the stopband width of the mirror. Using the formalism presented above for periodic structures, the reflection coefficient of the DBR defined on figure 2.5 is given by:

$$r_N = |r_N| e^{i\varphi_N} = \frac{\tilde{m}_{12}}{\tilde{m}_{22}} = \frac{r_1 r_2 (\zeta^N - \zeta^{-N})}{r_2 \zeta^N - r_1 \zeta^{-N}} \quad (2.41)$$

where  $\zeta = \frac{1}{2} Tr[m] + \sqrt{\frac{1}{4} (Tr[m])^2 - 1}$  and  $[m]$  is the matrix corresponding to one period of the stack (see figure 2.5). Note that the positions of the planes limiting the DBR structure correspond to the first interfaces between high index outside media and low index layers. The method presented leads to analytical expressions for the complex reflection and transmission coefficients of symmetrical DBRs. They will be used to derive simple analytical approximations in chapter 4. The other advantage of this method is that a product of  $N$  matrices can be converted into a single matrix. This allows very efficient and rapid numerical simulations, especially in the case of top-emitting MCLEDs which require a high number of DBR periods as we will see.

The detailed calculations of the  $r_N$  and  $t_N$  properties are given in the Appendix A. We summarize here the important results. Let us first examine the properties of the DBR at normal incidence. It is possible to demonstrate that  $|r_N(1 - \delta)| = |r_N(1 + \delta)|$  and  $\varphi_N(1 - \delta) = -\varphi_N(1 + \delta)$  where  $\delta = \frac{\lambda_0}{\lambda}$  can be considered as the normalized energy of the plane wave. This means that the reflection (and also the transmission) coefficients have symmetry properties with respect to the energy (and not wavelength). As an example, we give in figure 2.6 the amplitude and the phase of  $r_N$  in the case of  $n_1 = 3.1$  and  $n_2 = 3.5$  for  $N = 50$  pairs. We will use these indexes values throughout the chapters 2 and 4 because they correspond to the refractive indexes of  $Al_{0.5}Ga_{0.5}As$  and  $AlAs$  respectively (see appendix B). The DBRs used in practice for the red MCLEDs presented in this work are indeed made of such materials. It must be strongly emphasized that the theoretical results obtained for DBRs in this chapter assume that all the layers are lossless. In practice, these assumptions are correct for  $Al_{0.5}Ga_{0.5}As/AlAs$  based DBRs operating at 650 nm like it will be the case in this work. Note also that we neglect the material dispersion.

The reflectivity is almost constant within the interval  $[\delta_1^N, \delta_2^N]$  which defines the stopband of the mirror. The phase varies almost linearly with respect to  $\delta$  and is zero at the center of the stopband (at the Bragg frequency defined by  $\delta = 1$ ). As  $N$  converges towards  $\infty$ , then the reflectivity converges towards unity in the stopband defined by  $[\delta_1^\infty, \delta_2^\infty]$ . It is possible to analytically calculate the stopband

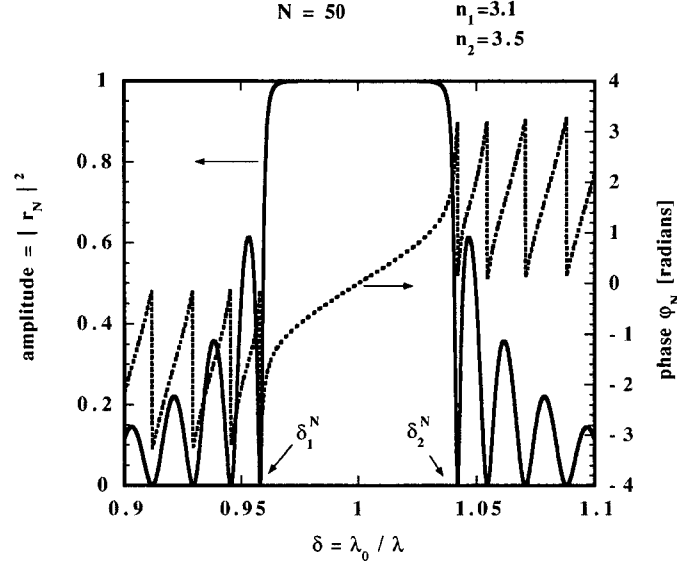


Figure 2.6: Amplitude and phase of the reflection coefficient  $r_N$  calculated at normal incidence for a DBR with  $N=50$  pairs and refraction indexes  $n_1 = 3.1$  and  $n_2 = 3.5$ .

width of an infinite DBR [93]:

$$\delta_2^\infty - \delta_1^\infty = 2 - \frac{2}{\pi} \arccos \left[ \frac{(n-1)^2 - 4n}{(n+1)^2} \right] \quad (2.42)$$

where  $n = \frac{n_2}{n_1} > 1$ .

We calculate this formula using the condition  $\frac{1}{2} Tr[m] = 1$ , which defines two different regimes for  $\zeta$ . It is straightforward to show that if  $\frac{1}{2} Tr[m] < 1$  then  $\zeta$  is imaginary which corresponds to  $\delta < \delta_1^\infty$  or  $\delta_2^\infty < \delta$ , hence to propagating waves. If  $\frac{1}{2} Tr[m] > 1$  then  $\zeta$  is real and  $\delta_1^\infty < \delta < \delta_2^\infty$ : this corresponds to evanescent waves [129]. We are then in the case of a photonic bandgap (the light is not allowed to propagate in the DBR, hence the name stopband).

For a finite number of pairs  $N$ , the stopband width (exact formula) is given by:

$$\delta_2^N - \delta_1^N = 2 - \frac{2}{\pi} \arccos \left[ \frac{(n-1)^2 - 4n \cos(\frac{\pi}{N})}{(n+1)^2} \right] \quad (2.43)$$

which converges towards (2.42) when  $N$  increases towards infinity ( $n = \frac{n_2}{n_1} > 1$ ). Equation (2.43) shows that the stopband width decreases rapidly as the number of pairs in the DBR increases, and saturates to the value given in (2.42). Note that this definition of the stopband is based on the properties of the  $\zeta$  parameter. In practice, the DBRs used in MCLEDs are made of a periodic sequence of III/V semiconductor layers grown on a substrate and ended by air. The periodicity is then not perfect and the definition of the stopband used here, is no longer useful. Usually the stopband width is defined as the range of energy corresponding to a minimal reflectivity and then increases with the number of periods.

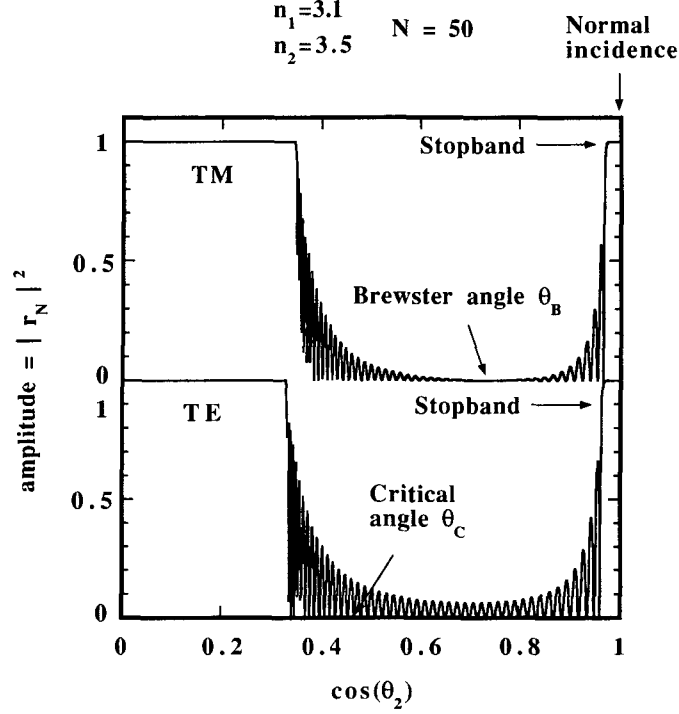


Figure 2.7: Amplitude of the complex reflection coefficient  $r_N$  calculated at the Bragg wavelength and plotted versus angle  $\theta_2$  for a symmetrical DBR with  $N=50$  pairs.

It is interesting to note that the stopband width  $\delta_1^N - \delta_2^N$  is exactly equal to two for  $N = 1$ . This is because  $r_N$  is periodic with respect to  $\delta$ ,  $\delta = 2$  being the period. We demonstrate in the appendix A that the Bragg condition occurs at  $\delta = 1 + 2p$  ( $p$  integer).

We can calculate the amplitude and the phase of the complex reflection coefficient  $r_N$  for different angles and at a fixed wavelength. We choose to do the calculations at the Bragg frequency  $\delta = 1$  and for angles  $\theta_2$  varying between 0 and  $\pi/2$  in the medium of index  $n_2$ . We consider the same structures as before. The amplitude  $|r_N|^2$  is plotted on figure 2.7 (for TE and TM polarizations) and the phases are given on figure 2.8.

One can see that the reflectivity is high within an angular stopband and that the corresponding phase varies almost linearly with respect to the cosine of  $\theta_2$ . Outside this range, the amplitude of the reflection coefficient is rather small until total internal reflection occurs. The waves emitted in this angle range can "leak" inside the mirror. This is especially true for the TM polarization for which the transmission is unity at the Brewster angle ( $\tan\theta_B = n_1/n_2$ ). The critical angle between layer of index  $n_2$  and layer of index  $n_1$  is given by  $\sin\theta_c = n_1/n_2$ : if  $\theta_2 > \theta_c$  the plane wave coming from the medium of index  $n_2$  is totally reflected and an evanescent wave is transmitted in the layer of index  $n_1$ . In the DBR, the layer of index  $n_1$  is followed by another layer of index  $n_2$ : there is then the possibility for the evanescent wave to tunnel through the layer of index  $n_1$  so as it is transformed into a plane wave in the next layer of index  $n_2$ . This explains why the amplitude of the reflection coefficient is not equal to one at the critical angle. This effect is known as the total internal frustrated reflection [80].

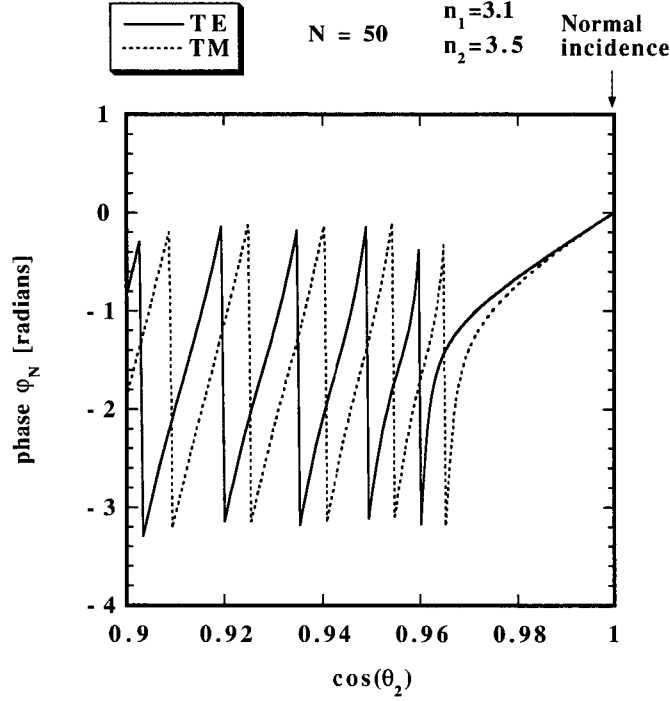


Figure 2.8: Phase of the complex reflection coefficient  $r_N$  calculated at the Bragg wavelength and plotted versus angle  $\theta_2$  for a symmetrical DBR with  $N=50$  pairs.

As it is shown in the Appendix A, the reflection coefficients  $r_N$  depend on the wavelength via the normalized energy. The angular dependence is held in the coefficients  $\gamma_{zi}$  which appear in the calculation of  $r_N$  with  $i$  being an index referring to the different dielectrics which make the structure. The  $\gamma_{zi}$  parameter is simply the normalized projection of the wave vector  $\vec{k}_i$  onto the axis  $z$ :

$$\gamma_{zi} = \frac{\vec{k}_i \cdot \vec{e}_z}{|\vec{k}_i|} = \cos(\theta_i) \quad (2.44)$$

with

$$|\vec{k}_i| = \frac{2\pi}{\lambda} n_i. \quad (2.45)$$

Since there are as many angles as there are different indexes of refraction in the structure, it is convenient to define an observation angle  $\theta_0$  and an observation index  $n_0$ , such that the Snell's law (2.17) is satisfied. It is then possible to express all the  $\gamma_{zi}$  with respect to  $\gamma_{z0} = \cos(\theta_0)$  and  $n_0$ :

$$\gamma_{zi} = \frac{1}{n_i} \sqrt{n_i^2 - n_0^2 + n_0^2 \cos(\theta_0)^2}. \quad (2.46)$$

As it will be shown in chapter 3, it is interesting to evaluate the emission properties in the outside medium (so as to evaluate the extraction efficiency), or in the cavity medium (so as to calculate the

fraction of emitted light which is lost in leaky and guided modes). The observation index  $n_0$  will then be equal to the outside medium index, respectively, to the cavity medium index. Considering equation (2.46),  $\gamma_{zi}$  can be either real (for propagating plane waves) or complex (for evanescent waves), which justifies the generalized transfer matrix expressions we chose at the beginning of this chapter.

The results shown on figures 2.6, 2.7 and 2.8 lead us to approximate the amplitude of the reflection and transmission coefficients by a constant value for coordinates  $(\delta, \theta_0)$  not too far from the Bragg condition  $(\delta = 1, \theta_0 = 0)$ . We show in Appendix A that the phase can be developed around the  $(\delta = 1, \theta_0 = 0)$  coordinates at the first order with respect to the  $\delta$  and  $\cos(\theta_0)$  variables. We find then the following exact relations (for lossless layers):

$$r_N = |r_N| e^{i\varphi_N} \quad (2.47)$$

$$t_N = |t_N| e^{i(\varphi_N + \frac{\pi}{2})} \quad (2.48)$$

$$|r_N|^2 + |t_N|^2 = 1 \quad (2.49)$$

$$|r_N(\delta = 1, \theta_0 = 0)| = \frac{n^{2N} - 1}{n^{2N} + 1} \equiv r_N^0 \quad (2.50)$$

$$\left. \frac{d\varphi_N}{d\delta} \right|_{(\delta=1, \theta_0=0)} = \frac{\pi}{2} \left[ \left( \frac{n+1}{n-1} \right) r_N^0 - 1 \right] \equiv D_\delta^N \quad (2.51)$$

$$\left. \frac{d\varphi_N}{d\cos\theta_0} \right|_{(\delta=1, \theta_0=0)} = \frac{\pi}{2} \tilde{n}^2 \left[ \left( \frac{2n^2 - n + 1}{n-1} \right) r_N^0 - 1 \right] \equiv D_\theta^N \quad (2.52)$$

where  $n = n_2/n_1 > 1$  and  $\tilde{n} = n_0/n_2 \leq 1$ . It is interesting to note that when  $\tilde{n} = 1$ ,  $D_\theta^N$  and  $D_\delta^N$  are simply related by the relation:

$$D_\theta^N - D_\delta^N = \pi n r_N^0. \quad (2.53)$$

We can use these relations to approximate the complex coefficients of reflection and transmission around the  $(\delta = 1, \theta_0 = 0)$  coordinates:

$$r_N = r_N^0 e^{i[D_\theta^N(\cos\theta_0 - 1) + D_\delta^N(\delta - 1)]} \quad (2.54)$$



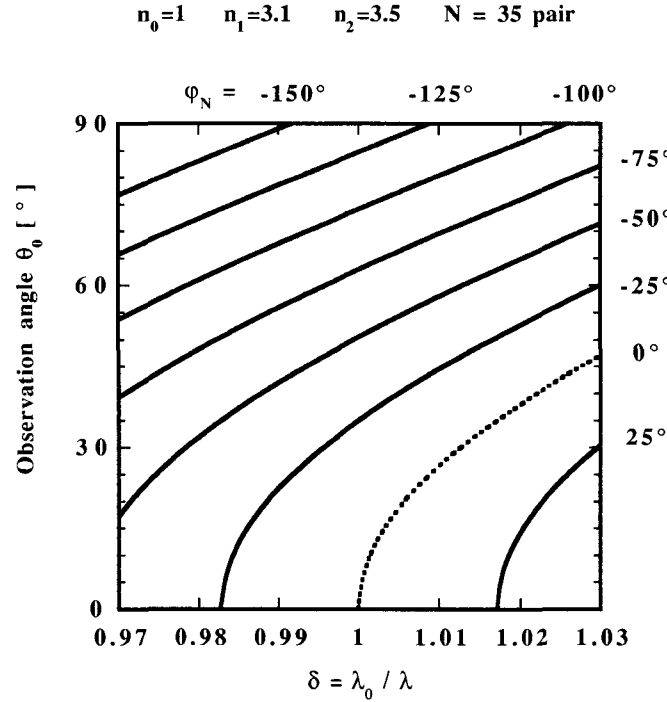


Figure 2.9: Contour plot of the phase  $\varphi_N$  of the reflection coefficient  $r_N$  for a symmetrical DBR having  $N=35$  pairs. Indexes of refraction are  $n_1 = 3.1$  and  $n_2 = 3.5$  and the observation index is  $n_0 = 1$ .

$$t_N = \sqrt{1 - (r_N^0)^2} e^{i[D_\theta^N (\cos \theta_0 - 1) + D_\delta^N (\delta - 1) + \frac{\pi}{2}]} \quad (2.55)$$

These relations are very important, and will be used throughout the rest of this work. For angles close to normal incidence it is then possible to approximate the phase  $\varphi_N$  of the reflection coefficient  $r_N$  by the following expression:  $\varphi_N = D_\theta^N (\cos \theta_0 - 1) + D_\delta^N (\delta - 1)$ . The contour lines of  $\varphi_N$  in the  $(\delta, \theta_0)$  plane are plotted on figure 2.9. A DBR with  $N = 35$  pairs and the same indexes of refraction as before is considered. The index of observation is chosen to be  $n_0 = 1$ , which means that if the observation angle  $\theta_0$  runs from 0 to  $\pi/2$ , then the angles in the layer of index  $n_2$  will be scanned from 0 to  $\theta_2 = \arcsin(1/n_2) = 16.6^\circ$ . The normalized energy  $\delta$  is chosen to vary inside the stopband limits of the reflectivity curve measured at normal incidence. The points  $(\delta_{FP}, \theta_0)$  for which the phase of the reflection coefficient is zero are plotted on dotted line. Since these points correspond to the Bragg condition, the stopband of the reflectivity shifts towards smaller wavelengths as the angle is increased:  $\delta_{FP} - 1 = (D_\theta^N / D_\delta^N) (1 - \cos \theta_0)$  which gives an analytical approximation of the DBR angle-energy dispersion relation.

It is now possible to consider a more complex structure (shown in figure 2.10) which is very useful in practice: an interface with an outside medium different from  $n_2$  is added on the left side of the DBR considered in figure 2.5.

The outside medium are  $n_a$  on the left side and  $n_2$  on the right side. We define their ratio as  $\bar{n} = \frac{n_a}{n_2}$ . We define the complex reflectivity coefficients on both sides of the structures as:  $r_a = |r_a| e^{i\varphi_a}$  and

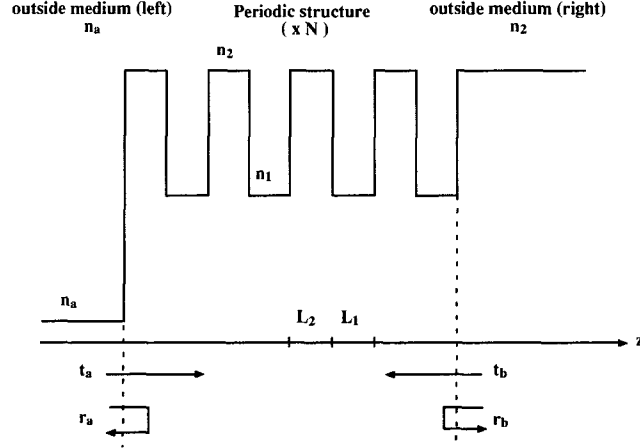


Figure 2.10: Asymmetric Distributed Bragg Reflector: definitions.

$r_b = |r_b| e^{i\varphi_b}$ . The amplitude of the reflection coefficient  $r_b$  calculated for the angle  $\theta_2$  in the medium of index  $n_2$  and for the Bragg wavelength is plotted on figure 2.11. Air is assumed to be the outside medium (left side), so  $n_a = 1$  and the mirror has 50 periods.

Because of the semiconductor/air interface, the plane waves propagating with an internal angle  $\theta_2$  greater than the critical angle  $\theta_2^c$  (defined as  $\sin\theta_2^c = n_a/n_2$ ) are totally reflected. Hence  $|r_b|^2$  is equal to 1 for  $\cos(\theta_2)$  varying between 0 and  $\cos\theta_2^c$ . For angles smaller than the critical angle, the reflectivity of the DBR varies with respect to the angle, displaying the same kind of behavior as the one displayed on figure 2.7. In our case, the angular stopband width of the DBR (without the air interface) is larger than the escape window defined by the range  $[\cos(\theta_2^c), 1]$ : the stopband part of figure 2.7 is then only visible, the rest of this curve being cut by the total internal reflection. The reflectivity at the center of the stopband is very high because of the high number of pairs chosen ( $N = 50$ ): for TE polarization the reflectivity is then close to the maximum for the whole angle range. We must point out that the displayed curve was calculated at the Bragg wavelength. We saw in figure 2.9 that the center of the stopband shifts with respect to the angle. Hence for a wavelength out of the wavelength stopband, the amplitude of  $r_b$  will vary significantly in the escape window. For TM polarization a clear dip is observed: the angular stopband width is smaller than for TE polarization and smaller than the escape window width. The dip simply corresponds to the edge of the angular stopband of the DBR in TM polarization. For higher outside medium index  $n_a$ , the escape window width is larger and first oscillations outside of the stopband appear as can be shown on figure 2.12 describing the case of epoxy ( $n_a = 1.5$ ). Our purpose is now to derive some simple approximations for  $r_a$  and  $r_b$  close to the Bragg condition.

The interface between the outside medium of index  $n_a$  and the first high index layer in the DBR is taken into account by using the coefficients  $\alpha = \frac{1}{2} (1 + \bar{n})$  and  $\beta = \frac{1}{2} (1 - \bar{n})$ .

Complete calculations of the following expressions can be found in Appendix A:

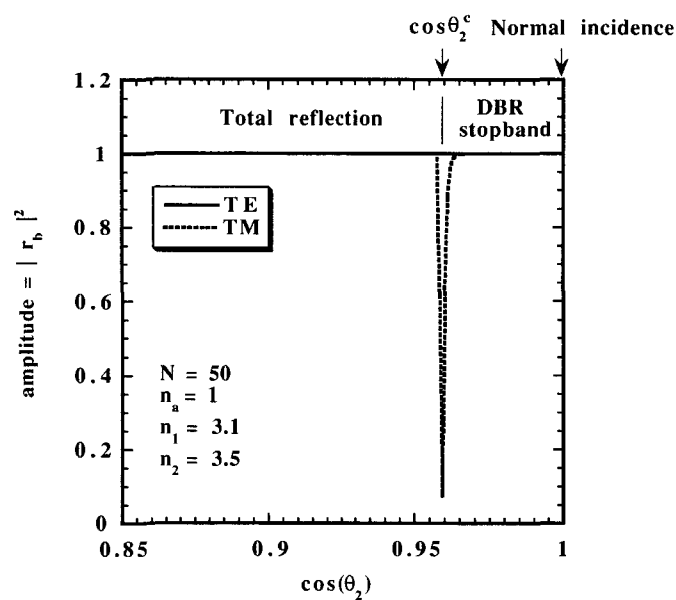


Figure 2.11: Amplitude of the reflection coefficient  $r_b$  defined from the right side of the structure and plotted versus the angle in this medium at the Bragg wavelength. The outside medium is air.

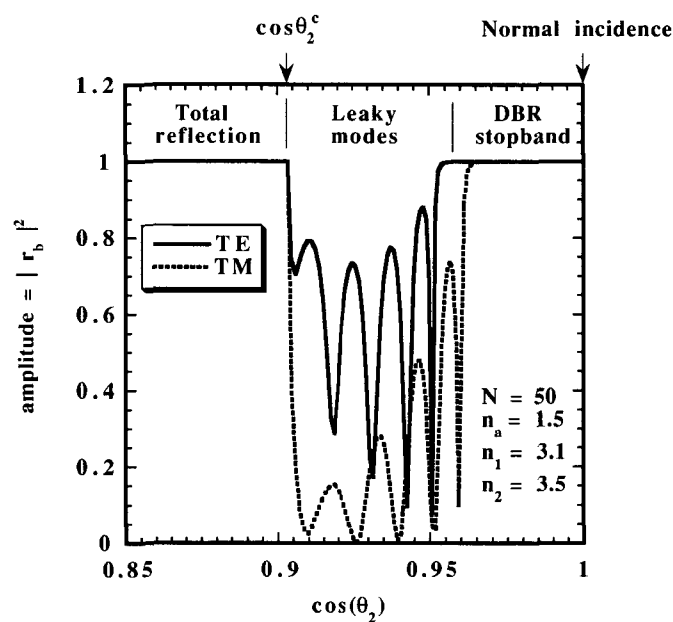


Figure 2.12: Amplitude of the reflection coefficient  $r_b$  defined from the right side of the structure and plotted versus the angle in this medium at the Bragg wavelength. The outside medium is epoxy with  $n_a = 1.5$ .

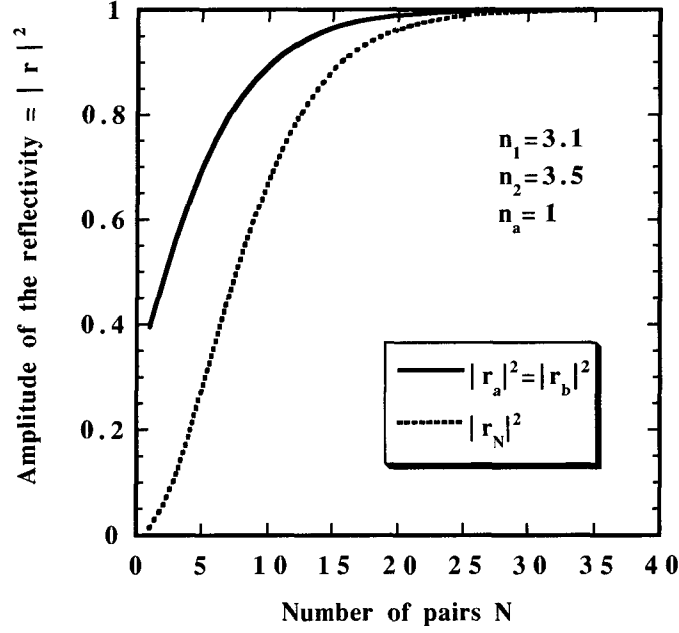


Figure 2.13: Amplitude of the reflection coefficient plotted versus the number of pairs  $N$  of a DBR with and without interface with air.

$$|r_a(\delta = 1, \theta_0 = 0)| = \frac{\alpha r_N^0 + \beta}{\alpha + \beta r_N^0} \equiv r_a^0 \quad (2.56)$$

$$|r_b(\delta = 1, \theta_0 = 0)| = r_a^0 \equiv r_b^0 \quad (2.57)$$

$$|t_a(\delta = 1, \theta_0 = 0)| = \frac{-\bar{n} [1 - (r_N^0)^2]}{\alpha + \beta r_N^0} \equiv t_a^0 \quad (2.58)$$

$$|t_b(\delta = 1, \theta_0 = 0)| = \frac{1}{\bar{n}} t_a^0 \equiv t_b^0. \quad (2.59)$$

Energy conservation (for lossless media) gives the following relations:

$$|r_a|^2 + \frac{1}{\bar{n}} |t_a|^2 = |r_b|^2 + \bar{n} |t_b|^2 = 1. \quad (2.60)$$

Figure 2.13 displays the reflectivity of the structure presented on figure 2.10 (interface with the air). One can see that adding this interface to a symmetrical DBR with  $N$  pairs increases significantly its reflectivity: with the chosen parameters it has the same effect as adding six pairs to the symmetrical DBR.

First derivatives of the phases with respect to the  $(\delta, \theta_0)$  coordinates are given below and calculated in Appendix A:

$$D_\delta^a = \left. \frac{d\varphi_a}{d\delta} \right|_{(\delta=1, \theta_0=0)} = \frac{(\alpha^2 - \beta^2) r_N^0}{[\alpha r_N^0 + \beta] [\alpha + \beta r_N^0]} [D_\delta^N + \pi] \quad (2.61)$$

$$\begin{aligned} D_\delta^b &= \left. \frac{d\varphi_b}{d\delta} \right|_{(\delta=1, \theta_0=0)} \\ &= \frac{2\alpha\beta + (\alpha^2 + \beta^2) r_N^0}{[\alpha r_N^0 + \beta] [\alpha + \beta r_N^0]} D_\delta^N + \frac{\alpha\beta [1 - (r_N^0)^2]}{[\alpha r_N^0 + \beta] [\alpha + \beta r_N^0]} \pi \end{aligned} \quad (2.62)$$

$$D_\theta^a = \left. \frac{d\varphi_a}{d\cos\theta_0} \right|_{(\delta=1, \theta_0=0)} = \frac{(\alpha^2 - \beta^2) r_N^0}{[\alpha r_N^0 + \beta] [\alpha + \beta r_N^0]} [D_\theta^N + \pi \tilde{n}^2] \quad (2.63)$$

$$D_\theta^b = \left. \frac{d\varphi_b}{d\cos\theta_0} \right|_{(\delta=1, \theta_0=0)} \quad (2.64)$$

$$= \frac{2\alpha\beta + (\alpha^2 + \beta^2) r_N^0}{[\alpha r_N^0 + \beta] [\alpha + \beta r_N^0]} D_\theta^N + \frac{\alpha\beta [1 - (r_N^0)^2]}{[\alpha r_N^0 + \beta] [\alpha + \beta r_N^0]} \pi \tilde{n}^2. \quad (2.65)$$

Figure 2.14 shows the dependence of  $D_\delta^N$ ,  $D_\delta^a$ ,  $D_\delta^b$ ,  $D_\theta^N$ ,  $D_\theta^a$  and  $D_\theta^b$  with respect to the number of pairs for the DBR structure previously shown on figure 2.10, and for an observation index  $n_0 = n_2$ . We choose this index of observation, because we will use these results in chapter 4.

The parameters plotted on figure 2.14 increase rapidly with respect to the number of pairs in the DBR, to reach an asymptotic value which corresponds to the case of the infinite DBR. The presence of the air interface makes  $D_\delta^b$  and  $D_\theta^b$  increase faster than  $D_\delta^a$  and  $D_\theta^a$ . It can be shown that the  $D_\delta$  parameters can be related to the concept of penetration depth into the DBR provided the number of pairs is high enough [29], [8]. We will not use this concept in our work since we will be interested in calculating the phase of DBRs with some small number of pairs and also because it is difficult to give a physical interpretation of  $D_\theta$ . We will rather consider  $D_\delta$  and  $D_\theta$  as convenient mathematical parameters which will be useful to approximate the phases near the Bragg resonance. As we did it previously, we can use these relations to approximate the complex coefficients of reflection and transmission around the  $(\delta = 1, \theta_0 = 0)$  coordinates for the structure described on figure 2.10:

$$r_a = r_a^0 e^{i[D_\delta^a (\cos\theta_0 - 1) + D_\delta^a (\delta - 1) + \pi]} \quad (2.66)$$

$$t_a = \sqrt{\tilde{n} [1 - (r_a^0)^2]} e^{i[D_\theta^a (\cos\theta_0 - 1) + D_\theta^a (\delta - 1) + \frac{3\pi}{2}]} \quad (2.67)$$

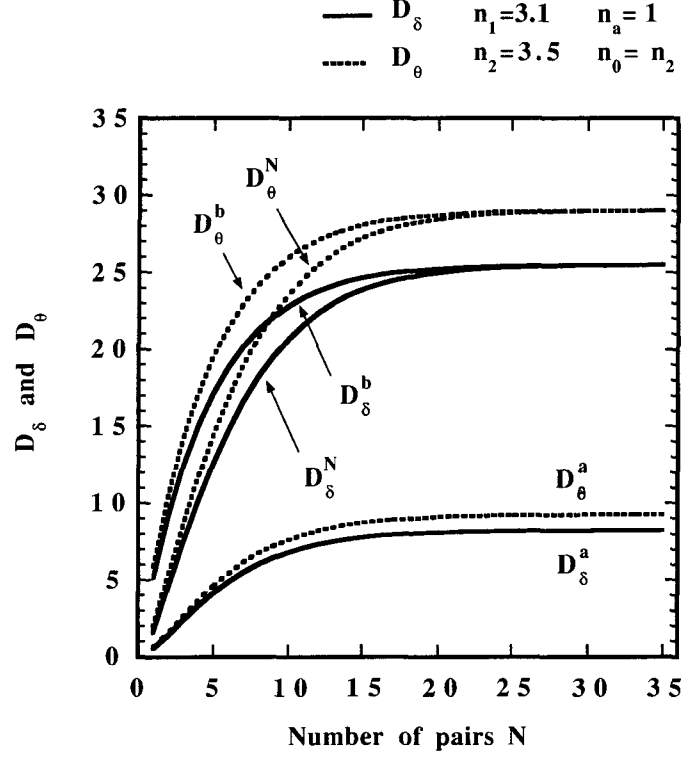


Figure 2.14: First derivative of the phase of the complex reflection coefficient with respect to the normalized energy and the angle cosine, versus the number of DBR pairs  $N$ .

$$r_b = r_b^0 e^{i[D_\theta^b(\cos \theta_0 - 1) + D_\delta^b(\delta - 1)]} \quad (2.68)$$

$$t_b = \sqrt{\frac{[1 - (r_b^0)^2]}{\bar{n}}} e^{i[D_\theta^b(\cos \theta_0 - 1) + D_\delta^b(\delta - 1) + \frac{\pi}{2}]} \quad (2.69)$$

These equations will be used in chapter 4, and will be very useful to take into account the existence of the air to semiconductor interface at the end of the top DBR of the MCLED structure.

### 2.3 Study of the Fabry-Pérot resonator

Basic properties of DBRs being presented, we can study the properties of the dielectric Fabry-Pérot resonator. This structure is made of two DBRs surrounding a dielectric cavity and has the properties to confine light at certain resonance frequencies. In practice, the DBRs used in our structures are made of  $Al_{0.5}Ga_{0.5}As/AlAs$  layers. The MCLED will be made of one such DBR grown on a GaAs substrate, followed by a given sequence of AlGaInP-based layers (defining the cavity of the resonator), and by a second DBR coupling the emission to an outside medium (air or epoxy typically). The generic structure is shown on figure 2.15. The purpose of this section is to describe the optical properties of the

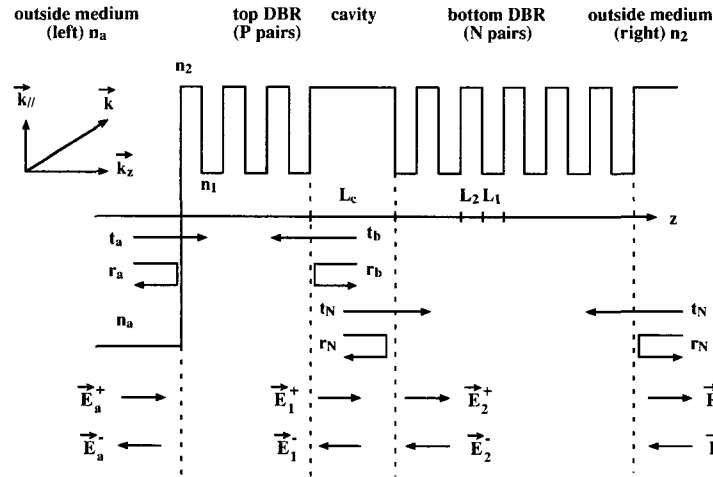


Figure 2.15: Fabry Pérot resonator: definitions.

passive structure: we will consider a plane wave of wavevector  $\vec{k}$  polarized either TE or TM, incoming from the left outside medium of index  $n_a$  and we will be interested in calculating the transmittance of the structure.

In order to calculate this parameter, we will use the following transfer matrices:

$$\begin{bmatrix} E_b^+ \\ E_b^- \end{bmatrix} = \frac{1}{t_N} \begin{bmatrix} t_N^2 - r_N^2 & r_N \\ -r_N & 1 \end{bmatrix} \begin{bmatrix} E_2^+ \\ E_2^- \end{bmatrix} \quad (2.70)$$

$$\begin{bmatrix} E_1^+ \\ E_1^- \end{bmatrix} = \frac{1}{t_b} \begin{bmatrix} \Delta t_b^2 - r_a r_b & r_b \\ -r_a & 1 \end{bmatrix} \begin{bmatrix} E_a^+ \\ E_a^- \end{bmatrix} \quad (2.71)$$

$$\begin{bmatrix} E_2^+ \\ E_2^- \end{bmatrix} = \begin{bmatrix} e^{2i\varphi_c} & 0 \\ 0 & e^{-2i\varphi_c} \end{bmatrix} \begin{bmatrix} E_1^+ \\ E_1^- \end{bmatrix} \quad (2.72)$$

where  $r_N$  and  $t_N$  correspond to the reflection and transmission coefficients of the bottom DBR (with  $N$  pairs), and  $r_a$ ,  $r_b$ ,  $t_a$  and  $t_b$  are related to the top DBR (with  $P$  pairs) including the interface with the outside medium of index  $n_a$ . We assume that the DBR stopbands are centered at the Bragg energy  $E_0 \sim \lambda_{Bragg}^{-1}$  such that their thicknesses are given by  $4n_1 L_1 = 4n_2 L_2 = \lambda_{Bragg}$ . The thickness of the cavity is for the moment arbitrary and equal to  $L_c$ . We can define the order of the cavity by the number:

$$m_c = \frac{2n_2 L_c}{\lambda_{Bragg}}. \quad (2.73)$$

A cavity for which  $n_2 L_c = \lambda_{Bragg}$  is called a lambda cavity and its order is  $m_c = 2$ . We recall that  $\Delta = k_{za}/k_{z2}$ , and  $\varphi_c = k_{z2} L_c/2$ .

The transmission coefficient of the whole structure (considered from the left side), is given by:

$$t = \frac{E_b^+}{E_a^+} \Big|_{E_b^- = 0} = \frac{t_N t_b e^{2i\varphi_c}}{1 - r_N r_b e^{4i\varphi_c}}. \quad (2.74)$$

Using (2.30), the transmittance of the structure is:

$$T = \frac{1}{\Delta} |t|^2. \quad (2.75)$$

If we consider normal incidence,  $T$  can be calculated using the approximations proposed in the previous section:

$$T = \frac{T_{FP}}{1 + \left(\frac{2F}{\pi}\right)^2 \sin^2\left(\frac{\varphi}{2}\right)} \quad (2.76)$$

with

$$T_{FP} = \left(\frac{n_a}{n_2}\right) \frac{(t_N^0)^2 (t_b^0)^2}{(1 - r_N^0 r_b^0)^2} \quad (2.77)$$

and

$$F = \frac{\pi \sqrt{r_N^0 r_b^0}}{1 - r_N^0 r_b^0}. \quad (2.78)$$

For a given structure,  $T_{FP}$  and  $F$  are constant.  $T$  varies only with respect to the phase  $\varphi$  which is given by:

$$\varphi = 4\varphi_c + \varphi_N + \varphi_b = (2\pi m_c + D_\delta^N + D_\delta^b) \delta - (D_\delta^N + D_\delta^b) \quad (2.79)$$

where  $D_\delta^N$  and  $D_\delta^b$  were calculated in the previous section. On figure 2.16 is plotted the transmittance  $T$  calculated for a structure with  $P = 15$  and  $N = 35$  pairs in the top and respectively bottom DBRs. The indexes of refractions are  $n_1 = 3.1$ ,  $n_2 = 3.5$ ,  $n_a = 1$  and we assumed that the cavity was a lambda cavity.

The low transmittance window around  $\delta = 1$  originates from the stopbands of the two DBRs. One can observe a resonance centered on  $\delta = 1$  which is called the Fabry-Pérot (FP) mode. As we explained it in the previous section, the DBR can be considered as a photonic bandgap. If the cavity thickness is equal to the thickness of the high index DBR layer, then the whole structure is a DBR with  $P + N$  pairs. If the cavity thickness is different, then the cavity can be considered as an impurity in a large DBR structure. The Fabry-Pérot mode can then be regarded as an impurity level in a one-dimensional



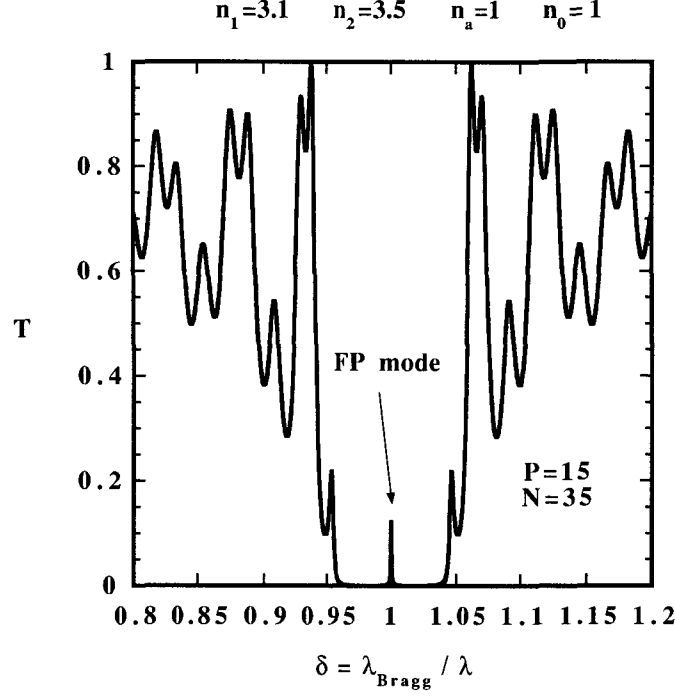


Figure 2.16: Transmittance of the Fabry-Pérot resonator plotted versus the normalized energy. The top and bottom DBRs have  $P=15$ , respectively  $N=35$  pairs. Indexes of refraction are  $n_1 = 3.1$  and  $n_2 = 3.5$  and an interface with air ends the top DBR.

photonic bandgap [145], [161], [73], [72]. Using the periodicity properties of the DBRs, it is clear that  $T$  is periodic with respect to  $\delta$ :  $T(\delta) = T(\delta + 2)$ .

Outside the stopband appear some periodic and narrow peaks of transmission which are called leaky modes. The explanation of this denomination will be explained in the chapter 4. Figure 2.17 displays the variation of  $T_{FP}$  with respect to the number  $P$  of pairs of the top mirror, assuming a fixed number of pairs for the bottom DBR. As expected  $T_{FP}$  increases with respect to  $P$  until the reflectivity of the top mirror equals the one of the bottom DBR. If  $P$  increases further, then  $T_{FP}$  decreases. This point will be important in the design of efficient top-emitting MCLEDs. In order to have efficient top emission, the number of pairs of the bottom DBR will have to be as high as possible. In the rest of this section we will fix the number of pairs of the bottom DBR to  $N = 35$ , and we will vary the number of pairs  $P$  of the top DBR only.

The parameter  $F$  is known as the finesse of the resonator and describes the "width" of the transmission mode. Figure 2.18 shows how  $F$  varies with  $P$  for the considered structure.

The finesse increases rapidly with respect to the number of pairs of the top DBR and saturates to a value  $F_{lim} = \pi \sqrt{r_N} / (1 - r_N)$  limited by the bottom DBR reflectivity. It is clear that the finesse increases towards infinity with the reflectivity of both DBRs. Considering equation (2.75), it is possible to approximate  $T$  by a Lorentzian lineshape by developing the  $\sin$  function around  $\delta = 1$ :

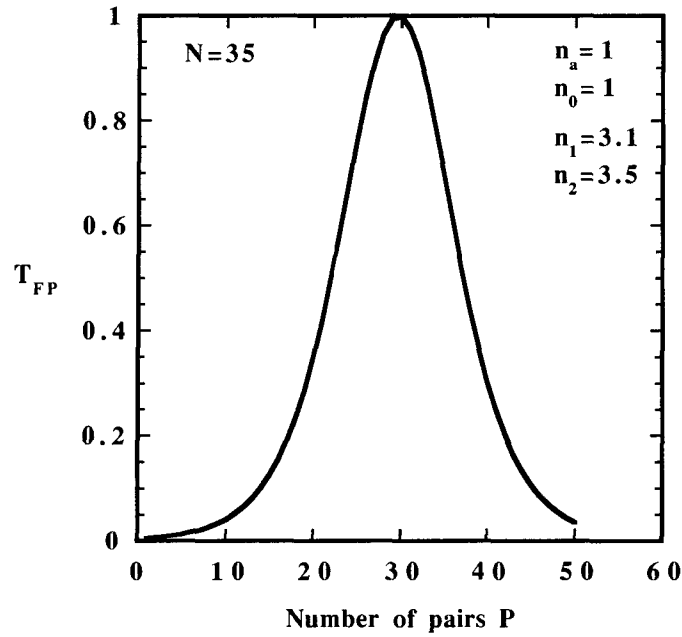


Figure 2.17: Amplitude of the Fabry-Pérot mode versus the number of pairs  $P$  of the top DBR. The bottom DBR has  $N=35$  pairs and indexes of refraction are  $n_1 = 3.1$  and  $n_2 = 3.5$ . An interface with air ends the top DBR.

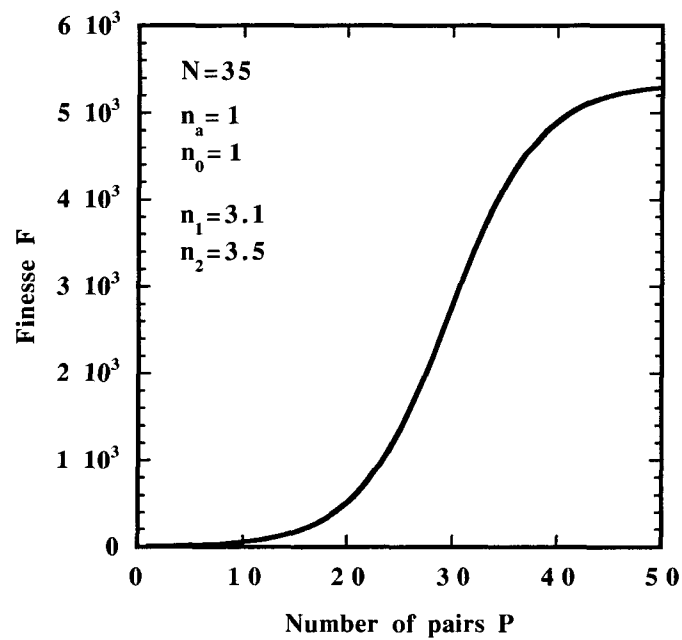


Figure 2.18: Finesse of the Fabry-Pérot resonator plotted versus the number of pairs  $P$  of the top DBR. The bottom DBR has  $N=35$  pairs and indexes of refraction are  $n_1 = 3.1$  and  $n_2 = 3.5$ . An interface with air ends the top DBR.

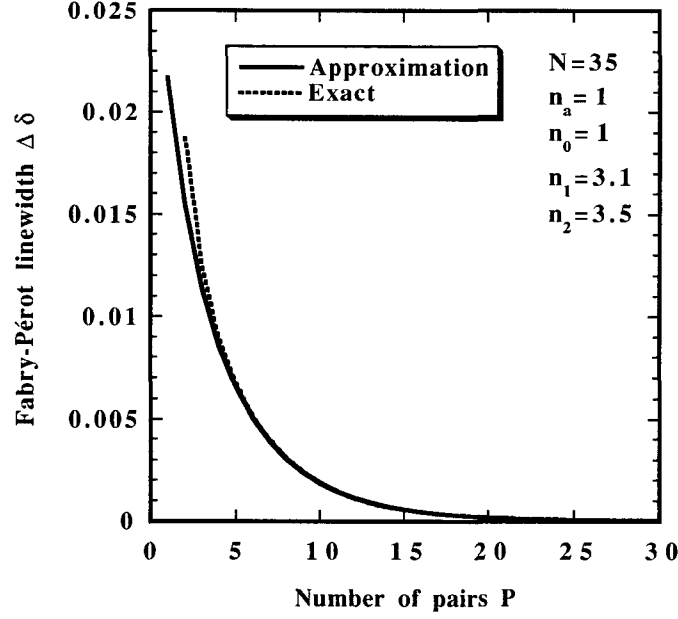


Figure 2.19: Fabry-Pérot mode linewidth plotted versus the number of pairs  $P$  of the top DBR. The bottom DBR has  $N=35$  pairs and indexes of refraction are  $n_1 = 3.1$  and  $n_2 = 3.5$ . An interface with air ends the top DBR.

$$T = \frac{T_{FP}}{1 + \left(\frac{F\varphi}{\pi}\right)^2}. \quad (2.80)$$

It is then possible to calculate the mode linewidth  $\Delta\delta = \delta_{FP}^2 - \delta_{FP}^1$  where  $T(\delta_{FP}^1) = T(\delta_{FP}^2) = T_{FP}/2$ :

$$\Delta\delta = \frac{2\pi}{F} \frac{1}{2\pi m_c + D_\delta^N + D_\delta^b}. \quad (2.81)$$

The mode linewidth is inversely proportional to the finesse, the order of the cavity and the  $D_\delta$  parameters. Figure 2.19 shows the dependence of  $\Delta\delta$  with respect to the number of pairs of the top DBR, using equation (2.81) and compares it to the linewidth exactly calculated by numerical simulations.

As expected the linewidth decreases rapidly with the number of pairs  $P$  and we also see that the approximation given by equation (2.81) is good for high reflectivity mirrors. When the number of pairs is small, the error coming from the Lorentzian approximation (2.80) starts to be significant.



## Chapter 3

# Description of quantum well spontaneous emission by a distribution of oscillating dipoles

### 3.1 Dipole emission in a multilayer structure (discrete dipoles)

The problem we want to solve is a generalization of the case studied by Lukosz in references [102], [103], [100], [99], [58]: we consider a single electric dipole of moment  $\vec{\mu}$  placed inside an arbitrary multilayer structure, surrounded by two lossless semi-infinite media of refractive indexes  $n_a$  and  $n_b$ . The dipole has an arbitrary orientation for the moment and is supposed to be placed in a lossless semiconductor of refractive index  $n_s$ . Figure 3.1 displays the structure investigated: the planes of the multilayer are called interface planes, and perpendicular to them is the plane of observation in which we want to calculate the dipole radiation. The axis  $\vec{e}_z$  is perpendicular to the interface planes.

The optical structures surrounding the dipole on its left and right sides can be described by their transfer matrix  $[m^0]$  and  $[m^2]$ . These matrices can be expressed in terms of the complex reflection and transmission coefficients as explained in chapter 2. The definitions of these complex coefficients are displayed on figure 3.1. Using plane wave expansion of the dipole emission, Lukosz demonstrates in his papers [102], [103], [100], [99] that the power per unit of solid angle  $\Pi_a$  (emitted in the outside medium of refractive index  $n_a$ ) by a dipole placed inside the optical structure, can be related to the power per unit of solid angle  $\Pi_\infty$  emitted by the same dipole radiating in an infinite medium of refractive index  $n_s$ . The corresponding mathematical expression is given below:

$$\Pi_a = \frac{\text{Re}(\vec{S}_a) \cdot \vec{e}_z dS}{\text{Re}(\vec{S}_\infty) \cdot \vec{e}_z dS} \frac{d\Omega_s}{d\Omega_a} \Pi_\infty. \quad (3.1)$$

The ratio  $d\Omega_s/d\Omega_a$  relates the solid angles in both media and can be calculated using Snell's law, which gives:

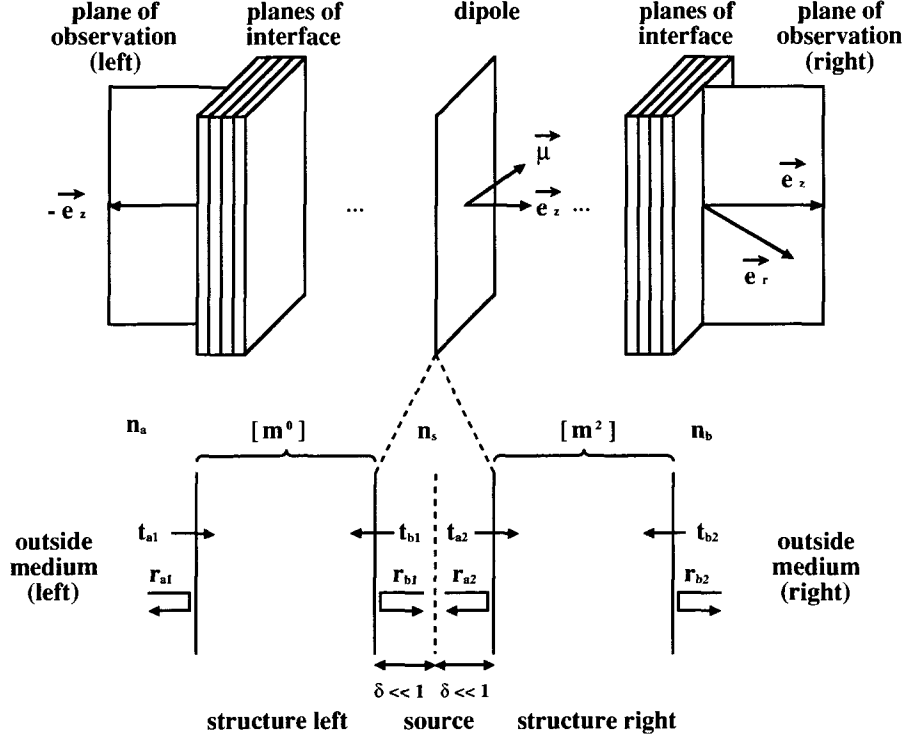


Figure 3.1: Structure investigated: definitions.

$$\frac{d\Omega_s}{d\Omega_a} = \frac{n_a k_{za}}{n_s k_{zs}}. \quad (3.2)$$

The expressions  $Re(\vec{S}_a) \cdot \vec{e}_z dS$  and  $Re(\vec{S}_\infty) \cdot \vec{e}_z dS$  correspond to the luminous intensities radiated by the dipole through a surface unit  $dS$  of the interface plane. From equation (3.1) we conclude that  $\frac{\Pi_i d\Omega_i}{Re(\vec{S}_i) \cdot \vec{e}_z dS}$  is constant across an interface (i is an index referring to the refractive index  $n_i$  of the layer considered).

The vector  $\vec{S}_a$  which appears in the expression (3.1) is the Poynting vector of the electromagnetic field emitted in the medium of refractive index  $n_a$  for each plane wave of the decomposition. To determine  $\vec{S}_a$  we need to calculate the electric field emitted by the source in this medium. We use the transfer matrix formalism for that purpose with the vector phasors defined on figure 3.2.

The arrows indicate the direction of the plane wave with respect to the axis  $\vec{e}_z$  only, and not the orientations of the propagation vector which can be arbitrary. We call  $A^+$  and  $A^-$  the phasors of the normalized fields emitted by the dipole in an infinite medium. We have  $A^+ = A^- = 1$  for all the angles since the angular dependence of the dipole emission is held in the  $\Pi_\infty$  term of expression (3.1). Very close to the dipole we define  $E_{as}^\pm$  and  $E_{sb}^\pm$  as the phasors on the left and respectively right sides of the structure. Since the source is located inside the structure, the inward pointing vector phasors  $E_a^+$  and  $E_b^-$  are zero in the outside media of refractive indexes  $n_a$  and  $n_b$ .

Because of the symmetry of the problem, we can decompose any dipole on three fixed dipoles  $\vec{\mu}_s$ ,

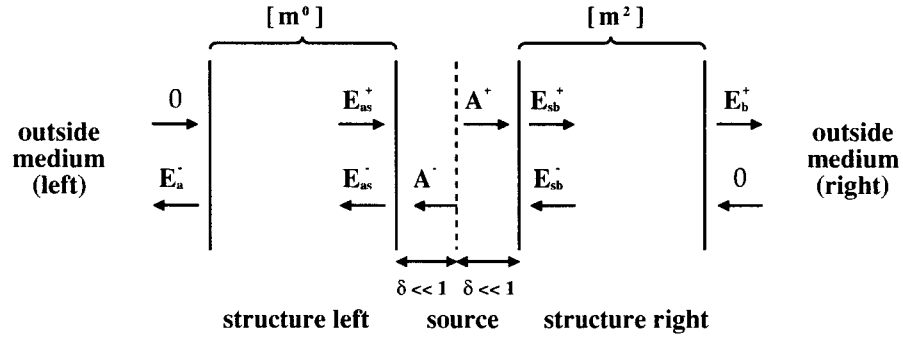


Figure 3.2: Definitions of the vector phasors.

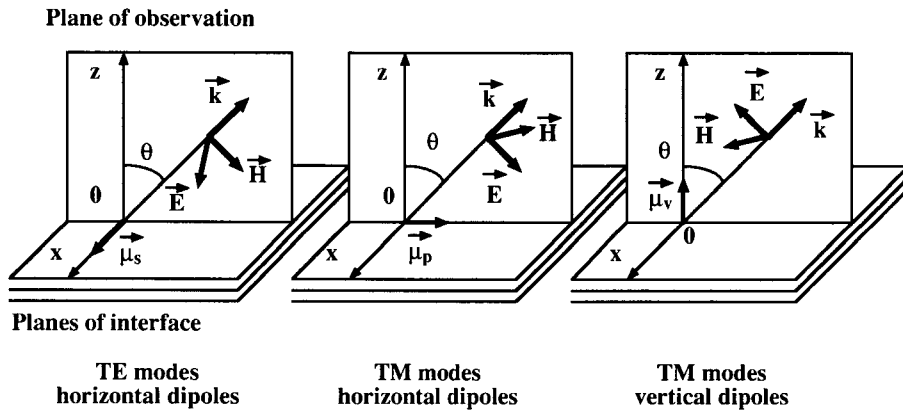


Figure 3.3: Definitions of horizontal and vertical dipoles.

$\vec{\mu}_p$  and  $\vec{\mu}_v$  which are defined on figure 3.3 and which form a base. We call horizontal dipoles the ones which are placed in the planes of interface, and vertical dipoles the ones perpendicular to these planes. If we consider the directions of these three dipoles with respect to a fixed plane of observation, we observe that the horizontal dipole perpendicular to the plane of observation emits TE waves in this last plane. The horizontal dipoles parallel to the plane of observation and the vertical dipoles emit TM waves in the plane of observation. The dipole we will consider in the following calculations is one of the three dipoles forming the orthonormal base: the waves emitted by the dipole in the plane of observation will then be either purely TE or purely TM. Using the *transfer matrix formalism* it is possible to relate the phasors using the  $[m^0]$  and  $[m^2]$  matrices:

$$\begin{bmatrix} E_{as}^+ \\ E_{as}^- \end{bmatrix} = \begin{bmatrix} m_{11}^0 & m_{12}^0 \\ m_{21}^0 & m_{22}^0 \end{bmatrix} \begin{bmatrix} 0 \\ E_a^- \end{bmatrix} \quad (3.3)$$

$$\begin{bmatrix} E_{sb}^+ \\ E_{sb}^- \end{bmatrix} = \begin{bmatrix} m_{11}^2 & m_{12}^2 \\ m_{21}^2 & m_{22}^2 \end{bmatrix} \begin{bmatrix} E_b^+ \\ 0 \end{bmatrix}. \quad (3.4)$$

From continuity considerations, one can link the phasors  $E_{sb}^\pm$  to the phasors  $E_{as}^\pm$  by the relation:

$$\begin{bmatrix} E_{sb}^+ \\ E_{sb}^- \end{bmatrix} = \begin{bmatrix} E_{as}^+ \\ E_{as}^- \end{bmatrix} + \begin{bmatrix} \pm A^+ \\ A^- \end{bmatrix} \quad (3.5)$$

where  $+A^+$  has to be used for horizontal dipoles and  $-A^+$  for vertical ones.

Using equations (3.3), (3.4) and (3.5), one can easily find the expressions of the phasors defined on figure 3.2:

$$E_a^- = \frac{t_{b1} [1 \pm r_{a2}]}{1 - r_{a2} r_{b1}} \quad (3.6)$$

$$E_b^+ = \frac{t_{a2} [r_{b1} \pm 1]}{1 - r_{a2} r_{b1}} \quad (3.7)$$

$$E_{as}^- = \frac{1 \pm r_{a2}}{1 - r_{a2} r_{b1}} \quad (3.8)$$

$$E_{as}^+ = \frac{r_{b1} [1 \pm r_{a2}]}{1 - r_{a2} r_{b1}} \quad (3.9)$$

$$E_{sb}^- = \frac{r_{a2} [r_{b1} \pm 1]}{1 - r_{a2} r_{b1}} \quad (3.10)$$

$$E_{sb}^+ = \frac{r_{b1} \pm 1}{1 - r_{a2} r_{b1}}. \quad (3.11)$$

The plus sign has to be used for horizontal dipoles in the previous expressions, whereas the minus one corresponds to vertical dipoles. Formula (3.6)-(3.11) are intuitively clear: the extracted field  $E_a^-$  for example, has a contribution coming from the field transmitted directly from the source ( $t_{b1}$ ) and a contribution coming from the field reflected by the right side of the structure and transmitted through its left side ( $t_{b1} r_{a2}$ ). The sum of these two factors is sometimes called the antinode factor.



The denominator  $1 - r_{a2} r_{b1}$  gives the multiple beam interference contribution due to the reflections between the left and the right sides of the structure. This last factor is characteristic from Fabry-Pérot interferometers and is often called Airy factor.

The last step before getting the detailed expressions for  $\Pi$  is to express the Poynting vector  $\vec{S}$  in terms of the electric field phasors  $\vec{E}^\pm$ . We are interested in calculating the Poynting phasors in the media of refractive indexes  $n_a$ ,  $n_b$  and  $n_s$  which were assumed to be real. In the transfer matrix formalism, the fields are decomposed into a wave propagating in the  $\vec{e}_z$  direction with a propagation vector  $\vec{k}^+$  with  $\vec{k}^+ \cdot \vec{e}_z > 0$  (its phasor being called  $\vec{E}^+$ ), and a wave propagating in the  $-\vec{e}_z$  direction with a propagation vector  $\vec{k}^-$  with  $\vec{k}^- \cdot \vec{e}_z < 0$  (its phasor being called  $\vec{E}^-$ ). Because of Snell's law, we have  $\vec{k}^+ \cdot \vec{e}_z = -\vec{k}^- \cdot \vec{e}_z$ . The two plane waves are characterized by their phasors  $\vec{E}^\pm = \vec{E}_0^\pm e^{i\vec{k}^\pm \cdot \vec{r}}$  for the electric field and  $\vec{H}^\pm = \frac{n}{\eta_0} \frac{\vec{k}^\pm \wedge \vec{E}^\pm}{|\vec{k}^\pm|}$  for the magnetic field, with  $\eta_0$  the vacuum impedance and  $n$  the refractive index of the medium. The Poynting phasor is then given by  $\vec{S}_c = (1/2) (\vec{E}^+ + \vec{E}^-) \wedge (\vec{H}^+ + \vec{H}^-)^*$  which finally gives:

$$\vec{S}_c \cdot \vec{e}_z = \frac{k_z}{2\eta_0} [|\vec{E}^+|^2 - |\vec{E}^-|^2]. \quad (3.12)$$

One should be very careful using this last relation which is strictly correct for lossless media only. If one wants to calculate the Poynting phasor in a lossy medium, then an expression of the form  $\vec{S}_c = (1/2) (\vec{E} \wedge \vec{H}^*) e^{-2\text{Im}(\vec{k}) \cdot \vec{r}}$  must be used [39], [38].

Using (3.1) and (3.12), we finally get for a lossless medium:

$$\Pi_a = \frac{n_a k_{za}^2}{n_s k_{zs}^2} |\vec{E}_a^-|^2 \quad \Pi_\infty = \frac{n_a k_{za}^2}{n_s k_{zs}^2} \frac{|t_{b1}|^2 |1 \pm r_{a2}|^2}{|1 - r_{a2} r_{b1}|^2} \Pi_\infty \quad (3.13)$$

$$\Pi_b = \frac{n_b k_{zb}^2}{n_s k_{zs}^2} |\vec{E}_b^+|^2 \quad \Pi_\infty = \frac{n_b}{n_s} \frac{|t_{b2}|^2 |r_{b1} \pm 1|^2}{|1 - r_{a2} r_{b1}|^2} \Pi_\infty. \quad (3.14)$$

Using (3.1) we can calculate the power per unit solid angle emitted on each side of the dipole:

$$\Pi_{as} = \frac{n_s k_{zs}^2}{n_a k_{za}^2} \left[ \frac{|\vec{E}_{as}^+|^2 - |\vec{E}_{as}^-|^2}{0 - |\vec{E}_a^-|^2} \right] \quad \Pi_a = \frac{[1 - |r_{b1}|^2] |1 \pm r_{a2}|^2}{|1 - r_{a2} r_{b1}|^2} \Pi_\infty \quad (3.15)$$

$$\Pi_{sb} = \frac{n_s k_{zs}^2}{n_b k_{zb}^2} \left[ \frac{|\vec{E}_{sb}^+|^2 - |\vec{E}_{sb}^-|^2}{|\vec{E}_b^+|^2 - 0} \right] \quad \Pi_b = \frac{[1 - |r_{a2}|^2] |r_{b1} \pm 1|^2}{|1 - r_{a2} r_{b1}|^2} \Pi_\infty. \quad (3.16)$$

We can check that for a symmetrical structure,  $\Pi_a = \Pi_b$  because  $r_{a2} = r_{b1}$ ,  $t_{b1} = t_{a2}$  and  $t_{b1} = \frac{k_{za}}{k_{zb}} t_{b2}$  (see chapter 2). The powers per unit of solid angle  $\Pi_a$ ,  $\Pi_b$ ,  $\Pi_{as}$  and  $\Pi_{sb}$  depend on: 1) the orientation of the dipole which fixes the angular dependence of  $\Pi_\infty$ , 2) the polarization to be considered in the calculation of the reflection and transmission coefficients, and 3) the sign of the  $|1 \pm r|^2$  terms as mentioned at the beginning of this section.

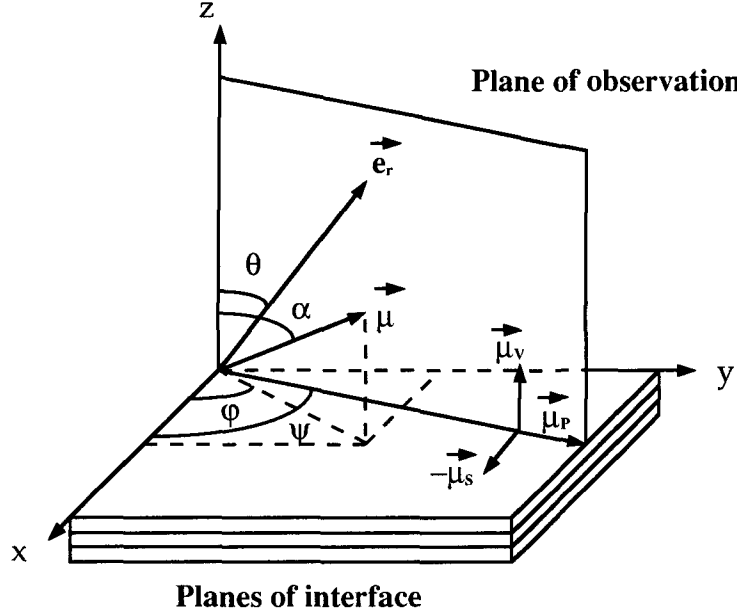


Figure 3.4: Angles definitions of an arbitrary dipole.

### 3.2 Dipole emission in a multilayer structure (3D distribution of dipoles)

In the previous section we have shown how to calculate the powers per unit of solid angle of the three discrete dipoles oriented in such a way that they form an orthogonal base. Because of the correspondence principle, it is possible to model the spontaneous emission of a semiconductor by the radiation of a collection of classical electric dipoles. We will assume in this section that we know the distribution of these dipoles which is described by a probability function  $g(\alpha, \varphi)$  where  $g(\alpha, \varphi) \sin(\alpha) d\alpha d\varphi$  is the probability per unit of solid angle that an electron-hole recombination radiates like an oscillating electric dipole with a moment oriented along  $\vec{\mu}(\alpha, \varphi)$ . We have of course :

$$\int_0^\pi \int_0^{2\pi} g(\alpha, \varphi) \sin(\alpha) d\alpha d\varphi = 1. \quad (3.17)$$

where the angles are defined on figure 3.4.

We assume that an orthonormal base  $(\vec{e}_x, \vec{e}_y, \vec{e}_z)$  is fixed with respect to the planes of interface. In this base we consider a plane perpendicular to the planes of interface, making an angle  $\psi$  with respect to the axis  $\vec{e}_x$ . This plane is the plane of observation in which we want to calculate the dipole emission for all the  $\vec{e}_r$  directions with  $\theta$  being the angle between  $\vec{e}_z$  and  $\vec{e}_r$ . We know that for an arbitrary dipole of moment  $\vec{\mu}$ , the electromagnetic far fields are given by:

$$\vec{H} = H_0 (\vec{e}_r \wedge \vec{\mu}) \quad (3.18)$$

$$\vec{E} = E_0 (\vec{e}_r \wedge \vec{\mu}) \wedge \vec{e}_r. \quad (3.19)$$

For the chosen plane of observation we define a dipole moment base  $(\vec{\mu}_x, \vec{\mu}_y, \vec{\mu}_z)$  as shown on figure 3.4. The angle  $\psi$  (varying between 0 and  $2\pi$ ), is chosen in such a way that we have  $\vec{\mu}_s = \vec{e}_y$  and  $\vec{\mu}_p = \vec{e}_x$  when  $\psi = 0$ . We calculated the emission of each of these dipoles in the previous section. If we decompose  $\vec{\mu}$  on the  $(\vec{\mu}_x, \vec{\mu}_y, \vec{\mu}_z)$  base, we have:

$$\vec{\mu} = \sin(\varphi - \psi) \sin(\alpha) \vec{\mu}_s - \cos(\varphi - \psi) \sin(\alpha) \vec{\mu}_p + \cos(\alpha) \vec{\mu}_v \quad (3.20)$$

and for the electromagnetic fields:

$$\vec{H} = \sin(\varphi - \psi) \sin(\alpha) \vec{H}_s - \cos(\varphi - \psi) \sin(\alpha) \vec{H}_p + \cos(\alpha) \vec{H}_v \quad (3.21)$$

$$\vec{E} = \sin(\varphi - \psi) \sin(\alpha) \vec{E}_s - \cos(\varphi - \psi) \sin(\alpha) \vec{E}_p + \cos(\alpha) \vec{E}_v \quad (3.22)$$

where  $\vec{E}_{s,p,v}$  and  $\vec{H}_{s,p,v}$  are the fields (perpendicular to each other) radiated by the dipoles of moments  $\vec{\mu}_{s,p,v}$ . The Poynting vector  $\vec{S}_c$  is given by  $\vec{S}_c = \frac{1}{2} \vec{E} \wedge \vec{H}^*$  which gives after a few calculations:

$$\vec{S}_c = \sin^2(\varphi - \psi) \sin^2(\alpha) \vec{S}_s + \cos^2(\varphi - \psi) \sin^2(\alpha) \vec{S}_p + \quad (3.23)$$

$$\cos^2(\alpha) \vec{S}_v - \cos(\varphi - \psi) \sin(\alpha) \cos(\alpha) \vec{S}_{pv} \quad (3.24)$$

where

$$\vec{S}_{s,p,v} = \frac{1}{2} \vec{E}_{s,p,v} \wedge \vec{H}_{s,p,v}^* \quad (3.25)$$

and

$$\vec{S}_{pv} = \frac{1}{2} (\vec{E}_p \wedge \vec{H}_v^* + \vec{E}_v \wedge \vec{H}_p^*). \quad (3.26)$$

The Poynting vectors  $\vec{S}_c$ ,  $\vec{S}_{s,p,v}$  and  $\vec{S}_{pv}$  are oriented along the  $\vec{e}_r$  vector and it is possible to calculate the averaged value of  $\vec{S}_c$  with respect to the dipole distribution, which gives:

$$\langle \vec{S}_c \rangle = \alpha_s(\psi) \vec{S}_s + \alpha_p(\psi) \vec{S}_p + \alpha_v(\psi) \vec{S}_v - \alpha_{pv}(\psi) \vec{S}_{pv} \quad (3.27)$$

with

$$\alpha_s(\psi) = \int_0^\pi \int_0^{2\pi} g(\alpha, \varphi) \sin^2(\varphi - \psi) \sin^3(\alpha) d\alpha d\varphi \quad (3.28)$$

$$\alpha_p(\psi) = \int_0^\pi \int_0^{2\pi} g(\alpha, \varphi) \cos^2(\varphi - \psi) \sin^3(\alpha) d\alpha d\varphi \quad (3.29)$$

$$\alpha_v(\psi) = \int_0^\pi \int_0^{2\pi} g(\alpha, \varphi) \cos^2(\alpha) \sin(\alpha) d\alpha d\varphi \quad (3.30)$$

$$\alpha_{pv}(\psi) = \int_0^\pi \int_0^{2\pi} g(\alpha, \varphi) \cos(\varphi - \psi) \sin^2(\alpha) \cos(\alpha) d\alpha d\varphi. \quad (3.31)$$

It is interesting to note that:

$$\alpha_s(\psi) + \alpha_p(\psi) + \alpha_v(\psi) = 1 \quad (3.32)$$

$$\alpha_s(\psi) = \alpha_s(\psi \pm \pi) \quad (3.33)$$

$$\alpha_p(\psi) = \alpha_p(\psi \pm \pi) = \alpha_s\left(\psi \pm \frac{\pi}{2}\right) \quad (3.34)$$

$$\alpha_v(\psi) = \alpha_v. \quad (3.35)$$

A cross term  $\vec{S}_{pv}$  appears in the chosen decomposition because the dipoles of moments  $\vec{\mu}_p$  and  $\vec{\mu}_v$  emit both TM waves. The cross terms involving two different polarizations cancel in the calculations since  $\vec{E}_{TE} \wedge \vec{H}_{TM}^* = \vec{E}_{TM} \wedge \vec{H}_{TE}^* = 0$ . We will show further that  $\alpha_{pv}(\psi)$  is zero in a lots of cases provided the  $g(\alpha, \varphi)$  function displays some symmetry properties.

We saw on section 3.1 that:

$$\Pi^{s,p,v} = \frac{\text{Re}\left(\vec{S}^{s,p,v}\right) \cdot \vec{e}_z dS}{\text{Re}\left(\vec{S}_{\infty}^{s,p,v}\right) \cdot \vec{e}_z dS} \frac{d\Omega_s}{d\Omega} \Pi_{\infty}^{s,p,v}. \quad (3.36)$$

After a few manipulations we can finally calculate the power per unit of solid angle  $\Pi$  emitted by the dipole distribution  $g(\alpha, \varphi)$  in the plane of observation defined by the angle  $\psi$ :

$$\begin{aligned} \Pi(\theta, \psi) = & \alpha_s(\psi) \Pi^s(\theta) + \alpha_p(\psi) \Pi^p(\theta) + \alpha_v(\psi) \Pi^v(\theta) \\ & - \alpha_{pv}(\psi) \sqrt{\Pi^p(\theta) \Pi^v(\theta)}. \end{aligned} \quad (3.37)$$

In order to calculate  $\Pi$ , we need to explicitly give the powers per unit of solid angle  $\Pi_{\infty}^{s,p,v}$  emitted by the dipoles of the chosen base in an infinite medium of refraction index  $n_s$ . The powers per unit of solid angle emitted by discrete dipoles in an infinite medium are given by [99]:

$$\Pi_{\infty}^s = \Pi_{\infty}^0 \quad (3.38)$$

$$\Pi_{\infty}^p = \Pi_{\infty}^0 \gamma_{zs}^2 \quad (3.39)$$

$$\Pi_{\infty}^v = \Pi_{\infty}^0 (1 - \gamma_{zs}^2) \quad (3.40)$$

where  $k_{zs} = (2\pi/\lambda) n_s \gamma_{zs}$ . The constant  $\Pi_{\infty}^0$  is a normalization constant that we can calculate by normalizing to one the power emitted by the dipole distribution:

$$\int_0^{\pi} \int_0^{2\pi} \Pi_{\infty}(\theta, \psi) \sin(\theta) d\theta d\psi = 1 \quad (3.41)$$

with

$$\begin{aligned} \Pi_{\infty}(\theta, \psi) = & \alpha_s(\psi) \Pi_{\infty}^s(\theta) + \alpha_p(\psi) \Pi_{\infty}^p(\theta) + \alpha_v(\psi) \Pi_{\infty}^v(\theta) \\ & - \alpha_{pv}(\psi) \sqrt{\Pi_{\infty}^p(\theta) \Pi_{\infty}^v(\theta)}. \end{aligned} \quad (3.42)$$

After some simple calculations, we find that  $\Pi_{\infty}^0 = 3/(8\pi)$ . As expected, this parameter depends neither on the dipole distribution nor on the position of the observation plane.

We finally have:

$$\Pi_{\infty}^s = \frac{3}{8\pi} \quad (3.43)$$

$$\Pi_{\infty}^p = \frac{3}{8\pi} \gamma_{zs}^2 \quad (3.44)$$

$$\Pi_{\infty}^v = \frac{3}{8\pi} (1 - \gamma_{zs}^2). \quad (3.45)$$

We can now calculate completely the power per unit of solid angle emitted by any dipole distribution (which has to be given), using equation (3.37) with  $\Pi^{s,p,v}$  given in section 3.1 and  $\Pi_{\infty}^{s,p,v}$  given in (3.43), (3.44) and (3.45).

It is interesting to calculate the  $\alpha_{s,p,v}$  and  $\alpha_{pv}$  coefficients for some special distributions. If we consider a 3D isotropic distribution of dipoles, we have  $g(\alpha, \varphi) = 1/(4\pi)$  which gives  $\alpha_s(\psi) = \alpha_p(\psi) = \alpha_v(\psi) = 1/3$  and  $\alpha_{pv} = 0$ . We have then:

$$\Pi_{3D} = \frac{1}{3} \Pi_s + \frac{1}{3} \Pi_p + \frac{1}{3} \Pi_v. \quad (3.46)$$

If we consider a 2D isotropic distribution of dipoles, we have  $g(\alpha, \varphi) = 1/(2\pi)$  which gives  $\alpha_s(\psi) = \alpha_p(\psi) = 1/2$  and  $\alpha_v(\psi) = \alpha_{pv}(\psi) = 0$ . We have then

$$\Pi_{2D} = \frac{1}{2} \Pi_s + \frac{1}{2} \Pi_p. \quad (3.47)$$

If the dipole distribution displays a rotational symmetry around the  $\vec{e}_z$  axis of the structure, we have then  $g(\alpha, \varphi) = g(\alpha)$  independent of the angle  $\varphi$ . This assumption is reasonable for bulk or quantum well emission in most of the semiconductors used to fabricate LEDs. We must point out that in some cases (depending on the growths conditions) the ternary compound GaInP (used for red LEDs) can display some ordering effects inducing some strong polarization anisotropies [48]. For that particular case the assumption  $g(\alpha, \varphi) = g(\alpha)$  is not valid. Using equations (3.28) with  $g(\alpha, \varphi) = g(\alpha)$ , we easily calculate that:

$$\alpha_s(\psi) = \alpha_p(\psi) = \pi \int_0^{\pi} g(\alpha) \sin^3(\alpha) d\alpha = \alpha_{//} \quad (3.48)$$

$$\alpha_v(\psi) = 2\pi \int_0^{\pi} g(\alpha) \cos^2(\alpha) \sin(\alpha) d\alpha = \alpha_{\perp} \quad (3.49)$$

$$\alpha_{pv}(\psi) = 0. \quad (3.50)$$

The  $\alpha_{//}$  and  $\alpha_{\perp}$  are simply connected by the relation (3.32), which gives:

$$2\alpha_{//} + \alpha_{\perp} = 1. \quad (3.51)$$

The power per unit of solid angle is then given by:

$$\Pi = \alpha_{//} [\Pi_s + \Pi_p] + \alpha_{\perp} \Pi_v. \quad (3.52)$$

## Chapter 4

# Top-emitting MCLEDs with two DBRs: analytical formalism and design rules

The objective of this chapter is to give some general design rules to optimize the extraction efficiency of top-emission MCLEDs based on two DBRs. We present a new analytical model which takes into account the source lineshape, the polarization and the number of pairs of the DBRs. These calculations generalize the model of Benisty [13].

### 4.1 Extraction efficiency of top-emitting MCLEDs: exact formula

The purpose of this work is to study red MCLEDs grown on GaAs substrates. Because of the GaAs being strongly absorbant at wavelengths below 700 nm, it is clear that a top-emission structure can be considered only. The realization of a bottom emission MCLED would require the use of transparent substrates (such as GaP for example). Conventional LEDs based on such transparent substrates exist [79], [88] but they require rather sophisticated wafer bonding techniques [57] which are not easy to implement. The basic MCLED structure which is extensively studied in this work is displayed on figure 4.1.

It consists of two distributed Bragg reflectors (DBRs) surrounding a cavity. The DBRs are made of alternating high ( $n_2$ ) and low ( $n_1$ ) index layers of thickness  $L_2$  and  $L_1$  with  $\lambda_{Bragg} = 4 n_1 L_1 = 4 n_2 L_2$  where  $\lambda_{Bragg}$  is the Bragg wavelength of the mirrors. We define the index ratio  $n = \frac{n_2}{n_1} > 1$  and  $\bar{n} = \frac{n_a}{n_2}$  where  $n_a$  is the refractive index of the outside medium in which we want to calculate the emission properties of the MCLED. We will restrict our study to the cases of  $n_a = 1$  (air) and  $n_a = 1.5$  (epoxy) which are of practical interest for packaging reasons. In this chapter we will assume that the materials are not absorbant ( $n_a$ ,  $n_1$  and  $n_2$  are then real parameters). We assume that the top (respectively bottom) DBRs are made of P (respectively N) periods where P and N correspond to the number of low index ( $n_1$ ) layers. The case of one-lambda cavities will be investigated in this work: as explained in reference [13], [143], the effective order of the cavity must be as small as possible so as to extract the

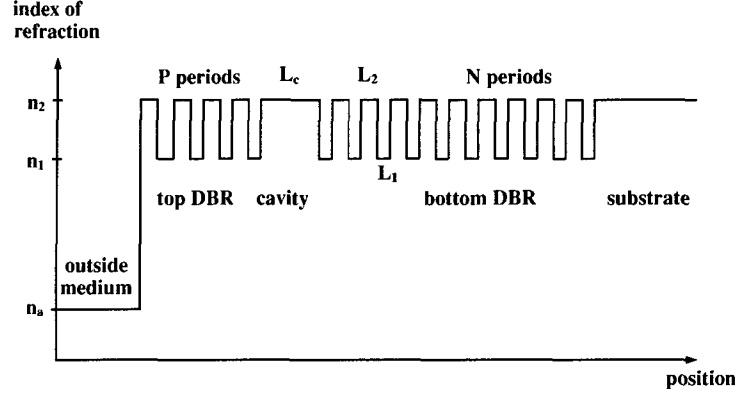


Figure 4.1: Basic structure investigated.

maximum of light in the outside medium. The cavity thickness  $L_c$  is then given by  $\lambda_{Bragg} = n_2 L_c$ .

We define two planes of observation perpendicular to the planes of interface: one in the outside medium of index  $n_a$  (in which we will calculate the power per unit of solid angle  $\bar{\Pi}_a$ ) and one in the cavity medium of index  $n_2$  (in which we will calculate the power per unit of solid angle  $\bar{\Pi}_2$ ). These planes are displayed on figure 4.2.

The angles  $\theta_a$  and  $\theta_2$  are defined in the same figure and are related by the Snell's law ( $n_2 \sin \theta_2 = n_a \sin \theta_a$ ). In order to simplify the notations, we introduce the parameter  $\gamma_{za}$  with  $\vec{k}_a \cdot \vec{e}_z = k_{za} = \frac{2\pi}{\lambda} n_a \gamma_{za}$  where  $\vec{k}_a$  is the propagation vector of the plane wave travelling in the medium of refractive index  $n_a$  with a wavelength  $\lambda/n_a$  (the same definition applies for  $\gamma_{z2}$ ). As done in previous chapters we introduce the normalized energy  $\delta = \frac{\lambda_{Bragg}}{\lambda}$ , where  $\lambda_{Bragg}$  is the Bragg wavelength which is assumed to be fixed. The parameters  $\gamma_{za}$  and  $\gamma_{z2}$  are related by the Snell's law:

$$\gamma_{z2} = \sqrt{1 - \left(\frac{n_a}{n_2}\right)^2 (1 - \gamma_{za}^2)}. \quad (4.1)$$

When the angle  $\theta_a$  scans the range  $[0, \pi/2]$  ( $\gamma_{za}$  scans the range  $[0, 1]$ ), then the angle  $\theta_2$  scans  $[0, \theta_2^c]$  (and  $\gamma_{z2}$  scans  $[0, \gamma_{z2}^c]$ ). The critical angle  $\theta_2^c$  is defined by  $\cos \theta_2^c = \gamma_{z2}^c = \sqrt{1 - \left(\frac{n_a}{n_2}\right)^2}$ . The solid angle element in the medium of index  $n_a$  is given by

$$d\Omega_a = \sin(\theta_a) d\theta_a d\varphi = d\gamma_{za} d\varphi. \quad (4.2)$$

It is related to the solid angle element in the medium of index  $n_2$  by the relation

$$n_a^2 \gamma_{za} d\Omega_a = n_2^2 \gamma_{z2} d\Omega_2 \quad (4.3)$$



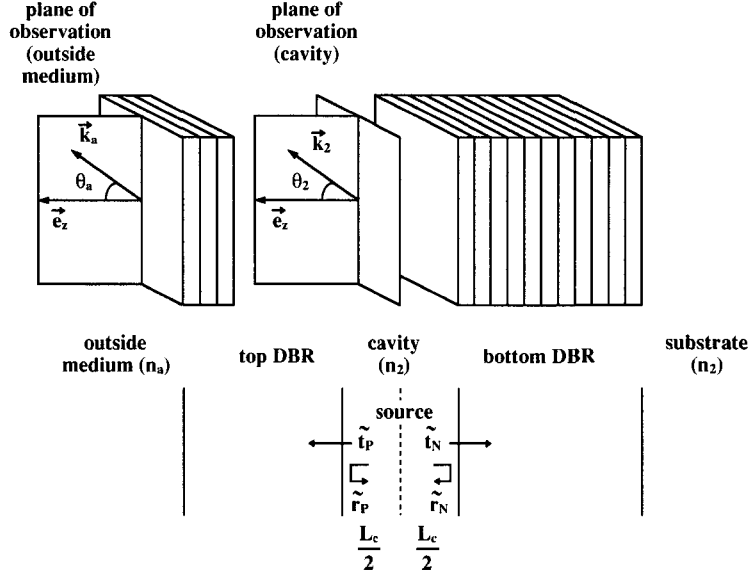


Figure 4.2: MCLED structure: definitions.

which can be derived by using the Snell's law. This means that when  $d\Omega_a$  scans the half-solid angle  $2\pi$  in the outside medium of index  $n_a$ , then  $d\Omega_2$  scans the extraction cone defined by the angle  $\theta_2$  in the medium of index  $n_2$ . Since we will always have  $n_2 > n_1 > n_a$ , we will not have to deal with the propagation of evanescent waves emitted by the dipole distribution.

We have defined on figure 4.2 the complex reflection ( $\tilde{r}_P, \tilde{r}_N$ ) and transmission ( $\tilde{t}_P, \tilde{t}_N$ ) coefficients of the two DBRs, seen from inside the cavity. These coefficients can be calculated exactly by using results of chapter 2.

In MCLED structures, the source is generally made of one or several quantum wells. Several fundamental reasons impose the use of quantum wells rather than bulk active regions. First, it is necessary to place the source at the maximum of the electric cavity field in order to maximize the coupling between the cavity and the source fields [13]. For a one-lambda cavity this means that the source must be localized at the center of the cavity which justifies the use of a quantum well active region. We will show in this chapter that the extraction efficiency decreases as the source spectral width increases. It is then necessary to use a source for which the spectral width is as small as possible. A quantum well is then to be preferred to bulk material since its emission linewidth is smaller, due to the reduced dimensionality [122]. We will also show that the extraction efficiency can be maximized by carefully adjusting the wavelength detuning between the cavity resonance (defined at normal incidence) and the source emission wavelength (for which the spectral density is maximum). It is then important to have a source with a stable emission wavelength in terms of current injection or temperature. The reduced dimensionality of quantum wells is once again an advantage compared to bulk regions. Quantum wells emission wavelength can be precisely tuned by controlling the thickness, the depth or the strain of the well, allowing an accurate and easy control of the cavity-source detuning [29], [164].

We will then consider that the source is a quantum well placed in the center of the one-lambda cavity.

In order to calculate the emission properties of the MCLEDs, we first calculate the power per unit of solid angle  $\bar{\Pi}_2$  emitted by the source in the center of the cavity. We know from chapter 3 that this parameter is related to the power per unit of solid angle  $\bar{\Pi}_2^\infty$  emitted by the same source in an infinite medium of refractive index  $n_2$ . The emission of the bare quantum well is described by  $\bar{\Pi}_2^\infty$  which can be expressed as the product of a term describing the interaction of the light with the medium and by another term describing the spectral density of the emission. The spectral density  $r_{spont}$  varies with respect to the normalized energy (defined by  $\delta = \frac{\lambda_{Bragg}}{\lambda}$ ), and is peaked at a normalized energy called  $\delta_o$ . If  $\lambda_{spont}$  is the peak wavelength of intrinsic spontaneous emission, we have then  $\delta_o = \frac{\lambda_{Bragg}}{\lambda_{spont}}$ . The full width at half maximum of  $r_{spont}$  is called  $\sigma_o$  and  $r_{spont}$  is normalized to one when integrated from minus to plus infinity. For mathematical reasons we will use in this chapter a Lorentzian lineshape to describe the source broadening (this function offers the possibility to analytically approximate the extraction efficiency). In fact we will see in chapter 6 that the spontaneous emission spectrum of conventional LEDs (without cavity) is better approximated by a combination of two exponential tails (at low current density at least), but this will not change the general results derived in the present chapter. The spontaneous spectral density is then given by:

$$r_{spont}(\delta - \delta_o, \sigma_o) = \frac{\frac{2}{\pi \sigma_o}}{1 + \left(\frac{2}{\sigma_o}\right)^2 (\delta - \delta_o)^2}. \quad (4.4)$$

It must be pointed out that the  $r_{spont}(\delta - \delta_o, \sigma_o)$  is normalized to one when integrated between minus to plus infinity since it is a spectral density. It follows from the previous considerations that:

$$\boxed{\bar{\Pi}_2(\gamma_{z2}, \delta, \delta_o, \sigma_o) = \Pi_2(\gamma_{z2}, \delta) r_{spont}(\delta - \delta_o, \sigma_o)} \quad (4.5)$$

where  $\Pi_2(\gamma_{z2}, \delta)$  is calculated for a monochromatic dipole distribution (with a rotational symmetry around the axis  $\vec{e}_z$ ) by the relation:

$$\boxed{\Pi_2(\gamma_{z2}, \delta) = \alpha_{//} [\Pi_{2s}(\gamma_{z2}, \delta) + \Pi_{2p}(\gamma_{z2}, \delta)] + \alpha_{\perp} \Pi_{2v}(\gamma_{z2}, \delta)}. \quad (4.6)$$

The parameters  $\alpha_{//}$  and  $\alpha_{\perp}$  refer to the horizontal and vertical dipole proportions in the dipole distribution respectively, and are related by the relation  $2\alpha_{//} + \alpha_{\perp} = 1$  as derived in chapter 3.

By using equation (3.13) derived in chapter 3, we can calculate explicitly the power per unit of solid angle  $\Pi_{2s}(\gamma_{z2}, \delta)$ ,  $\Pi_{2p}(\gamma_{z2}, \delta)$  and  $\Pi_{2v}(\gamma_{z2}, \delta)$ :

$$\Pi_{2s}(\gamma_{z2}, \delta) = \zeta_h^{TE}(\gamma_{z2}, \delta) \mathcal{A}^{TE}(\gamma_{z2}, \delta) \Pi_{2s}^\infty(\gamma_{z2}) \quad (4.7)$$

$$\Pi_{2p}(\gamma_{z2}, \delta) = \zeta_h^{TM}(\gamma_{z2}, \delta) \mathcal{A}^{TM}(\gamma_{z2}, \delta) \Pi_{2p}^\infty(\gamma_{z2}) \quad (4.8)$$

$$\Pi_{2v}(\gamma_{z2}, \delta) = \zeta_v^{TM}(\gamma_{z2}, \delta) \mathcal{A}^{TM}(\gamma_{z2}, \delta) \Pi_{2v}^\infty(\gamma_{z2}). \quad (4.9)$$

The  $\zeta$  parameters correspond to the antinode factors which quantify the coupling of the cavity field with the dipoles. They are expressed by:

$$\zeta_h^{TE}(\gamma_{z2}, \delta) = |1 + \tilde{r}_N^{TE} e^{2i\varphi_c}|^2 \quad (4.10)$$

$$\zeta_h^{TM}(\gamma_{z2}, \delta) = |1 + \tilde{r}_N^{TM} e^{2i\varphi_c}|^2 \quad (4.11)$$

$$\zeta_v^{TM}(\gamma_{z2}, \delta) = |1 - \tilde{r}_N^{TM} e^{2i\varphi_c}|^2 \quad (4.12)$$

where  $\varphi_c$  describes a phase shift related to the position of the source with respect to the cavity edges

$$\varphi_c = \pi \delta \gamma_{z2} \quad (4.13)$$

for a source placed at the center of a one-lambda cavity. The superscripts TE and TM indicate that the reflection coefficients have to be calculated for the corresponding polarization by using transfer matrices given in chapter 2. The terms  $\tilde{r}_N^{TE, TM}$  correspond to the reflectivity of the bottom DBR defined from the cavity at its right edge (see figure 4.2). This explains why a phase term  $e^{2i\varphi_c}$  appears in the expression given by equation (3.13) for which  $r_{a2}$  was defined at the center of the cavity.

The  $\mathcal{A}$  factors correspond to the Airy functions describing the optical properties of the passive cavity. They can be calculated according to:

$$\mathcal{A}^{TE, TM}(\gamma_{z2}, \delta) = \frac{1 - |\tilde{r}_P^{TE, TM}|^2}{|1 - \tilde{r}_P^{TE, TM} \tilde{r}_N^{TE, TM} e^{4i\varphi_c}|^2}. \quad (4.14)$$

The  $\Pi_{2s}^\infty$ ,  $\Pi_{2p}^\infty$  and  $\Pi_{2v}^\infty$  factors describe the source terms of the dipole distribution. They were calculated in chapter 3 and are given by equations (3.38) to (3.40).

If the complex reflection coefficients  $\tilde{r}_P$  and  $\tilde{r}_N$  are known, the power per unit of solid angle  $\bar{\Pi}_2(\gamma_{z2}, \delta, \delta_o, \sigma_o)$  emitted at the position of the source can be calculated for various cavity angles and different energies. As mentioned in chapter 3, the power per unit of solid angle  $\bar{\Pi}_a(\gamma_{za}, \delta, \delta_o, \sigma_o)$  emitted in the outside medium can be simply calculated by:

$$\bar{\Pi}_a(\gamma_{za}, \delta, \delta_o, \sigma_o) = \frac{d\Omega_2}{d\Omega_a} \bar{\Pi}_2(\gamma_{z2}, \delta, \delta_o, \sigma_o). \quad (4.15)$$

This term is nothing else than the angle-resolved emission spectrum of the MCLED. We will show on chapter 6 some experimental measurements of  $\bar{\Pi}_a(\gamma_{za}, \delta, \delta_o, \sigma_o)$ .

We want to calculate the extraction efficiency  $\bar{\eta}$  of the MCLED in the outside medium. This parameter is given by the ratio of the optical power emitted in the outside medium to the total optical power emitted at the source (in the cavity). We have then:

$$\bar{\eta}(\delta_o, \sigma_o) = \frac{\int_0^1 \int_{-\infty}^{+\infty} \bar{\Pi}_a(\gamma_{za}, \delta, \delta_o, \sigma_o) d\delta d\gamma_{za}}{\int_{-1}^1 \int_{-\infty}^{+\infty} \bar{\Pi}_2(\gamma_{z2}, \delta, \delta_o, \sigma_o) d\delta d\gamma_{z2}}. \quad (4.16)$$

By using (4.2) and (4.15), we find:

$$\bar{\eta}(\delta_o, \sigma_o) = \frac{\int_{\gamma_{z2}^c}^1 \int_{-\infty}^{+\infty} \bar{\Pi}_2(\gamma_{z2}, \delta, \delta_o, \sigma_o) d\delta d\gamma_{z2}}{\int_{-1}^1 \int_{-\infty}^{+\infty} \bar{\Pi}_2(\gamma_{z2}, \delta, \delta_o, \sigma_o) d\delta d\gamma_{z2}}. \quad (4.17)$$

As it was extensively studied in references [105], [101], [100], [16], [126], [62], [35], placing an oscillating dipole inside a microcavity leads to a change of the dipole radiative lifetime, which can be expressed as:

$$\frac{\tau_\infty(\delta)}{\tau(\delta)} = \Delta\tau(\delta) = 2\pi \int_{-1}^1 \Pi_2(\gamma_{z2}, \delta) d\gamma_{z2} \quad (4.18)$$

where  $\Pi_2(\gamma_{z2}, \delta)$  has to be calculated in the cavity and is given by equation (4.6). The radiative lifetime of the dipole distribution in an infinite medium and in the cavity are defined as  $\tau_\infty$  and  $\tau$  respectively.

After a few manipulations, we can express the extraction efficiency by:

$$\bar{\eta}(\delta_o, \sigma_o) = \frac{1}{\Delta\bar{\tau}(\delta_o, \sigma_o)} 2\pi \int_{\gamma_{z2}^c}^1 \int_{-\infty}^{+\infty} \bar{\Pi}_2(\gamma_{z2}, \delta, \delta_o, \sigma_o) d\delta d\gamma_{z2} \quad (4.19)$$

where  $\Delta\bar{\tau}(\delta_o, \sigma_o)$  is the averaged radiative lifetime modification given by:

$$\Delta\bar{\tau}(\delta_o, \sigma_o) = \int_{-\infty}^{+\infty} \Delta\tau(\delta) r_{spont}(\delta - \delta_o, \sigma_o) d\delta. \quad (4.20)$$

Without justifying it in this section we set this parameter equal to one. As pointed out by references [1], [152] radiative lifetime modification  $\Delta\tau(\delta)$  is quite small for monochromatic dipoles placed in dielectric one-dimensional cavities. We will also see in section 4.4 that because of spectral broadening of the source emission, it is reasonable to consider that  $\Delta\bar{\tau}(\delta_o, \sigma_o) \approx 1$ . We will then calculate the extraction efficiency in the next two sections by using the following expression:

$$\bar{\eta}(\delta_o, \sigma_o) = 2\pi \int_{\gamma_{z2}^c}^1 \int_{-\infty}^{+\infty} \bar{\Pi}_2(\gamma_{z2}, \delta, \delta_o, \sigma_o) d\delta d\gamma_{z2} \quad (4.21)$$

## 4.2 Extraction efficiency of top-emitting MCLEDs: analytical approximations

In order to calculate the extraction efficiency  $\bar{\eta}(\delta_o, \sigma_o)$ , we need to evaluate the complex coefficients of reflection  $\tilde{r}_P$  and  $\tilde{r}_N$  (see figure 4.2). We showed in chapter 2 how to analytically calculate them by

using diagonalization techniques. It is then possible to directly introduce these expressions in equations (4.10)-(4.12) and (4.14). From such calculations, it is possible to accurately evaluate  $\bar{\eta}(\delta_o, \sigma_o)$ , but it does not offer the possibility to really understand the physical mechanisms which influence the extraction efficiency. For that purpose a simple model of MCLED emission is required. To reach this goal we will use the approximations derived in section 2.2 to calculate the reflection coefficients of DBRs. We remind the reader that  $\tilde{r}_P$  and  $\tilde{r}_N$  depend on the parameters  $\delta = \frac{\lambda_{Bragg}}{\lambda}$  and  $\gamma_{z2}$ . We showed in section 2.2 that it was possible to develop the phase of the reflection coefficients around the Bragg condition ( $\delta = 1$  and  $\gamma_{z2} = 1$ ) and to assume that their amplitudes were constant. We set then:

$$\tilde{r}_{P,N} = r_{P,N} e^{i\varphi_{P,N}} \quad (4.22)$$

where  $r_{P,N}$ , and  $\varphi_{P,N}$  are real constants (as mentioned in the previous section, we assume that all the layers are made of non-absorbing materials). The amplitudes are given by:

$$r_P = \frac{\alpha r_P^o + \beta}{\alpha + \beta r_P^o} \quad (4.23)$$

$$r_P^o = \frac{n^{2P} - 1}{n^{2P} + 1} \quad (4.24)$$

$$r_N = \frac{n^{2N} - 1}{n^{2N} + 1} \quad (4.25)$$

with

$$\alpha = \frac{1}{2}(1 + \bar{n}) \quad (4.26)$$

$$\beta = \frac{1}{2}(1 - \bar{n}). \quad (4.27)$$

The phases are given by:

$$\varphi_P = \bar{D}_\theta^P (\gamma_{z2} - 1) + \bar{D}_\delta^P (\delta - 1) \quad (4.28)$$

$$\varphi_N = D_\theta^N (\gamma_{z2} - 1) + D_\delta^N (\delta - 1) \quad (4.29)$$

with

$$D_\theta^{P,N} = \frac{\pi}{2} \left[ \left( \frac{2n^2 - n + 1}{n - 1} \right) r_{P,N}^o - 1 \right] \quad (4.30)$$

$$D_\delta^{P,N} = \frac{\pi}{2} \left[ \left( \frac{n + 1}{n - 1} \right) r_{P,N}^o - 1 \right] \quad (4.31)$$

$$\bar{D}_{\theta,\delta}^P = \frac{2\alpha\beta + (\alpha^2 + \beta^2)r_P^o}{(\alpha r_P^o + \beta)(\alpha + \beta r_P^o)} D_{\theta,\delta}^P + \frac{\alpha\beta[1 - (r_P^o)^2]\pi}{(\alpha r_P^o + \beta)(\alpha + \beta r_P^o)}. \quad (4.32)$$

These approximations are reasonable provided that:

1) the normalized energy varies around the Bragg condition ( $\delta \approx 1$ ) and is still in the DBR stopband: this assumption is reasonable here since we will be interested in calculating the extraction efficiency for emitters whose emission wavelength will be close to the Bragg wavelength

2) the incidence angle is close to the normal ( $\gamma_{z2} \approx 1$ ): as can be shown in equation (4.21), we only need to calculate  $\bar{\Pi}_2(\gamma_{z2}, \delta, \delta_o, \sigma_o)$  for  $\gamma_{z2}$  values between  $\gamma_{z2}^c$  and 1; since we are mainly interested in studying MCLED structures based on AlGaAs DBRs ( $3 < n_2 < 4$ ) and since the outcoupling medium was chosen to be air ( $n_a = 1$ ) or epoxy ( $n_a = 1.5$ ), we conclude that we have at worst  $\gamma_{z2}^c \approx 0.9$  which leads to reasonable approximations.

Note that the approximations of the TE and TM reflection coefficient give the same expressions. The reason is that the two polarizations are degenerated at the Bragg condition. The polarizations will be indirectly accounted for in the source terms and in the sign of the antinode factors (4.7)-(4.9).

With these approximations, we can apply formula (4.7)-(4.9) with

$$\zeta_h^{TE}(\gamma_{z2}, \delta) = \zeta_h^{TM}(\gamma_{z2}, \delta) = \zeta_h(\gamma_{z2}, \delta) = |1 + r_N e^{i(2\varphi_c + \varphi_N)}|^2 \quad (4.33)$$

$$\zeta_v^{TM}(\gamma_{z2}, \delta) = \zeta_v(\gamma_{z2}, \delta) = |1 - r_N e^{i(2\varphi_c + \varphi_N)}|^2 \quad (4.34)$$

and

$$\mathcal{A}^{TE}(\gamma_{z2}, \delta) = \mathcal{A}^{TM}(\gamma_{z2}, \delta) = \mathcal{A}(\gamma_{z2}, \delta) = \frac{1 - r_P^2}{|1 - r_P r_N e^{i(4\varphi_c + \varphi_N + \varphi_P)}|^2}. \quad (4.35)$$

We can easily check that for a source placed in the center of a one-lambda cavity and close to the Bragg condition, we have  $\zeta_h(\gamma_{z2}, \delta) \approx 4$  and  $\zeta_v(\gamma_{z2}, \delta) \approx 0$ . We immediately conclude that the vertical dipole contribution of the source distribution will not be extracted from the microcavity. It can be shown that for a quantum well, the vertical dipole contribution comes from the recombination between light holes and electrons [164], [11], [10]. Hence it will be necessary to minimize this recombination mechanism and to favour recombinations between heavy holes and electrons so as to maximize the extraction. By using equations (4.6) and (3.38)-(3.40), we can approximate the power per unit of solid angle emitted by a 3D distribution of monochromatic dipoles (with a rotational symmetry along the  $\vec{e}_z$  axis):

$$\Pi_2(\gamma_{z2}, \delta) = 4 \alpha_{//} \mathcal{A}(\gamma_{z2}, \delta) \frac{3}{8\pi} [1 + \gamma_{z2}^2]. \quad (4.36)$$

We can explicitly calculate the Airy function by using the previous results:

$$\mathcal{A}(\gamma_{z2}, \delta) = \frac{1 - r_P^2}{(1 - r_N r_P)^2} \frac{1}{1 + \left(\frac{2F}{\pi}\right)^2 \sin^2\left(\frac{\varphi}{2}\right)} \quad (4.37)$$

where the phase  $\varphi$  is:

$$\varphi = 4\varphi_c + \varphi_N + \varphi_P = 4\pi\delta\gamma_{z2} + D_\theta(\gamma_{z2} - 1) + D_\delta(\delta - 1) \quad (4.38)$$

with

$$D_{\theta,\delta} = \bar{D}_{\theta,\delta}^P + D_{\theta,\delta}^N. \quad (4.39)$$

The parameter  $F$  is the cavity finesse given by:

$$F = \frac{\pi \sqrt{r_N r_P}}{1 - r_N r_P}. \quad (4.40)$$

The Airy factor displays some periodic resonances which can be found setting that  $\varphi = 2\pi p$  where  $p$  is an integer. We find at the resonance (labelled by the sub/superscript FP) the following relation between the normalized energies and the angles:

$$\delta_{FP} = \frac{2\pi p + D_\delta - D_\theta(\gamma_{z2}^{FP} - 1)}{4\pi\gamma_{z2}^{FP} + D_\delta}. \quad (4.41)$$

Since we must have  $\delta_{FP} = 1$  at the Bragg condition, we conclude that  $p = 2$ . This result was to be expected since  $p$  corresponds to the order of the physical cavity (which is here a one-lambda cavity). This relation gives the angle/energy relation for the Fabry-Pérot mode around the Bragg condition. By converting the internal angle  $\theta_2$  into the external  $\theta_a$  (using (4.1)), one can easily check that  $\delta_{FP}$  increases with  $\theta_a$ , meaning that the Fabry-Pérot wavelength is blue-shifted as the angle  $\theta_a$  increases.

The resonances of the Airy function occur then around the condition  $\varphi = 4\pi$ . Since the energy linewidth of the Airy function is usually smaller than the stopband width and since its angular linewidth is smaller than the escape window, we can develop the Airy function around its resonance (by a first order Taylor development), which gives after some manipulations:

$$\mathcal{A}(\gamma_{z2}, \delta) = \frac{1 - r_P^2}{(1 - r_N r_P)^2} \frac{1}{1 + \left(\frac{2}{\Delta\delta}\right)^2 (\delta - \delta_{FP})^2} \quad (4.42)$$

where  $\Delta\delta$  is the full width at half maximum (FWHM) of the Lorentzian evaluated at  $\gamma_{z2}$ , given by:

$$\Delta\delta = \frac{2\pi}{F} \frac{1}{4\pi\gamma_{z2} + D_\delta}. \quad (4.43)$$

One should notice that this FWHM formally varies with the angle. As already mentioned, we are interested in calculating the power per unit of solid angle for  $\gamma_{z2}$  values close to one. We can at first approximation neglect this dependence, fixing the value of  $\gamma_{z2}$  to one which gives:

$$\Delta\delta = \frac{2\pi}{F} \frac{1}{4\pi + D_\delta}. \quad (4.44)$$

For a broad spectrum source with a Lorentzian lineshape we can use (4.4) and (4.5) to calculate the power per unit of solid angle  $\bar{\Pi}_2(\gamma_{z2}, \delta, \delta_o, \sigma_o)$ . This expression which depends on the angle and on the energy can be integrated over the energies which gives formally:

$$\bar{\Pi}_2(\gamma_{z2}, \delta_o, \sigma_o) = \int_{-\infty}^{+\infty} \bar{\Pi}_2(\gamma_{z2}, \delta) r_{spont}(\delta - \delta_o, \sigma_o) d\delta. \quad (4.45)$$

This integral is nothing else than the convolution product of two Lorentzians which can be analytically calculated. We find an other Lorentzian whose linewidth is equal to the sum of the linewidths of the two convolved Lorentzians. We find:

$$\bar{\Pi}_2(\gamma_{z2}, \delta_o, \sigma_o) = 4\alpha_{//} \frac{3}{8\pi} (1 + \gamma_{z2}^2) \frac{1 - r_P^2}{(1 - r_P r_N)^2} \frac{\Delta\delta}{\sigma_o + \Delta\delta} \frac{1}{1 + \left(\frac{2}{\sigma_o + \Delta\delta}\right)^2 (\delta_o - \delta_{FP})^2}. \quad (4.46)$$

The angular dependence of the Lorentzian is hidden in the  $\delta_{FP}$  factor (by (4.41)). We can reorganize the terms so as to make appear the  $\gamma_{z2}$  variable which gives after a few manipulations:

$$\bar{\Pi}_2(\gamma_{z2}, \delta_o, \sigma_o) = 4\alpha_{//} \frac{3}{8\pi} (1 + \gamma_{z2}^2) \frac{1 - r_P^2}{1 - r_P r_N} \frac{\Delta\gamma_z}{\sigma} \frac{1}{1 + \left(\frac{2}{\sigma}\right)^2 (\gamma_{z2} - \gamma_o)^2}. \quad (4.47)$$

where we have defined:

$$\gamma_o = \frac{4\pi - D_\delta (\delta_o - 1) + D_\theta}{4\pi \delta_o + D_\theta}, \quad (4.48)$$

$$\Delta\gamma_z = \frac{2\pi}{F} \frac{1}{4\pi \delta_o + D_\theta} \quad (4.49)$$

and

$$\sigma = \frac{\Delta\gamma_z (\sigma_o + \Delta\delta)}{\Delta\delta}. \quad (4.50)$$

The  $\Delta\gamma_z$  parameter is the full width at half maximum of the Airy function  $\mathcal{A}(\gamma_{z2}, \delta)$  developed around its resonance with respect to the  $\gamma_{z2}$  variable. By doing the same kind of manipulations which lead to (4.42), we can calculate:

$$\mathcal{A}(\gamma_{z2}, \delta) = \frac{1 - r_P^2}{(1 - r_N r_P)^2} \frac{1}{1 + \left(\frac{2}{\Delta\gamma_z}\right)^2 (\gamma_{z2} - \gamma_{z2}^{FP})^2}. \quad (4.51)$$



Like we noticed it for the normalized energy full width at half maximum  $\Delta\delta$ ,  $\Delta\gamma_z$  formally varies with respect to the normalized energy  $\delta_o$ . Since  $\delta_o$  varies very few around  $\delta = 1$ , we can at first approximation neglect the normalized energy dependence by fixing the value of  $\delta_o$  to one from which it follows that:

$$\Delta\gamma_z = \frac{2\pi}{F} \frac{1}{4\pi + D_\theta}. \quad (4.52)$$

We conclude from these results that the effect of broadening the spectral width of the source of emission is to broaden the angular dependence of the Airy function. We check that we retrieve (4.36) when we set  $\sigma_o = 0$  (corresponding to a monochromatic source).

For an ideal Fabry-Pérot cavity, the mode linewidth is conversely proportional to the order of the cavity times its finesse [130]. We can then define an angular and an energy cavity order:

$$m_\theta = \frac{1}{F \Delta\gamma_z} = 2 + \frac{D_\theta}{2\pi} \quad (4.53)$$

$$m_\delta = \frac{1}{F \Delta\delta} = 2 + \frac{D_\delta}{2\pi}. \quad (4.54)$$

It must be noticed that for ideal mirrors ( $D_\theta = D_\delta = 0$ ), we have  $m_\theta = m_\delta = 2$  equal to the order of the physical cavity as expected.

We can then express the Lorentzian linewidth  $\sigma$  by:

$$\sigma = \sigma_o \left( \frac{m_\delta}{m_\theta} \right) + \frac{1}{F m_\theta}. \quad (4.55)$$

We can now calculate the extraction efficiency by using (4.21), (4.45) and (4.46):

$$\bar{\eta} = 3\alpha_{//} \frac{1 - r_P^2}{(1 - r_P r_N)^2} \frac{\Delta\gamma_z}{\sigma} \int_{\gamma_{z2}^c}^1 \frac{1 + \gamma_{z2}^2}{1 + \left(\frac{2}{\sigma}\right)^2 (\gamma_{z2} - \gamma_o)^2} d\gamma_{z2}. \quad (4.56)$$

This integral can be analytically evaluated [2] and after some approximations, one finds that:

$$\bar{\eta} = 3\alpha_{//} \frac{1 - r_P^2}{(1 - r_P r_N)^2} \frac{\Delta\gamma_z}{2} (1 + \gamma_o^2) \left[ \arctan\left(\frac{1 - \gamma_o}{\sigma/2}\right) - \arctan\left(\frac{\gamma_{z2}^c - \gamma_o}{\sigma/2}\right) \right]. \quad (4.57)$$

The integral term of (4.56) indicates how much of the Airy function enters in the escape window. This term is mainly responsible of the high extraction efficiency of the MCLED structure. It is clear that if the FWHM of the Lorentzian is small enough, then all the mode will have the possibility to fit in the escape window, hence to be extracted. We define then the parameter  $\bar{\mathcal{A}}$  which indicates the fraction of the Airy mode which enters the escape window:

$$\bar{\mathcal{A}} = \frac{1}{\pi} \left[ \arctan \left( \frac{1 - \gamma_o}{\sigma/2} \right) - \arctan \left( \frac{\gamma_{z2}^c - \gamma_o}{\sigma/2} \right) \right]. \quad (4.58)$$

This term converges towards 1 when  $\sigma$  converges towards zero (monochromatic source) which means that all of the mode is extracted.

We have calculated in section 2.3 the transmission coefficient  $T_{fp}$  of the Fabry-Pérot cavity at the Bragg condition. We found:

$$T_{fp} = \frac{(1 - r_P^2)(1 - r_N^2)}{(1 - r_P r_N)^2}. \quad (4.59)$$

The transmission coefficients of each DBR are simply given by  $T_{P,N} = 1 - r_{P,N}^2$ . It is then possible to use these expressions to simplify the relation (4.57).

We define a factor  $\Pi_o^\infty$  which represents the source term of the dipole distribution evaluated at the angle corresponding to  $\gamma_o$ :

$$\Pi_o^\infty = \frac{3}{8\pi} \alpha_{//} (1 + \gamma_o^2). \quad (4.60)$$

We can finally express the extraction efficiency as:

$$\bar{\eta} = 4\pi^2 \frac{T_{fp}}{T_N} \frac{\bar{\mathcal{A}}}{F} \frac{\Pi_o^\infty}{m_\theta}. \quad (4.61)$$

The next section is devoted to the study of equation (4.61) which takes into account the dipole distribution, the number of pairs of each DBR, their indices, the escape window angular size and the source linewidth. We will also compare the results given by equation (4.61) to the exact calculations (performed by numerical simulations).

### 4.3 Optimization of the extraction efficiency

The purpose of this section is to discuss the dependence of the extraction efficiency with respect to the source and the structure properties. We will compare the approximations described on previous section to the exact solution found by numerical simulations. The parameters of interest are: the indices of refraction  $n_a, n_1, n_2$  (see figure 4.1), the number of pairs of each DBR P and N, the collection angle  $\xi$  in the medium of refractive index  $n_a$ , the FWHM of the source  $\sigma_o$ , the normalized energy  $\delta_o$  at which the source spectrum is maximum and the fraction of horizontal dipoles  $\alpha_{//}$ .

We have shown in the previous section that the fraction of horizontal dipoles  $\alpha_{//}$  in the source distribution appeared only in the source term given by (4.60). We know from chapter 3 that  $\alpha_{//}$  is related to the fraction of vertical dipoles  $\alpha_\perp$  in the source distribution, according to the relation

$\alpha_{//} = \frac{1}{2}(1 - \alpha_{\perp})$ . As mentioned in chapter 4  $\alpha_{\perp}$  is related to the proportion of light hole/electron recombinations. It appears from (4.60) and (4.61) that it is necessary to minimize the light hole/electron recombinations so as to optimize the extraction efficiency. The corresponding vertical dipole emission is inhibited at angles close to zero because of the antinode factor (4.34).

In the rest of this section we will assume an isotropic 2D dipole distribution, hence  $\alpha_{\perp} = 0$  and  $\alpha_{//} = 0.5$ .

The second parameter of interest is the collection angle  $\xi$ . This angle is defined in the outside medium of refractive index  $n_a$ . We consider that all the light emitted in the cone defined by this angle can be detected. This definition is useful for calculating the extraction efficiency of a diode placed in front of an optical fiber. We have then  $\xi = \sin^{-1}(N.A.)$  where  $N.A.$  corresponds to the numerical aperture of the optical fiber (we typically have  $N.A. = 0.2$  for glass optical fibers and  $N.A. = 0.5$  for polymer optical fibers). If the light can be collected in the half-hemisphere defined in the outside medium (as it can be done by placing a bonded diode inside an integrating sphere), then  $\xi = \frac{\pi}{2}$ . Equation (4.16) assumes implicitly this last case. For the general case ( $\xi \neq \frac{\pi}{2}$ ), the results presented in the previous section still hold provided  $\gamma_{z2}^c$  is calculated according to:

$$\gamma_{z2}^c = \sqrt{1 - \left(\frac{n_a}{n_2}\right)^2 (1 - \cos^2 \xi)}. \quad (4.62)$$

The escape window width (in terms of the  $\gamma_{z2}$  variable) is obviously determined by the collection angle  $\xi$ . The array below gives the values of  $\gamma_{z2}^c$  for the case of air ( $n_a = 1$ ) or epoxy ( $n_a = 1.5$ ) with  $n_2 = 3.5$  (GaAs at red/ infrared wavelengths) and for three realistic numerical apertures.

$\gamma_{z2}^c$	N.A.=1	N.A.=0.5	N.A.=0.2
$n_a = 1$ (air)	0.9583	0.9897	0.9984
$n_a = 1.5$ (epoxy)	0.9035	0.9768	0.9963

As expected, the escape window size increases as the numerical aperture increases. The  $\gamma_{z2}^c$  parameters appears only in the  $\bar{\mathcal{A}}$  expression given by (4.58). Figure 4.3 displays  $\bar{\mathcal{A}}$  plotted with respect to the  $\gamma_o$  variable for two different values ( $\gamma_{z2}^c = 0.9583$  and  $\gamma_{z2}^c = 0.9897$ ), and for the spectral widths  $\sigma = 1e-3$  and  $\sigma = 1e-4$ .

This figure shows that  $\bar{\mathcal{A}}$  is defined on the escape window range  $[\gamma_{z2}^c, 1]$  and is symmetrical around its maximum  $\bar{\mathcal{A}}_{max}$  given by:

$$\bar{\mathcal{A}}_{max} = \frac{2}{\pi} \arctan \left( \frac{1 - \gamma_{z2}^c}{\sigma} \right). \quad (4.63)$$

From this last relation it appears that  $\bar{\mathcal{A}}_{max}$  increases as the spectral width  $\sigma$  decreases. When  $\sigma$  converges towards zero,  $\bar{\mathcal{A}}$  converges towards a unity function in the escape window.  $\bar{\mathcal{A}}$  describes how much of the Airy function enters in the escape window: when  $\sigma$  is far smaller than the escape window width, the Airy mode can then be completely extracted.

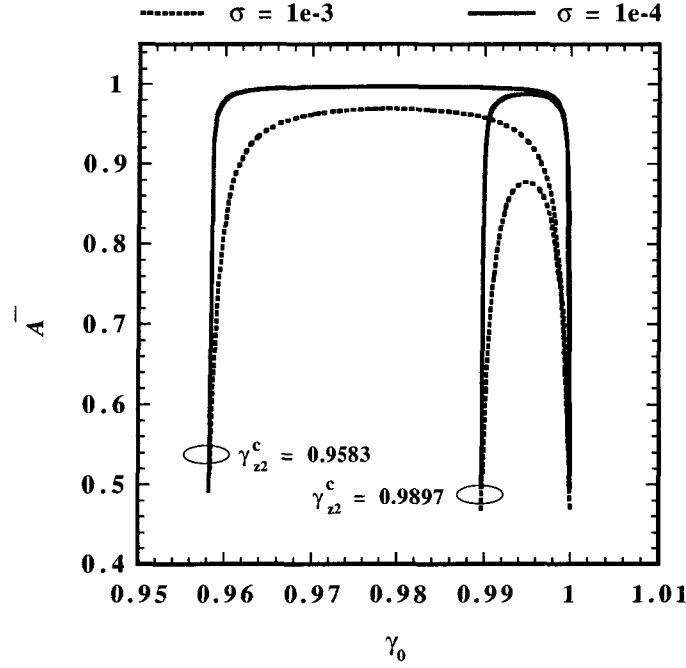


Figure 4.3:  $\bar{\mathcal{A}}$  parameter plotted versus  $\gamma_o$  representing the cosine of the angle corresponding to the maximum of the source emission.  $\bar{\mathcal{A}}$  is represented for two different escape window widths  $\gamma_{z2}^c$  and two different source linewidths  $\sigma$ .

This figure also shows that decreasing the escape window width while keeping the spectral width  $\sigma$  constant has the effect of decreasing the maximum value of  $\bar{\mathcal{A}}$ : the Airy mode fits better in a large escape window than in a smaller one. It comes immediately from these considerations that the extraction efficiency decreases when the spectral width  $\sigma$  increases. When the escape window width decreases, it is more and more difficult to make the Airy mode completely enter the escape window, hence the spectral width  $\sigma$  is required to be smaller. The other factor of expression (4.61) varying with respect to  $\gamma_o$ , is the source term  $\Pi_o^\infty$  which increases slowly from  $\frac{3}{16\pi}(\gamma_{z2}^c)^2$  to  $\frac{3}{16\pi}$  as  $\gamma_o$  scans the escape window. Since  $\gamma_{z2}^c$  is generally very close to one,  $\Pi_o^\infty$  increases very slowly as  $\gamma_o$  increases.

From the previous considerations, it follows that the product  $\bar{\mathcal{A}}\Pi_o^\infty$  describes completely the dependence of the extraction efficiency  $\bar{\eta}$  with the  $\delta_o$  parameter because  $\gamma_o$  and  $\delta_o$  are related by the relation (4.48). Note that  $\delta_o$  is the emission energy corresponding to the maximum of the source spectrum, normalized to the Bragg energy ( $\delta_o = \frac{\lambda_{Bragg}}{\lambda}$ ). It can easily be checked that  $\delta_o$  decreases from  $\delta_c$  to 1 as  $\gamma_o$  increases from  $\gamma_{z2}^c$  to 1 with  $\delta_c$  given by:

$$\delta_c = \frac{4\pi + D_\delta - D_\theta(\gamma_{z2}^c - 1)}{4\pi\gamma_{z2}^c + D_\delta}. \quad (4.64)$$

This equation simply represents the Fabry-Pérot dispersion relation between energy and angles. The  $\delta_o$  parameter can be understood as a detuning between the cavity mode (fixed at normal incidence by the Bragg wavelength) and the source emission wavelength. In the literature, the detuning parameter is usually defined as  $\Delta\lambda = \pm(\lambda - \lambda_{Bragg})$  [22], [37], but we keep our definition which is more appropriate

to the analytical formalism we are presenting.

Since  $\gamma_{z2}^c$  is generally very close to one,  $\Pi_o^\infty$  increases very slowly as  $\gamma_o$  increases. We define  $\gamma_{opt}$  as the  $\gamma_o$  value for which the extraction  $\bar{\eta}$  is maximal. This value is found by determining the maximum of the product  $\bar{\mathcal{A}} \Pi_o^\infty$  with respect to the parameter  $\gamma_o$ . This unfortunately leads to a transcendental equation. If we neglect the  $\gamma_o$  dependence of the  $\Pi_o^\infty$  term, we easily find that  $\bar{\mathcal{A}}$  is maximum for

$$\gamma_{opt} = \frac{1 + \gamma_{z2}^c}{2} \quad (4.65)$$

corresponding to the center of the escape window. This means physically that  $\bar{\mathcal{A}}$  is maximum when the Airy mode is centered in the escape window as previously mentioned by Benisty [13]. From this approximation it follows that  $\gamma_{za}^{opt} = \frac{1}{\sqrt{2}} = \cos(\theta_a)$  giving  $\theta_a = 45^\circ$  as calculated in reference [13]. The corresponding optimal detuning is given by:

$$\delta_{opt} = \frac{8\pi + 2D_\delta - D_\theta(\gamma_{z2}^c - 1)}{2\pi(\gamma_{z2}^c + 1) + 2D_\delta}. \quad (4.66)$$

With this approximation, the optimal extraction efficiency is finally given by:

$$\bar{\eta}_{opt} = \frac{3\pi}{4} \frac{T_{fp}}{T_N} \frac{1}{F} \frac{1}{m_\theta} (1 + \gamma_{opt}^2) \bar{\mathcal{A}}_{max}. \quad (4.67)$$

In fact neglecting the  $\gamma_o$  dependence of the  $\Pi_o^\infty$  term can not be justified if one wants to find  $\gamma_{opt}$ : the parabolic dependence given in (4.60) is enough to shift  $\gamma_{opt}$  somewhere between  $\gamma_{z2}^c$  and  $\frac{1+\gamma_{z2}^c}{2}$ . The optimal detuning is then between 1 and  $\delta_{opt}$  given in (4.66). Since the optimal detuning  $\delta_{opt}$  must be greater than one, it follows that in order to get an optimal extraction efficiency, the source must emit at a smaller wavelength than the Fabry-Pérot wavelength.

On figure 4.4 is plotted the extraction efficiency  $\bar{\eta}$  with respect to the detuning  $\delta_o$ , calculated with (4.61) (dotted line) and calculated by numerical simulation (solid line). We have assumed a structure with  $P = 5$  and  $N = 35$  pairs, indices of refraction  $n_a = 1$ ,  $n_2 = 3.5$  and  $n_1 = 3.1$ , and different source linewidths ( $\sigma_o = 0, 0.02, 0.04, 0.08$ ).

We observe that the agreement between the simplified model and the exact calculation is good for any value of the source linewidth  $\sigma_o$ .

The same structure was simulated using a refractive index in the outside medium  $n_a = 1.5$  corresponding to epoxy instead of air. The result is displayed on figure 4.5.

The agreement is still qualitatively correct. The escape window width calculated with epoxy is twice the one with air (see table 4.3). Developing the Airy function into a Lorentzian lineshape leads to some significant errors far from the resonance (the tails of the Airy function are not well approximated by the Lorentzian). Our model agrees well with numerical simulations for values close to  $\delta_o = 1$  for which the approximations of the DBR reflectivities are the best. It is clear that when  $\delta_o$  moves away from the Bragg condition the approximation becomes less and less correct.

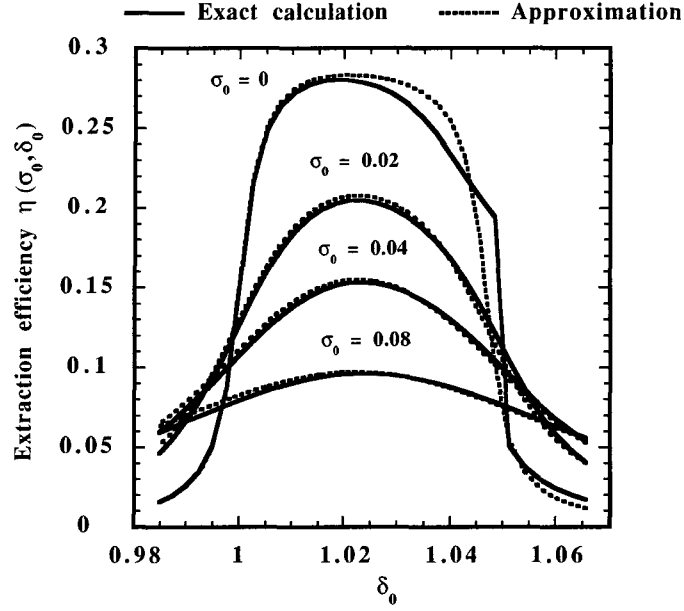


Figure 4.4: Extraction efficiency plotted versus the normalized energy corresponding to the maximum of the source spectral density. The outside medium is assumed to be air.

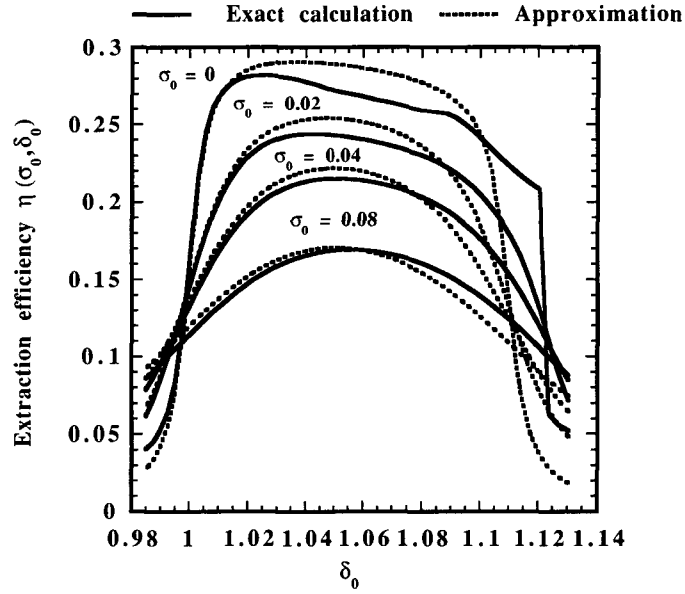


Figure 4.5: Extraction efficiency plotted versus the normalized energy corresponding to the maximum of the source spectral density. The outside medium is assumed to be epoxy.

It is evident from what precedes that the escape window width expressed in  $\gamma_o$  variable translates into an escape window width in  $\delta_o$  variable. This interval corresponds to the detuning range for which the extraction efficiency is high (see figures 4.4 and 4.5). Outside of this interval, only the tails of the Airy mode are extracted, which leads to a poor extraction efficiency.

After having discussed the effect of  $\alpha_{//}$ ,  $\xi$ ,  $\sigma_o$  and  $\delta_o$  on the extraction efficiency, we will study the effect of the number of pairs  $P$  and  $N$  on  $\bar{\eta}_{opt}$ .

In what follows we consider a structure with  $n_a = 1$ ,  $n_2 = 3.5$  and  $n_1 = 3.1$ ,  $N = 25$  or  $N = 55$  pairs for the bottom DBR, and we make the number of pairs  $P$  of the top DBR vary between 1 and 50. The parameters  $T_{fp}$ ,  $T_N$ ,  $F$  and  $m_{theta}$  depend only on  $P$  and  $N$ .

The orders of the cavity  $m_\theta$  and  $m_\delta$  depend on the parameters  $D_\theta$  and  $D_\delta$  as given by (4.39) and (4.30)-(4.32). When the numbers of pairs  $P$  and  $N$  increase,  $m_\theta$  and  $m_\delta$  also increase to saturate to the values (calculated for  $P$  and  $N$  infinite) given by:

$$m_\theta^\infty = \frac{n^2 + n - 1}{n - 1} \quad (4.68)$$

$$m_\delta^\infty = \frac{2n - 1}{n - 1} \quad (4.69)$$

these two parameters being simply related by the relation:

$$m_\theta^\infty - m_\delta^\infty = n. \quad (4.70)$$

The dependence of  $m_{\theta,\delta}$  with the number of pairs  $P$  is displayed on figure 4.6.

We observe that the phase effect induced by the DBRs on the cavity order is very important:  $m_{\theta,\delta}$  are close to ten whereas the cavity order of the physical cavity is equal to two.

The term  $\frac{T_{fp}}{T_N}$  appears in the expression of the extraction efficiency. This factor increases to reach a maximum when the condition  $r_N = r_P$  is fulfilled, then it decreases towards zero when  $r_P$  converges towards one. This behavior is displayed on figure 4.7 for the cases of  $N = 25$  and  $N = 55$  (the curves were normalized to one at their maximum).

The maximum of  $\frac{T_{fp}}{T_N}$  occurs for  $P = N - 5$  pairs which corresponds to the situation  $r_P = r_N$  ( $P \neq N$  because the air-semiconductor interface adds its reflectivity to the top DBR reflectivity). This factor has a simple physical meaning: it describes how much of power is directed towards the top of the structure compared to the substrate. When  $r_P > r_N$  this factor decreases with  $P$  because the emission is mainly directed towards the substrate.

The product  $\frac{1}{m_\theta F}$  is simply equal to the FWHM  $\Delta\gamma_z$  of the Airy function  $\mathcal{A}(\gamma_{z2}, \delta)$  which completely describes the properties of the passive cavity. For a finite number of pairs  $N$  of the bottom DBR and for an increasing number of pairs  $P$  of the top DBR,  $\Delta\gamma_z$  decreases continuously to saturate to a value given by  $\frac{1}{m_\theta} \frac{1-r_N}{\pi \sqrt{r_N}}$ . The dependence of  $\Delta\gamma_z$  with respect to the reflectivity  $r_P$  comes mainly from the finesse  $F$ , since  $m_\theta$  saturates rapidly to a constant value as mentioned previously. It is important to

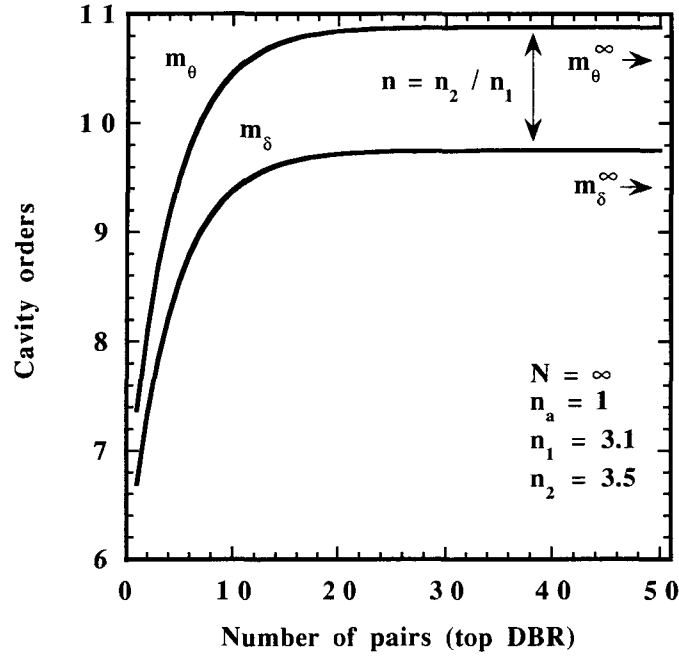


Figure 4.6: Effective angular  $m_\theta$  and spectral  $m_\delta$  cavity orders plotted with respect to the number of pairs of the top DBR, assuming a perfectly reflecting bottom DBR.

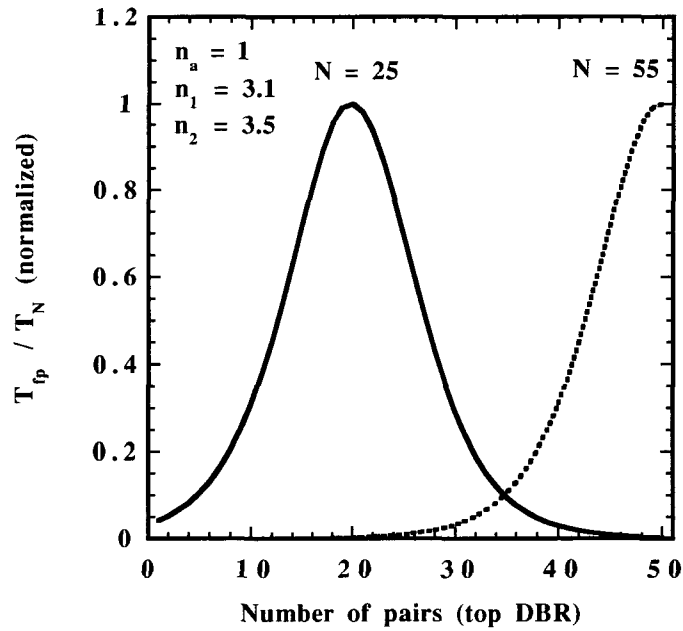


Figure 4.7:  $\frac{T_{tp}}{T_N}$  plotted versus the number of pairs of the top DBR, assuming 25 and 55 pairs for the bottom DBR.



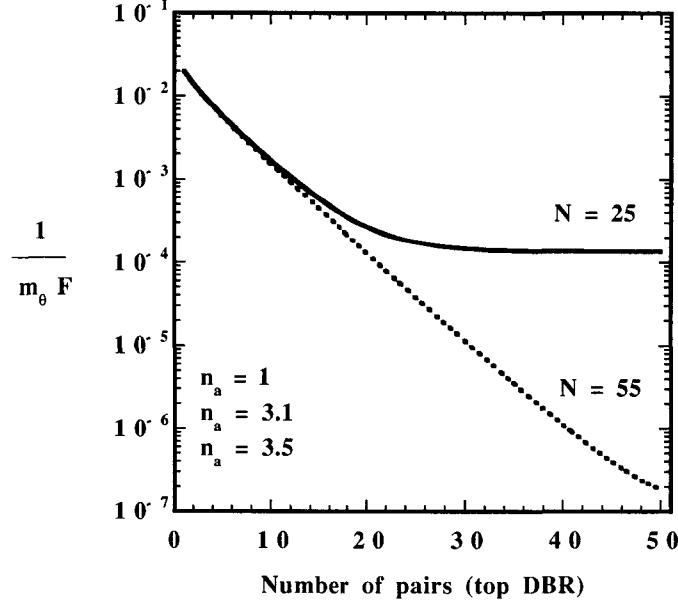


Figure 4.8: FWHM of the Airy function plotted versus the number of pairs of the top DBR, assuming 25 and 55 pairs for the bottom DBR.

bear in mind that the highest finesse value obtained by increasing the number of pairs  $P$  is determined by the reflectivity of the bottom DBR. This behavior is displayed on the figure 4.8.

The last term of equation (4.67) which depends on  $P$  and  $N$  is  $\bar{\mathcal{A}}_{max}$  which indicates how much of the Airy mode enters in the escape window. This dependence comes from the linewidth  $\sigma$  which is given by (4.55). We have  $\sigma = \sigma_o \frac{m_k}{m_\theta} + \Delta\gamma_z$ . It is clear then that  $\bar{\mathcal{A}}_{max}$  will continuously increase with respect to  $r_P$  and will saturate to a value determined by the highest finesse value. We have plotted  $\bar{\mathcal{A}}_{max}$  for various source linewidths  $\sigma_o = 0, 0.1, 0.3, 0.5$  on figure 4.9.

For a monochromatic source ( $\sigma_o = 0$ ), the linewidth  $\sigma$  is simply equal to  $\Delta\gamma_z$ . If the bottom DBR reflectivity is equal to one ( $N$  is infinite), then for  $P$  converging towards infinity, we find that  $\bar{\mathcal{A}}_{max}$  converges towards one. In this case the finesse becomes infinite and the Airy function converges towards a delta Dirac function. It is then possible to completely make all the Airy mode enters in the escape window. The factor  $\frac{T_{LP}}{T_N F}$  then simplifies into  $\frac{2}{\pi}$  giving an optimal extraction efficiency of

$$\bar{\eta}_{opt}(r_P = r_N = 1, \sigma_o = 0) = 8\pi \frac{\Pi_o^\infty}{m_\theta^\infty}. \quad (4.71)$$

Since  $\gamma_{z2}^c$  is usually higher than 0.9, this result can be simplified to  $\bar{\eta}_{opt}(r_P = r_N = 1, \sigma_o = 0) = \frac{3}{m_\theta^\infty}$  for a monochromatic source without vertical dipole contribution.

It is interesting to consider the case of a pure TE polarized source. In this situation the normalization constant of  $\frac{3}{8\pi}$  calculated in chapter 3 must be recalculated such that:

$$2\pi \int_{-1}^{+1} \Pi_{2s}^\infty = 1 \quad (4.72)$$

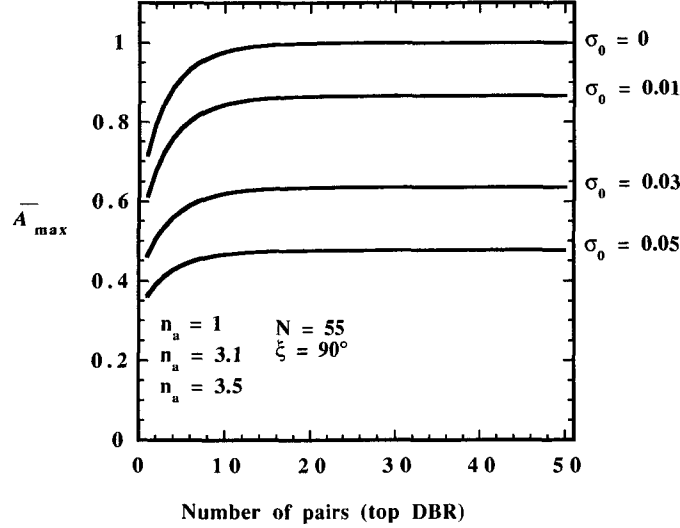


Figure 4.9: Maximum of the  $\bar{A}$  parameter plotted versus the number of pairs of the top DBR for various source linewidths  $\sigma_0$  assuming 55 pairs at the bottom DBR.

which gives  $\Pi_{2s}^\infty = \Pi_o^\infty = \frac{1}{4\pi}$ . We find then an optimal extraction efficiency of  $\bar{\eta}_{opt}(r_P = r_N = 1, \sigma_o = 0) = \frac{2}{m_\theta^\infty}$  which is the same result found by Stanley [143] who used a mode counting approach. This result shows the consistency of our approximations with existing methods used to describe the behavior of MCLEDs. If the source has a broad spectrum with a linewidth  $\sigma_o \neq 0$ , then the optimal extraction is given by:

$$\bar{\eta}_{opt}(r_P = r_N = 1, \sigma_o \neq 0) = 16\pi \frac{\Pi_o^\infty}{m_\theta^\infty} \arctan\left(\frac{1 - \gamma_{z2}^c}{\sigma_o} \frac{m_\theta^\infty}{m_\delta^\infty}\right). \quad (4.73)$$

In order to check our approximations, we have numerically calculated the optimal extraction efficiency for different conditions and compared the result to the optimal value found by using equation (4.61) (we used this expression rather than (4.67) which is less accurate). In figure 4.10, we plotted  $\bar{\eta}_{opt}$  with respect to the number of pairs  $P$  and for three given number of pairs  $N$  for the bottom DBR and for a monochromatic source.

We observe that the agreement between our model and numerical simulations is good. As expected the optimal extraction efficiency saturates to a constant value when the bottom mirror reflectivity is high. When  $N$  is small, the effect of  $\frac{T_{IP}}{T_N}$  appears for a small number of pairs  $P$  (when  $r_P$  approaches to  $r_N$ ). This is particularly clear for the case  $N = 25$  pairs: the effect of  $\frac{T_{IP}}{T_N}$  dominates  $\bar{\eta}_{opt}$ , and the extraction efficiency drops very rapidly with  $P$ . If a high number of pairs is required on the top DBR (for any reason like having a high spectral purity of the MCLED emission for instance [67]), it is then necessary to repel the maximum of  $\frac{T_{IP}}{T_N}$  as far as possible, hence to have a high bottom reflectivity. We observe that the agreement between our simple model and the simulations is not very good for  $P$  varying between 1 and 5 pairs. This comes from our approximation of the amplitude of the complex reflection coefficients within the DBR stopbands. For a small number of pairs, the reflection coefficient

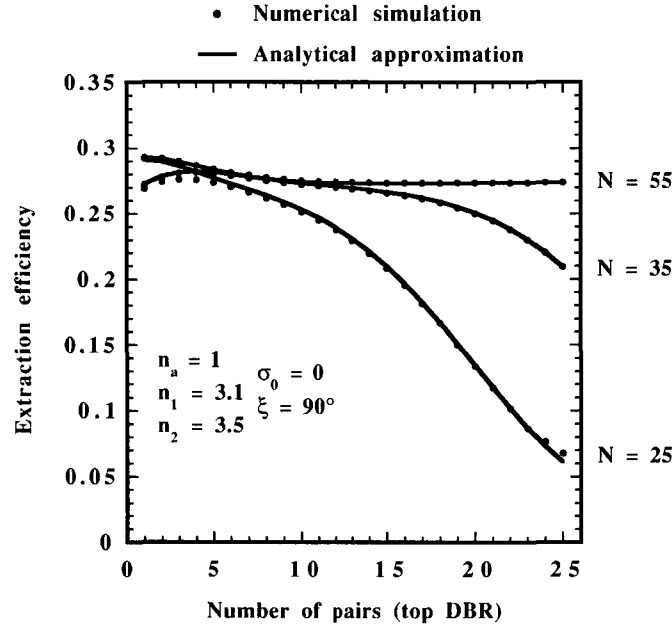


Figure 4.10: Optimal extraction efficiency plotted versus the number of pairs of the top DBR for a monochromatic source, assuming 25, 35 and 55 pairs at the bottom DBR: comparison between analytical approximation and exact simulations.

amplitude can not be assumed to be constant (as done in our model) for  $\delta$  and  $\gamma_{z2}$  values close to the Bragg condition ( $\delta = \gamma_{z2} = 1$ ). In fact, for such small reflectivities, the DBR stopband is not well defined. We could then wonder if taking into account the number of pairs  $P$  and  $N$  dependence in the calculation of  $m_\theta$  and  $m_\delta$  was necessary, since these parameters saturate rapidly towards  $m_\theta^\infty$  and  $m_\delta^\infty$  when  $P$  increases (see figure 4.6). The answer to this question is yes and this is illustrated on figure 4.11 below.

The extraction efficiency was calculated by using (4.61) with  $m_\theta$  and  $m_\delta$  depending on the DBR pairs numbers  $P$  and  $N$  (represented by the solid line). We used the same equation but we replaced the  $m_\theta$  and  $m_\delta$  parameters by their asymptotic values  $m_\theta^\infty$  and  $m_\delta^\infty$  which lead to the result represented by the dotted line on the figure. The solid circles represent the exact calculation obtained by numerical simulations. It is clear that taking into account the  $P$  and  $N$  dependence in the  $m_\theta$  and  $m_\delta$  is very important, which was to be expected simply by looking at figure 4.6: the cavity order varies between 7 and 10 for the chosen parameters which has a very significant effect on the linewidth  $\sigma$  hence on the extraction efficiency.

On figure 4.12 is plotted  $\bar{\eta}_{opt}$  for a broad spectrum source ( $\sigma_o = 0.05$ ). We obtain the same kind of result as in figure 4.10, but with a smaller saturation value for  $\bar{\eta}_{opt}$  as expected from our simple model.

Figure 4.13 shows the extraction efficiency calculated for  $N = 55$  pairs and for different source linewidths  $\sigma_o$ .

As explained previously, the extraction efficiency is limited by the  $\bar{\mathcal{A}}_{max}$  value as shown on figure 4.9. We calculated the detuning corresponding to the optimal extraction efficiency for the same structure.

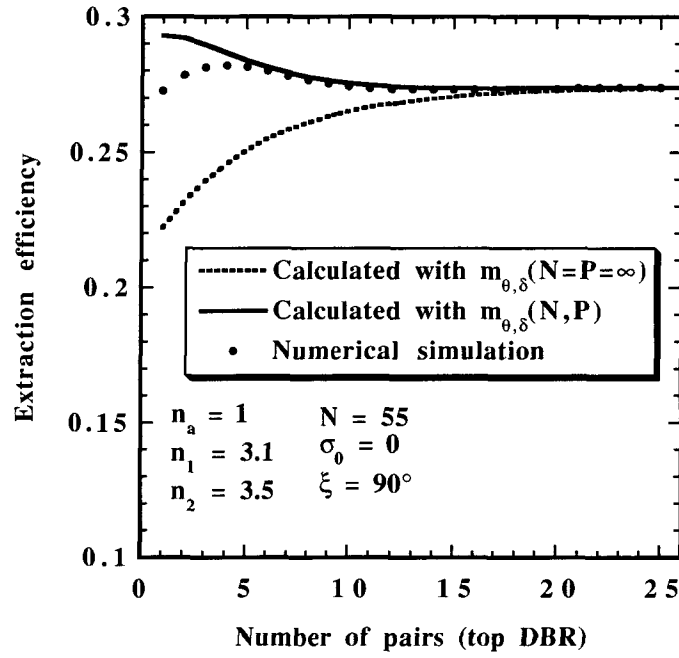


Figure 4.11: Optimal extraction efficiency plotted versus the number of pairs of the top DBR for a monochromatic source, assuming 55 pairs at the bottom DBR: comparison between analytical approximations and exact simulations.

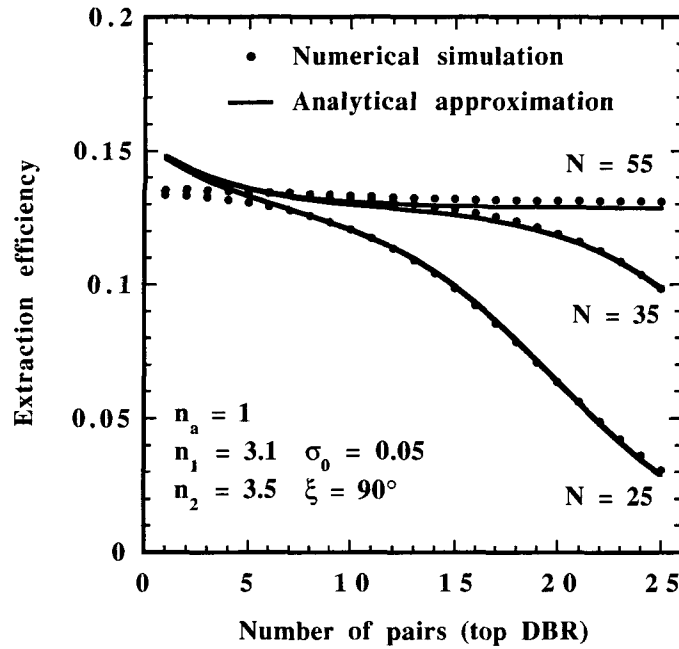


Figure 4.12: Optimal extraction efficiency plotted versus the number of pairs of the top DBR for a broad spectrum source, assuming 25, 35 and 55 pairs at the bottom DBR: comparison between analytical approximation and exact simulations.

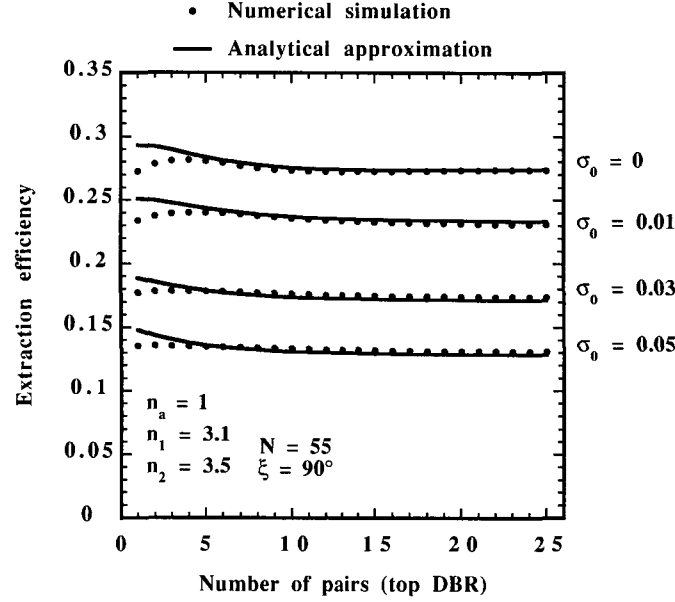


Figure 4.13: Optimal extraction efficiency plotted versus the number of pairs of the top DBR for a broad spectrum source with different linewidths  $\sigma_0$ , assuming 55 pairs at the bottom DBR: comparison between analytical approximation and exact simulations.

The result is displayed on figure 4.14. We observe that once again the agreement between exact calculations (solid circles) and our simple model (solid lines) is good.

The results presented in this section were calculated for a collection angle  $\xi = 90^\circ$ . Considering a smaller collection angle would lead to a smaller angular escape window. The optimal detuning  $\delta_{opt}$  would then be smaller than for a larger escape window width ( $\gamma_{opt}$  increases with  $\xi$  because of (4.65) and (4.62)).

To conclude this section, the analytical formula (4.61) agrees very well with exact numerical simulations. This formula can then be used to design a MCLED structure with an optimized extraction efficiency. The model takes into account the source properties (dipole distribution, emission wavelength and linewidth), the number of pairs of the Bragg mirrors, the outside medium index of refraction and the collection angle.

## 4.4 Guided modes, Purcell effect and photon recycling

In the previous section we have extensively studied the MCLEDs extraction efficiency by examining how much of light could be redirected within the semiconductor escape cone by adjusting the cavity parameters. We saw that approximatively 30% of the light emitted at the source could be extracted in the outside medium. This section explains where the remaining 70% goes. We will assume a structure with the same indices of refraction as before, 5 pairs at the top DBR and 55 pairs at the bottom. We first assume that the source is monochromatic ( $\sigma_0 = 0$ ). In this section we will use the exact formalism presented in chapter 3, so as to calculate exactly the power per unit of solid angle  $\Pi_{as}$  and

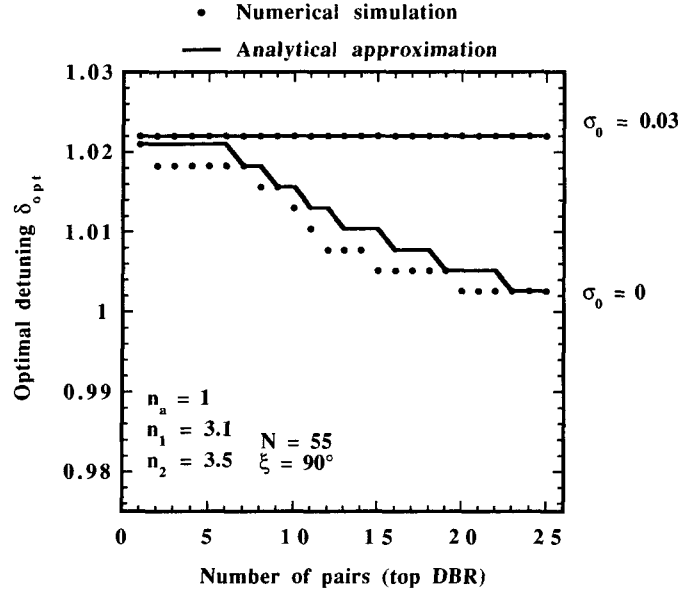


Figure 4.14: Optimal detuning plotted versus the number of pairs of the top DBR for a monochromatic and for a broad spectrum source, assuming 55 pairs at the bottom DBR: comparison between analytical approximation and exact simulations.

$\Pi_{sb}$  emitted at the source location (see chapter 3). We saw that  $\Pi_{as}$  and  $\Pi_{sb}$  could be expressed as the product of an antinode factor and an Airy function by (4.7)-(4.9). There is then the possibility that singularities occur for discrete values of  $\gamma_{z2}$  such that  $r_P r_N e^{i(4\varphi_c + \varphi_N + \varphi_P)} = 1$ . The corresponding modes are called guided modes: the unity round-trip condition allows self-sustained waves to exist in the structure [116], [14]. A necessary condition for such waves to exist is that the structure is lossless: the unity round-trip condition implies that  $|r_P| = |r_N| = 1$ . As we will see further, these conditions can exist in our generic MCLED structure even for finite number of pairs. Usually there is a finite and nonzero amount of power radiated into these modes which makes the calculation of guided modes very important for the determination of the total amount of power radiated by the source (which will give useful information on the radiative lifetime modification of dipoles placed inside a microcavity as will be seen further). One way to overcome this difficulty is to intentionally introduce a thin and weakly absorbing layer close to the source [12]. The power injected into guided modes goes then necessarily to the absorbers: the delta-Dirac guided modes are then converted into sharp peaks which can be numerically resolved by adaptive maximum search algorithms. It is important that such damping layer is placed close to the source: this ensures that the coupling between radiated modes and cavity modes is the same as the one of the source. A damping layer placed at a node of the cavity field would of course not allow detection of the guided modes. We have then assumed that a thin (1 nm thick) absorbing layer ( $\tilde{n}_2 = n_2 + 0.01i$ ) was placed 4 nm from the source, on the top side of the structure. We plotted on figure 4.15 the power per unit of solid angle  $\Pi_{as}$  (solid line) emitted by the source in the cavity medium and at the source position. The source was an horizontal dipole emitting TE polarized monochromatic radiation at a wavelength  $\lambda_o$  smaller than  $\lambda_{Bragg}$ . With  $\lambda_o = 640nm$  and

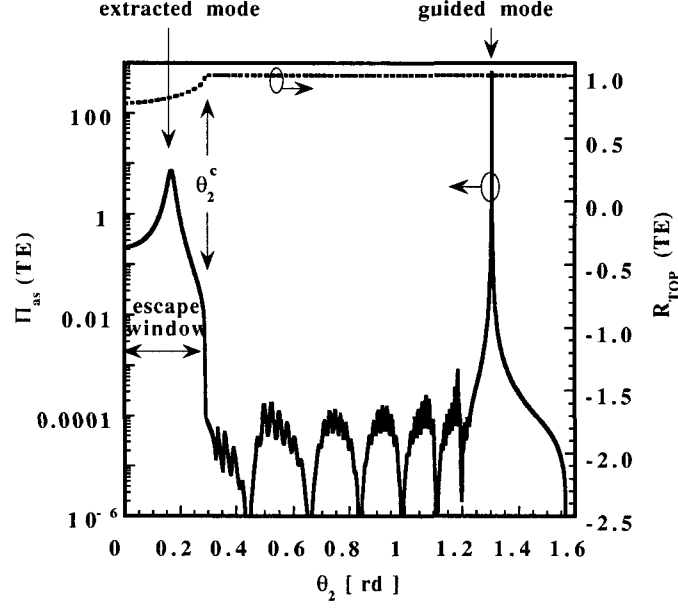


Figure 4.15: Power per unit of solid angle radiated towards the top of the MCLED at the position of an horizontal TE dipole (left axis) and reflectance of the top DBR calculated from the cavity (right axis).

$\lambda_{Bragg} = 650nm$ , we have a normalized energy of  $\delta_o = 1.0156$ . The angle  $\theta_2$  is defined in the cavity medium of refractive index  $n_2$ . Since  $n_a = 1$  and  $n_2 = 3.5$ , the critical angle  $\theta_2^c$  is  $0.29$  rd ( $16.6^\circ$ ) which defines the angular escape window (see figure 4.15). Since  $\delta_o > 1$ , we observe a resonance inside the escape window at  $\theta_2 = 0.16rd$ . For angles greater than  $\theta_2^c$ ,  $\Pi_{as}$  drops abruptly to very small values except at  $\theta_2 = 1.30rd$  where a very sharp and intense resonance is found.

In order to make this behavior clearer, we also plotted on figure 4.15 (dotted line) the amplitude of the top DBR reflectivity  $R_{top} = |r_P|^2$  calculated at  $\delta_o = 1.0156$ . Since this mirror has very few pairs ( $P = 5$ ), the DBR displays a moderate reflectivity close to normal incidence ( $\theta_2 = 0^\circ$ ). At  $\theta_2 > \theta_2^c$ ,  $R_{top}$  is equal to one because of total internal reflection between semiconductor (high index) and outside medium (low index  $n_a < n_2$ ). Plane waves are then totally reflected by the top mirror ( $R_{top} = 1$ ). There is then a possibility to find some guided modes provided the condition  $r_N = 1$  is also satisfied. We plotted on figure 4.16, the power per unit of solid angle  $\Pi_{sb}$  emitted towards the substrate (solid line) and the reflection coefficient  $R_{bottom} = |r_N|^2$  calculated at  $\delta_o = 1.0156$  (dotted line).

Since the bottom DBR ends up with a high index layer (corresponding to an infinite substrate of index  $n_2$ ),  $R_{bottom}$  displays an angular stopband which (with the parameters we chose) is larger than the escape window width. For angles between  $\theta_2 = 0.35rd$  and  $\theta_2 = 1.18rd$  the DBR reflectivity is poor and the mirror leaks. Most of the light emitted towards the substrate is then lost through the leaky modes. It is interesting to note that the leaky modes display a high frequency modulation corresponding to the DBR sidelobes on which is superposed a second modulation with a smaller frequency. This gives rise to a periodic inhibition of the leaky mode intensity. It can be shown that this effect comes from

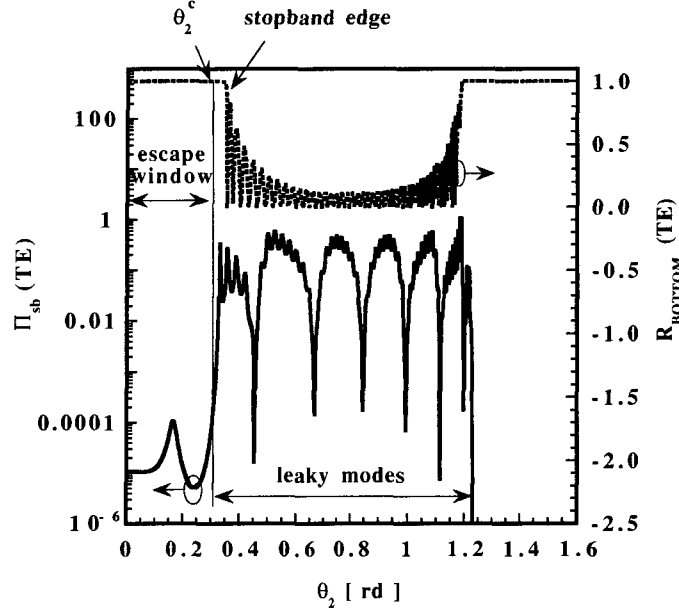


Figure 4.16: Power per unit of solid angle radiated towards the bottom of the MCLED at the position of an horizontal TE dipole (left axis) and reflectance of the bottom DBR calculated from the cavity (right axis).

the antinode factor of the power per unit of solid angle terms.

For angles greater than  $\theta_2 = 1.18rd$ , the DBR behaves like a perfect mirror because of the total internal reflection. The critical angle corresponding to total internal reflection between layers of high and low index in the DBR is given by  $\theta_{12}^c = \text{asin}(n_1/n_2) = 1.09rd$ . As we mentioned it in chapter 2, the effective total internal reflection occurs for a higher angle due to total internal frustrated reflections (also called optical tunnel effect [80]). As expected, the guided mode of figure 4.16 is found at an angle for which the condition  $|r_P| = |r_N| = 1$  is fulfilled. Since the damping layer is placed on top of the source, the guided mode is not displayed on figure 4.16. A resonance is found in the escape window of this last figure but with a very small amplitude compared to the one of figure 4.15. This is simply due to the fact that the emission is mainly directed towards top of the structure:  $|r_N|^2 \gg |r_P|^2$  (see section 4.3). We also clearly observe the existence of leaky modes which represent the major part of the light emitted towards the substrate. One can see on figure 4.15 sort of such leaky modes but with two orders of magnitude smaller amplitude. Theoretically, there should be no light emitted at these angles because of total internal reflection due to the outside medium semiconductor boundary. The observed oscillations come simply from the small absorbing layer placed on top of the structure which makes the reflectivity not strictly equal to one.

We can now evaluate the fraction of light emitted in the extracted ( $\eta_E$ ), leaky ( $\eta_L$ ) and guided ( $\eta_G$ ) modes. These terms were calculated according to the following formulas:



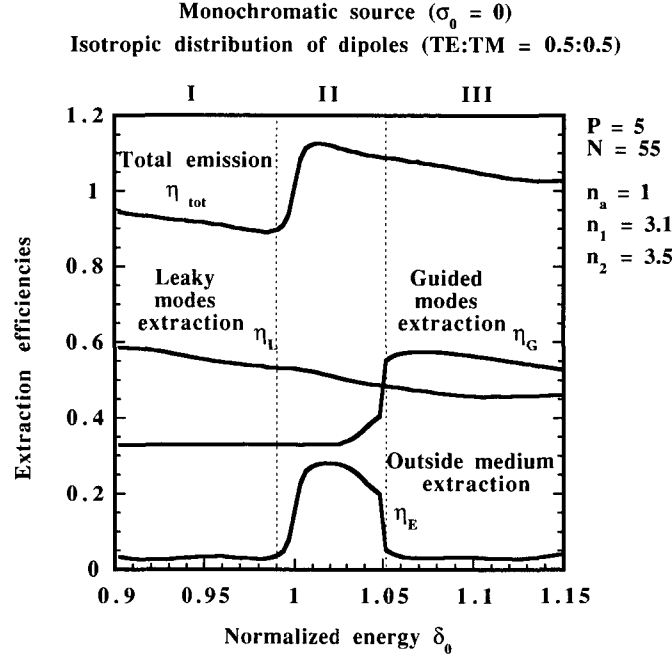


Figure 4.17: Extraction efficiencies for extracted, leaky and guided modes plotted versus the detuning  $\delta_0$ . The total emission is also represented.

$$\eta_E(\delta_o) = 2\pi \int_{\gamma_{z2}^c}^1 [\Pi_{as}(\gamma_{z2}, \delta_o) + \Pi_{sb}(\gamma_{z2}, \delta_o)] d\gamma_{z2} \quad (4.74)$$

$$\eta_L(\delta_o) = 2\pi \int_0^{\gamma_{z2}^c} \Pi_{sb}(\gamma_{z2}, \delta_o) d\gamma_{z2} \quad (4.75)$$

$$\eta_G(\delta_o) = 2\pi \int_0^{\gamma_{z2}^c} \Pi_{as}(\gamma_{z2}, \delta_o) d\gamma_{z2}. \quad (4.76)$$

The overall power emitted by the dipole distribution is given by:

$$\eta_{tot}(\delta_o) = \eta_E(\delta_o) + \eta_L(\delta_o) + \eta_G(\delta_o). \quad (4.77)$$

These extraction efficiencies are displayed on figure 4.17.

We have delimited three regions called I, II and III depending on the values taken by the source normalized energy  $\delta_o$ . In regions I and III, the extraction efficiency  $\eta_E$  is very small because the cavity resonance is not in the escape window (hence not extracted). As calculated in section 4.3,  $\eta_E$  approaches 30 % in region II. The leaky mode contribution  $\eta_L$  to the total power is very large since it represents approximatively 50 % of the emitted light. This light is then completely lost in the substrate. The guided mode efficiency  $\eta_G$  is more or less constant in regions I and II (30 %) and jumps to a higher value in region III (55 %). This is due to the fact that the Airy mode shifts from small angles  $\theta_2$  to higher ones as  $\delta_o$  increases as explained in section 4.3. When it goes out of the escape window, the Airy mode is transformed into a guided mode which explains the step in the  $\eta_G$

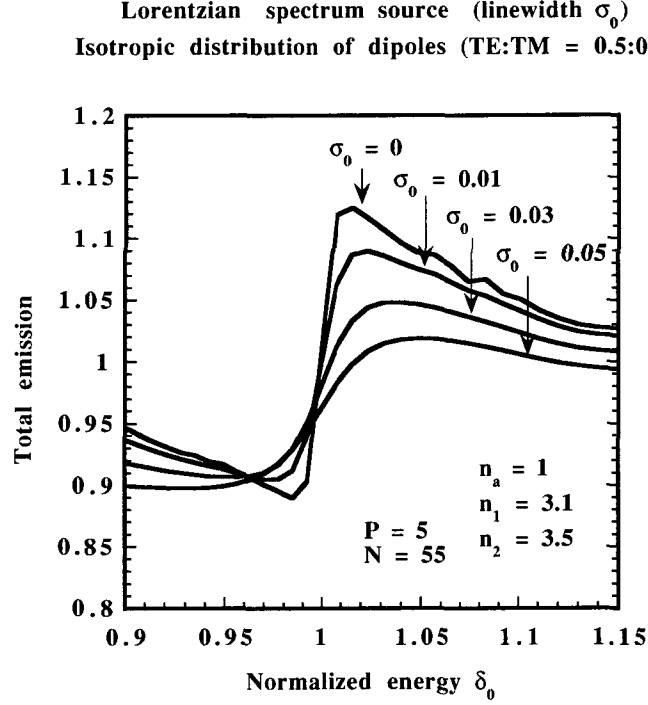


Figure 4.18: Total emission plotted versus the detuning  $\delta_0$  for a broad spectrum source with various linewidths.

which occurs at the limit between regions II and III. The total emission  $\eta_{tot}$  is represented on the same figure. One can observe that its value is not constant and differs from one, which is the value we calculated for the total emission of any dipole distribution in an infinite medium (see chapter 3). Physically, a change in the total power emitted by a dipole distribution representing radiative electron-holes recombinations, is related to a change of recombination rate, hence in lifetime [9], [105], [104], [87]. Many authors studied this effect in details [100], [56], [17], [162], [64]. Our results confirm those of references [1], [152] demonstrating that in one dimensional DBR-based microcavities, the radiative lifetime modification is limited. The change of radiative lifetime due to the presence of a cavity is known as the Purcell effect and is given by  $\eta_{tot}$  which also corresponds to  $\Delta\tau(\delta)$  (see equation (4.18)). In the case of a broad spectrum source (with a Lorentzian lineshape), the averaged Purcell factor is given by equation (4.20) and is displayed on figure 4.18 for various linewidths  $\sigma_0$ .

As expected, the effect of enlarging the spectral width is to average out the normalized energy dependence of the Purcell factor. These results justify the assumption we made in section 4.3 to neglect the radiative lifetime change. We can conclude this chapter by observing that a significant part of the source emission is lost in the guided and in the leaky modes. One solution to increase the extraction efficiency is to convert the leaky modes into guided modes and to recycle them by using reabsorption mechanism [114], [135], [136] or to extract the guided modes on the edges of the structure [132], [155]. These solutions are examined in great detail in the reference [117].

## Chapter 5

# Effect of the detuning on the extraction: theory and experiments

The purpose of this chapter is to show experimentally the critical role that the detuning has on external quantum efficiency. Section 5.1 discusses the different possibilities which can be used to experimentally change the detuning across a wafer. Section 5.2 briefly presents the growth system which was used and explains how it is possible to control the thickness gradients on the wafer. Then section 5.3 describes the processing steps as well as the characteristics of the mask designed (5.4). The last section (5.5) of this chapter presents the MCLED structures fabricated. The influence of detuning on the extraction efficiency as well as on the pattern of emission is shown. Finally, we exploit these results to estimate the internal quantum efficiency of these devices.

### 5.1 Controlled detuning in MCLEDs

In the previous chapter we discussed in detail the importance of the detuning parameter for the optimization of the extraction efficiency. The detuning was defined as the ratio between the electroluminescence peak wavelength  $\lambda_{QW}$  of the quantum well emission and the Fabry-Pérot wavelength  $\lambda_{FP}$  defined at normal incidence.  $\lambda_{QW}$  can be controlled by modifying the thickness, the composition or the strain of the quantum wells [29], [122].  $\lambda_{FP}$  can be modified by changing the optical thicknesses of the layers. Usually the physical thicknesses are more easily modified than the indices of refraction. In this chapter we will assume that the indices of refraction are fixed. Their values are given in section 2.3. We will assume that the structure has  $P = 5$  pairs on the top DBR and  $N = 35$  at the bottom. For the structure presented in figure 2.15, we have  $\lambda_{FP} = 4 n_1 L_1 = 4 n_2 L_2 = n_2 L_c$  where the subscripts "1", "2", "c" refer respectively to the high and low indices DBR layers and to the cavity layer. For device production, a good layer uniformity is required for the wafer: fixing the detuning to a given value can easily be done by adjusting  $\lambda_{QW}$  or  $\lambda_{FP}$ . For some applications, it is important to be able to make vary the detuning across the wafer surface and to control this non-uniformity. The experimental investigation of the effect of detuning on the MCLED external quantum efficiency is an example of such an application and is the object of this chapter. Another example is the realization of densely-packed

2D arrays of multiwavelength emitting devices which can find applications in wavelength division multiplexing (WDM) [43], [60], [90], [157]. In this chapter we consider the structure presented in figure 2.15. The normalized energy  $\delta = \frac{\lambda_0}{\lambda}$  is defined with respect to the fixed wavelength  $\lambda_0 = n_2 L_c$ . The Fabry-Pérot mode of the structure corresponds then to the normalized energy  $\delta_{FP} = 1$ . We examine in this section the effect of changing one growth parameter only: we can choose to change  $L_{1,2}$  or  $L_c$ , which will clearly modify  $\lambda_{FP}$ . However, it is necessary to check that the properties of the structure remain the same. For that purpose we focus on the properties of the Fabry-Pérot mode (linewidth and amplitude).

In the study of the Fabry-Pérot resonator (chapter 2), we introduced the phase  $\varphi$  equal to the sum of a phase shift term  $4\varphi_c$  due to the cavity and of two phase shifts  $\varphi_b$  and  $\varphi_N$  related to the dielectric mirrors. We want to determine how  $\delta_{FP}$  is modified when the physical thickness of the DBR layers  $L_{dbr}^{1,2}$  and of the cavity  $L_{cav}$  differ from  $L_{1,2}$  and  $L_c$  respectively. For that purpose, the parameters  $\xi_{dbr}$  and  $\xi_{cav}$  are introduced with:

$$L_{cav} = \xi_{cav} L_c \quad (5.1)$$

$$L_{dbr}^{1,2} = \xi_{dbr} L_{1,2}. \quad (5.2)$$

For the reference structure we have  $\xi_{cav} = \xi_{dbr} = 1$ . The phases  $\varphi_c$  and  $\varphi_b + \varphi_N$  are given at normal incidence by:

$$\varphi_c = \pi \delta \xi_{cav} \quad (5.3)$$

$$\varphi_b + \varphi_N = D_\delta (\xi_{dbr} \delta - 1) \quad (5.4)$$

where we defined  $D_\delta = D_\delta^b + D_\delta^N$ . We remind the reader that  $D_\delta^b$  and  $D_\delta^N$  can be calculated by using equations (2.62) and (2.51). These parameters depend on the indices  $n_a, n_1, n_2$  and on the numbers of pairs N and P only. Note that the DBR stopband is centered around the normalized Bragg energy  $\xi_{dbr} \delta$ .

Considering equation (2.76), one sees that the Fabry-Pérot resonances are found when  $\varphi = 2\pi p$  with  $p$  integer, which gives the Fabry-Pérot normalized energy:

$$\delta_{FP} = \frac{2\pi p + D_\delta}{4\pi \xi_{cav} + D_\delta \xi_{dbr}}. \quad (5.5)$$

This equation takes into account the fact that we consider a lambda cavity for the reference structure, hence  $p = 2$  such as  $\delta_{FP} = 1$  when  $\xi_{cav} = \xi_{dbr} = 1$ . This expression shows that the Fabry-Pérot wavelength varies linearly with respect to the normalized thicknesses  $\xi_{cav}$  and  $\xi_{dbr}$ . Considering figure 2.14, one sees that  $D_\delta = D_\delta^b + D_\delta^N$  is of the order of 50 which has to be compared to  $4\pi \approx 12$  (1% of variation on the DBR thickness will shift the Fabry-Pérot wavelength more efficiently in comparison

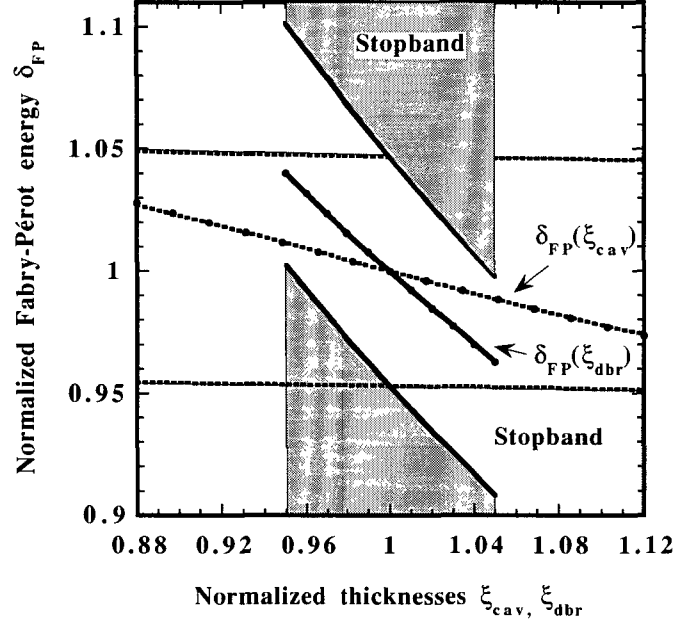


Figure 5.1: Normalized Fabry-Pérot energies plotted versus the normalized thickness  $\xi_{cav}$  for  $\xi_{dbr} = 1$  (dotted line) and versus the normalized thickness  $\xi_{dbr}$  for  $\xi_{cav} = 1$  (solid line). Solid circles represent values of  $\delta_{FP}$  calculated with the analytical approximation.

to 1% of variation on the cavity thickness). In figure 5.1 are plotted  $\delta_{FP}(\xi_{cav})$  versus the normalized thickness  $\xi_{cav}$  for  $\xi_{dbr} = 1$  (dotted line) and  $\delta_{FP}(\xi_{dbr})$  versus the normalized thickness  $\xi_{dbr}$  for  $\xi_{cav} = 1$  (solid line). These values were calculated by using the transfer matrix method (see chapter 2). The solid dots represent  $\delta_{FP}$  calculated with equation (5.5). The accuracy of this analytical approximation is very good.

The shaded areas represent the stopband positions for the two kinds of structures. The stopband position does not change with  $\xi_{cav}$  while keeping  $\xi_{dbr}$  constant. This is to be expected since the DBRs transmittances are centered at the normalized energy  $\delta_{Bragg} = 1$ . The stopband position changes rapidly with respect to the normalized thickness  $\xi_{dbr}$  even if the cavity thickness is kept constant (this can be easily understood considering that the DBRs transmittances are centered at the Bragg energies  $\delta_{Bragg} = \frac{\lambda_0}{4n_2 L_2 \xi_{dbr}} = \frac{1}{\xi_{dbr}}$ ). Note that the FP mode remains approximatively at the center of the stopband in this case. Therefore, the properties of the FP mode (i.e. linewidth and amplitude) should not be affected by changing  $\xi_{dbr}$ .

In figures 5.2 and 5.3, we plot the parameters  $T_{max}$  and  $\Delta\delta$  as function of  $\xi_{cav}$  and  $\xi_{dbr}$ . The exact solutions are compared with the analytical formulas (2.77) and (5.6).

$$\Delta\delta = \frac{2\pi}{F} \frac{\delta_{FP}}{4\pi + D_\delta}. \quad (5.6)$$

We see clearly that the analytical formulas are correct when  $\xi_{dbr}$  changes but not with  $\xi_{cav}$ . The reflectivity of the DBRs varies across the stopband, so by changing  $\xi_{dbr}$ , the Fabry-Pérot mode remains in the center of the stopband, hence the mirror properties remain constant.

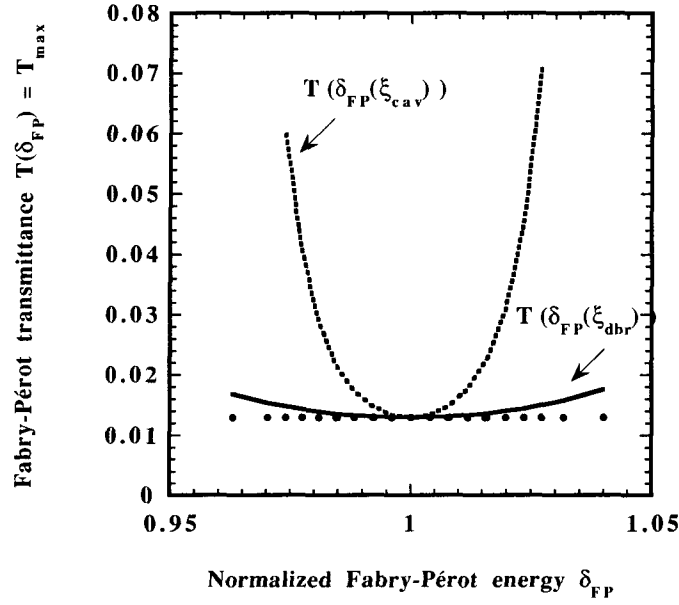


Figure 5.2: Fabry-Pérot transmittance plotted versus the normalized Fabry-Pérot energy:  $T(\delta_{FP}(\xi_{cav}))$  for  $\xi_{dbr} = 1$  (dotted line) and  $T(\delta_{FP}(\xi_{dbr}))$  for  $\xi_{cav} = 1$  (solid line). Solid dots represent analytical approximations.

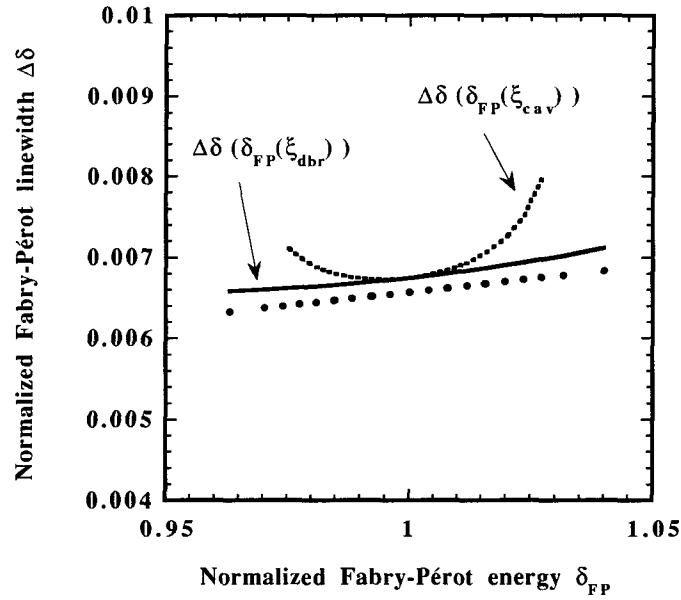


Figure 5.3: Fabry-Pérot linewidth plotted versus the normalized Fabry-Pérot energy:  $\Delta\delta(\delta_{FP}(\xi_{cav}))$  for  $\xi_{dbr} = 1$  (dotted line) and  $\Delta\delta(\delta_{FP}(\xi_{dbr}))$  for  $\xi_{cav} = 1$  (solid line). Solid dots represent analytical approximations.

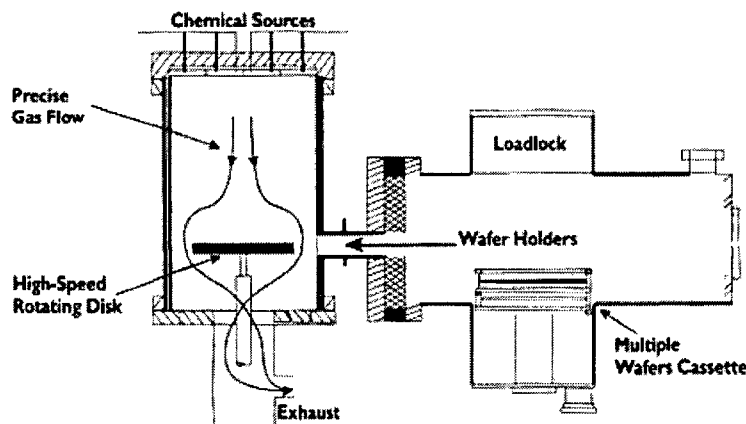


Figure 5.4: Design of the vertical Emcore reactor.

In conclusion, modifying the DBR layers thicknesses while keeping the cavity thickness constant is to be preferred to the contrary: the Fabry-Pérot energy shift is large while the Fabry-Pérot mode remains in the center of the stopband which has the effect to not distort the Fabry-Pérot mode shape too much (especially its amplitude and its linewidth). This is the solution we then chose for the following experiment.

## 5.2 Description of the growth system used

The samples studied in this chapter were grown by Metal-Organic Vapor Phase Epitaxy (MOVPE) with an Emcore reactor. The purpose of this section is to briefly present the characteristics of this reactor. More detailed information concerning the MOVPE growth can be found in [30]. Figure 5.4 presents a schematic of the vertical reactor used.

In this system the metal-organic compounds are provided by six apertures connected in pairs, symmetrically placed in the center, in the middle and at the edge of the top of the reactor. Their fluxes can be controlled by three mass flow controllers which control the gas distribution in the reactor, and hence the growth rates. Since growth is performed during rotation of the substrate, it is possible to achieve a variation of layer thickness with a rotational symmetry around the growth direction. In order to demonstrate the controllability, three test AlAs/GaAs DBRs were grown opening one of the three pairs of gas inlets and closing the two others. We measured the reflectivities of these mirrors from the center of the wafer to its edges and observed a wavelength shift of the stopband. Assuming that the Bragg condition was fulfilled over the whole surface of the wafer, we fitted the measured reflectivity spectra by transfer matrix calculations and extracted the physical thicknesses of the mirrors layers. The thickness variation of the AlAs layer as a function of position is shown on figure 5.5.

The GaAs layer displays a similar variation. The results indicate that it is possible to get concave or convex (best fit) thickness profiles. By adjusting the three gas flows, it is then possible to achieve either very uniform growth rates [109] (deviation  $< 0.3\%$ ), or a controlled thickness variation as we

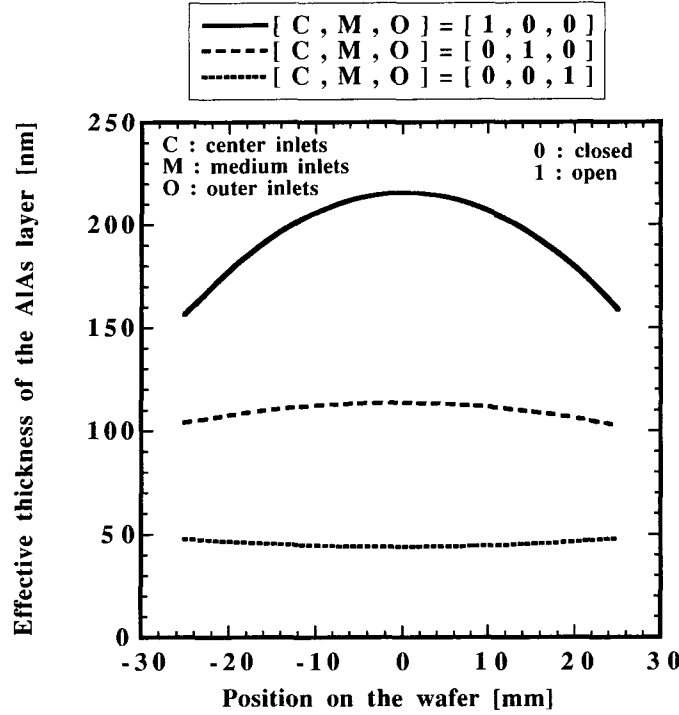


Figure 5.5: Dependence of AlAs layer thickness on gas inlet opening. Solid line: center gas inlet. Dashed line: medium gas inlet. Dotted line: outer gas inlet.

did here. In the latter case, the growth rate varies according to a parabolic law with respect to the position on the wafer as can be seen on figure 5.5.

Since we wanted to grow visible red MCLEDs, we used non-absorbing DBRs. Thus the mirrors were made of  $\text{Al}_{0.46}\text{Ga}_{0.54}\text{As}$  and AlAs materials. We grew several calibration DBRs before growing the whole MCLED structure, changing only the fluxes of the three gas inlets. As shown on figure 5.4, the mass flow controllers called O (for outer), M (for medium) and C (for center) control the gas fluxes we call  $\alpha$ ,  $\beta$  and respectively  $\gamma$ . The sum of these three fluxes was kept constant to the value  $\alpha + \beta + \gamma = 1200$  ccm and the middle flux was fixed at  $\beta = 600$  ccm. We grew three calibration DBRs changing the center and outer fluxes only with  $\alpha = 60, 96$  and  $135$  ccm. We measured the reflectivity spectra of the three corresponding wafers from their centers to their edges. By using conventional transfer matrix formalism we fitted these curves, from which we extracted the Bragg wavelengths displayed on figure 5.6.

These curves were fitted by a parabolic law of the form:  $\lambda(x) = ax + \lambda_0$  where  $\lambda_0$  is the Bragg wavelength at the center of the wafer (in nanometers),  $a$  the bowing coefficient of the parabola (in nanometers per millimeters) and  $x$  the position measured from the center of the wafer in millimeters. On figure 5.7 are plotted the parameters  $\lambda_0$  and  $a$  with respect to the gas flux  $\alpha$  for the three runs which were grown.

We observe that  $\lambda_0$  and  $a$  are linearly dependent of  $\alpha$ :



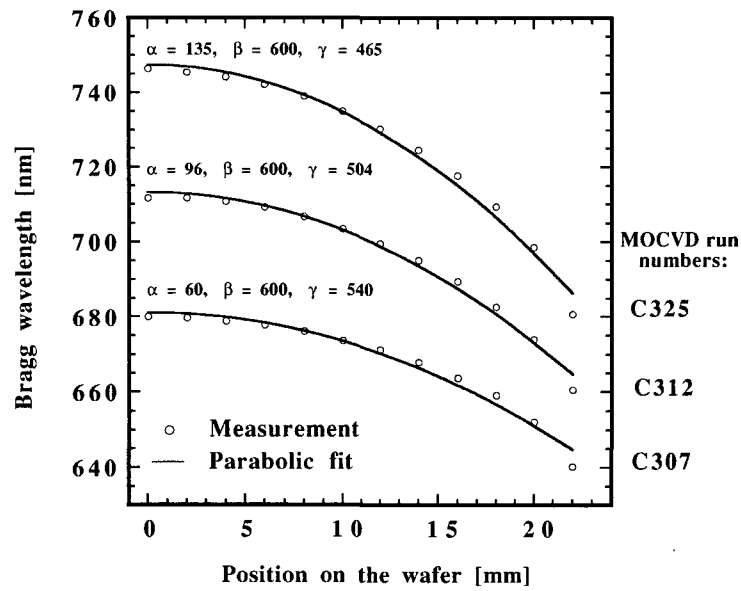


Figure 5.6: Bragg wavelengths of three calibration DBRs grown with various gas fluxes  $\alpha$  and  $\gamma$ ,  $\beta$  being kept constant, plotted with respect to the position on the wafer.

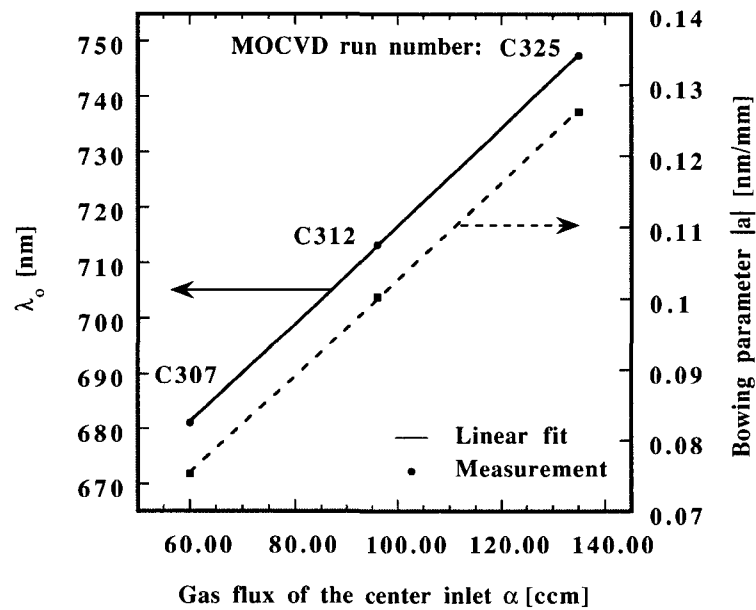


Figure 5.7: Bragg wavelengths of the three calibration DBRs measured at the center of the wafer and plotted versus the gas flux  $\alpha$ .

$$\begin{cases} \lambda_0[nm] = 628.14 + 0.88 \alpha[ccm] \\ a[nm/mm] = -3.468 \cdot 10^{-2} - 0.068 \cdot 10^{-2} \alpha[ccm]. \end{cases} \quad (5.7)$$

We are interested in having a large absolute value of the bowing parameter  $a$  in order to change significantly the detuning of the MCLED on the wafer. This requires a high gas flux  $\alpha$ . Considering the graph above we see that increasing the gas flux  $\alpha$  also increases the Bragg wavelength  $\lambda_0$  to values larger than the ones desired for red light emission. One way to control  $\lambda_0$  without affecting  $a$  is to change the growth time  $t$  (which was held to the constant value  $t_0$  in the previous experiment). The general dependence of the Bragg wavelength with respect to the position in function of the growth parameters can be written as follows:

$$\lambda_{Bragg}(x) = a(\alpha) x + \frac{t}{t_0} \lambda_0(\alpha). \quad (5.8)$$

We used two inches wafers for this experiment. It is then possible to estimate the shift of the Fabry-Pérot mode of a MCLED grown with some given growth parameters  $\alpha$  and  $t$  (we can estimate that for such a wafer the useful position range is from  $x = 0$  to  $x = 25$  mm).

If the fluxes  $\alpha$ ,  $\beta$  and  $\gamma$  are kept constant during the growth of the whole structure, then the layer thicknesses of the active region will also change with the position on the wafer. This influences the quantum well emission wavelength and the injection properties of the cavity. Although it is theoretically possible to calculate the emission wavelength dependence of the quantum well emission with the quantum well thickness [122], it is difficult to correct this effect with a good accuracy. Because of these considerations, the active region was grown with the gas fluxes giving uniform growth rates across the wafer. In addition, we observed experimentally that the growth of AlGaInP compounds with a thickness gradient leads to bad surface morphology. The three gas inlets fluxes ( $\alpha$ ,  $\beta$  and  $\gamma$ ) of the metal-organic compounds were set during the mirror growth to give a parabolic profile of the DBR layer thicknesses, but were changed during the growth of the cavity so as to achieve uniform layer thickness, ensuring a constant emission wavelength as well as similar injection conditions across the whole surface of the wafer. The gas fluxes  $\alpha = 250$ ,  $\beta = 600$ ,  $\gamma = 350$  ccm were chosen for the growth of the DBRs and the gas fluxes  $\alpha = 24$ ,  $\beta = 300$ ,  $\gamma = 876$  ccm ensured a very uniform growth of the active region [109]. The MCLED structure was grown on a n-doped GaAs substrate. The n-doped DBR consists of 34.5 pairs of Si-doped  $\text{Al}_{0.46}\text{Ga}_{0.54}\text{As}$  and AlAs quarter wavelength layers. The active layer, consisting of three GaInP quantum wells and  $(\text{Al}_{0.3}\text{Ga}_{0.7})_{0.5}\text{In}_{0.5}\text{P}$  barriers nominally undoped is surrounded by two  $(\text{Al}_{0.7}\text{Ga}_{0.3})_{0.5}\text{In}_{0.5}\text{P}$  spacer layers (Si-doped and Mg-doped) to form a one-lambda cavity. The outcoupling DBR consists of three pairs of Mg-doped  $\text{Al}_{0.46}\text{Ga}_{0.54}\text{As}$  and AlAs quarter wavelength layers. A 30 nm thick GaAs cap layer highly p-doped concludes the structure and is aimed at helping in having a good ohmic p-contact. Figure 5.8 summarizes the important parameters of the MCLED structure. The vertical axis shows the indices of refraction of each layer.

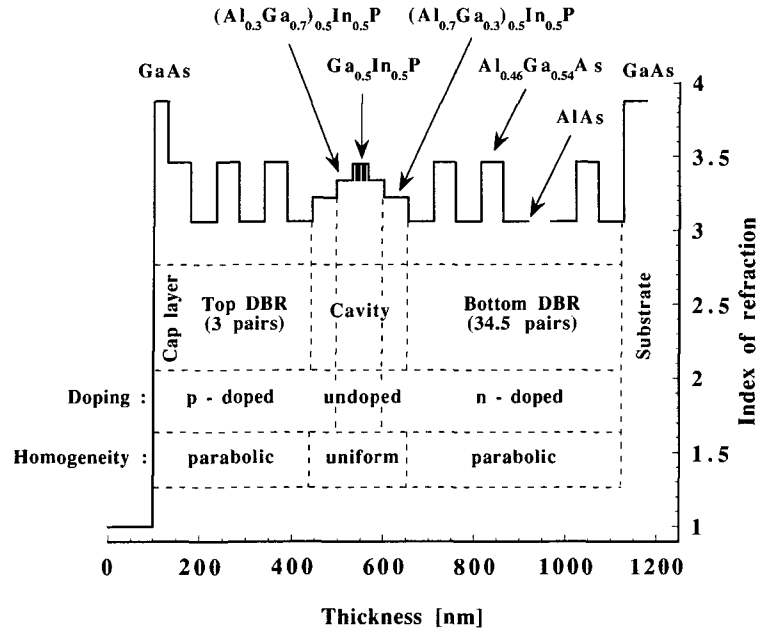


Figure 5.8: Description of the MCLED structure investigated in this chapter.

### 5.3 Description of the processing

The first step of processing consists of depositing the n-type bottom contact on the back side of the substrate. First, photoresist (S1818) was deposited on the top side of the wafer (so as to protect it), at 4000 rpm during 30 seconds. A hard bake was performed at 115 °C during 90 seconds. A solution of HCl:H<sub>2</sub>O with the ratio 1:1 was used during 5 seconds to remove the oxides of the back side of the substrate. The back side of the wafer was then metallized by e-beam evaporation. A sequence of Ge: Au: Ni: Au (23:47:30:150 nm) was deposited at a rate of 1 nm/s. The photoresist was removed in acetone (5 minutes), and the wafer was dipped in isopropanol (1 minute) and finally rinsed with water. The contact was then annealed in a nitrogen atmosphere at 410 °C for 30 seconds.

In a second step, mesas were formed on the top side of the wafer by Electron Cyclotron Resonance (ECR) plasma etching. Standard photolithography process was used (with a Carl Süss mask aligner) to define squared shape mesas. Photoresist S1818 was deposited at 4000 rpm during 30 seconds and prebaked at 115 °C during 90 seconds, before being exposed 6.5 seconds through the first level pattern of the mask. After developing the resist 45 seconds in a standard developer (MF319), the sample was postbaked 60 seconds at 120 °C then etched through the active zone, once the photoresist was removed with a standard hot (100 °C) remover solution of Microposit 1165 (see figure 5.9).

Etching rates and a detailed description of the ECR system can be found in [48]. Before performing the third processing step, the sample was cleaned by using Reactive Ion Etching (RIE) in an oxygen plasma in order to get rid of the residual photoresist.

In a third step, the whole surface of the structure was passivated with 120 nm of Si<sub>3</sub>N<sub>4</sub> deposited by Plasma Enhanced Chemical Vapor Deposition (PECVD). This layer is used for electrical isolation

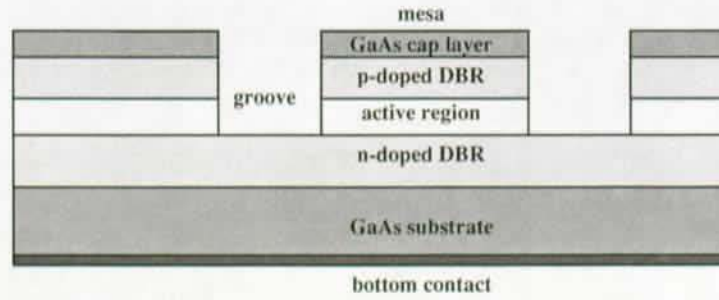


Figure 5.9: Processing step number 1: etching of the mesa.

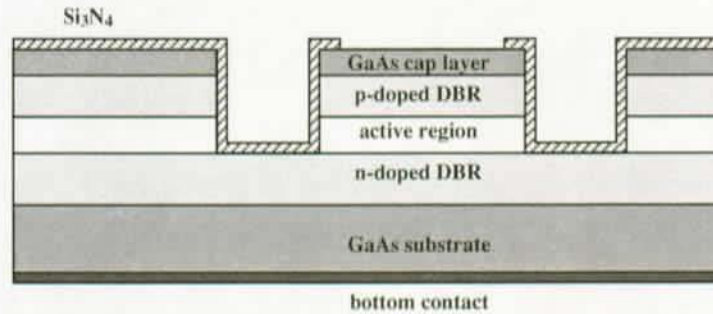


Figure 5.10: Processing step number 2:  $\text{Si}_3\text{N}_4$  deposition and window opening.

and for passivation of the etched sidewalls of the mesa.

The fourth processing step consists of defining a window on top of the mesa in the  $\text{Si}_3\text{N}_4$  layer. For that purpose S1818 photoresist was deposited 30 seconds at 4000 rpm and prebaked 60 seconds at 115 °C before being exposed 3.6 seconds through the second level of the mask. After 45 seconds of developing in the developer MF319, the sample was postbaked 30 seconds at 115 °C to harden the resist. The windows were then opened by RIE dry etching in a  $\text{CF}_4$  plasma. An end-point detection system was used to stop the RIE etch of the  $\text{Si}_3\text{N}_4$  layer: we observed that with the parameters used to tune the plasma, the (usually thin) GaAs cap layer could be etched at a slow rate of 2.5 nm/min, which made the end-point detection required. After removing the photoresist with hot (100 °C) Microposit 1165 remover, the processed device resemble to what is depicted on figure 5.10.

In the fifth step, non-alloyed p-contacts were evaporated on top of the mesa and patterned using the lift-off technique. These contacts were extended on the un-etched surface of the mesa in order to serve as a bond pad. Photoresist AZ5214E was deposited at 3000 rpm during 30 seconds on the sample, and prebaked 90 seconds at 90 °C before being exposed 2.5 seconds through the third level of the mask. A reversal bake was then performed 150 seconds at 120 °C and the sample was exposed without any mask (flood exposure) during 12 seconds. After 80 seconds of developing in MF319 developer, the sample was prepared for the final step of p-metallization: a short dip in  $\text{HCl}:\text{H}_2\text{O}$  (1:1) solution so as to remove any oxide before the p-metal evaporation. A sequence of Ti:Pt:Au:Pt (40:10:200:30 nm) was

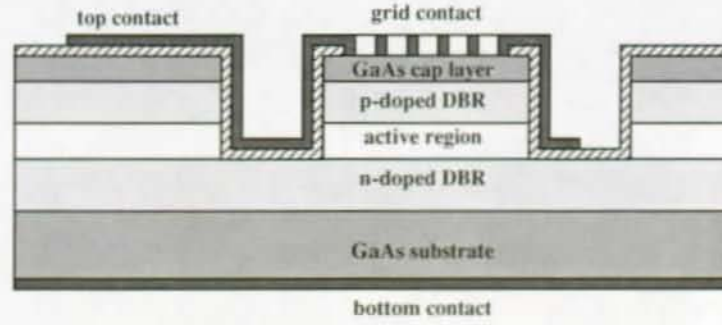


Figure 5.11: Processing step number 3: top contact deposition and lift-off.

deposited at a rate of 1 nm/s by e-beam technique. The processed wafer was finally placed at least one hour in hot (100 °C) remover (Microposit 1165) to perform the lift off, with the help of ultrasonic if necessary (not longer than 60 seconds, in order to not damage the p-contacts). The final processed device is represented on figure 5.11.

The current is injected in the mesa through the contacts evaporated at the edges of the mesa, and through a grid which covers the surface of the mesa. This grid is required for large mesa diameters because of current crowding near the contacts as explained in chapter 7. Different contact grid geometries and sizes were tested across the mask.

## 5.4 Description of the mask

The mask allows the fabrication of the following nominal device sizes:  $D_{metal} = 20, 40, 60, 80, 100, 150, 200, 250, 500, 1000, 1500$  and  $2000 \mu m$ . The larger sizes (greater or equal than  $500 \mu m$ ) are distributed near the top of the quarter wafer shape (see figure 5.12).

The smaller devices are distributed lower down on the mask in cells which have translational symmetry in the horizontal direction. Figure 5.13 shows one third of such a cell which consists of three times the pattern represented (hence twelve devices are available in one cell).

Alignments marks are placed on each device cell (as can be seen on figure 5.13), as well as in some specially designed alignment cells in which some test structures like Transmission Line Model (TLM) structures [15] are available. Several kinds of grid contacts were used in order to investigate the effect of current crowding on the external quantum efficiency of MCLEDs. Figure 5.14 shows examples of four contact geometries (the darker line surrounding the mesa corresponds to the mesa grooves). The spacing between the metal stripes are given on the figure. The stripe width varied between 3 and  $5 \mu m$  depending on the geometry. Some devices were designed without any grid covering the mesa's surface: the current is then injected through the edges of the mesa only, as can be seen on figure 5.15.

Figure 5.16 displays a cross section of a mesa, with some geometry definitions. We used as a general design rule that  $D_{Si_3N_4} = D_{metal} + 6 \mu m$  and  $D_{mesa} = D_{metal} + 12 \mu m$ . Note that in practice the sidewalls of the mesa are not vertical as shown (the directivity of the dry ECR etch depends on the

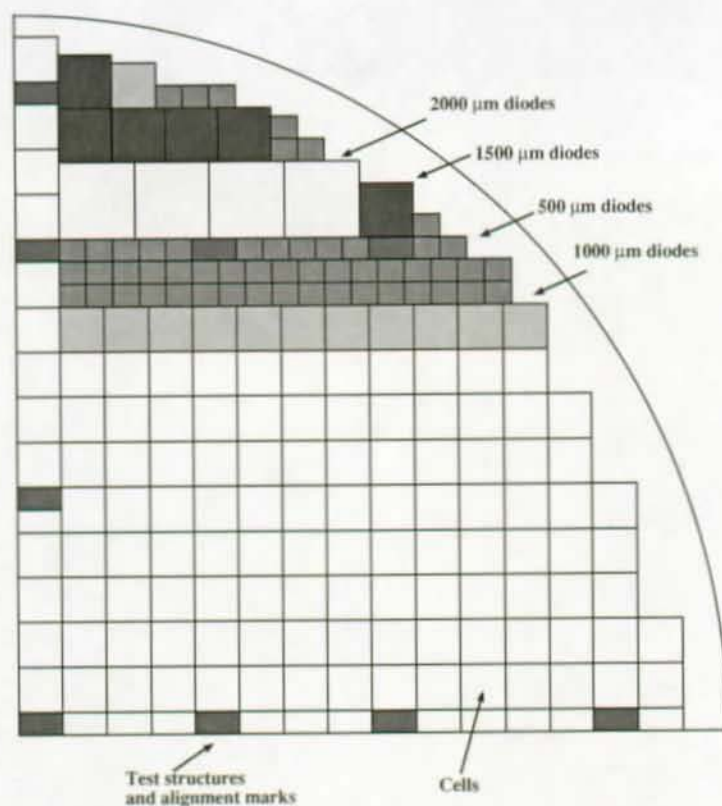


Figure 5.12: General description of the photolithographic mask.

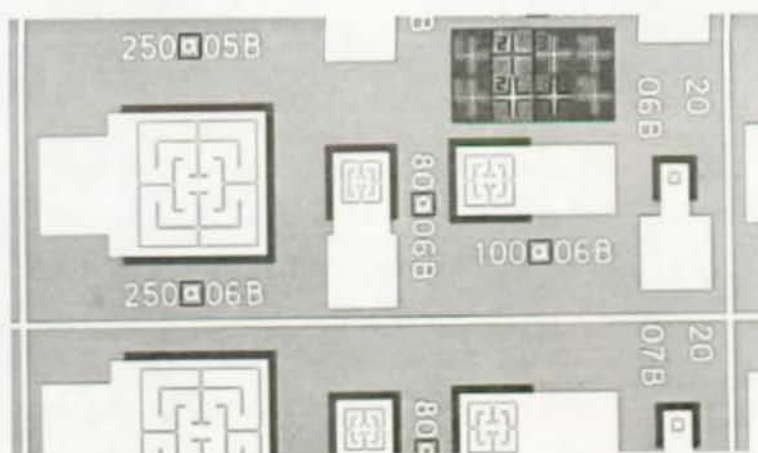


Figure 5.13: Optical microscope picture of processed devices.



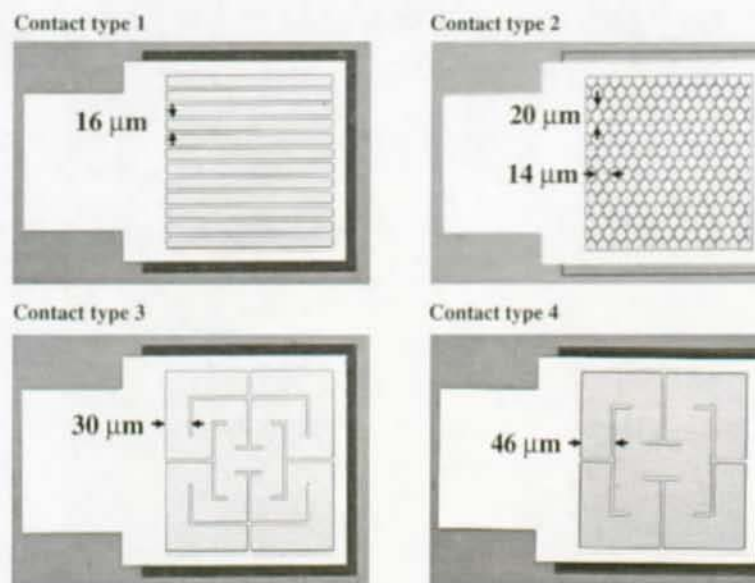


Figure 5.14: Optical microscope pictures of processed devices having different top contact geometries.

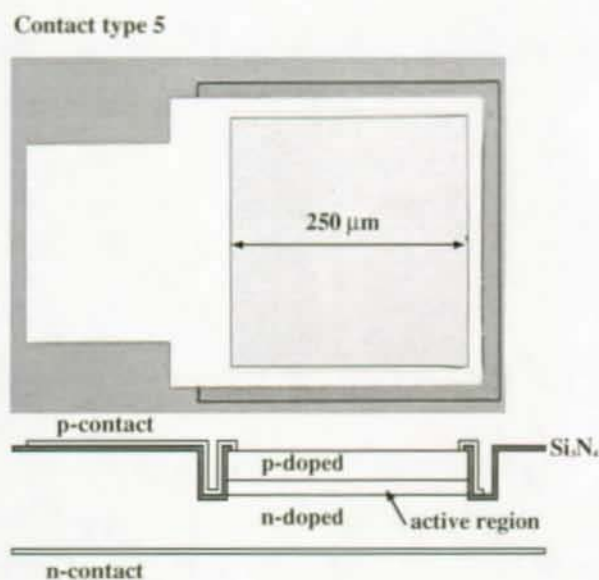


Figure 5.15: Optical microscope picture of a processed device. The current is injected through the edges of the mesa.

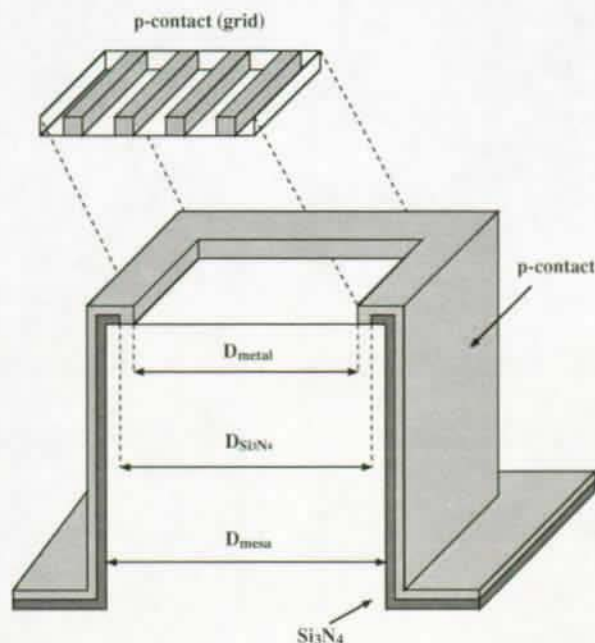


Figure 5.16: Definitions of the top contact parameters. An etched mesa is represented with the  $Si_3N_4$  passivation layer and the top p-contact.

Table 5.1: Characteristics of the contacts.

Contact type:	1	2	3	4	5
$\eta_s = S_{open}/S_{mesa}$	0.710	0.720	0.817	0.851	0.910

tuning parameters of the plasma [48]).

The ratio between the unmasked surface of the mesa to its overall surface is defined as  $\eta_s = S_{open}/S_{mesa}$ . Table 5.1 gives the values calculated for large size diodes (mesa width of  $262\ \mu m$ ) corresponding to the devices displayed on figures 5.14 and 5.15.

## 5.5 Characterization of the MCLED structure

After having processed a quarter wafer, we characterized 14 devices equally spaced by 1.5 mm along one radius of the wafer, at a current density of  $20\ A/cm^2$  injected with probes in continuous mode. Each diode belonged to one of the 14 cells arranged horizontally on the bottom of the mask (see figure 5.17). The mesa width of the devices was  $112\ \mu m$  and one example of the grid contact used can be seen on figure 5.13: the diodes we measured are identical to the diode labelled "100@06B". The grid covered 41.8% of the mesa surface and was designed in order to allow an efficient current spreading. We measured the top emission spectra of each of the 14 devices at normal incidence. The maximum emission wavelength (corresponding to the Fabry-Pérot mode) is plotted in figure 5.17 with respect to



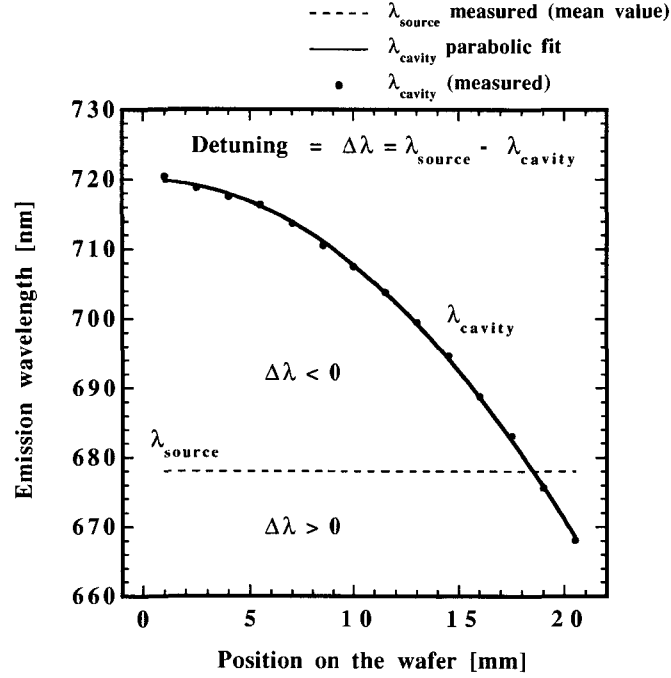


Figure 5.17: Emission wavelength versus wafer position of the measured devices. Dashed line: mean value of source emission wavelength  $\lambda_{\text{source}}$  (measured). Solid circles: cavity mode position  $\lambda_{\text{cavity}}$  measured at normal incidence under electroluminescence excitation. Solid line: parabolic fit of  $\lambda_{\text{cavity}}$ .

its position on the wafer.

As expected the wavelength of emission follows a parabolic law. In order to determine the quantum well emission without the influence of the microcavity, we measured the edge emission spectra. It was found to be centered at 678 nm for a current density of 20 A/cm<sup>2</sup> (continuous mode). From figure 5.17 we see that the source-cavity detuning ranges from negative to slightly positive values for the 14 different devices. Zero detuning occurs when the maximum of the spontaneous emission is in resonance with the cavity mode at normal incidence. The resulting emission pattern is bell-shaped and highly directional in the normal direction. When the detuning is negative, the resonance between spontaneous emission and cavity is found at a larger angle and produces a heart-shape emission pattern when plotted in polar coordinates [37], [22]. Figure 5.18 displays the experimental angular emission profiles measured with the same experimental set up as described in reference [118].

The angle corresponding to maximum of emission increases as the detuning decreases. As explained in chapter 4, the spontaneous emission pattern can be redistributed in the microcavity such that the Fabry-Pérot mode is forced to fit in the escape cone. This is done by changing the source-cavity detuning and we showed that the optimal extraction efficiency occurs when  $\Delta\lambda = \lambda_{\text{source}} - \lambda_{\text{cavity}} < 0$ . The powers emitted by our diodes were measured by a square silicon photodetector (1 cm<sup>2</sup>) placed 6 mm above the devices (which corresponds to a collection half-angle of 40° or to a numerical aperture of 0.64). The normalized external quantum efficiencies are plotted on the left axis of figure 5.19 with respect to the emission wavelengths given by figure 5.17.

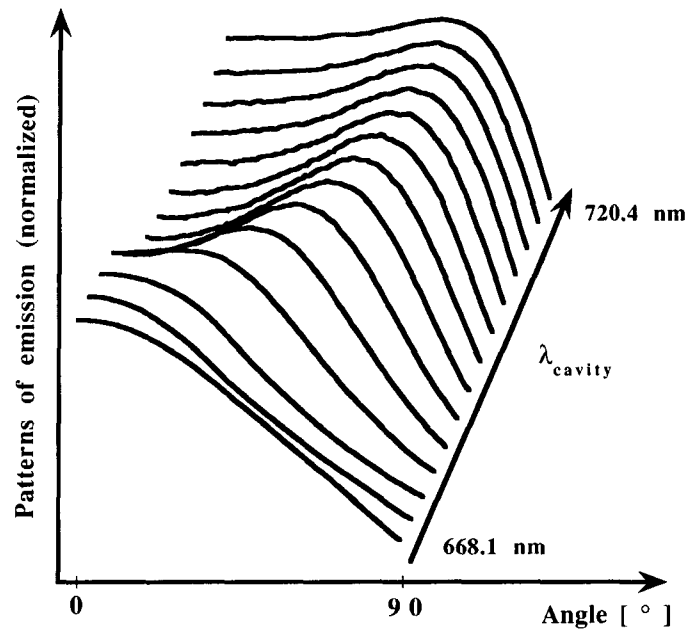


Figure 5.18: Normalized angular emission profiles plotted for different positions of the measured devices with different values of  $\lambda_{cavity}$ .

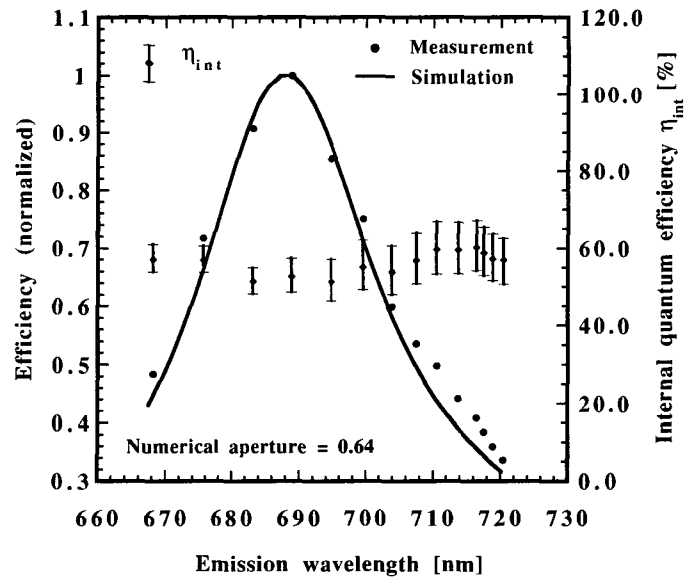


Figure 5.19: Internal quantum efficiency, with error bars, calculated from the comparison of experimental (solid circles) and simulated (solid line) extraction efficiencies.

A maximum external quantum efficiency of 1.2 % was reached for a detuning of -11 nm. Note that this gives the highest efficiency for a collection angle of 40°. The optimal detuning for an acceptance angle of 90° is slightly greater ( $\approx -15\text{nm}$ ) as explained in chapter 4.

We simulated the structures corresponding to the 14 measured devices with the method we presented in chapter 3. We calculated the thicknesses of the DBRs layers from the results of figure 5.17, and kept the source wavelength constant over the whole wafer. Edge emission measurements give an emission wavelength of 678 nm and a full width at half maximum of 20 nm. The extraction efficiencies were calculated by the program assuming a numerical aperture of 0.64. The results of these simulations were normalized and are displayed on figure 5.19 (solid line). We see that the simulation agrees very well with the experiment and that the parameters used to model the source were reasonable. From these results, after having multiplied the extraction efficiency by  $100 / 58.2$  to take into account the shadowing of the mesa surface by the grid top contact,  $\eta_{int}$  was calculated to be  $56\% \pm 5\%$  independent of the position on the wafer within experimental uncertainty. This confirms that the dependence on the external quantum efficiency with respect to the position on the wafer is due to change in detuning and not to device inhomogeneities.

It is then possible to take advantage of the microcavity light emitting diodes characteristics to estimate the internal quantum efficiency of devices based on spontaneous emission. The accuracy of the method we used to measure  $\eta_{int}$  depends mainly on the simulation accuracy. For a conventional LED, a precise description of the source is essential. In our simulations, the source was modeled by an isotropic distribution of dipoles oriented in a plane parallel to the interfaces of the structure. This was justified by the fact that for small current densities, the contribution of heavy holes is dominant in the recombination processes. In addition, vertical dipoles (perpendicular to the planes of interface) contribute only weakly to the extraction efficiency since these dipoles do not couple well to the escape modes of the cavity. For structures without a cavity this is no longer true and it is necessary to describe the source by a more complex distribution of dipoles whose characteristics depend also on temperature and injection. In addition, interface imperfections between the outside medium and the semiconductor can lead to severe uncertainties for the calculations of LEDs contrary to MCLEDs for which this interface is screened by several pairs of DBRs. The influence of this interface on the extraction efficiency can in fact be used to enhance luminous performances of LEDs [156].

Several conclusions can be obtained from the experiment presented in this section. First we observed that the simulations agreed very well with the measurements demonstrating the critical role of the detuning parameter on the external quantum efficiency and on the shape of the emission patterns. The second important information is that the internal quantum efficiency limits significantly the external quantum efficiency of red MCLEDs due to its small value compared to similar infrared devices. The purpose of the next chapter is to extensively study the optical properties of the MCLED emission so as to accurately determine the extraction efficiency of MCLEDs. The chapter 7 will then be devoted to a detailed study of the internal quantum efficiency in red MCLEDs.



## Chapter 6

# Emission properties of red MCLEDs

In this chapter the optical emission properties of MCLEDs are presented and compared to those of conventional p-i-n LEDs. We show in section 6.1 that spectral angle-resolved measurements of MCLED emission provides important information: by comparing them to numerical simulations, it is possible to experimentally determine the whole intrinsic spontaneous emission spectrum of the MCLED. This deconvolution procedure is also performed on a conventional LED in order to confirm the results obtained on the MCLED. Knowledge of the intrinsic emission spectrum allows a precise numerical calculation of the wavelength integrated pattern of the emission. For display or telecommunication applications, the emission pattern is an important property of the device. We present in section 6.2 some measurements of this parameter for both kind of devices and for various current densities. Since LEDs have the same active region as MCLEDs, their top-emission spectra correspond with a good approximation to the intrinsic spontaneous emission spectrum of the MCLED. In section 6.3 some experimental results showing how these spectra modify with respect to the current injection will be presented. This information will be useful to understand the emission properties modifications of MCLEDs with respect to the current injection. They will allow us to study the current density dependence of the extraction efficiency and of the internal quantum efficiency as it will be done in the chapter 7.

The structures investigated in this chapter were grown by MOVPE on (100) substrates misoriented 10 degrees towards (111), and are presented on figure 6.1 and 6.2. The real parts of the refractive indices (given at a wavelength of 650 nm) are given on the left axis of the figures, and their imaginary part (also called extinction coefficient) on the right axis. These figures describe the structures which were simulated by our program. The refraction indices dispersion was taken into account using references [3] for AlGaAs compounds and [110] for AlGaInP.

Figure 6.3 is a Transmission Electron Microscopy picture of the LED taken by a Philips EM430 Twin Microscope. The two  $(Al_{0.7}Ga_{0.3})_{0.5}In_{0.5}P$  cladding layers are clearly visible on this figure, as well as the cavity structure with the quantum wells. This picture was taken so as to measure accurately the thicknesses of the  $(Al_{0.7}Ga_{0.3})_{0.5}In_{0.5}P$  and  $Al_{0.5}Ga_{0.5}As$  layers (and thus to perform precise simulations on the optical emission properties of this structure).

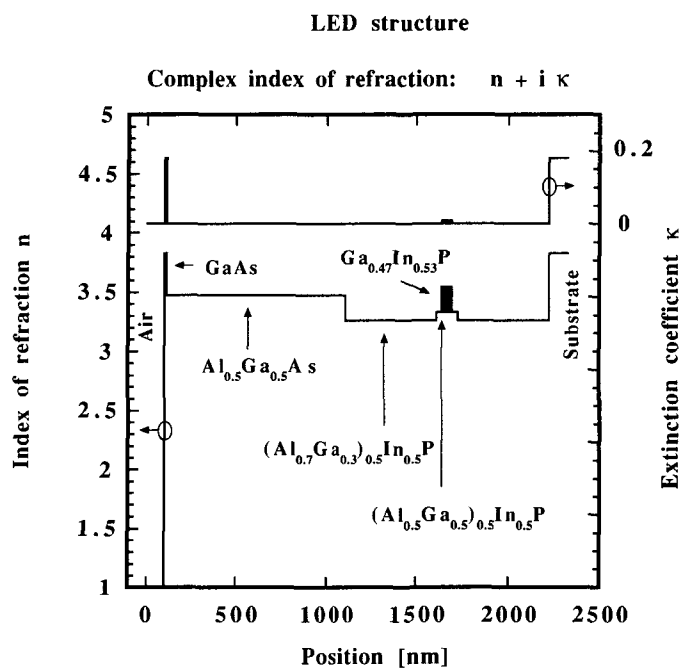


Figure 6.1: Refraction indices of the LED structure plotted versus the position along the growth axis.

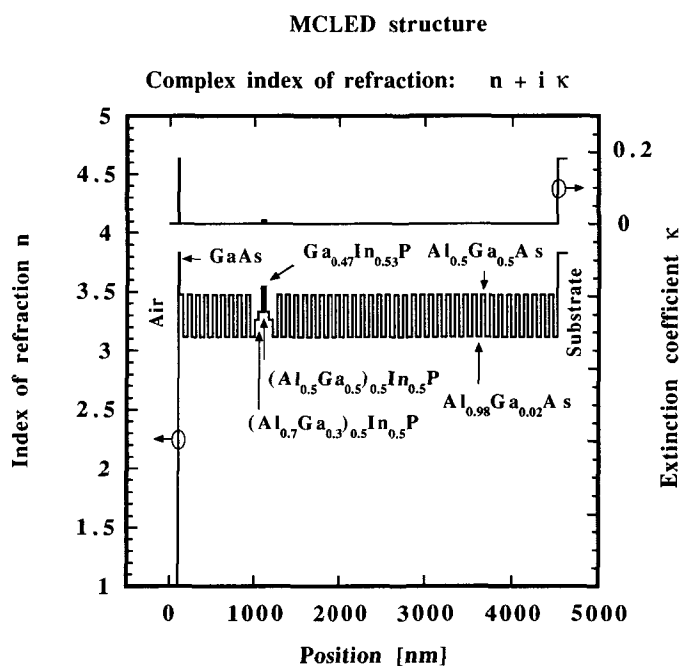


Figure 6.2: Refraction indices of the MCLED structure plotted versus the position along the growth axis.

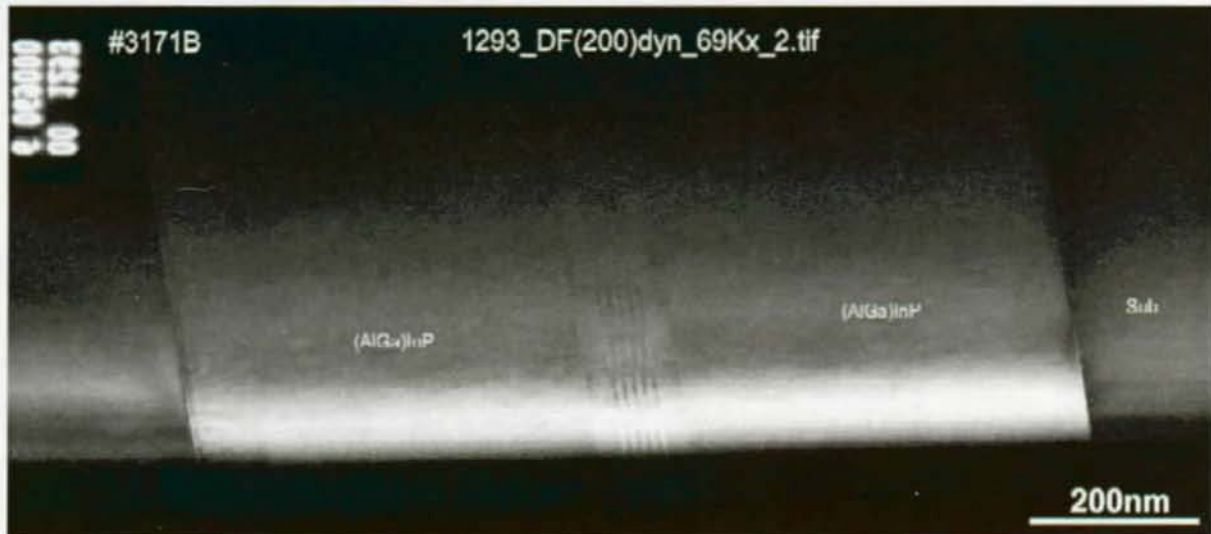


Figure 6.3: Transmission Electron Microscopy picture of the LED structure.

## 6.1 Angle resolved spectral measurements

We saw in chapter 3 that the power per unit of solid angle  $\bar{\Pi}_a$  emitted by a quantum well into a given outside medium (air in the case of this chapter), could be expressed as the product of the source intrinsic emission spectrum  $r_{spont}$  by the power per unit of solid angle  $\Pi_a$  emitted by a white source:

$$\boxed{\bar{\Pi}_a(\theta, \lambda) = r_{spont}(\lambda) \Pi_a(\theta, \lambda)} \quad (6.1)$$

The angle  $\theta$  is the angle (defined in air) with respect to the growth axis. Since  $\Pi_a$  can be easily calculated by numerical simulations, it appears that by measuring  $\bar{\Pi}_a$ , the intrinsic spectrum  $r_{spont}$  can be determined. One simple way to perform this measurement is to record the diode emission spectra for various angles using the set-up described on figure 6.4. A stepping motor was used to rotate an arm with a multimode optical fiber, which was connected to a high-resolution spectrometer with a CCD detector. The measured device was carefully aligned at the intersection between the motor axis and the arm trajectory and driven by probes connected to a pulsed voltage generator. The alignment is not trivial. Lensless fiber is used to reduce alignment errors. However the penalty is a weak signal in the fiber requiring long acquisition time. The motor and the spectrometer were connected to a computer and the whole set-up controlled by a Labview program.

The diodes were processed according to the procedure described on chapter 5. We chose to investigate the properties of large diodes with mesa widths of  $262 \mu\text{m}$  and with web-like top contact geometry (see for example the diode labelled "250a06B" in figure 5.13). We measured 64 spectra equally spaced between  $-80^\circ$  and  $+80^\circ$ . The measurement was carried out under pulsed operation at a frequency of  $1.2454 \text{ [kHz]}$  with a pulse width of  $80 \text{ [\mu s]}$  (duty cycle of 10%) and an amplitude of  $3.5 \text{ [V]}$  corresponding to a current density of  $40 \text{ [A/cm}^2\text{]}$ . The recorded spectra were stored on a matrix

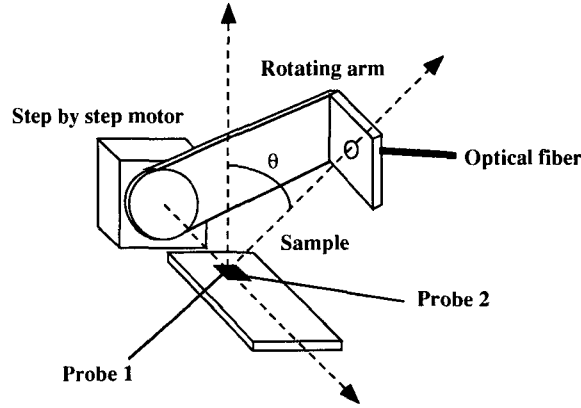


Figure 6.4: Description of the set-up used to measure the angle-resolved emission spectra.

and plotted as contour lines in the bottom part of figures 6.5 (for LEDs) and 6.6 (for MCLEDs).

In the top part of these two figures are displayed the contour plots of the power per unit of solid angle  $\Pi_a(\theta, \lambda)$  simulated for a white source. We neglected the contributing vertical dipoles in our source model. This assumption is well justified for MCLEDs because the absolute value of  $\Pi_a^v(\theta, \lambda)$  is at least one order of magnitude smaller than  $\Pi_a^{s,p}(\theta, \lambda)$ . As we saw it in chapter 4, the vertical dipole emission is not well extracted for a MCLED because of the very small corresponding antinode factor. For LEDs this assumption is reasonable provided light-hole recombination is small compared to heavy-hole recombinations, which is the case at small current densities (recombination energy of light-holes is higher than those of heavy holes for the compressively strained quantum wells which were grown here).

On figures 6.5 and 6.6 the light grey color corresponds to high spectral intensity whereas it is the contrary for the dark grey color. Examining the LED measurements we observe that  $\bar{\Pi}_a(\theta, \lambda)$  does not vary much with respect to the angle and that the amplitude is maximum for wavelengths centered around 650 nm. Looking at  $\Pi_a(\theta, \lambda)$  we see a much more complex behavior on which is superposed a wavelength modulation. Although the reflection from the  $Al_{0.5}Ga_{0.5}As/(Al_{0.7}Ga_{0.3})_{0.5}In_{0.5}P$  and  $GaAs/(Al_{0.7}Ga_{0.3})_{0.5}In_{0.5}P$  interfaces are weak, they are similar in magnitude, leading to Fabry-Pérot effects, resulting in a weak modulation, whose periodicity is sensitive to the lengths of the  $(Al_{0.7}Ga_{0.3})_{0.5}In_{0.5}P$  and  $Al_{0.5}Ga_{0.5}As$  layers. Since  $\bar{\Pi}_a(\theta, \lambda)$  varies continuously with respect to the angle and the wavelength, we conclude that  $\bar{\Pi}_a(\theta, \lambda)$  is mainly determined by the intrinsic source emission spectrum  $r_{spont}(\lambda)$ .

Considering the MCLED, we observe that the maxima of  $\Pi_a(\theta, \lambda)$  (calculated) follows a cosine-like shape in the  $(\theta, \lambda)$  plane and that the absolute maximum of  $\Pi_a(\theta, \lambda)$  is found at  $(\theta = 0^\circ, \lambda = 658.5 \text{ nm})$ . These coordinates correspond to the Fabry-Pérot mode, which shifts towards smaller wavelengths as



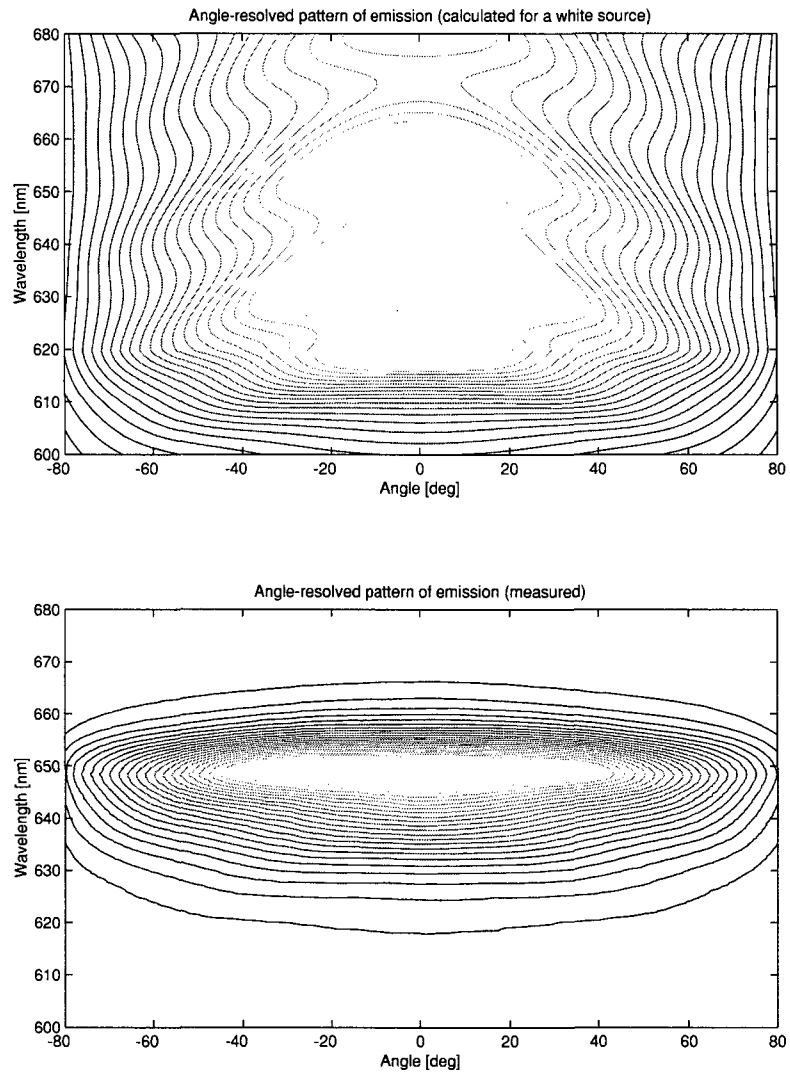


Figure 6.5: Simulation of  $\Pi_a(\theta, \lambda)$  (top plot) and measurement of  $\bar{\Pi}_a(\theta, \lambda)$  (bottom plot) for the conventional LED.

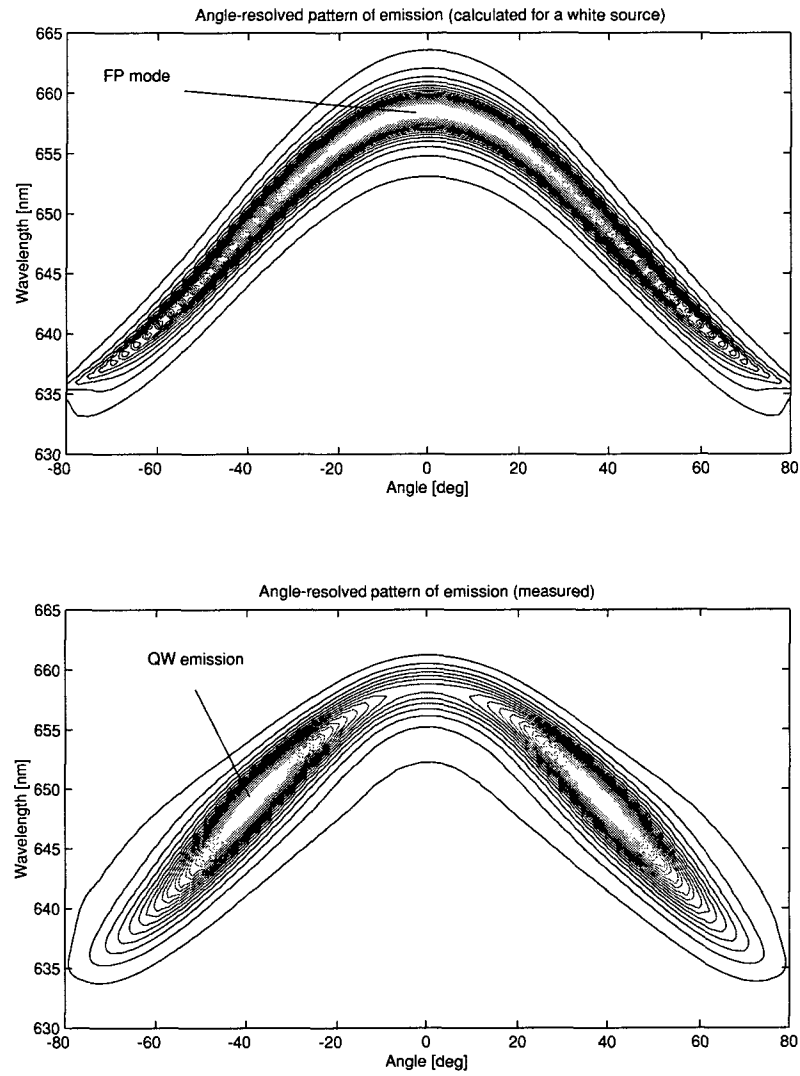


Figure 6.6: Simulation of  $\Pi_a(\theta, \lambda)$  (top plot) and measurement of  $\bar{\Pi}_a(\theta, \lambda)$  (bottom plot) for the MCLED.

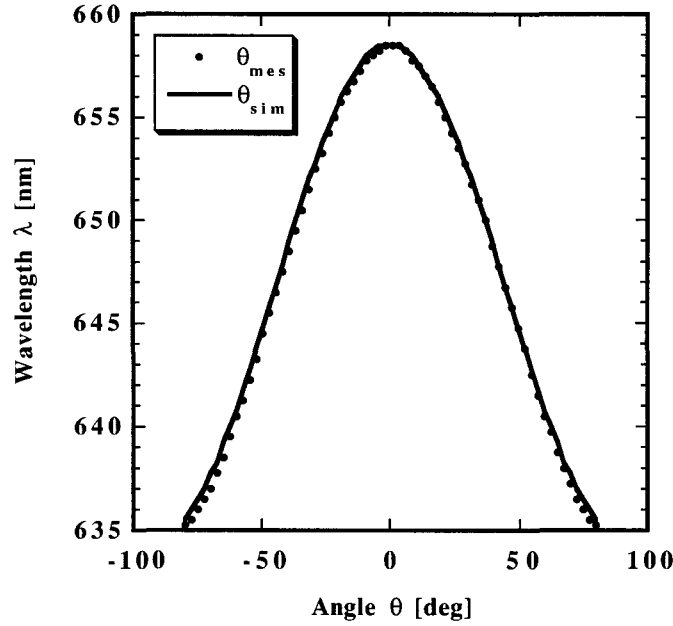


Figure 6.7: Angles corresponding to the local maxima of  $\Pi_a(\theta, \lambda)$  and  $\bar{\Pi}_a(\theta, \lambda)$  plotted versus the wavelength.

the angle increases. This cosine-like behavior was calculated in chapter 4 and describes the angle-wavelength dispersion relation of the Fabry-Pérot (equation (4.41)). Looking at the local maxima of the measurement  $\bar{\Pi}_a(\theta, \lambda)$ , we observe the same kind of dispersion relation with the very important difference that two absolute maxima are found at the coordinates  $(\theta = \pm 39^\circ, \lambda = 648.5 \text{ nm})$ . To better understand this, we plotted on figure 6.7 the angles corresponding to the local maxima of  $\Pi_a(\theta, \lambda)$  and  $\bar{\Pi}_a(\theta, \lambda)$  versus the wavelength (left axis). The absolute values of these maxima are given on figure 6.8.

We call  $\theta_{mes}$  and  $\theta_{sim}$  the angles (represented on figure 6.7) solutions of  $\frac{\partial \Pi_a(\theta, \lambda)}{\partial \theta} = \frac{\partial \bar{\Pi}_a(\theta, \lambda)}{\partial \theta} = 0$ . The two partial derivatives must be equal because of equation (6.1), hence we must have  $\theta_{mes} = \theta_{sim}$  which is what we observe.

This result is very important because it experimentally justifies the relation (6.1). By using this equation, we can deduce the intrinsic emission spectrum:

$$r_{spont}(\lambda) = \frac{\bar{\Pi}_a(\theta_{mes}, \lambda)}{\Pi_a(\theta_{sim}, \lambda)} \quad (6.2)$$

where  $\Pi_a(\theta_{sim}, \lambda)$  and  $\bar{\Pi}_a(\theta_{mes}, \lambda)$  are given on figure 6.8.

This procedure is formally equivalent to a deconvolution. The result is displayed on the solid line of figure 6.9 and corresponds to what we call the method 1. Since  $\theta_{mes}$  is limited between  $-90^\circ$  and  $+90^\circ$ ,  $r_{spont}(\lambda)$  can be calculated with this method over a limited wavelength range related to the escape window of the structure (see chapter 4).

Since  $\Pi_a(\theta_{mes}, \lambda)$  varies slowly with respect to  $\lambda$ , we can directly estimate the MCLED detuning

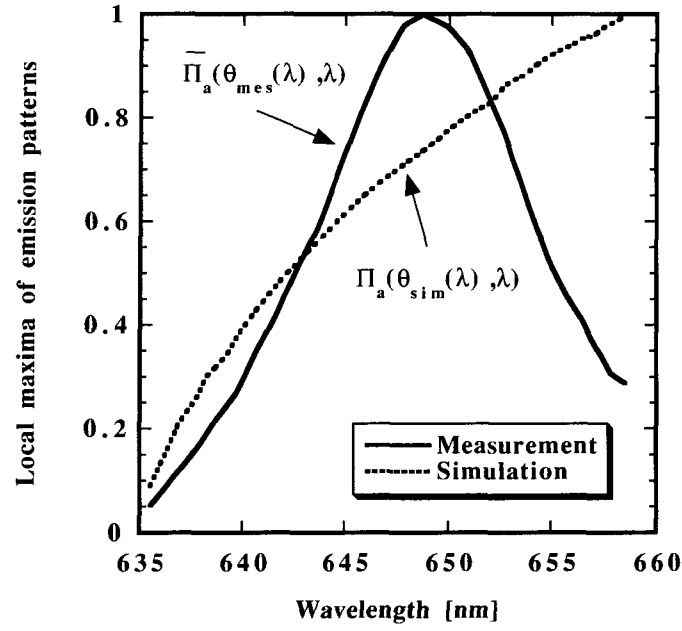


Figure 6.8:  $\Pi_a(\theta_{sim}, \lambda)$  (dotted line) and  $\bar{\Pi}_a(\theta_{mes}, \lambda)$  (solid line) plotted with respect to the wavelength.

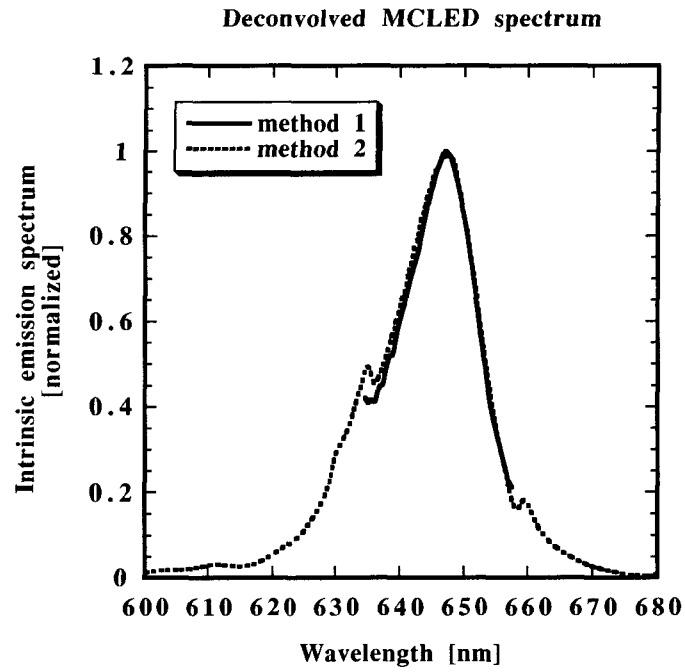


Figure 6.9: Intrinsic MCLED emission spectrum deconvolved from angle-resolved spectral measurements. Two methods are compared.

by considering the bottom part of figure 6.6. The detuning is approximatively given by the difference between the wavelength corresponding to the absolute maxima of  $\bar{\Pi}_a(\theta, \lambda)$  and the Fabry-Pérot wavelength. We have then  $\Delta\delta = 648.5 - 658.5 = -10 [nm]$ . This methods gives useful information provided the detuning is negative (the peak wavelength of the intrinsic emission spectrum must then be maximum in the wavelength range related to the escape window).

Considering equation (6.1) we see that for a fixed wavelength  $\lambda_0$ , the curves  $\Pi_a(\theta, \lambda_0)$  and  $\bar{\Pi}_a(\theta, \lambda_0)$  must have the same angular dependence. Some examples are given on figure 6.10 for the LED and on figure 6.11 for the MCLED. One can see the very good agreement between measurement and simulations, confirming the accuracy of our numerical simulations.

In order to determine the intrinsic source emission spectrum, we calculated the ratio:

$$r_{spont}(\lambda) = \frac{\int_{-80^\circ}^{+80^\circ} \bar{\Pi}_a(\theta, \lambda) d\theta}{\int_{-80^\circ}^{+80^\circ} \Pi_a(\theta, \lambda) d\theta}. \quad (6.3)$$

As it can be seen on figure 6.11, the MCLED spectrum  $\bar{\Pi}_a(\theta, \lambda)$  displays very sharp peaks in angles which are not well resolved by the measurements: more than one hour of measurements was required to take 64 angular points for the range  $[-80^\circ, +80^\circ]$ . We would then need several hours of measurement so as to precisely resolve the spectra. By using equation (6.3) we can get rid of this problem: the integral averages the errors related to the bad angular sampling. The result of this procedure is given in dotted line on the figure 6.9 presented above. One can observe that the two spectra  $r_{spont}(\lambda)$  calculated with equations (6.2) and (6.3) are in very good agreement. The two small peaks observed on the dotted line curve of figure 6.9 correspond to the bounds of the wavelength escape window (the limits of the solid line curve of the same figure). These two peaks appear because of numerical uncertainties and have no physical meaning. For wavelengths outside of this range, the MCLED spectrum  $\bar{\Pi}_a(\theta, \lambda)$  has a poor signal to noise ratio which leads to some noticeable errors in the deconvolution procedure.

The same deconvolution technique was performed on the LED structure. The result is displayed on figure 6.12 which shows the intrinsic source emission spectrum of the MCLED (solid line) compared to one of the LED (dotted line). The LED spectrum was blue-shifted by two nanometers so as to compare the shapes of both spectra.

The agreement between these two curves is very good for wavelengths between the two local maxima of the solid line curve. The result is less satisfactory for others wavelengths because of the angle resolution as previously explained. We must point out that the two devices were measured in the same conditions and at the same current density. Their active regions being theoretically the same, one should expect their intrinsic spectrum to be the same. This is what we experimentally demonstrate. This deconvolution is to our knowledge the only way to determine accurately the intrinsic spectrum of MCLEDs, which is of primary importance for precise calculation of the extraction efficiency of these devices. We will use this information to determine the MCLEDs internal quantum efficiency in chapter 7. An other important conclusion is that the intrinsic spectrum of the LED is not very different from the spectrum measured at normal incidence. We can then conclude that the shape

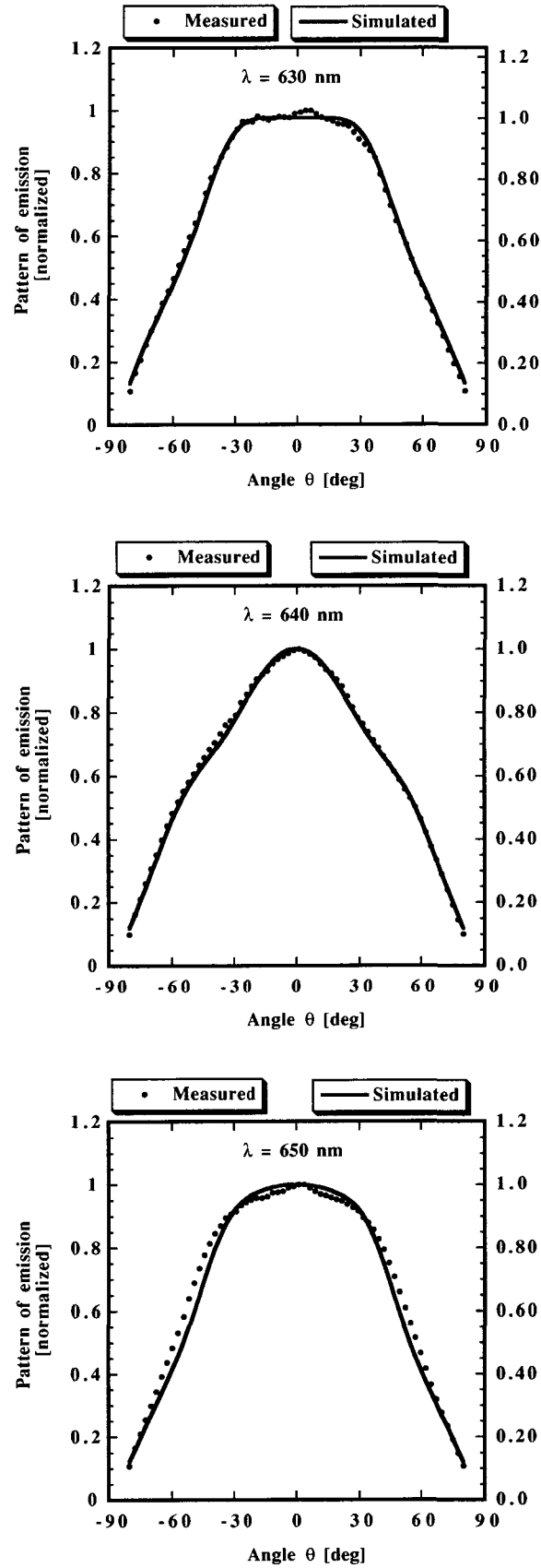


Figure 6.10: LED: comparison between  $\Pi_a(\theta, \lambda_0)$  (simulated, solid line) and  $\bar{\Pi}_a(\theta, \lambda_0)$  (measured, solid circles) for  $\lambda_0 = 630, 640, 650 \text{ [nm]}$ .

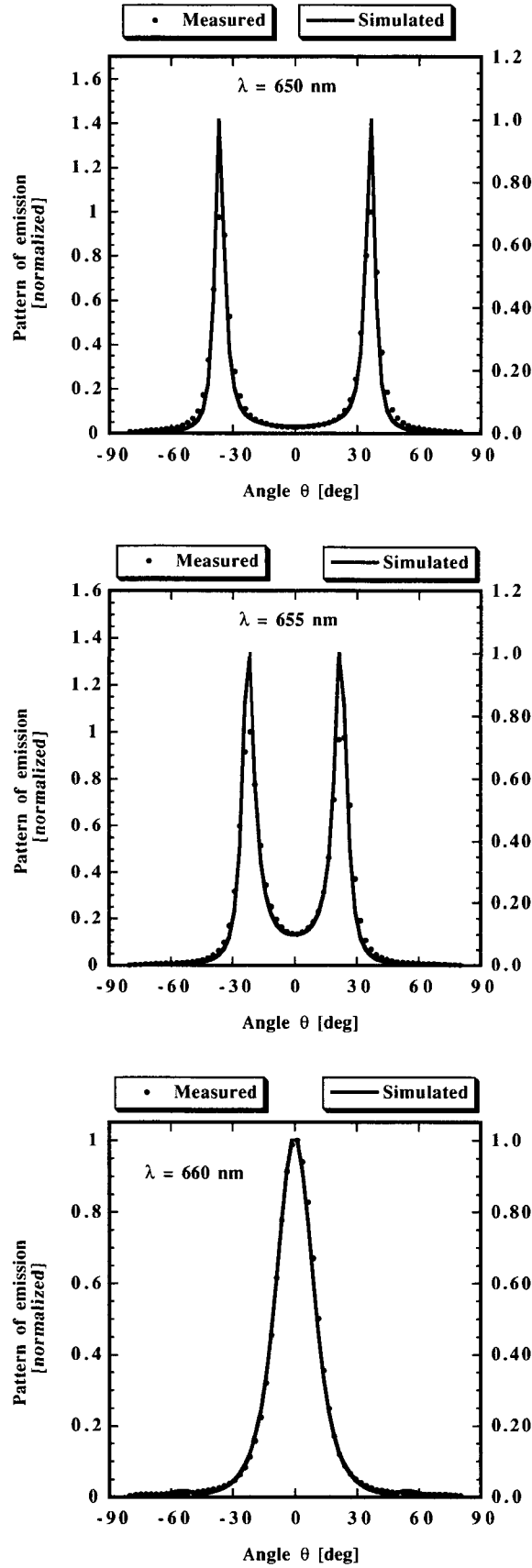


Figure 6.11: MCLED: comparison between  $\Pi_a(\theta, \lambda_0)$  (simulated, solid line) and  $\bar{\Pi}_a(\theta, \lambda_0)$  (measured, solid circles) for  $\lambda_0 = 650, 655, 660$  [nm].

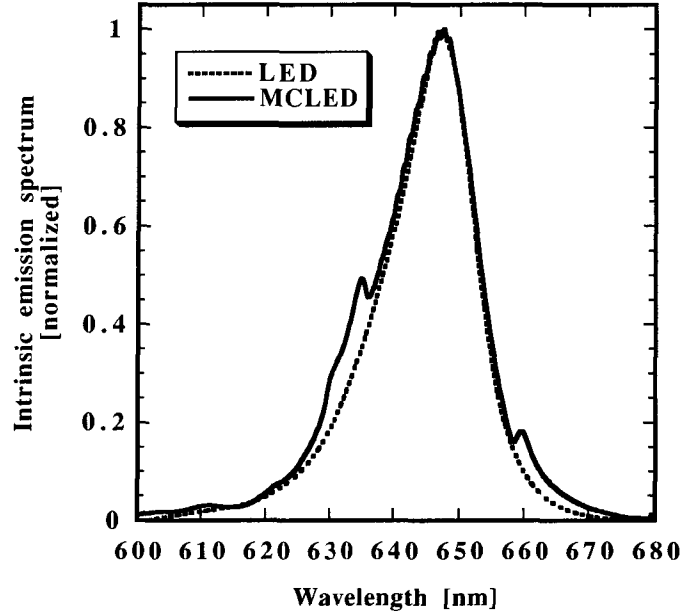


Figure 6.12: Intrinsic emission spectra deconvolved from angle-resolved spectral measurements for the LED (dotted line) and for the MCLED (solid line).

of the MCLED intrinsic spectrum is reasonably well described by the shape of the LED spectrum measured at normal incidence. Note that this does not diminishes the usefulness of the deconvolution method which accurately gives the wavelength position of the intrinsic spectrum maximum.

## 6.2 Angular emission profiles of LEDs and MCLEDs: comparison

In this section we compare the angular emission profiles  $\bar{\Pi}_a(\theta)$  of MCLEDs to those of LEDs. The emission pattern, is of great interest for the characterization of (MC)LEDs performances, since it indicates how much (wavelength integrated) power is emitted by the device with respect to the angle, and determines the coupling efficiency of (MC)LEDs to optical fibers for telecommunication applications. It can also be used to estimate the brightness of (MC)LEDs when display applications are concerned.

The emission pattern can be numerically calculated according to:

$$\bar{\Pi}_a(\theta) = \frac{\int_{-\infty}^{+\infty} r_{spont}(\lambda) \Pi_a(\theta, \lambda) d\lambda}{\int_{-\infty}^{+\infty} r_{spont}(\lambda) d\lambda} \quad (6.4)$$

(provided the intrinsic spectrum  $r_{spont}(\lambda)$  is known), and measured by using a modified version of the set-up presented on figure 6.4. For this measurement the optical fiber mounted on the rotating arm is replaced by a photodetector connected to a lock-in amplifier according to the schematic given on figure 6.13. An aperture followed by a focusing lens is placed in front of the photodetector to reduce the solid angle of the detection system.



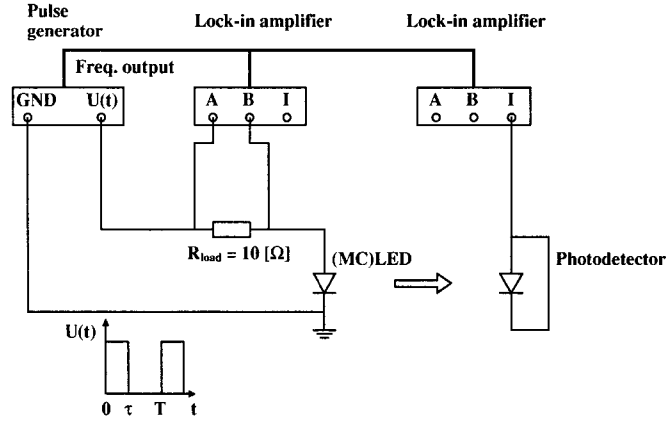


Figure 6.13: Schematic of the emission pattern measurement set-up.

A lock-in is used to detect the light emitted by the device which is driven by a pulsed voltage source. A second lock-in measures the injected current from the voltage drop at a calibrated resistance of  $10 \text{ } [\Omega]$ .

Figures 6.14 and 6.15 display respectively the emission patterns of the LED and of the MCLED. The solid lines represent  $\bar{\Pi}_a(\theta)$  calculated by using (6.4) with the deconvolved intrinsic spectra determined in previous section. The dotted lines correspond to the emission patterns measured with the set-up described on figure 6.13.

The measurements were performed on large size diodes and at low current density. Both experiments and simulations agree confirming the consistency of our previous results.

Figures 6.16 and 6.17 show the emission patterns of small diameter LED and MCLED. The mesa width is of  $32 \text{ } [\mu\text{m}]$  and the top-contact consists of a metal ring leaving an open window of  $20 \text{ } [\mu\text{m}]$  on top of the mesa. The different current densities are displayed on the right side of these figures.

The shape of the LED emission pattern does not change with respect to the injection while that of the MCLED changes dramatically. Indeed the full calculation of  $\Pi_a(\theta, \lambda)$  (shown on top of figure 6.5) does not display rapid variations versus the wavelength. This is not surprising considering that the LED structure can be mainly regarded as a dipole source placed in front of a semiconductor-air interface. One should not expect an important wavelength dependence in this case because there are no strong resonance effects. Hence even if the intrinsic spectrum properties vary strongly with respect to the current density, the emission pattern  $\bar{\Pi}_a(\theta)$  will not change a lot.

These observations are no longer valid for the MCLED. We saw in section 6.1 that the detuning was negative implying a heart shape emission pattern. Two parameters can characterize this kind of pattern: the angle at which the emission is maximal (that we call  $\theta_{max}$ ), and the ratio of the intensity emission at normal incidence to the one at the angle  $\theta_{max}$  that we define as:  $\alpha_0 = \bar{\Pi}_a(\theta = 0) / \bar{\Pi}_a(\theta_{max})$ . This last parameter is equal to one when the pattern is bell-shape and varies between 0 and 1 when it

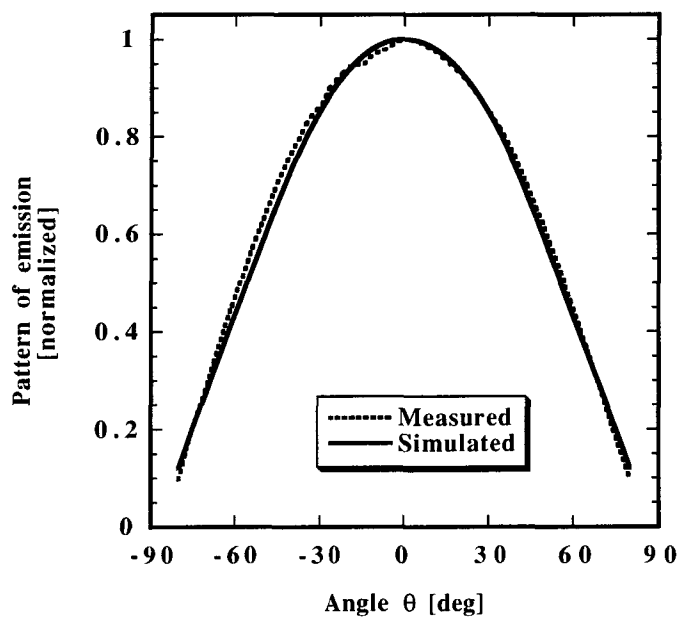


Figure 6.14: Wavelength integrated emission pattern of the LED. Solid line: simulated. Dotted line: measured.

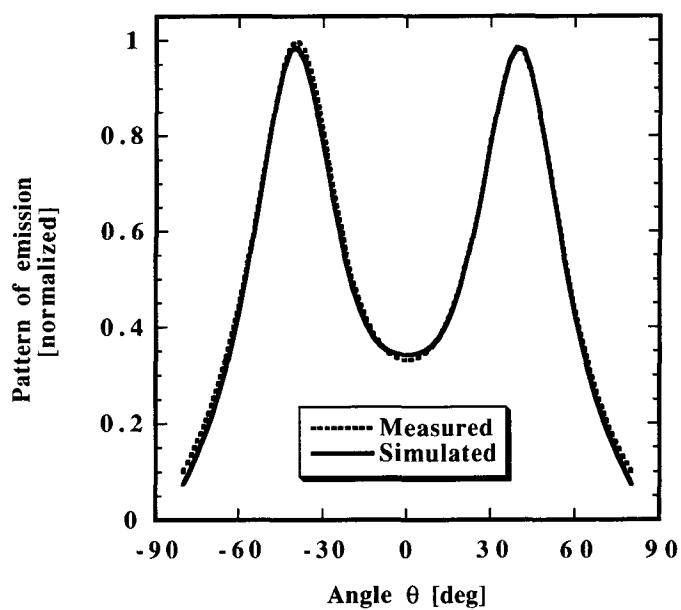


Figure 6.15: Wavelength integrated emission pattern of the MCLED. Solid line: simulated. Dotted line: measured.

zero. This is due to the superposition of different Airy modes due to the finite linewidth of the intrinsic emission. Hence measuring a single lobe emission on a MCLED does not necessarily imply that the detuning is positive, as it would be the case for a monochromatic intrinsic spontaneous emission. One example of this can be seen on figure 6.17. For very high current density the heart shape pattern broadens and becomes a single lobe. For fixed detuning values  $\theta_{max}$  decreases slowly as the detuning increases and  $\alpha_0$  increases slowly towards one. By comparing the different figures, we conclude that  $\theta_{max}$  and  $\alpha_0$  are more sensitive to the detuning than to the source linewidth. This is not surprising since a modification of the cavity-source detuning implies a direct modification of the Airy modes positions, whereas a modification of the source linewidth induces broadening effects on these modes.

We conclude then that the emission pattern of MCLED is sensitive to changes in the intrinsic emission spectrum in comparison to conventional LEDs. The consequences of this for MCLED extraction efficiency will be discussed on chapter 7.

### 6.3 Current density dependence of the intrinsic spontaneous emission spectrum

Let us examine how the spontaneous emission spectrum of conventional LEDs changes on a function of current density. These measurements were carried out under pulsed voltage operation with varying duty cycle on devices with different mesa widths. The emission was detected at normal incidence by using a multimode optical fiber connected to an optical spectrum analyzer (OSA). Figure 6.23 shows the spectra of a 72  $\mu m$  diameter large LED recorded for various current densities. The pulse width of the applied voltage was of 500  $\mu s$  for a period of 1  $ms$  (duty cycle of 50%). The spectra are displayed on logarithm scale and normalized in order to compare their shapes. Figure 6.24 displays the spectra measured for the same device but for a duty cycle of 10%.

We observe in both cases a red-shift of the peak electroluminescence spectra with respect to the current density. Three basic effects are found to significantly alter the peak wavelength of  $r_{spont}(\lambda)$  in semiconductors [122]. Bandfilling effect blue shifts the spontaneous emission: since electrons and holes are fermions, they obey to Pauli exclusion principle. Each  $\vec{k}$  state in a semiconductor band can be occupied twice only (due to spin degeneracy). Because of the principle of energy minimization, the carriers in quasi-equilibrium occupy the available states from the bottom of the band so that the energetically lowest states are occupied first. This results in filling the states near the bottom of the conduction band by electrons and the top of the valence band by holes implying a blue shift of the emission. The second effect is a consequence of Coulomb correlations for the particles and results in a bandgap shrinkage (also called bandgap renormalization), hence to a red shift of the emission as the carrier density increases. The third effect is due to temperature: when electron-hole pairs recombine non-radiatively, they give their energy to the crystal through phonon emission, which corresponds to lattice heating. For most materials this leads to a bandgap reduction and, hence to a red shift of the emission [120]. For electrically injected devices, heating of the lattice is also produced by Joule

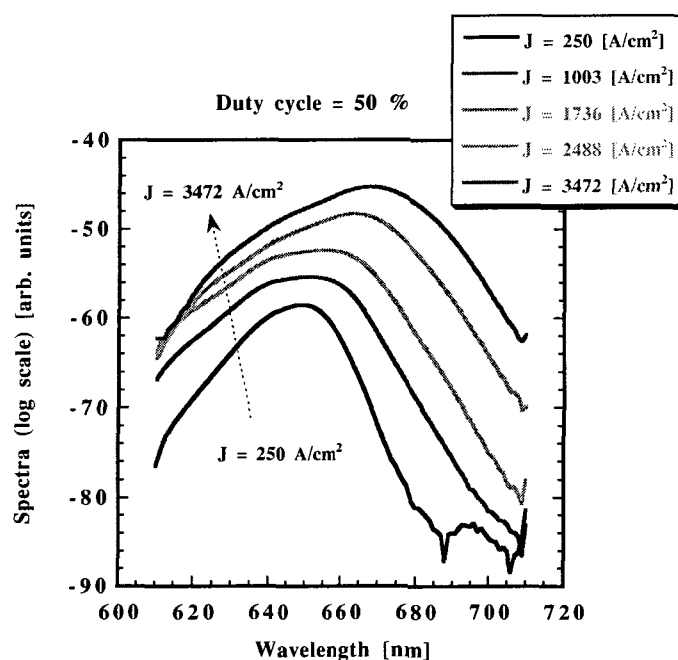


Figure 6.23: Electroluminescence spectra of a conventional LED (mesa width = 72  $\mu\text{m}$ ) measured at different current densities. Duty cycle of the pulsed voltage is 50 %.

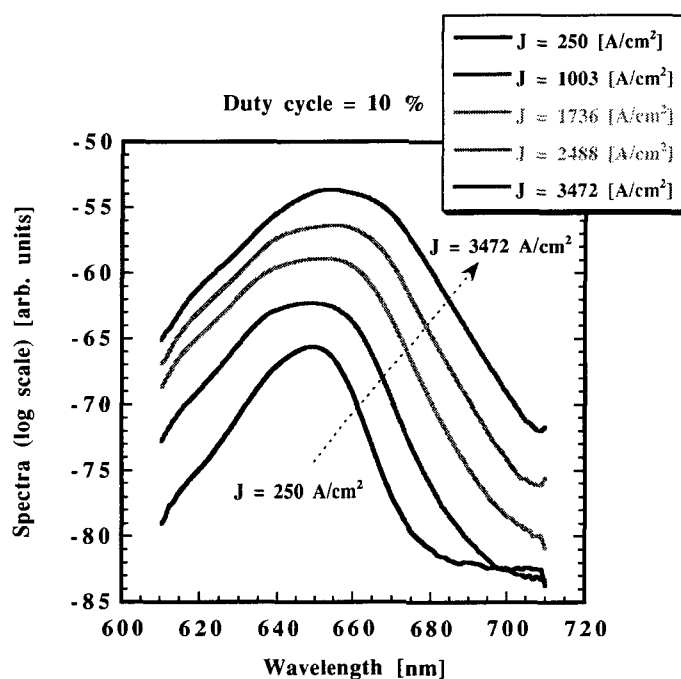


Figure 6.24: Electroluminescence spectra of a conventional LED (mesa width = 72  $\mu\text{m}$ ) measured at different current densities. Duty cycle of the pulsed voltage is 10 %.

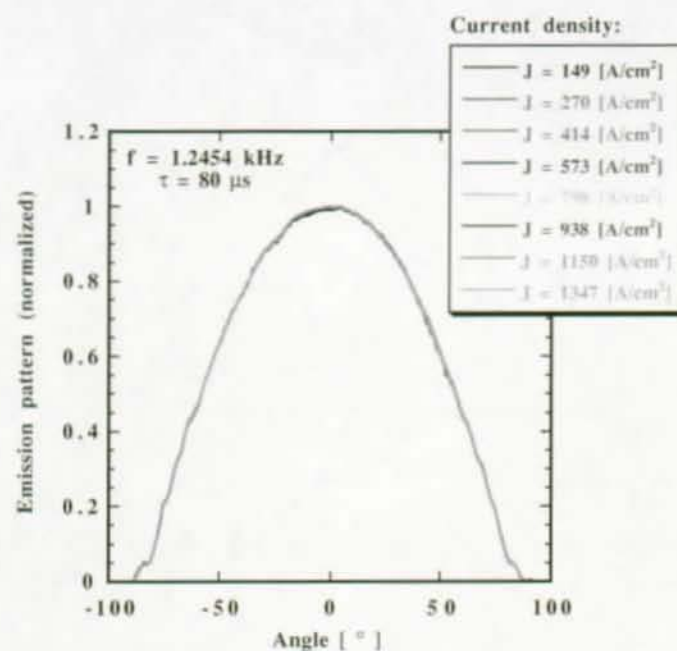


Figure 6.16: Wavelength integrated emission pattern of a small LED (width width of  $32\text{ }\mu\text{m}$ ) measured at different current densities.

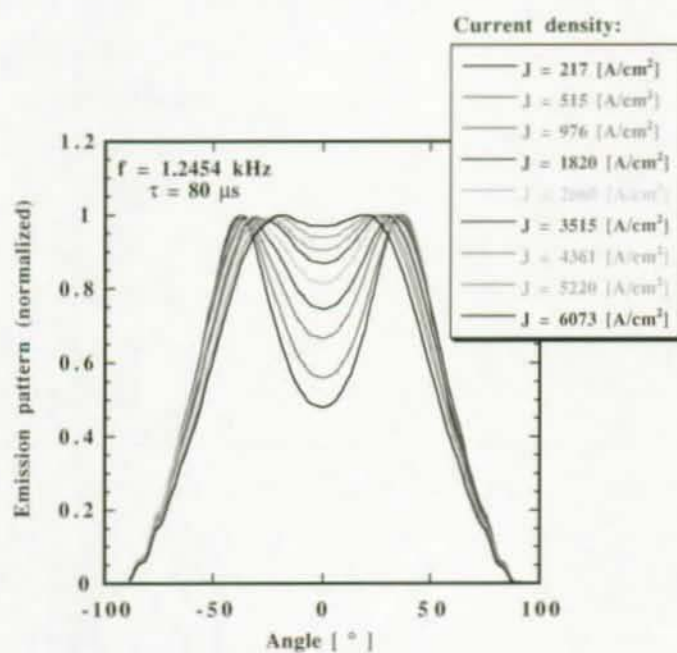


Figure 6.17: Wavelength integrated emission pattern of a small MCLED (mesa width of  $32\text{ }\mu\text{m}$ ) measured at different current densities.

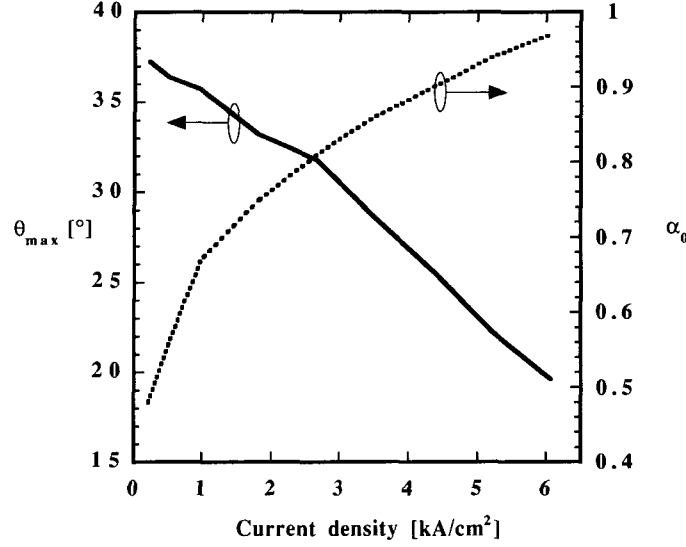


Figure 6.18: Characteristic parameters  $\theta_{max}$  (left axis) and  $\alpha_0$  (right axis) of the wavelength integrated emission patterns measured on a small MCLED (mesa width =  $32\text{ }\mu\text{m}$ ) measured at different current densities.

is heart-shape. Figure 6.18 shows that the parameters  $\theta_{max}$  and  $\alpha_0$  vary significantly with respect to the current density.

The angle  $\theta_{max}$  decreases almost linearly with respect to the current density whereas  $\alpha_0$  increases as a power law with respect to the same parameter. It is clear that these effects are due to a modification of the intrinsic emission spectrum as the current density increases. Similar observations were reported for the case of infrared MCLEDs [37]. In order to quantitatively study the influence of the detuning and of the source linewidth on the emission pattern characteristics, we performed numerical simulations on the structure given on 6.2. The angular emission profile  $\bar{\Pi}_a(\theta)$  was calculated assuming an intrinsic spectrum shape given by equation (6.7) (see section 6.3). We plotted  $\theta_{max}$  and  $\alpha_0$  versus the detuning  $\Delta\delta$  for different fixed values of  $\sigma$  on figures 6.19 and 6.20. The same parameters were calculated for fixed detuning values and plotted versus the source linewidth  $\sigma$  on figures 6.21 and 6.22. Note that if  $\theta_{max}$  and  $\alpha_0$  are known, then  $\Delta\delta$  and  $\sigma$  can be determined. This method will be used in chapter 7. These graphs are useful for choosing the  $\Delta\delta$  and  $\sigma$  parameter of a MCLED, depending on the kind of application for which this device is to be used. For fiber coupling applications for instance, it is clear that  $\theta_{max}$  will have to be smaller than the acceptance angle of the optical fiber. For that kind of application, and for a spectral width of 40 nm, the detuning will have to be slightly negative, such that the extraction efficiency is good and the angle  $\theta_{max}$  small.

As the detuning increases from negative values to positive ones,  $\theta_{max}$  decreases, whereas  $\alpha_0$  increases to saturate at  $\alpha_0 = 1$ . For a monochromatic source ( $\sigma = 0$ ),  $\theta_{max}$  is zero and  $\alpha_0$  is one when  $\Delta\delta$  is greater or equal to zero. This behavior was predicted in the simple model we presented in chapter 4: as the detuning changes, the Airy mode shifts in the escape window. For a polychromatic source ( $\sigma > 0$ ),  $\theta_{max}$  is zero and  $\alpha_0$  is one when  $\Delta\delta$  is greater or equal to a detuning value slightly lower than

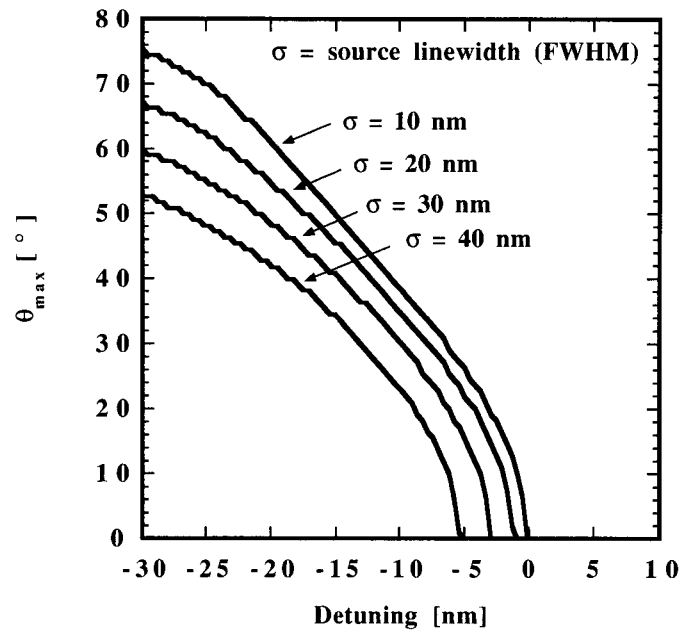


Figure 6.19: Parameter  $\theta_{max}$  plotted versus the detuning  $\Delta\delta$  for different intrinsic source linewidths  $\sigma$  (FWHM).

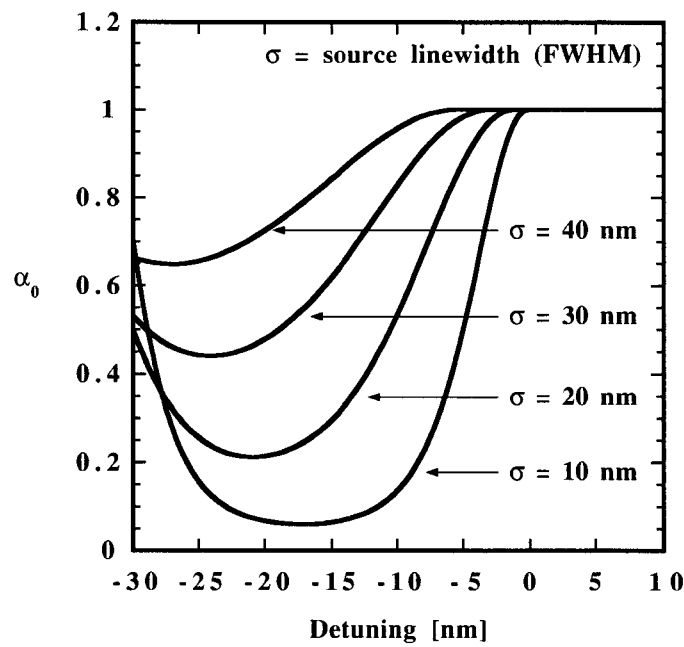


Figure 6.20: Parameter  $\alpha_0$  plotted versus the detuning  $\Delta\delta$  for different intrinsic source linewidths  $\sigma$  (FWHM).

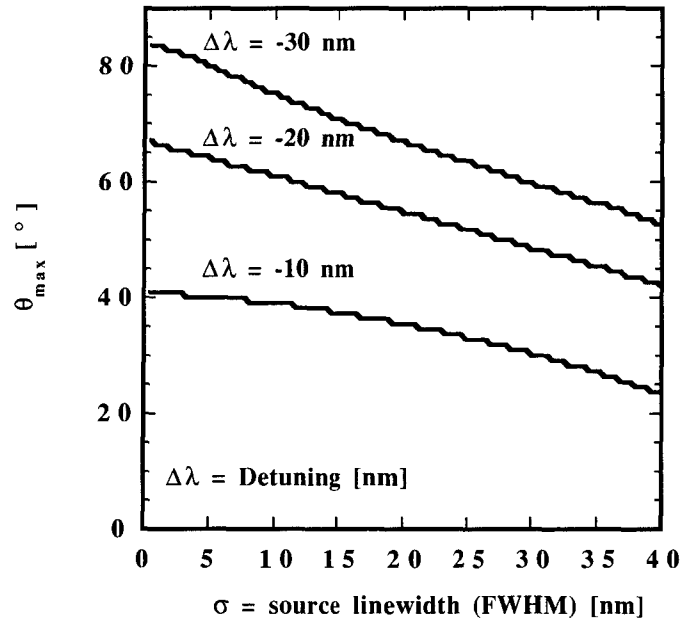


Figure 6.21: Parameter  $\theta_{max}$  plotted versus the intrinsic source linewidth  $\sigma$  (FWHM) for different detuning  $\Delta\delta$  values.

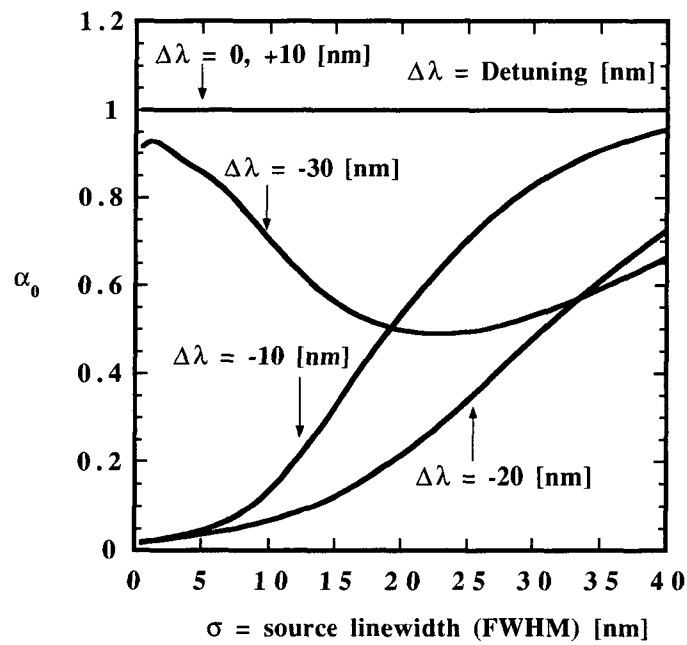


Figure 6.22: Parameter  $\alpha_0$  plotted versus the intrinsic source linewidth  $\sigma$  (FWHM) for different detuning  $\Delta\delta$  values.



zero. This is due to the superposition of different Airy modes due to the finite linewidth of the intrinsic emission. Hence measuring a single lobe emission on a MCLED does not necessarily imply that the detuning is positive, as it would be the case for a monochromatic intrinsic spontaneous emission. One example of this can be seen on figure 6.17. For very high current density the heart shape pattern broadens and becomes a single lobe. For fixed detuning values  $\theta_{max}$  decreases slowly as the detuning increases and  $\alpha_0$  increases slowly towards one. By comparing the different figures, we conclude that  $\theta_{max}$  and  $\alpha_0$  are more sensitive to the detuning than to the source linewidth. This is not surprising since a modification of the cavity-source detuning implies a direct modification of the Airy modes positions, whereas a modification of the source linewidth induces broadening effects on these modes.

We conclude then that the emission pattern of MCLED is sensitive to changes in the intrinsic emission spectrum in comparison to conventional LEDs. The consequences of this for MCLED extraction efficiency will be discussed on chapter 7.

### 6.3 Current density dependence of the intrinsic spontaneous emission spectrum

Let us examine how the spontaneous emission spectrum of conventional LEDs changes on a function of current density. These measurements were carried out under pulsed voltage operation with varying duty cycle on devices with different mesa widths. The emission was detected at normal incidence by using a multimode optical fiber connected to an optical spectrum analyzer (OSA). Figure 6.23 shows the spectra of a 72  $\mu\text{m}$  diameter large LED recorded for various current densities. The pulse width of the applied voltage was of 500  $\mu\text{s}$  for a period of 1  $\text{ms}$  (duty cycle of 50%). The spectra are displayed on logarithm scale and normalized in order to compare their shapes. Figure 6.24 displays the spectra measured for the same device but for a duty cycle of 10%.

We observe in both cases a red-shift of the peak electroluminescence spectra with respect to the current density. Three basic effects are found to significantly alter the peak wavelength of  $r_{spont}(\lambda)$  in semiconductors [122]. Bandfilling effect blue shifts the spontaneous emission: since electrons and holes are fermions, they obey to Pauli exclusion principle. Each  $\vec{k}$  state in a semiconductor band can be occupied twice only (due to spin degeneracy). Because of the principle of energy minimization, the carriers in quasi-equilibrium occupy the available states from the bottom of the band so that the energetically lowest states are occupied first. This results in filling the states near the bottom of the conduction band by electrons and the top of the valence band by holes implying a blue shift of the emission. The second effect is a consequence of Coulomb correlations for the particles and results in a bandgap shrinkage (also called bandgap renormalization), hence to a red shift of the emission as the carrier density increases. The third effect is due to temperature: when electron-hole pairs recombine non-radiatively, they give their energy to the crystal through phonon emission, which corresponds to lattice heating. For most materials this leads to a bandgap reduction and, hence to a red shift of the emission [120]. For electrically injected devices, heating of the lattice is also produced by Joule

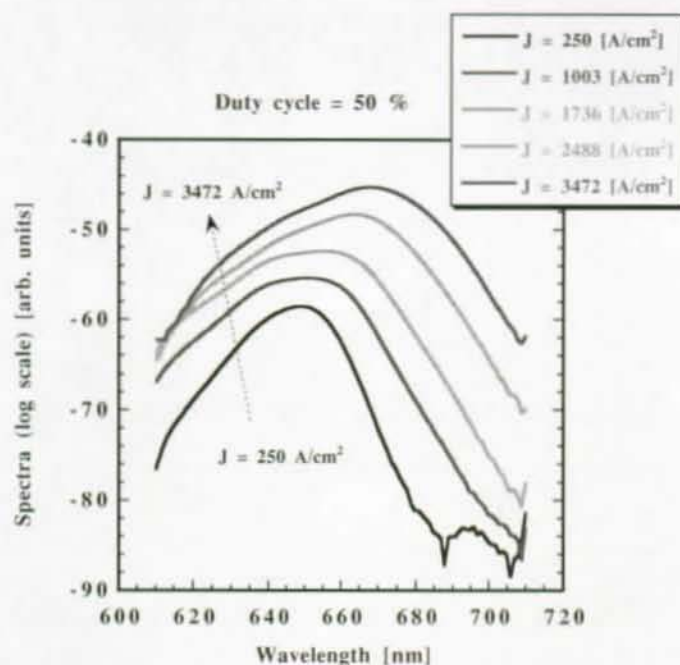


Figure 6.23: Electroluminescence spectra of a conventional LED (mesa width =  $72 \mu\text{m}$ ) measured at different current densities. Duty cycle of the pulsed voltage is 50 %.

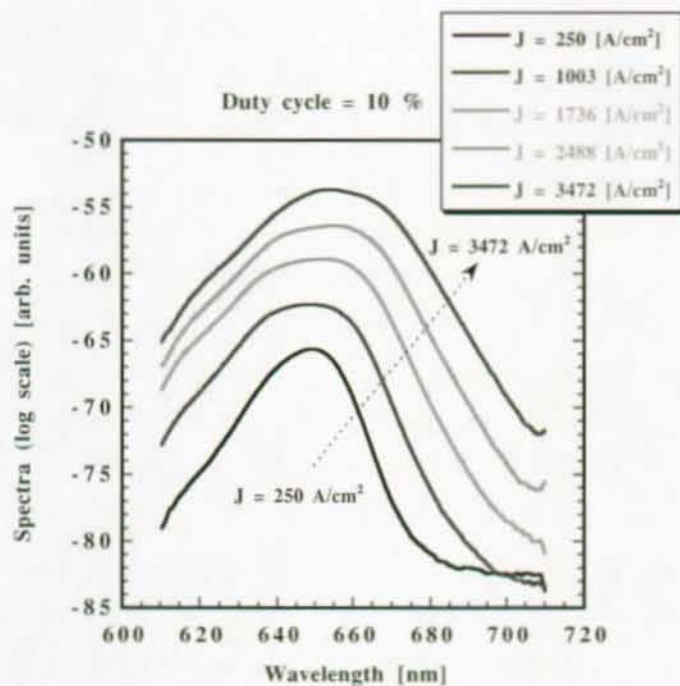


Figure 6.24: Electroluminescence spectra of a conventional LED (mesa width =  $72 \mu\text{m}$ ) measured at different current densities. Duty cycle of the pulsed voltage is 10 %.

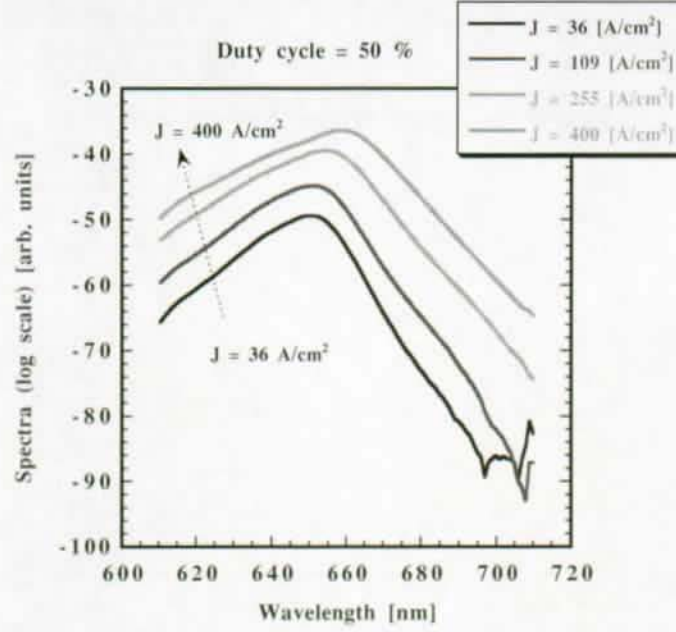


Figure 6.25: Electroluminescence spectra of a conventional LED (mesa width =  $262\text{ }\mu\text{m}$ ) measured at different current densities. Duty cycle of the pulsed voltage is 50 %.

heating: the devices present a significant series resistance which acts as a heating source when current is injected. We clearly see on figures 6.23 and 6.24 that decreasing the duty cycle of the pulsed applied voltage reduces the red shift of the emission, indicating that the dominant effect in these structures is the thermal heating due to the series resistance of the device. An other consequence of increasing the current density is the spectral broadening of the emission because of the energetic modification of the carrier distribution. We observe this effect on the low and on the high energy tails of the spectra. We also note that the spectra become flatter as the current density gets larger. Broadening at low energy comes from heating (phonon tail) and collision broadening, while broadening at high energy is due to heating, band filling and contribution of other bands (second level of quantum wells and light holes).

Figure 6.25 shows the electroluminescence spectra of a  $262\text{ }\mu\text{m}$  diameter LED for various current densities. Duty cycle of the pulsed voltage is of 50 %.

We observe that the emission linewidth of these large diodes is smaller than for the smaller devices, which is normal since the current density is one order of magnitude smaller. The red shift is however still present.

Figure 6.26 shows (right axis) the electroluminescence peak wavelength  $\lambda_{max}$  versus the current density of two LEDs having different sizes ( $72\text{ }\mu\text{m}$  and  $262\text{ }\mu\text{m}$ ). Duty cycle of the pulsed voltage was of 50 %. One can show that  $\lambda_{max}$  increases rapidly with the current density, and that this effect is more important for large size diodes: at same current density the large size diodes dissipate more heat than small ones. If we call  $R_d$  the total resistance of the device (including series resistance and contact resistance), we can express the total injected power in the device  $P_{tot}$  as:

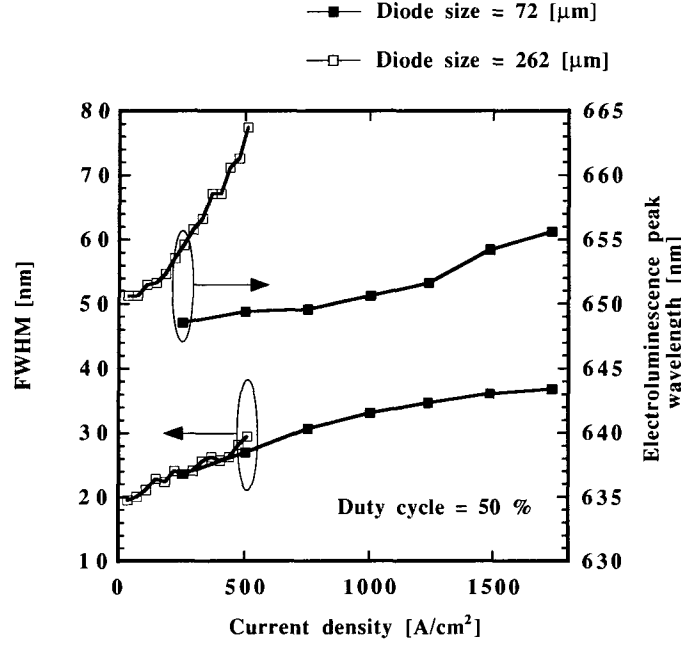


Figure 6.26: Electroluminescence peak wavelength (right axis) and spectra linewidths (left axis) plotted versus the current density of two LEDs having different sizes ( $72\text{ }\mu\text{m}$ ) and  $262\text{ }\mu\text{m}$ ). Duty cycle of the pulsed voltage is 50 %.

$$P_{tot} = U_d I + R_d I^2 \quad (6.5)$$

with  $I$  the injected current and  $U_d$  the ideal diode voltage which is related to the injected current density  $J = I/S$  by:

$$J = J_0 e^{\frac{e U_d}{n k T}} \quad (6.6)$$

where  $S$  is the diode surface. A fraction  $\eta_{wp}$  (called wall-plug efficiency) of the total power  $P_{tot}$  is optically radiated by the device whereas  $(1 - \eta_{wp}) P_{tot}$  is dissipated in the device. The resistance  $R_d$  is conversely proportional to the diode surface  $S$ . The power dissipated as heat in the structure will then scale with the surface of the device, for a constant current density. This agrees with what is observed in figure 6.26: the wavelength shift of the electroluminescence peak is larger for the large diode than for the small one, indicating more heating for the same current density. Note that for the same reasons, the small diodes dissipate more heat than the large one at constant current.

On the left axis of figure 6.26 the linewidth  $\sigma$  (full-width at half maximum) of the spectra is plotted. The linewidths of both diodes overlap and increase with the current density. The dependence of  $\sigma$  with respect to the current density  $J$  is found to vary according a law of the form  $\sigma(J) = \sigma_0 J^a$  with  $0 < a < 1$ .

Calculation of the intrinsic emission spectrum is beyond the scope of this work [164], [28]. Nevertheless it was found [144] that the emission spectra (at low current densities) could be approximated

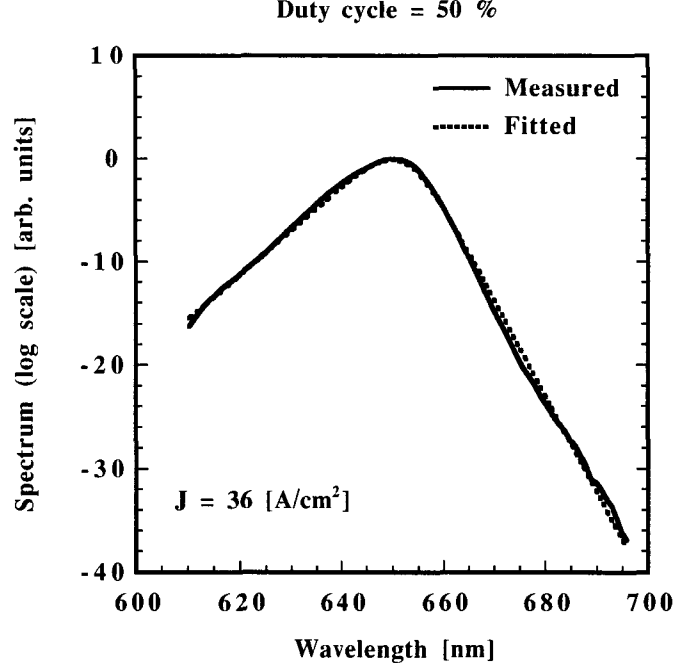


Figure 6.27: Electroluminescence spectrum measured at normal incidence (solid line) for a large LED (mesa width =  $262 \text{ } \mu\text{m}$ ) and at a current density of  $36 \text{ [A/cm}^2\text{]}$ . Duty cycle of the pulsed voltage is 50 %. Dotted line represents an empirical fit of the emission spectrum.

by the following empirical relation:

$$r_{spont}(\lambda) = \frac{2 e^c m (\lambda - \lambda_{qw})}{2 - c + c e^{2m(\lambda - \lambda_{qw})}} \quad (6.7)$$

where  $\lambda_{qw}$  is the peak emission wavelength of the spectrum, and  $m$ ,  $c$  some fitting constants. This function presents two exponential tails for wavelengths far from  $\lambda_{qw}$ , with different slopes. This function displays a maximum at  $\lambda = \lambda_{qw}$ . The parameter  $c$  describes the asymmetry of the function whereas  $m$  is related to its full-width at half-maximum (FWHM). When  $c = 1$ ,  $r_{spont}(\lambda)$  is symmetrical and its FWHM is of  $2 \ln(2 + \sqrt{3})/m$ . An example of such an empirical fit is given on figure 6.27 showing an excellent agreement with the measurement taken at a current density of  $36 \text{ [A/cm}^2\text{]}$  on a large diode.

We conclude from this section that the lineshape of the intrinsic spontaneous emission is very sensitive to the intensity of the injected current density. An empirical function was found to well describe the intrinsic spontaneous emission lineshape, and will be used in the next chapter.



## Chapter 7

# Study of the external quantum efficiency of red MCLEDs

In chapter 5 we showed that comparing the extraction efficiency (calculated) with the external quantum efficiency (experimentally determined) gave indication of the internal quantum efficiency. Clearly this approach is very simplified. In chapter 6 we saw the complex dependence of the MCLED emission on the linewidth and on the detuning. We also showed how these parameters in turn depend on the current density. In addition, surface-emitting devices are injected through a grid, so current density will vary laterally in the structure. In this chapter we put these ideas together: we first identify the different physical mechanisms which determine the internal quantum efficiency. Then, each contribution is studied and discussed.

### 7.1 Factors determining the external quantum efficiency

In this section we follow the general definitions given by Coldren in the reference [29]. The electrical (MC)LED structures are basically made of a p-i-n junction (see for example figure 5.8). The active region consists of  $N_{qw}$  quantum wells of thickness  $e_{qw}$ , placed in the nominally undoped region of the diode. Under high injection levels (relevant to the devices studied here) charge neutrality dictates that the electron density  $N$  (in units of  $[cm^{-3}]$ ) equals the hole density  $P = N$  in the active region. When current is injected in the structure, some carriers are generated at a rate  $G_{gen}$  whereas some others recombine radiatively or non-radiatively at a rate  $R_{rec}$ . The corresponding rate equation is given by:

$$\frac{dN}{dt} = G_{gen} - R_{rec}. \quad (7.1)$$

We define  $\eta_i$  as the injection efficiency, corresponding to the fraction of terminal current that generates carriers in the active region. The generation rate is given by

$$G_{gen} = \frac{\eta_i dI}{e V_{qw}} \quad (7.2)$$

where  $dI$  is an increment of the injected current,  $e$  the electron charge, and  $V_{qw}$  the volume of the active region. The total recombination rate  $R_{rec}$  is the sum of a spontaneous recombination rate  $R_{sp}$ , a non-radiative recombination rate  $R_{nr}$ , a carrier leakage rate  $R_l$ , and a stimulated recombination rate  $R_{st}$ :  $R_{rec} = R_{sp} + R_{nr} + R_l + R_{st}$ .

The band-to-band radiative recombination rate  $R_{sp}$  varies as [85]:

$$R_{sp} = B N P = B N^2 \quad (7.3)$$

where  $B$  is the bimolecular recombination coefficient in units of  $[cm^3/s]$ . The non-radiative recombinations rate can be expressed as:

$$R_{nr} = \left( A_0 + \frac{4 v_s}{D} \right) N + C N^3 \quad (7.4)$$

where  $v_s$  is a recombination rate velocity (in units of  $[cm s^{-1}]$ ) describing surface and interface non-radiative recombination mechanisms [55]. The parameter  $D$  represents the diameter of an active region having a square geometry (as it is the case for our devices). The term  $A_0$  (in units of  $[s^{-1}]$ ) is the inverse of a capture rate describing non-radiative recombinations related to bulk defects and impurities. The cubic dependence is due to Auger non-radiative transitions. For high bandgap alloys like AlGaInP, this effect is usually negligible because the split off valence bandgap ( $\Delta_0 \sim 0.1 eV$ ) is much smaller than the direct band-gap energy ( $E_\Gamma \sim 2 eV$ ) [21] resulting in small Auger coefficients [29]. The term  $R_l$  describes carrier leakage rate out of the active region. This effect can not be neglected when the potential barriers confining the carriers in the active region are not sufficiently high as it is the case for AlGaInP-based active regions. Electron confinement is a problem known from a long time in realization of red VCSELs [133], [134], [21], [68], [160], [53], [24], [108], [149]. Analytical expressions can be found in references [21] and [29] for calculation of the corresponding carrier leakage rate. The stimulated recombination rate  $R_{st}$  can be neglected in most of the devices which operate in the spontaneous regime, as it is the case for (MC)LEDs.

Under steady-state conditions ( $dN/dt = 0$ ) the generation rate equals the recombination rates:

$$G_{gen} = R_{sp} + R_{nr} + R_l. \quad (7.5)$$

The optical power  $dP_{source}$  spontaneously generated inside the structure by a monochromatic emitter of energy  $h\nu$  is obtained by multiplying the number of photons generated per unit time per unit volume  $R_{sp}$ , by the energy per photon  $h\nu$  and the volume of the active region  $V_{qw}$ .

After some simple manipulations, one finds:

$$dP_{source} = \eta_i \frac{h\nu}{e} \eta_r dI \quad (7.6)$$



where  $\eta_r$  is defined as the radiative efficiency and given by:

$$\eta_r = \frac{R_{sp}}{R_{sp} + R_{nr} + R_l}. \quad (7.7)$$

We calculated in chapter 4 the extraction efficiency of a polychromatic source characterized by a spontaneous spectral density  $r_{spont}(\delta)$ : the extraction efficiency  $\bar{\eta}$  is given by equation (4.19). The optical power  $d\bar{P}_{out}$  spontaneously generated outside the structure by the broad spectrum source is then given by:

$$d\bar{P}_{out} = \bar{\eta} d\bar{P}_{source} \quad (7.8)$$

where the optical power  $d\bar{P}_{source}$  spontaneously generated inside the structure by the broad spectrum source is calculated by averaging (7.6):

$$d\bar{P}_{source} = \int_{-\infty}^{\infty} \eta_i \frac{h\nu}{e} \eta_r dI r_{spont}(\delta) d\delta. \quad (7.9)$$

The parameter  $\delta$  is the ratio between the photon energy  $h\nu$  and a given (and fixed) energy  $h\nu_o$ :  $\delta = \frac{h\nu}{h\nu_o}$ . We can choose for instance  $h\nu_o$  as the electroluminescence peak energy of the intrinsic spontaneous spectrum  $r_{sp}(\delta)$ .

Combining equations (7.8) and (7.9), one gets:

$$d\bar{P}_{out} = \bar{\eta} \eta_i dI \frac{h\nu_o}{e} \int_{-\infty}^{\infty} \delta \eta_r(\delta) r_{spont}(\delta) d\delta. \quad (7.10)$$

The radiative efficiency  $\eta_r$  depends on  $R_{sp}$  which is modified by microcavity effects, according to reference [105]:

$$\boxed{\frac{R_{sp}(\delta)}{R_{sp}^{\infty}(\delta)} = \frac{\tau_{\infty}(\delta)}{\tau(\delta)} = \Delta\tau(\delta)} \quad (7.11)$$

where  $\Delta\tau$  is the radiative lifetime modification due to the microcavity (see equation (4.18)) and  $R_{sp}^{\infty}$  the spontaneous emission rate for a source placed in an infinite medium (without cavity effects). We can assume that the non-radiative recombination rates are not influenced by microcavity effects. We can define in this last case a radiative efficiency  $\eta_r^{\infty}$  with:

$$\eta_r^{\infty} = \frac{R_{sp}^{\infty}}{R_{sp}^{\infty} + R_{nr} + R_l}. \quad (7.12)$$

From equations (7.7) and (7.12) it follows that:

$$\eta_r = \frac{\Delta\tau}{\Delta\tau + \left(\frac{1-\eta_r^\infty}{\eta_r^\infty}\right)}. \quad (7.13)$$

Considering equation (7.10), one can define an averaged radiative efficiency taking into account the radiative lifetime modifications:

$$\bar{\eta}_r = \int_{-\infty}^{\infty} \frac{\delta \Delta\tau r_{spont}(\delta)}{\Delta\tau + \left(\frac{1-\eta_r^\infty}{\eta_r^\infty}\right)} d\delta. \quad (7.14)$$

Note that the averaged radiative efficiency  $\bar{\eta}_r$  is simply equal to  $\eta_r^\infty$  if no microcavity effects are present ( $\Delta\delta = 1$ ) and if the source is monochromatic and emits at the frequency  $\nu_o$ .

The spontaneously emitted power can then be expressed as  $d\bar{P}_{out} = \eta_i \bar{\eta} \bar{\eta}_r \frac{h\nu_o}{e} dI$ .

It must be pointed out that this expression is calculated for an infinitively wide active region which emits photons towards a given outside medium (air or epoxy for instance). The actual (MC)LED devices were processed by etching square shape mesa through the active region as described in section 5.3. The voltage is applied between the top contact deposited on the surface of the mesa (see figure 5.16 for example) and the bottom contact covering the substrate. It is then reasonable to estimate that only a fraction  $\eta_{sh}$  of the optical power  $d\bar{P}_{out}$  will be output in the outside medium. We define  $\eta_{sh}$  as the shadowing efficiency since this parameter describes grid contact effects. Photons impinging on the grid contact and emitted at the  $(x, y)$  position of the active plane will be either absorbed or reflected back in the structure. If we neglect reabsorption effects, we can consider that  $\eta_{sh}(x, y) = 0$  in this case. Far from the contact stripes, it is clear that  $\eta_{sh}(x, y) = 1$ . Close to the edges of the stripes,  $\eta_{sh}(x, y)$  is between zero and one because the output photons must lie in the escape cone and because the grid contacts are deposited relatively close to the active region (1 to 1.5  $\mu m$ ) as it is typically the case for (MC)LED).

The optical power spontaneously generated outside the structure is then expressed as:

$$d\bar{P}_{out} = \eta_i \bar{\eta} \bar{\eta}_r \eta_{sh} \frac{h\nu_o}{e} dI \quad (7.15)$$

in each point  $(x, y)$  of the active region.

As it will be discussed in section 7.3, the current is not uniformly distributed across the surface of the active region because of current crowding effects. Hence the current density  $J$  (in units of  $[A/cm^2]$ ), defined as  $dI = J dS$  (where  $dS = dx dy$  is a surface element of the active region in cartesian coordinates) varies strongly with respect to the coordinates  $J = J(x, y)$ .

If we define  $S_{mesa}$  as the total surface of the active region, we can calculate the total power emitted by the device by integrating equation (7.15):

$$\bar{P}_{out} = \int \int_{S_{mesa}} d\bar{P}_{out}. \quad (7.16)$$

The external quantum efficiency  $\eta_{ex}$  of a LED is defined by [29], [130]:

$$\bar{P}_{out} = \eta_{ex} \frac{h \nu_o}{e} I \quad (7.17)$$

where  $h \nu_o$  is the peak energy of the emission.

We can then explicitly calculate  $\eta_{ex}$ :

$$\eta_{ex} = \frac{\int \int_{S_{mesa}} \eta_i(J) \bar{\eta}(J) \bar{\eta}_r(J) \eta_{sh}(x, y) J(x, y) dx dy}{\int \int_{S_{mesa}} J(x, y) dx dy}. \quad (7.18)$$

The LED external quantum efficiency  $\eta_{ex}$  is traditionally defined as the product of an internal quantum efficiency  $\eta_{int}$  (related to the electrical properties of the structure) by the extraction efficiency  $\bar{\eta}$  (related to the optical properties of the structure):  $\eta_{ex} = \eta_{int} \bar{\eta}$ . Because the injection efficiency  $\eta_i$ , the radiative efficiency  $\bar{\eta}_r$  and the extraction efficiency  $\bar{\eta}$  depend on the current density  $J$ , they also depend on the coordinates  $(x, y)$ . If  $\eta_i(J)$ ,  $\bar{\eta}(J)$  and  $\bar{\eta}_r(J)$  do not vary too rapidly with respect to  $J$ , they can be taken out of the integral (7.18) and estimated at the averaged value  $J_o$  of the current density with  $I = \int \int_{S_{mesa}} J(x, y) dx dy = J_o S_{mesa}$ :

$$\eta_{ex}(J_o) = \eta_i(J_o) \bar{\eta}(J_o) \bar{\eta}_r(J_o) \frac{\int \int_{S_{mesa}} \eta_{sh}(x, y) J(x, y) dx dy}{\int \int_{S_{mesa}} J(x, y) dx dy}. \quad (7.19)$$

We can then define an integrated shadowing efficiency  $\bar{\eta}_{sh}$  by:

$$\bar{\eta}_{sh}(J_o) = \frac{\int \int_{S_{mesa}} \eta_{sh}(x, y) J(x, y) dx dy}{\int \int_{S_{mesa}} J(x, y) dx dy}. \quad (7.20)$$

This parameter depends on the injection level since the  $(x, y)$  dependence of  $J$  is related to current spreading effects which depend strongly on the applied voltage (see section 7.3). We can finally express the external quantum efficiency as:

$$\eta_{ex}(J_o) = \eta_{int}^{app}(J_o) \bar{\eta}(J_o) = \eta_i(J_o) \bar{\eta}_r(J_o) \bar{\eta}_{sh}(J_o) \bar{\eta}(J_o) \quad (7.21)$$

where  $\eta_{int}^{app}$  is an apparent internal quantum efficiency. We define the internal quantum efficiency  $\eta_{int}$  as:

$$\eta_{int}(J_o) = \eta_i(J_o) \bar{\eta}_r(J_o) \quad (7.22)$$

in order to get rid of the contact geometry dependence. Hence  $\eta_{int}(J_o)$  is mainly determined by the electrical characteristics of the structure.

The next section is devoted to the study of  $\eta_{int}^{app}(J_o)$  for (MC)LEDs in the case where the current is assumed to be uniformly spread.

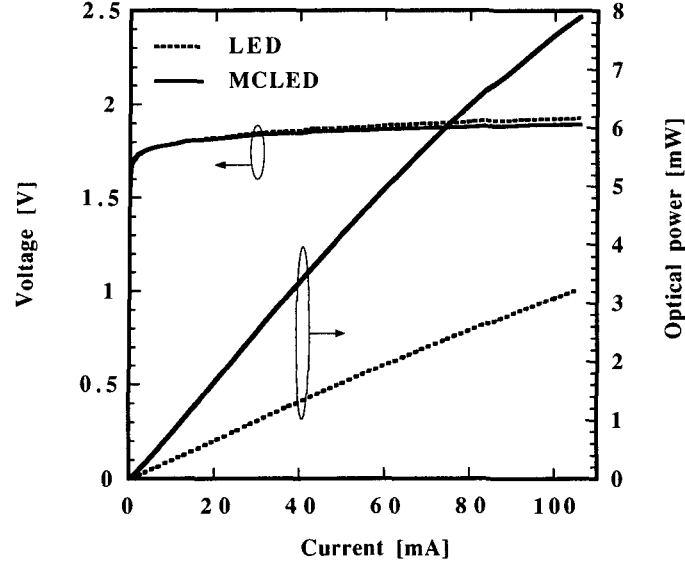


Figure 7.1: Voltage-current characteristics (left axis) and power-current characteristics (right axis) for the LED (dotted line) and for the MCLED (solid line). The mesa width is  $262\text{ }\mu\text{m}$  and the contact has a honeycomb shape.

## 7.2 Determination of the internal quantum efficiency

The purpose of this section is to study the output characteristics of large diameter LEDs and MCLEDs, and to determine the current density dependence of the extraction efficiency  $\bar{\eta}(J_o)$ . The mesa width is of  $262\text{ }\mu\text{m}$  and the current is injected from the top-contact through a honeycomb grid. A picture of such a processed device is displayed on the top right corner of figure 5.14. The diodes were measured in quasi-continuous mode: voltages pulses of  $500\text{ }\mu\text{s}$  were applied at a frequency of  $1\text{ kHz}$  (duty cycle of 50%). As the injected current varied between 0 and 100 [mA], the maximum injected current density was of  $145\text{ A/cm}^2$ . The optical power and the current were measured by using the electrical set-up described on figure 6.13. The devices were bonded on TO-46 headers, and an integrating sphere was used to collect all the emitted light. Results of such measurements are given on figure 7.1.

The measured external quantum efficiencies of both devices are displayed on figure 7.2. A maximum of 4.5 % is reached at 37 [mA] for the MCLED whereas 1.75 % is obtained at the same current for the LED.

Our purpose is first to calculate the current density dependence of the MCLED extraction efficiency  $\bar{\eta}(J)$  so as to determine its internal quantum efficiency  $\eta_{int}(J)$ . The geometry of the contact was chosen such that we can assume that the current is homogeneously spread in the active region. We explained in chapters 3 and 4 how to numerically calculate  $\bar{\eta}(J)$ . Knowing the structure parameters (the composition and the thicknesses of the layers), it is simple to calculate the extraction efficiency of any monochromatic source. Knowledge of the intrinsic emission spectrum is required for the evaluation of  $\bar{\eta}(J)$ . We saw in chapter 6 that for large mesa widths and for small current densities, the intrinsic emission spectrum is very well fitted by the phenomenological function given in relation (6.7). This

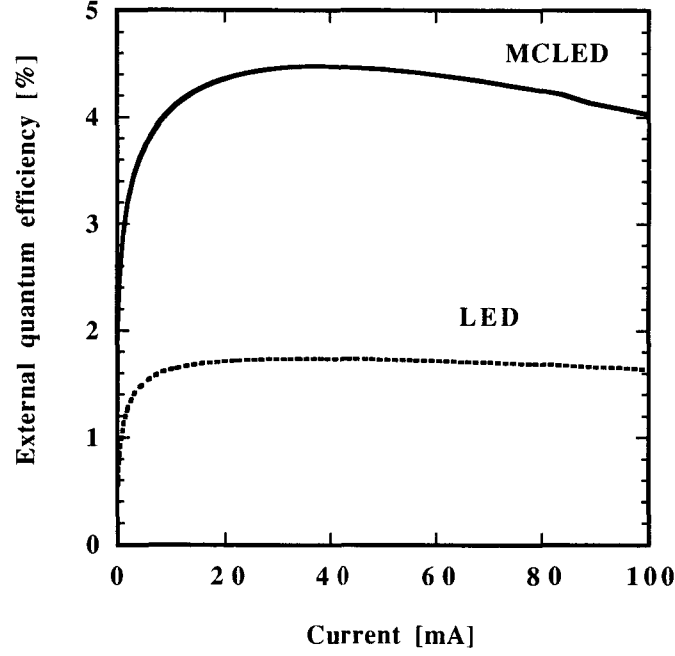


Figure 7.2: Measured external quantum efficiency plotted versus current for the LED (dotted line) and for the MCLED (solid line). The mesa width is  $262\text{ }\mu\text{m}$  and the contact has a honeycomb shape.

function is completely determined by three parameters: the peak electroluminescence wavelength  $\lambda_{qw}$  and two coefficients  $c$  and  $m$  describing respectively the asymmetry and the linewidth of the spectrum. By measuring the spontaneous emission spectrum of the LED at current densities up to  $145\text{ [A/cm}^2\text{]}$ , and by fitting the spectra with the analytical function (6.7), we observed that the asymmetry parameter was reasonably constant and equal to  $c = 1.5$ . This left us with two unknown parameters  $\lambda_{qw}$  and  $m$ , which have to be determined so as to evaluate  $\bar{\eta}$ . One way to determine them is to measure the (spectrally integrated) emission patterns and to numerically fit them with the simulations so as to minimize an error function [118]. We used here a slightly modified and simplified version of this method. The patterns of emission were simulated for different detuning values and different spectral linewidths. By angle-resolved measurements we determined that the detuning was negative (see chapter 6), hence we can characterize the emission patterns by two parameters  $\alpha_0$  and  $\theta_{max}$  (defined in section 6.2). For each couple of detuning-linewidth value, we reported the contour plots corresponding of a given value of  $\alpha_0$  and  $\theta_{max}$ . Figure 7.3 displays the result of this procedure.

We observe that the contour plots of  $\alpha_0$  and  $\theta_{max}$  intersect only once: hence for a given couple of source linewidth-detuning value, it corresponds a single couple of  $\alpha_0$ - $\theta_{max}$  parameters. The patterns of emission were measured every ten milliamperes from 10 to 100 [mA] (hence from 15 to  $145\text{ [A/cm}^2\text{]}$ ). We reported on the figure 7.3 the measured values of  $\alpha_0$  and  $\theta_{max}$  for each pattern. As we observed it on figure 6.18,  $\theta_{max}$  decreases and  $\alpha_0$  increases as the current density increases. From figure 7.3, the source linewidth and the detuning corresponding to each current density can be determined. Note that these parameters increase with the current density, confirming the results presented in section 6.2.

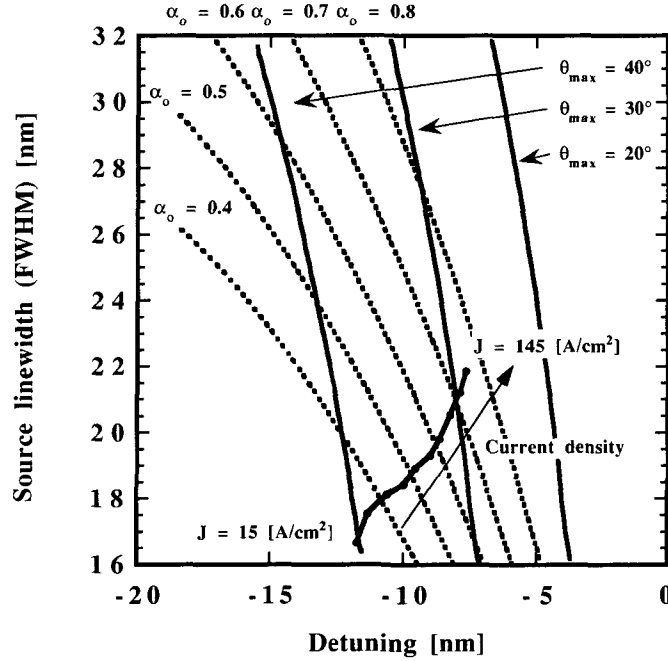


Figure 7.3: Contour plot of the  $\alpha_0$  parameter (dotted line) and of the  $\theta_{max}$  parameter (solid line) numerically calculated for different values of cavity-source detuning and intrinsic source linewidth. Solid circles represent the same parameters measured at different current densities.

The parameters determining the intrinsic lineshape (6.7) are then completely known and it is possible to calculate the extraction efficiency of the MCLED as well as its angular emission profile. An example of such a (normalized) pattern is given on figure 7.4 (black dots). The solid line represents the angular emission profile which was numerically simulated. We observe an excellent agreement between measurement and simulations, indicating that the numerically calculated values of the extraction efficiency are very accurate.

Figure 7.5 displays in solid line the optimal extraction efficiency (left axis) which can be theoretically obtained for a given intrinsic spectrum linewidth. The corresponding optimal detuning value which is shown in solid line on the right axis. As predicted by our simple model (see chapter 4) the optimal detuning is negative and the optimal extraction efficiency decreases as the intrinsic spectrum broadens. Black dots represent the parameters calculated for the source linewidth and for the detuning values extracted from our fits. It is interesting to observe that the structure is overdetuned at low current density. As the current density increases the source linewidth broadens and the detuning red-shifts, converging towards the optimal value. At  $145 \text{ [A/cm}^2\text{]}$  the extraction efficiency is optimal and approximatively equal to 11 %.

Figure 7.6 shows the contour lines of the extraction efficiency which were numerically calculated for different detuning and source linewidth values. The extraction efficiency calculated from the fits is displayed on the same plot for the measured current densities.

It is very interesting to observe that the measured extraction efficiencies follow approximately the

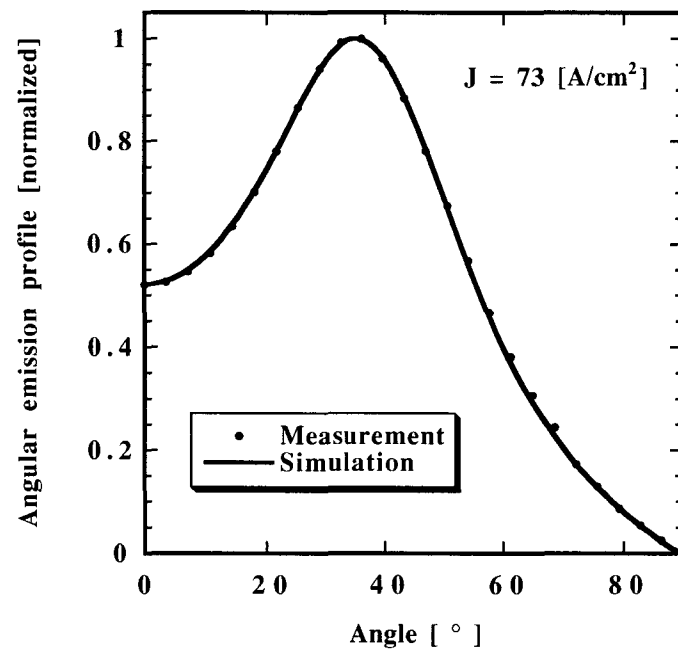


Figure 7.4: Angular emission profile (spectrally integrated) plotted versus the angle: solid circles represent measured values and solid line corresponds to the numerical simulation.

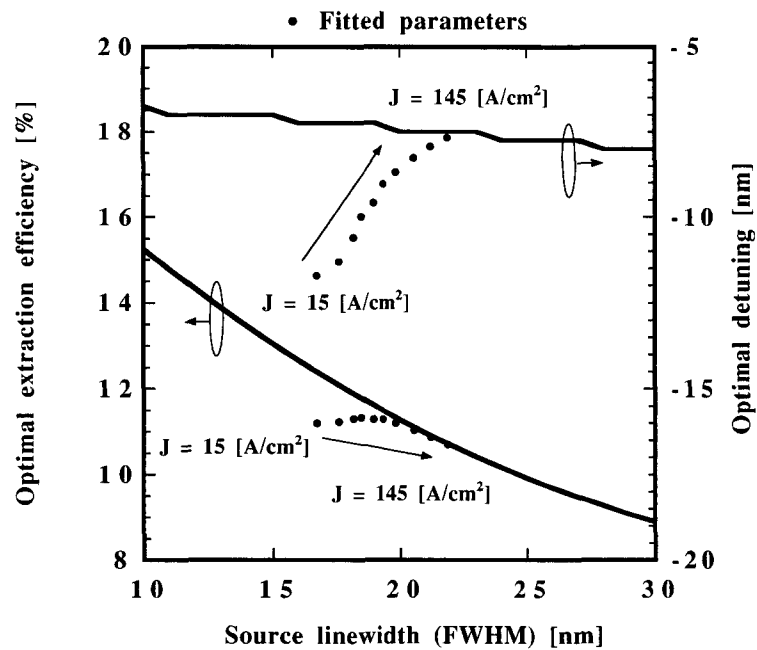


Figure 7.5: Optimal extraction efficiency calculated numerically (left axis) and corresponding optimal values of detuning (right axis) plotted versus the intrinsic spectrum linewidth. The parameters obtained by numerical simulations are represented as solid circles.

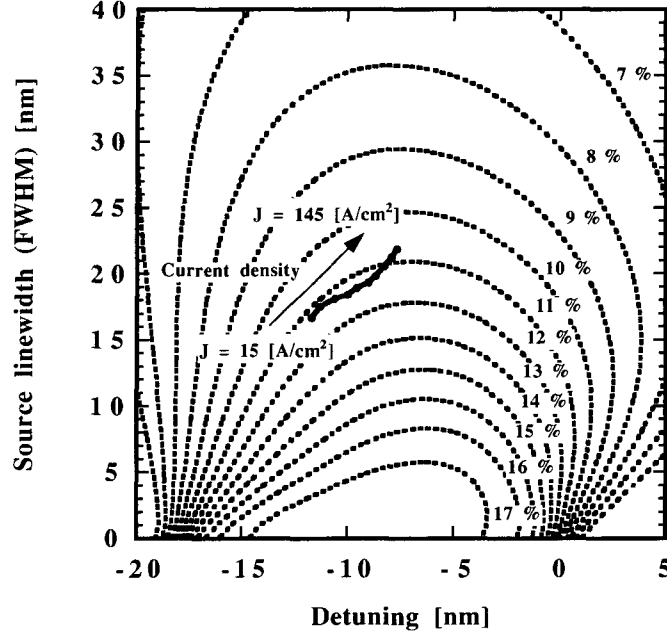


Figure 7.6: Contour plot of the extraction efficiency numerically calculated for different values of detuning and source linewidth. Solid circles represent the values estimated from the fits at different current densities.

11% contour line of the figure. One concludes that it is possible to compensate the effect of spectral broadening on the efficiency, by blue shifting the detuning. On the contrary, one sees that if the cavity was not enough detuned, then the measured extraction efficiencies would have followed the gradient of the contour lines, implying a significant drop of the efficiency with respect to the injected current.

The ratio of the external quantum efficiency  $\eta_{ex}$  (measured) by the extraction efficiency  $\bar{\eta}$  (calculated) is plotted on figure 7.7 with respect to the current density. We performed the same calculation on the LED. Considering equation (7.21), the parameter plotted corresponds to the apparent internal quantum efficiency  $\eta_{int}^{app}$ .

### 7.3 Effect of the current spreading on the external quantum efficiency

The purpose of this section is to study the influence of the grid contact geometry on the external quantum efficiency  $\eta_{ex}$ . Estimation of the apparent internal quantum efficiency was performed in the previous section on large size diodes (diameter of  $262[\mu m]$ ). For these devices the current was injected through a honeycomb grid. We measured four other devices with the same mesa width but different contact geometries. Details of the contact geometries can be found in figures 5.14 and 5.15. We measured the LED and the MCLED devices based on the structures shown on figures 6.1 and 6.2. Conditions of measurements are described in section 7.1 of this chapter. The external quantum efficiencies measured on the five considered MCLEDs are displayed on figure 7.8. The numbers 1 to 5 correspond to the contact types which are defined on figure 5.15.



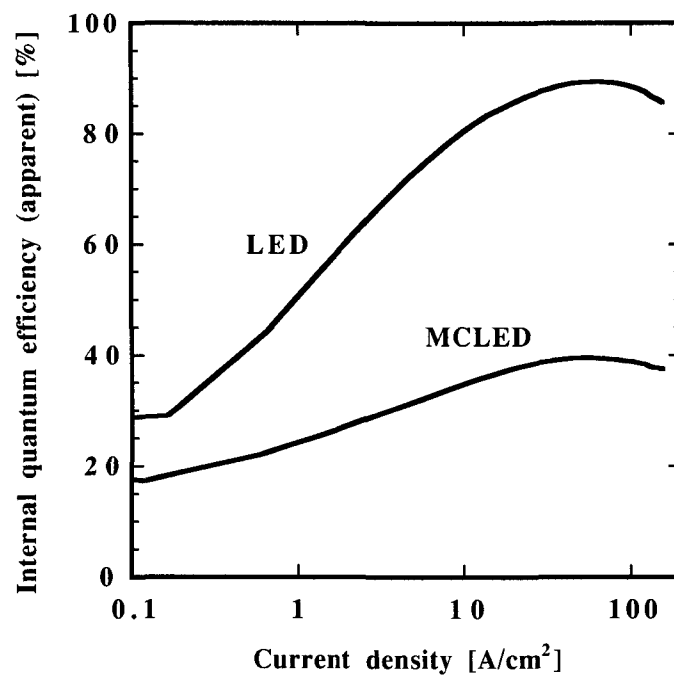


Figure 7.7: External quantum efficiency divided by the extraction efficiency plotted versus the current density for the MCLED and the LED. The mesa width is  $262\text{ }\mu\text{m}$  and the contact has a honeycomb shape.

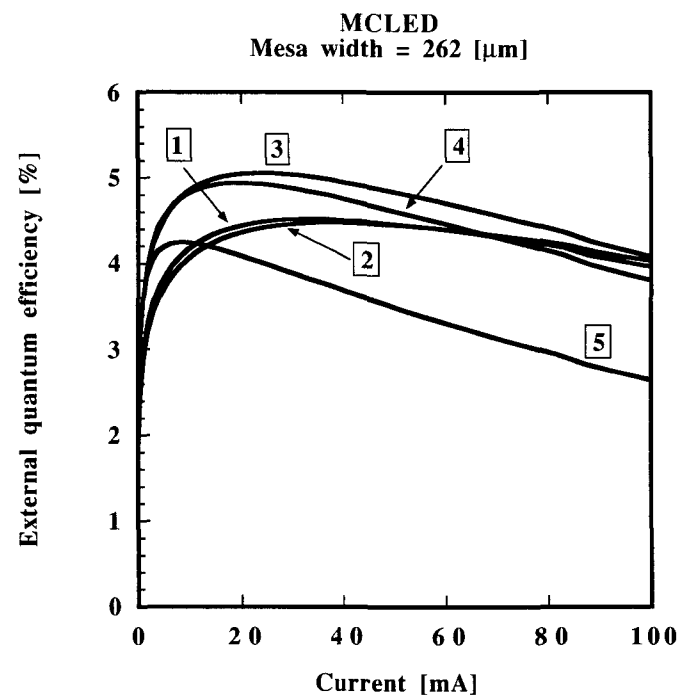


Figure 7.8: External quantum efficiency measured on five large size MCLEDs with different contact geometries.

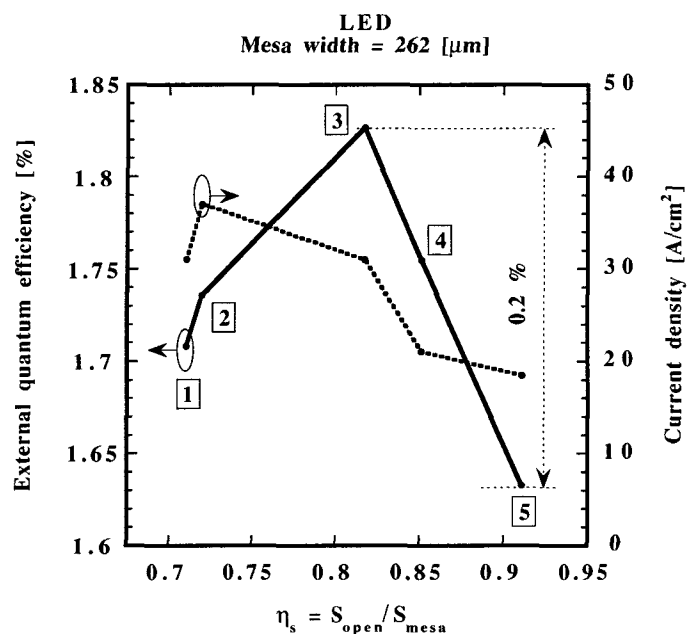


Figure 7.9: Maximum external quantum efficiency (left axis) and corresponding current density (right axis) measured on five large size LEDs having different contact geometries.

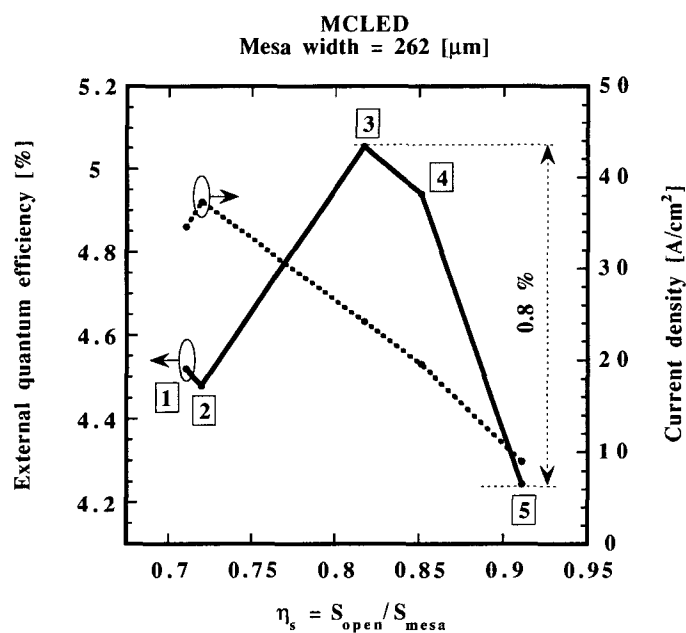


Figure 7.10: Maximum external quantum efficiency (left axis) and corresponding current density (right axis) measured on five large size MCLEDs having different contact geometries.

On figures 7.9 (LED) and 7.10 (MCLED) are plotted the maximum of external quantum efficiency  $\eta_{ex}$  (left axis) and the current density at which this optimum is reached (right axis). The horizontal axis corresponds to the ratio of the unmasked surface of the mesa to its overall surface. LEDs and MCLEDs exhibit the same general behavior: the extraction efficiency is maximum for the contact type 3. The improvement of external quantum efficiency (absolute value) is of 0.2% for the LED and 0.8% for the MCLED, which corresponds to a relative improvement of 12% (respectively 19%) with respect to the lowest efficiencies. The current density at which this optimum is reached decreases as the unmasked surface of the mesa increases.

The devices having the same mesa width and being processed on the same part of the wafer, the differences observed on the external quantum efficiency curves are then due to the different distributions of the current density  $J(x, y)$  across the mesa. This will give different values for the shadowing efficiency (see equation (7.20)). Because of current crowding, the current density distribution  $J(x, y)$  will depend on the applied voltage, hence the shadowing efficiency and the external quantum efficiency also (by equation (7.19)).

Current spreading in stripe-geometry semiconductor lasers is a well known phenomenon. It occurs whenever contacts supply current to a vertical semiconductor junction. Because of the voltage gradient, a horizontal component of the current density exists which tends to spread the current outside the contacts. Current spreading refers to the case where this effect is large, whereas current crowding refers to the opposite situation (the current is mainly injected below the contacts in this last case). This problem was studied in detail in the seventies (see references [50], [49], [74], [75] for example) and several techniques were proposed to laterally confine the current and prevent current spreading: oxide-confined structures, proton implantation, etched mesa are some examples [29].

For top-emitting devices, the problem is different, since one wants to efficiently spread the current across the surface of the active zone so as to minimize the radiative recombinations below the contacts. Several solutions were proposed in the following references to optimize the current spreading of LEDs: [44], [20], [7], [96], [148], [147], [107]. Current spreading is also required for VCSELs: because of the high current density at which they operate, current crowding can be responsible for spatial hole burning increasing the threshold current [140]. Current spreading is moreover highly desired for realization of intracavity contacted VCSELs [139], [66], [63].

In order to qualitatively understand the origin of the current spreading, it is necessary to calculate the current density distribution  $J(x, y)$  across the surface of a mesa. For that purpose, several models can be found in the literature: the model of Joyce [76], [74] takes into account the ohmic current which flows horizontally in the top p-doped layer and the diffusion of the carriers in the nominally undoped active region. This requires five coupled differential equations to be solved and knowledge of the radiative recombination rates and applied voltage as function of the carrier concentrations. A simplified version of Joyce's model can be found in references [54], [55] and [139]: it describes the device structure by a network of diodes and resistances. This model is a generalization of the

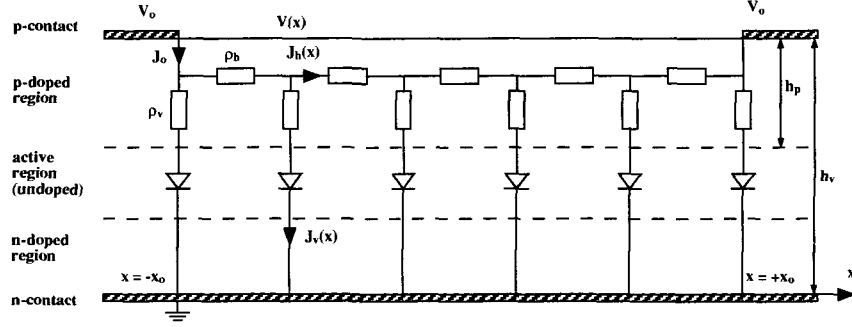


Figure 7.11: Sketch of the device geometry used in the model.

transmission line model (also called TLM) used to measure the contact resistances [15], [154]. We use this model in this work because of its simplicity and because of the good agreement with our experiments. The geometry of the problem investigated is given in figure 7.11.

The structure is assumed to be infinite in the direction perpendicular to the cross section of the device and we restrict our study to a one-dimensional geometry. The bottom contact covers the whole surface of the n-doped region, whereas the top contacts ends at the positions  $x = \pm x_0$ .

A voltage  $V_0$  is applied at the top contact. Thicknesses of the p-doped and active regions are respectively  $h_p$  and  $h_v$ . The material resistivity  $\rho_h$  (in units of  $[\Omega m]$ ) corresponds to the p-doped region. If this region is made of several layers with different material composition, it is possible to calculate the effective resistivity  $\rho_h$  by calculating the parallel equivalent of the multilayers.

The horizontal current density is given by Ohm's law:

$$\frac{dV(x)}{dx} = -\rho_h J_h(x). \quad (7.23)$$

The vertical current density can be expressed by using the current continuity equation:

$$h_p \frac{dJ_h(x)}{dx} = -J_v(x). \quad (7.24)$$

The semiconductor junction is described by an ideal heterojunction diode:

$$J_v(x) = J_t e^{\frac{V_d(x)}{nV_t}} \quad (7.25)$$

where  $n$  is the ideality factor of the diode and  $V_t = \frac{k_b T}{e} = 25.875 [mV]$  at  $T = 300 [K]$ .

The potential  $V(x)$  is then given by Ohm's law:

$$V(x) = \rho_v h_v J_v(x) + V_d(x) \quad (7.26)$$

where  $\rho_v$  and  $h_v$  are respectively the resistivity and the thickness of the whole vertical structure (the vertical resistances are displayed in the p-doped region on figure 7.11 for drawing convenience only).

Resolution of equations (7.23) to (7.26) leads to a second order differential equation with the following boundary conditions:

$$V(x = \pm x_0) = V_0 \quad (7.27)$$

$$\left. \frac{dV(x)}{dx} \right|_{x=0} = 0. \quad (7.28)$$

In the general case, the solution of equations (7.23) to (7.26) is very complex and has to be solved numerically. It is however possible to analytically solve the problem in two simple cases.

If we do not take into account the voltage drop due to the junction ( $V_d(x) = 0$ ), we are left with the TLM resistance network problem. The vertical current density is then given by:

$$J_v(x) = \frac{V_0}{\rho_v h_v} \frac{\cosh(x/L_p)}{\cosh(x_0/L_p)} \quad (7.29)$$

where  $L_p$  is a decay length (in units of [m]) given by:

$$L_p = \sqrt{\frac{\rho_v h_v h_p}{\rho_h}}. \quad (7.30)$$

From this equation it appears that the decay length is large (hence the current spreading is good) if the sheet resistivity of the p-doped region is small and if the vertical resistance is high. We remind the reader that the sheet resistivity is expressed in units of  $[\Omega/\square]$ . It is given in our case by  $R_{sh} = \rho_h/h_p$ . It is possible to use this simple model in the case of a semiconductor junction by assuming that the vertical resistance corresponds to the differential resistance of the diode. Hence as the diode becomes forward biased, the low dynamic resistance of the diode shunts the lateral resistance of the top layer, resulting in an increase of the current crowding.

We can calculate this effect more accurately by solving the equations (7.23) to (7.26) in the case where the vertical resistance is neglected.

After some simple calculations, the vertical current density is found to be:

$$J_v(x) = \frac{J_0}{\cos^2\left(\sqrt{\frac{J_0}{J_t}} \frac{x}{L_q}\right)} \quad (7.31)$$

where  $L_q$  is a decay length (in units of [m]) given by:

$$L_q = \sqrt{\frac{2 h_p n V_t}{\rho_h J_t}} = \sqrt{\frac{2 n V_t}{J_t R_{sh}}}. \quad (7.32)$$

The current density  $J_0 = J_v(x=0)$  is related to the applied voltage  $V_0$  by the following relation:

$$\frac{J_0}{\cos^2(\sqrt{\frac{J_0}{J_t}} \frac{x_0}{L_q})} = J_t e^{\frac{V_0}{n V_t}}. \quad (7.33)$$

Equation (7.31) shows that the effective decay length is  $\sqrt{\frac{J_t}{J_0}} L_q$ , implying that the current crowding increases as the applied voltage increases, which confirms the result of the simple resistance network model. Considering relation (7.32) one sees that the smaller is the sheet resistance and the best is the current spreading (at a fixed bias).

We measured the near field patterns of devices without any grid contact (see figure 5.15 for instance). For that purpose we imaged the mesa surface onto a CCD camera by using a microscope objective and some appropriate filters so as to avoid camera saturation effects. An example of such a pattern is displayed on top of figure 7.12.

Bottom of figure 7.12 shows the near field emission pattern sampled at the center of the mesa in the vertical direction of the figure and displayed along the horizontal direction. The dots represent the measurement and the solid line corresponds to a fit using equation (7.31). This approximation is good because of the linear dependence between the current density and the emitted optical power which is measured in the experiment (see equation (7.15)). In fact, drift and diffusion of carriers in the active region (not taken into account in our model) deplete the region below the contacts as shown by Joyce [74]. This means that in reality, less optical power is emitted below the contacts than in the model. It must also be pointed out that a one-dimensional model was applied to a two-dimensional one. Since we scanned the near field pattern at the center of the mesa, we assume that this effect is small. Figure 7.12 shows that the agreement between the fitted and the measured curves is good.

The same measurements and fits were performed on the LED and MCLED at different current densities. We report on figure 7.13 the effective decay lengths  $\sqrt{\frac{J_t}{J_0}} L_q$  extracted from the fits. As expected this value decreases as the injected current density increases. Since  $J_0$  can be also extracted from the fit, it is possible to determine the decay length  $L_q$ , which should not depend on the injected current density according to expression (7.32). We find  $\sqrt{J_t} L_q = 146 \pm 3 [\sqrt{A}]$  for the LED and  $\sqrt{J_t} L_q = 189 \pm 10 [\sqrt{A}]$  for the MCLED. The current spreading is better in the MCLED than in the LED.

To check this, we measured the sheet resistance on the two wafers, using TLM (transfer length method) structures available on our mask. We found  $R_{sh} = 650 [\Omega/\square]$  for the LED and  $R_{sh} = 310 [\Omega/\square]$  for the MCLED. The decay length being given by equation (7.32), we conclude that (provided  $J_t$  is the same for both devices) the decay length of the MCLED should be  $\sqrt{650/310} = 1.45$  times larger than the one of the LED. We experimentally found out a ratio of  $189/146 = 1.3$  by near field measurements, which is reasonable, considering the simple model used.

We conclude that the effective decay length significantly decreases as the current density increases and that the current spreading is better for the MCLED than for the LED. Since top grid contacts

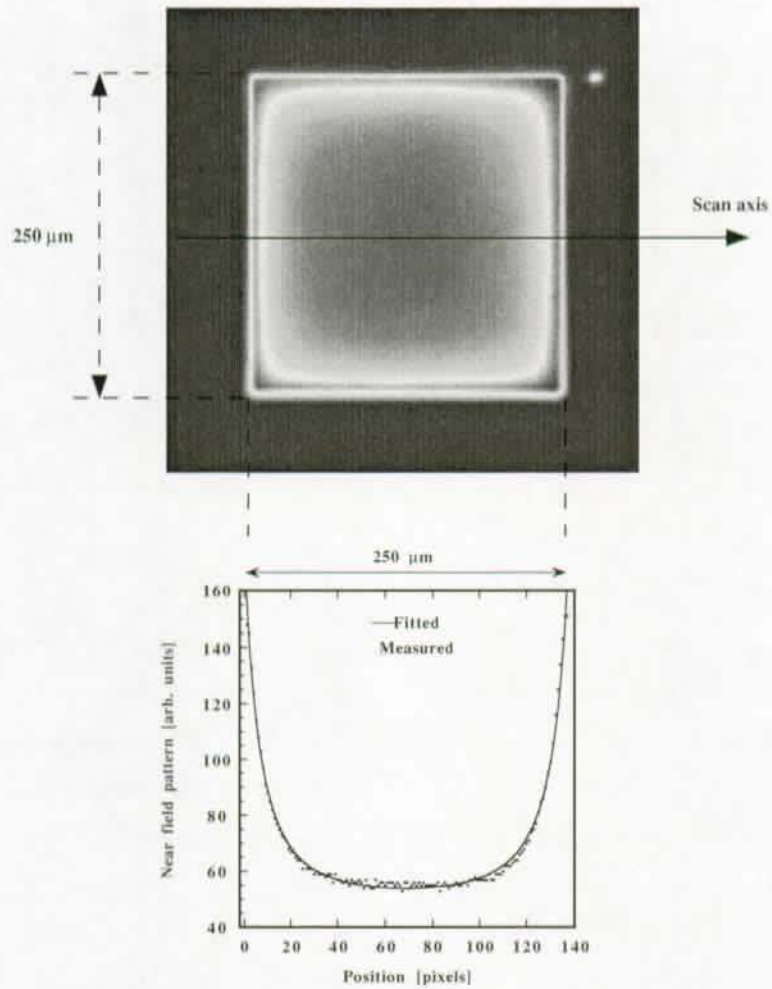


Figure 7.12: Near field pattern of a large size diode being injected through its edges only (injected current is  $50\text{ [mA]}$ ). The current is severely crowded and luminescence occurs close to the edges of the mesa leaving dark the center of the mesa. Bottom part of the figure displays the near field pattern measured along the scan axis.

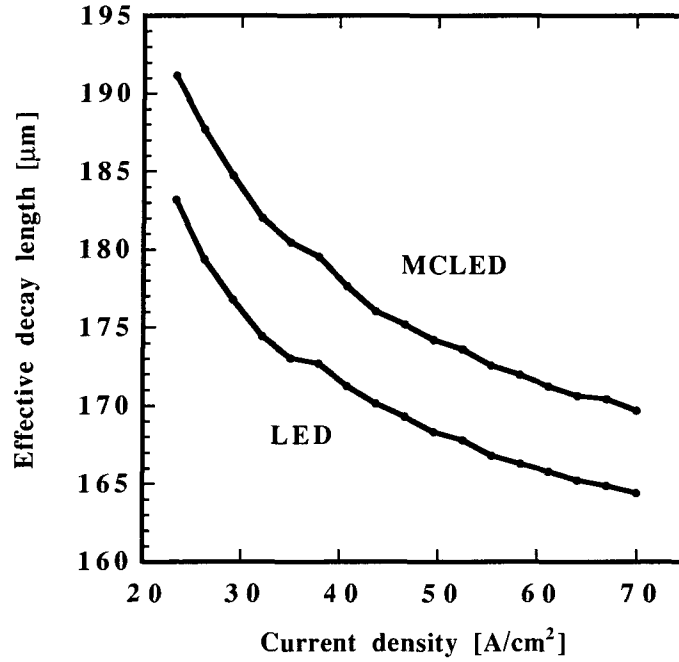


Figure 7.13: Effective decay length  $\sqrt{\frac{J_t}{J_0}} L_q$  plotted versus the injected current density for both kind of devices (LED and MCLED).

of type 2 are strongly interconnected (honeycomb shape), we can assume that the corresponding devices are uniformly injected. If we define  $\bar{\eta}_{sh}(c)$  as the shadowing efficiency of the device having a c-type contact (with  $c = 1, 2, 3, 4, 5$ ), we can then assume that  $\bar{\eta}_{sh}(2)$  is independent of the injected current density. Since the product  $\eta_i \bar{\eta}_r$  does not depend on the contact shape, the ratio  $\bar{\eta}_{sh}(c)/\bar{\eta}_{sh}(2)$  gives the current density dependence of the shadowing efficiency, normalized to the constant shadowing efficiency  $\bar{\eta}_{sh}(2)$ . These parameters are displayed on figures 7.14 and 7.15 for the LED and the MCLED respectively. They were calculated by simply dividing the external quantum efficiencies of the devices having c-type contacts by the external quantum efficiency of the device having contact of type 2 ( $\eta_{ex}(c)/\eta_{ex}(2) = \bar{\eta}_{sh}(c)/\bar{\eta}_{sh}(2)$ ).

We observe that the shadowing efficiencies generally decrease with the current density which was to be expected from the simple model. The type 1 and type 2 contacts have approximately the same effect on the current spreading. We observe that  $\bar{\eta}_{sh}(5)$  decreases very rapidly with respect to the current density which has to be related to the absence of any grid covering the mesa, hence to a very strong current crowding. Current crowding occurs also for contact types 3 and 4, but with less intensity. Comparing figures 7.9 and 7.10 with figures 7.14 and 7.15, one can conclude that the external quantum efficiency  $\eta_{ex}$  of devices having type 1 and 2 contacts is limited by the large fraction of the mesa which is masked by the contacts. Since the current spreading is good, the current density at which  $\eta_{ex}$  is maximum (the position of the roll-over) is determined by the product  $\eta_i \bar{\eta}_r$ .

The opposite situation corresponds to the case of the type 5 contact (no grid and injection through the edges of the device). In this case the current is severely crowded, and the rapid decrease of  $\bar{\eta}_{sh}(5)$



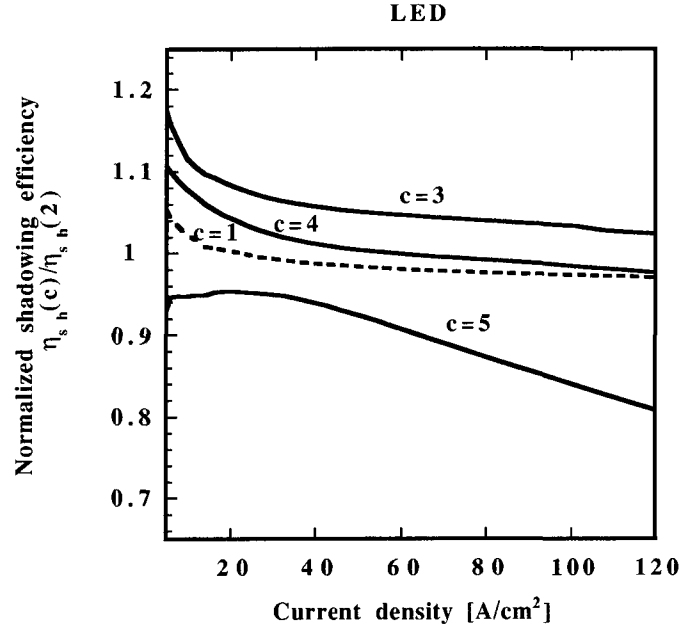


Figure 7.14: Current density dependence of the shadowing efficiencies for different grid contact geometries (for LED). These parameters are normalized to the constant shadowing efficiency of the type 2 contact. The curves were calculated by taking the ratio between the external quantum efficiency of the devices with contacts types  $c=1, 3, 4, 5$  and the external quantum efficiency of the device with contact type  $c=2$ .

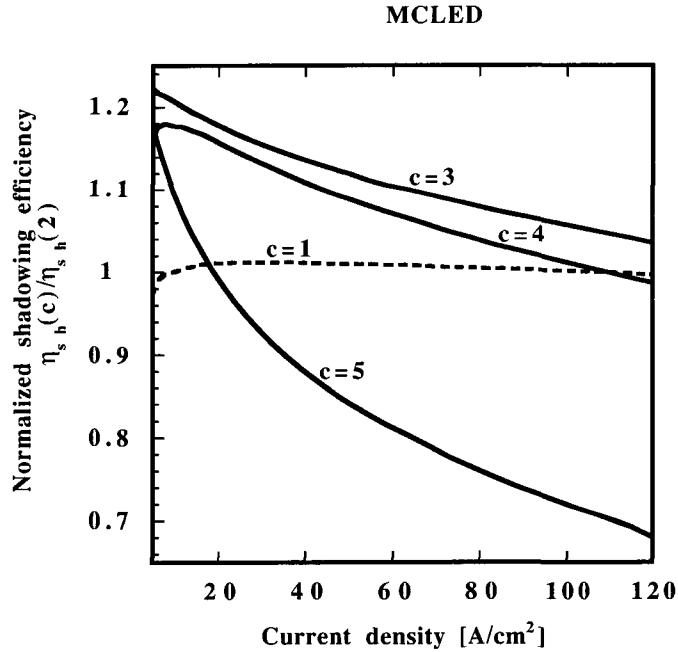


Figure 7.15: Current density dependence of the shadowing efficiencies for different grid contact geometries (for MCLED). These parameters are normalized to the constant shadowing efficiency of the type 2 contact. The curves were calculated by taking the ratio between the external quantum efficiency of the devices with contacts types  $c=1, 3, 4, 5$  and the external quantum efficiency of the device with contact type  $c=2$ .

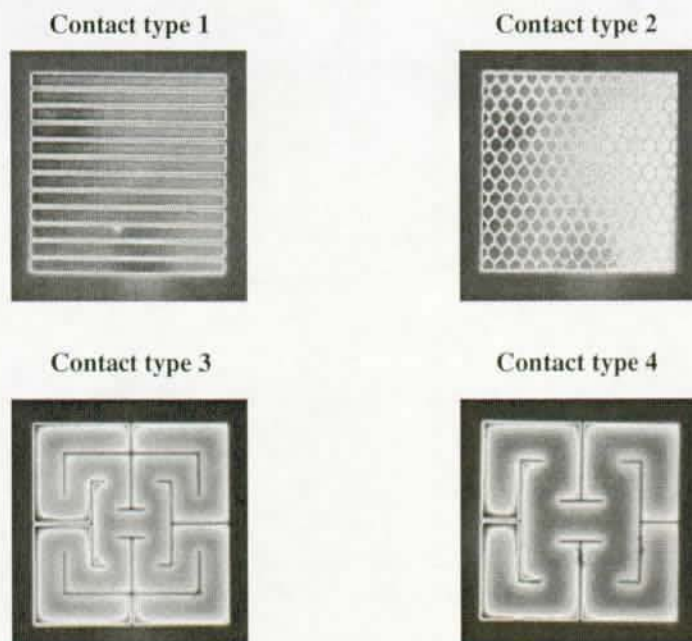


Figure 7.16: Near field patterns of different top contact geometries (measured at a current density of  $50 \text{ [A/cm}^2\text{)]}$ ).

with respect to the current density is responsible for the small external quantum efficiency and for the small current density value at which the roll-over occurs.

The contact geometries of type 3 and 4 have a good masking coefficient (given in table 5.1), and cover the whole surface of the mesa, leading to a good current spreading. Current crowding occurs as the current density increases but at a smaller rate than for the type 5 contact.

Figure 7.16 displays the near field patterns of four of the MCLEDs devices. It is seen that the current spreading is better for structures with type 1 and 2 grid shapes, than for the others. Comparing near field patterns of figure 7.16 with the optical microscope pictures given in figure 5.14, one sees that there is more light generated close to the pad of the top contact than elsewhere. This is simply due to the finite resistivity of the contact stripes: the current flows across a smaller resistance close to the contact pad.

To summarize these results, the external quantum efficiency is optimized when  $\bar{\eta}_{sh}$  is high (which requires that the contact surface is minimized), and when  $d\bar{\eta}_{sh}/dJ$  is small such that the roll-over due to the current crowding occurs after the rollover due to  $\eta_i \bar{\eta}_r$ . This last requirement is unfortunately incompatible with the first one since the more the contact is interconnected (hence the larger is the masking of the mesa) and the best is the spreading. A trade-off has to be found between small contact masking and good current spreading. The web-shape geometry (contact type 3) is then optimum in

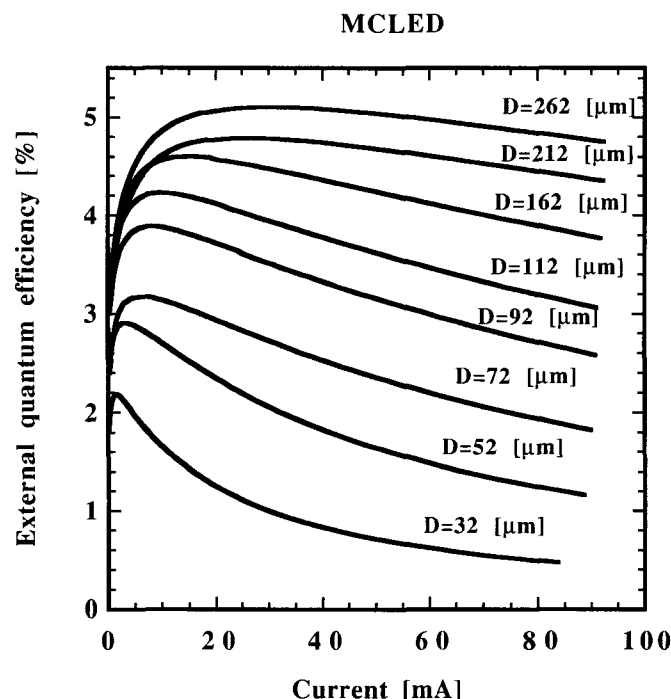


Figure 7.17: External quantum efficiencies measured on MCLEDs having different mesa widths  $D$  and plotted versus the injected current. The top contact geometry is of type 3.

this respect.

## 7.4 Effect of the device size on the external quantum efficiency

In this last section, the influence of the device size on the external quantum efficiency is investigated. Devices having mesa widths of 32, 52, 72, 92, 112, 162, 212, 262  $\mu\text{m}$  were measured under pulsed excitation: voltage pulses of 80  $\mu\text{s}$  were applied at a frequency of 1.25  $\text{kHz}$  (duty cycle of 10%). The top contact have the same geometry as the device displayed on the bottom left corner of figure 5.14 (contact type 3). The diodes being bonded on TO-46 headers, it was possible to accurately measure the emitted power with an integrating sphere. We measured LED and MCLED devices with the structures displayed on figures 6.1 and 6.2. The external quantum efficiencies were calculated by using relation (7.17) and are represented on figure 7.17 for the MCLED. For each diode, the maximum of external quantum efficiency  $\eta_{ex}^{max}$  and the current  $I_{max}$  at which this maximum is reached were determined. The parameters  $\eta_{ex}^{max}$  and  $I_{max}$  are displayed on the figure 7.18, respectively figure 7.19 with respect to the mesa surfaces expressed in units of  $\text{cm}^2$ .

These coefficients increase with the device surface. In order to understand these characteristics, we propose a simplified model of the external quantum efficiency  $\eta_{ex}$ . Let first consider the radiative efficiency  $\bar{\eta}_r$ . This parameter is the ratio between radiative recombination rate and total recombination rate in the active region (see equation (7.7)), which can be expressed with respect to the carrier density in the active region by:

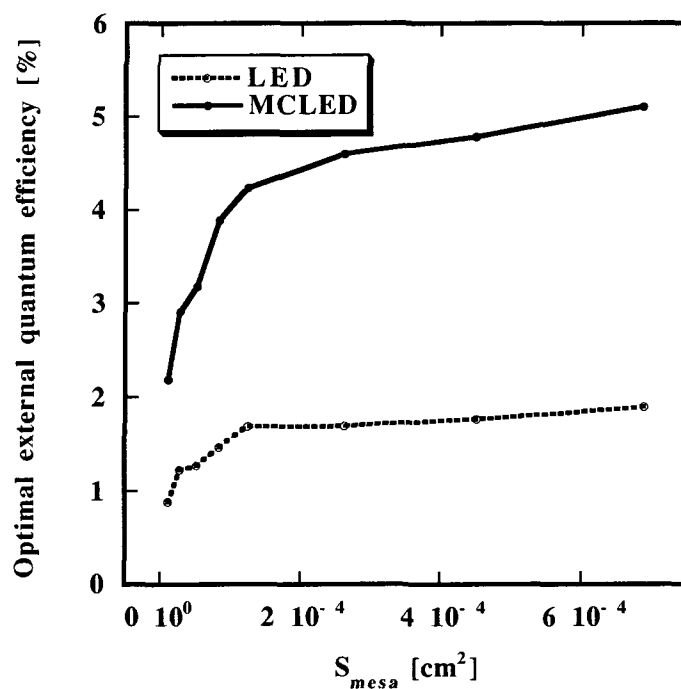


Figure 7.18: Maximum external quantum efficiencies plotted versus the devices surfaces for LED (dotted line) and MCLED (solid line).

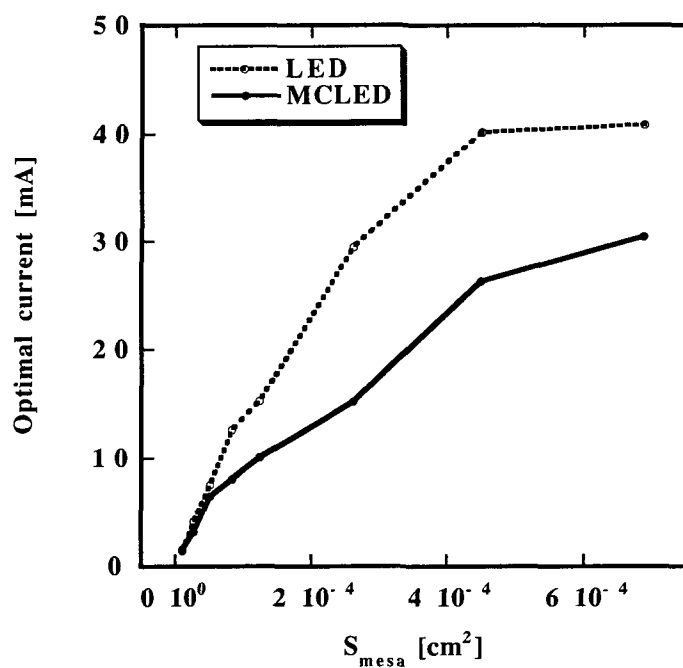


Figure 7.19: Current at which the external quantum efficiency is maximum, plotted versus the devices surfaces for LED (dotted line) and MCLED (solid line).

$$\bar{\eta}_r = \frac{B N^2}{A N + B N^2} \quad (7.34)$$

with

$$A = A_0 + \frac{4 v_s}{\sqrt{S_{mesa}}}. \quad (7.35)$$

Definitions of  $A_0$  and  $v_s$  were given on section 7.1. Equation (7.5) can be written as:

$$\frac{\eta_i I}{e V_{qw}} = A N + B N^2 \quad (7.36)$$

where  $I$  corresponds to the current injected in the device. Solving equation (7.36), it is possible to express  $N$  as function of  $I$  and to inject it in equation (7.34), which gives:

$$\bar{\eta}_r(I) = \frac{I_0}{\eta_i I} \left[ 1 + \frac{\eta_i I}{I_0} - \sqrt{1 + \frac{2 \eta_i I}{I_0}} \right] \quad (7.37)$$

where  $I_0$  has units of a current and is given by:

$$I_0 = \frac{e e_{qw}}{2} \frac{A_0^2}{B} S_{mesa} \left[ 1 + \frac{4 v_s}{A_0 \sqrt{S_{mesa}}} \right]^2. \quad (7.38)$$

Since the injection efficiency depends on the current ( $\eta_i = \eta_i(I)$ ), the current dependence of the radiative efficiency is unfortunately quite complicated. If  $\eta_i(I)$  does not vary too much with respect to the current (which can be reasonably assumed), we can write the following approximation which decouples the injection efficiency from the radiative efficiency:

$$\boxed{\bar{\eta}_r(I) = \frac{I_0}{I} \left[ 1 + \frac{I}{I_0} - \sqrt{1 + \frac{2 I}{I_0}} \right]}. \quad (7.39)$$

This expression continuously increases with the current and saturates to one. When the carrier density is large enough, the radiative recombination rate (varying as  $N^2$ ) dominates the non-radiative recombination rate (varying as  $N$ ). The smallest is the current  $I_0$ , and the quickest  $\bar{\eta}_r(I)$  converges towards one. This behavior is displayed on top part of figure 7.20 for two different currents  $I_{01}$  and  $I_{02} > I_{01}$ .

Since the external quantum efficiency is given by equation (7.21), we need to express the current dependence of  $\eta_i(I) \bar{\eta}_{sh}(I) \bar{\eta}(I)$  that we define as  $\eta_0(I)$ . These three efficiencies decrease with the current as shown in sections 7.2 and 7.3. We use the following empirical function to describe this current dependence:

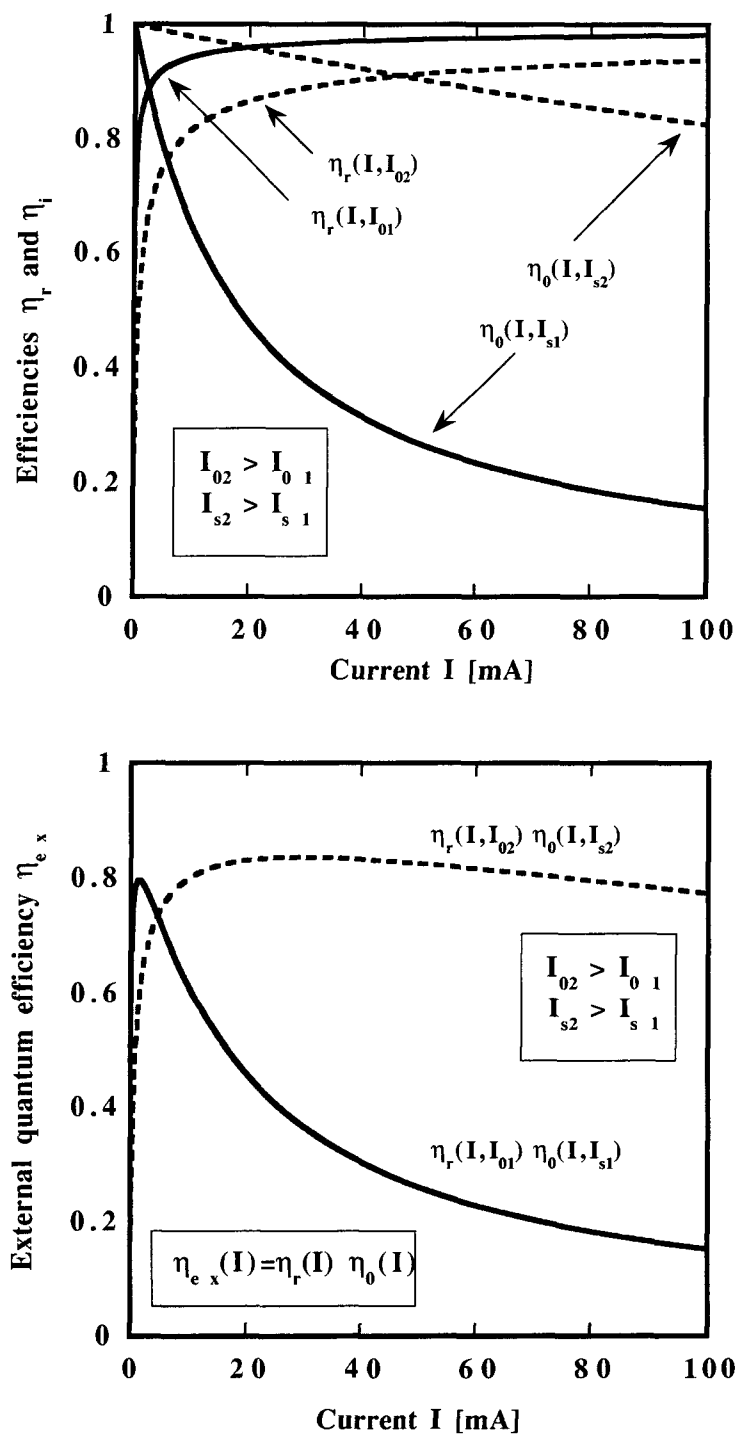


Figure 7.20: Plots of the efficiencies  $\eta_r(I)$ ,  $\eta_0(I)$  and  $\eta_{ex}(I)$  with respect to the current  $I$  and for different parameters  $I_0$  and  $I_s$ .

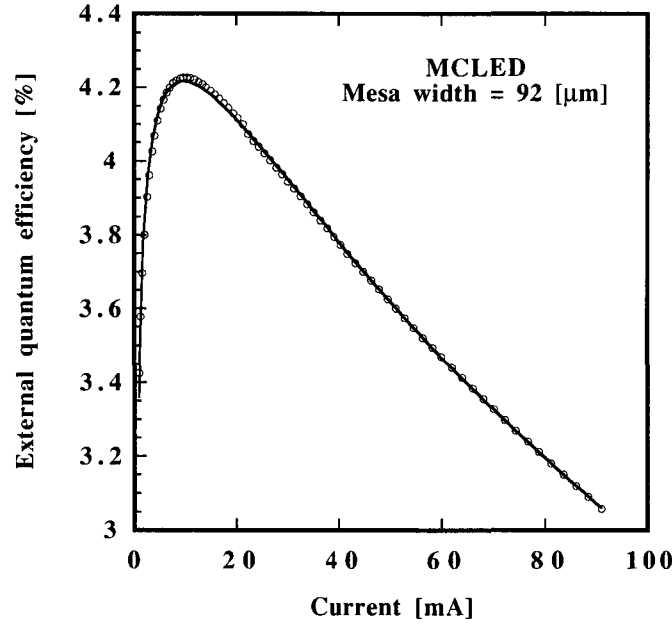


Figure 7.21: External quantum efficiency measured on a MCLED device (mesa width is 92 [μm]) and plotted versus the injected current (open circles). The solid line represents the result of the simple fitting model.

$$\eta_0(I) = \eta_i(I) \bar{\eta}_{sh}(I) \bar{\eta}(I) = \frac{\eta_0}{1 + \frac{I}{I_s}} \quad (7.40)$$

where  $\eta_0 = \eta_0(I = 0)$  and  $I_s$  are two constants. The function  $\eta_0(I)/\eta_0$  is close to one at very small current, and decreases with respect to  $I$ . The higher is  $I_s$  and the slower the function decreases. Figure 7.20 shows this behavior for  $\eta_0 = 1$  and for two different parameters  $I_{s1}$  and  $I_{s2} > I_{s1}$ . The product of  $\bar{\eta}_r(I)$  by  $\eta_0(I)$  gives the external quantum efficiency

$$\eta_{ex}(I) = \bar{\eta}_r(I) \eta_0(I) \quad (7.41)$$

which is displayed on the bottom part of figure 7.20. From this figure it appears that the higher are  $I_0$  and  $I_s$  and the higher is the current at which the roll-over on the external quantum efficiency curve occurs.

We have used the product of equation (7.39) by equation (7.40) to fit the experimental data on the LED and MCLED structures. Figure 7.21 shows that this simple model produces a good fit, with a small number of fitting parameters, which are  $\eta_0$ ,  $I_0$  and  $I_s$ .

Figure 7.22 displays values of the  $I_0$  parameter which were extracted from the fits as black (MCLED) and empty (LED) dots. These parameters are plotted versus the surfaces of the mesa. The surface dependence of the  $I_0$  parameter is explicitly given in equation (7.38) and was used to fit results displayed on figure 7.22. It appears that  $I_0$  increases continuously with respect to the mesa surface  $S_{mesa}$ . It

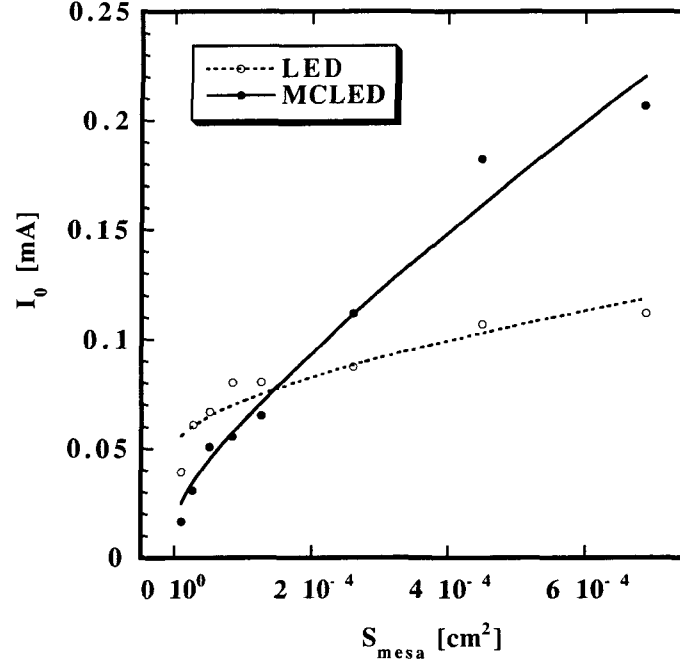


Figure 7.22: Values of the  $I_0$  parameter which were extracted from the fits of the external quantum efficiency are plotted as solid (MCLED) and open (LED) circles. The solid lines represent fits on  $I_0$ .

can be observed that if no surface recombinations are present, then  $I_0$  varies linearly with respect to  $S_{\text{mesa}}$ . On the contrary, if  $v_s$  is large enough, then  $I_0$  is independent on  $S_{\text{mesa}}$ . It is clear that  $I_0$  has to be as small as possible such that  $\bar{\eta}_r$  saturates rapidly towards one. This means that at constant current, a small device will have a higher radiative efficiency compared to a larger one. Because of the  $S_{\text{mesa}}$  dependence of equation (7.38), this is the contrary if one compares  $\bar{\eta}_r$  at a fixed current density (in this latter case the surface recombination rate decreases with the mesa's surface). For a given surface  $S_{\text{mesa}}$ ,  $I_0$  will be small if the bimolecular recombination coefficient  $B$  is high, the non-radiative recombination rate  $A_0$  small and the surface recombination velocity  $v_s$  small. In conclusion, for fixed parameters  $B$ ,  $v_s$ ,  $A_0$ ,  $\bar{\eta}_r(J)$  will shift towards small current densities and  $\bar{\eta}_r(I)$  will shift towards high currents as  $S_{\text{mesa}}$  will increase. From the fits performed on the data displayed on figure 7.22 we get:  $\frac{e e_{qw} A_0^2}{2B} = 22 [\text{mA}/\text{cm}^2]$  for the LED and  $\frac{e e_{qw} A_0^2}{2B} = 184 [\text{mA}/\text{cm}^2]$  for the MCLED. The ratio  $\frac{4v_s}{A_0}$  is equal to  $470 [\mu\text{m}]$  for the LED and  $84 [\mu\text{m}]$  for the MCLED. We will discuss these values in the last section of this chapter.

Figure 7.23 displays values of the  $I_s$  parameter which were extracted from the fits as solid (MCLED) and open (LED) circles. These parameters are plotted versus the surfaces of the mesa. We clearly observe on figure 7.23 that  $I_s$  increases with respect to  $S_{\text{mesa}}$ . It is reasonable to assume that the  $S_{\text{mesa}}$  dependence of this parameters comes only from the shadowing efficiency  $\bar{\eta}_{sh}$ . We indeed saw in section 7.3 that  $\bar{\eta}_{sh}$  decreases as the injected current increases because of current crowding (especially for the kind of contact geometry we have here).

Figure 7.24 shows the ratio of the unmasked surface of the mesa to its overall surface  $S_{\text{mesa}}$ ,



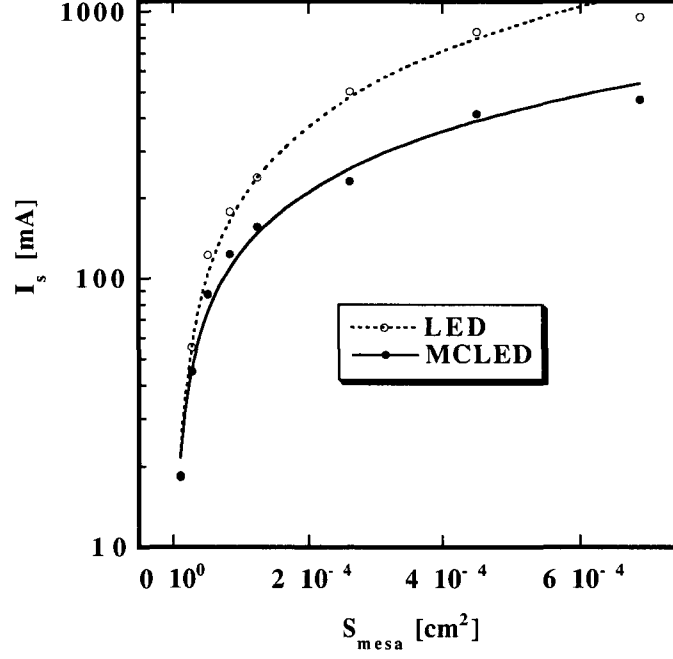


Figure 7.23: Values of the  $I_s$  parameter which were extracted from the fits of the external quantum efficiency are plotted as solid (MCLED) and open (LED) circles. The solid lines represent measurements interpolations by using power law.

plotted versus  $S_{\text{mesa}}$  for the 8 devices measured. One sees that  $S_{\text{open}}/S_{\text{mesa}}$  increases with  $S_{\text{mesa}}$ . The shadowing efficiency  $\bar{\eta}_{sh}$  is then expected to increase with  $S_{\text{mesa}}$ , which is what we observe on figure 7.23.

We observed that  $\eta_0(I)$  varies according to a dependence of the form  $\eta_0(I) = I_s^o S_{\text{mesa}}^k$ , where  $k < 1$  is a power and  $I_s^o$  is a constant. It follows that the higher  $S_{\text{mesa}}$ , the slower  $\eta_0(I)$  decreases with  $I$ . This is the contrary for the current density because  $k < 1$ . We can then conclude that increasing  $S_{\text{mesa}}$  shifts  $\bar{\eta}_r(I)$  and  $\eta_0(I)$  towards high current. Hence the current at which the roll-over on the external quantum efficiency curve is found, increases with the device size. This is what we experimentally observed on figures 7.18 and 7.19. This behavior goes into the opposite direction when current density is considered: the current density at which the roll-over on the external quantum efficiency curve is found, decreases as the device size increases.

Figure 7.25 displays values of the  $\eta_0$  parameter which were extracted from the fits as solid (MCLED) and open (LED) circles. These parameters are plotted versus the ratio of the unmasked surfaces of the mesas to their overall surfaces. It appears that  $\eta_0$  depends more or less linearly on  $S_{\text{openened}}/S_{\text{mesa}}$  which means that the masking of the mesa's surface by the grid contact has a significant effect on the size dependence. This is what we observed on the external quantum efficiency (figures 7.18 and 7.19).

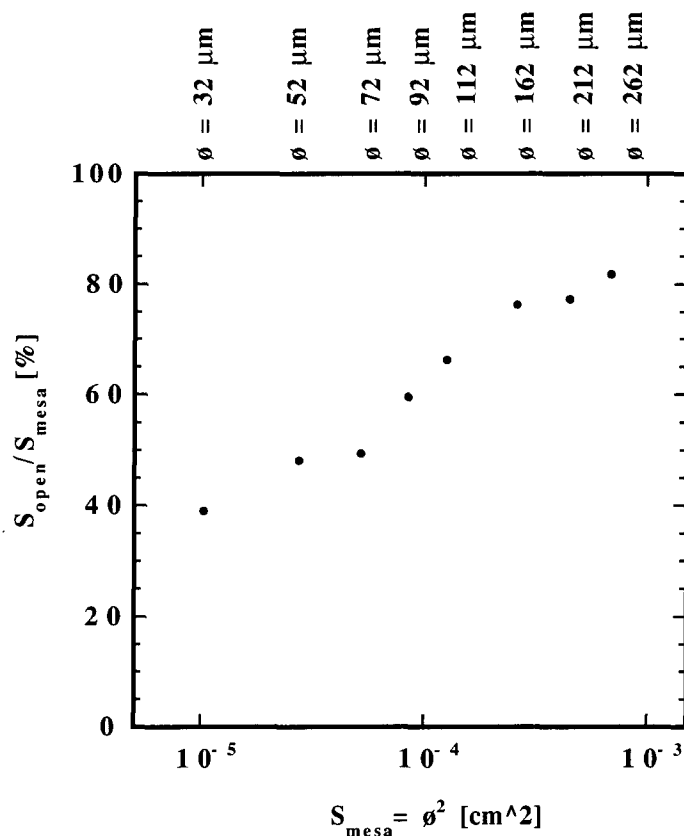


Figure 7.24: Masking coefficient plotted versus the surface of the mesa for the 8 measured structures.

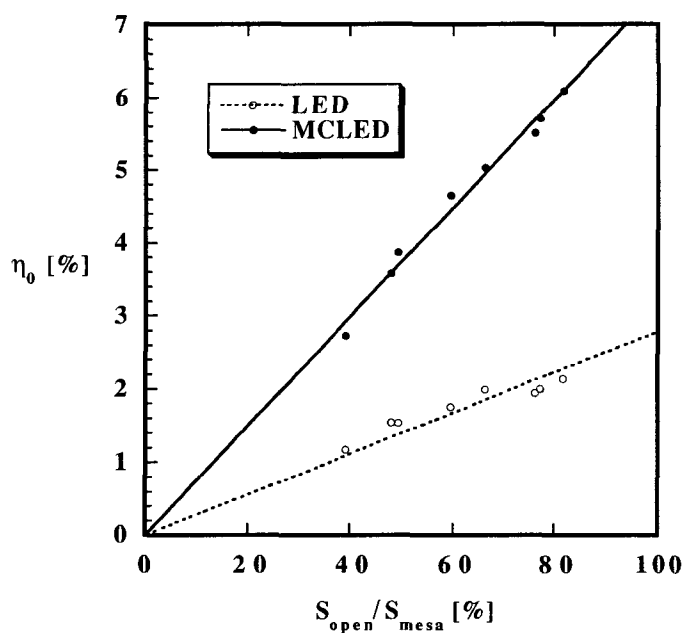


Figure 7.25: Values of the  $\eta_0$  parameter which were extracted from the fits of the external quantum efficiency are plotted as solid (MCLED) and open (LED) circles. The solid lines represent linear interpolations.

## 7.5 Conclusions

By using a model to describe the current dependence of the radiative efficiency we determined the parameters  $\frac{e e_{qw}}{2} \frac{A_0^2}{B}$  and  $\frac{4 v_s}{A_0}$  for both LED and MCLED. From these values it is possible to calculate  $I_0$ , hence the radiative efficiency (using equation (7.37)). For the device measured in section 7.2, we find that at a current density of  $55 [A/cm^2]$  (corresponding to the position of the roll-over on figure 7.7), the radiative efficiencies are  $\eta_r = 0.92$  for the LED and  $\eta_r = 0.90$  for the MCLED. This implies that the small apparent internal quantum efficiency which is found for the MCLED (and displayed on figure 7.7) is clearly not due to a bad material quality, as it could have been thought considering measured values of  $\frac{e e_{qw}}{2} \frac{A_0^2}{B}$  and  $\frac{4 v_s}{A_0}$ . We conclude then that the apparent internal quantum efficiency is limited by the injection efficiency in the MCLED.

The problem is probably due to a poor confinement of the electrons in the active region, which leak outside of it. The problem of electron confinement in AlGaInP-based devices was studied many years ago: it was observed that in red-emitting lasers, the threshold current increased super-linearly with temperature and that the external differential efficiency (above threshold) decreased with increasing temperature [52], [134]. This behavior is supposedly due to the small conduction-band discontinuity inherent in the AlGaInP material system (see appendix B). Leakage of electrons thermally activated from the active region through X-band of the p-cladding layer [21], [142] was proposed to explain the poor characteristics of red-laser, and was experimentally confirmed by references [160], [159]. The large difference of internal quantum efficiency between LED and MCLED is probably due to the difference in the active regions designs and especially to the presence of the AlGaAs-based DBR in the MCLED.



## Chapter 8

# Conclusion

The purpose of this work was to design and fabricate high efficiency MCLEDs emitting at 650 nm. These structures offer a number of advantages over conventional LEDs such as improved directionality, high spectral purity and enhanced extraction efficiency. They can compete with VCSELs for short and medium distance ( $< 5\text{ km}$ ) optical fiber communication systems because of their higher reliability, lower cost, simplicity of fabrication and thresholdless operation. Since red-emitting VCSELs are difficult to fabricate, MCLEDs are a viable alternative light source for local area network applications, where either silica or plastic optical fibers are used. Furthermore, red emitting MCLEDs have potential applications in printing, distance measurements, gas sensing or as densely packed arrays for monochromatic displays.

The first part of this work was devoted to the study of the optical properties of top-emitting MCLEDs (based on two DBRs). We found that the ultimate limit for the extraction efficiency is set by the DBR properties. If we assume an infinite number of pairs for both DBRs, and a monochromatic linewidth, the maximum extraction efficiency is roughly equal to three times the inverse of the effective cavity order, whose value is only determined in this case by the refractive indexes of the DBR layers. A limit value close to 11 was found for AlGaAs/AlAs based DBRs, leading to an ultimate efficiency of  $3/11 \approx 27\%$ . Hence, in order to significantly improve the extraction efficiency of this kind of structure, it is absolutely necessary to change the DBR materials. This task is difficult, because the DBR layers must have a good refractive index contrast, a reasonable conductivity, a small absorption and be lattice-matched to the rest of the structure. It was shown in this work that extraction efficiencies of 11% could be obtained and it is reasonably possible to reach 15% to 20% by finely optimizing the number of DBR pairs, reducing the absorption of the GaAs cap layer, improving the detuning, limiting the spectral broadening or encapsulating the structure in epoxy. If bottom emission can be considered, then transparent substrate structures based on metallic mirrors as top contact can be a good candidate for improved extraction efficiency. The cost of this solution is the requirement of complex wafer bonding techniques to replace the GaAs absorbant substrates by GaP ones.

In the second part of this work we showed that the apparent quantum efficient of the MCLEDs was only of 40%. This value is quite low, and we tried to separate the different physical mechanisms influencing the external quantum efficiency. It was first shown that depending on the geometry of

the grid contact, current crowding effects could severely decrease the external quantum efficiency. It was demonstrated that, by carefully designing the top contact geometry, an improvement of 20% of the external quantum efficiency could be obtained in comparison with a non-optimized contact. The optimal geometry is a trade-off between strong interconnection of the contact stripes (allowing a good current spreading), and a large distance between each of them (so as to minimize the masking of the emitting surface). A alternate approach could be to use selective oxidation so as to avoid current injection at the edges of the mesa and emission of light below the lateral contacts. With this solution, shadowing efficiencies higher than 95% can be expected. Going deeper in the study of the apparent internal quantum efficiency we investigated the effect of the diode sizes on the external quantum efficiency. From a simple model, we found out that the radiative efficiency was good and that the low apparent internal quantum efficiency measured on the MCLED was due to a bad current injection, and especially to electron leakage current. This problem is known from a long time in the red laser community, but at that time no satisfactory solution exist since the problem is mainly material related (weak electron confinement due to small bandgap energy difference between the active and the p-type cladding layers and high p-doping difficult to achieve). It appears that a factor of two could be obtained by improving the electron confinement of these structures. In conclusion, it appears that external quantum efficiencies higher than 15% can be reasonably expected at this wavelength from top-emitting planar MCLEDs, so three times that of the devices measured during this work. Nevertheless, the current generation of red MCLEDs have become a commercially viable option for plastic optical fiber systems [146].

## Appendix A

# Analytical approximations on DBR complex reflectivity.

In this appendix we want to calculate the complex reflection and transmission coefficients ( $r_N$  and  $t_N$ ) of the structure given on figure A.1.

The number  $N$  corresponds to the number of layers of index  $n_1$  and we define  $n = n_2/n_1$ . The input and output fields are related by:

$$\begin{bmatrix} E_2^+ \\ E_2^- \end{bmatrix} = \begin{bmatrix} r_{11}^N & r_{12}^N \\ r_{21}^N & r_{22}^N \end{bmatrix} \begin{bmatrix} E_1^+ \\ E_1^- \end{bmatrix}. \quad (\text{A.1})$$

The reflectivity coefficient is given by:

$$r_N = -\frac{r_{21}^N}{r_{22}^N} = \frac{r_{12}^N}{r_{22}^N} = |r_N| e^{i\varphi_N} \quad (\text{A.2})$$

In order to explicitly give the expressions of  $|r_N|$  and  $e^{i\varphi_N}$ , we will use the formalism presented in 2. For that purpose we need to diagonalize the transfer matrix  $[m]$  associated with one period of the structure (see figure A.2).

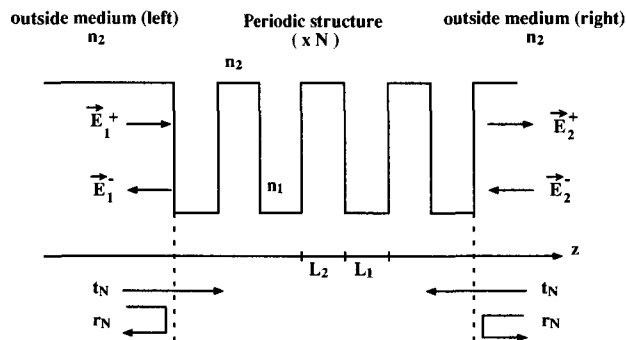


Figure A.1: Symmetrical Distributed Bragg Reflector: definitions.

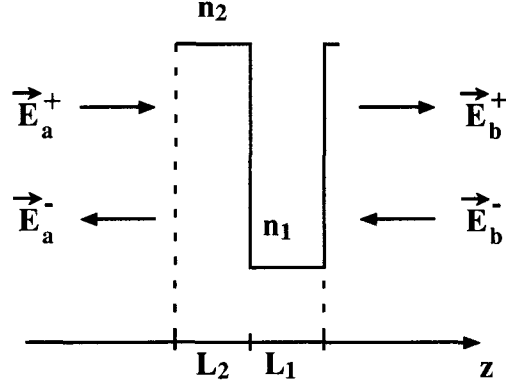


Figure A.2: One period of a symmetrical Distributed Bragg Reflector: definitions.

We examine the case of the TE polarization only, since we are interested in approximations around the normal incidence.

Using matrices given in section 2.1, it is easy to show that

$$\begin{bmatrix} E_b^+ \\ E_b^- \end{bmatrix} = [m] \begin{bmatrix} E_a^+ \\ E_a^- \end{bmatrix} \quad (\text{A.3})$$

with

$$[m] = \begin{bmatrix} m_{11} & m_{12} \\ m_{12}^* & m_{11}^* \end{bmatrix} \quad (\text{A.4})$$

where

$$m_{11} = A e^{iu} - B e^{-iv} \quad m_{12} = C [e^{-iu} - e^{iv}] \quad (\text{A.5})$$

with

$$A = \frac{(n\gamma_{z2} + \gamma_{z1})^2}{4n\gamma_{z1}\gamma_{z2}} \quad B = \frac{(n\gamma_{z2} - \gamma_{z1})^2}{4n\gamma_{z1}\gamma_{z2}} \quad C = \frac{n^2\gamma_{z2}^2 - \gamma_{z1}^2}{4n\gamma_{z1}\gamma_{z2}} \quad (\text{A.6})$$

and

$$u = \frac{\pi}{2} \delta(\gamma_{z1} + \gamma_{z2}) \quad v = \frac{\pi}{2} \delta(\gamma_{z1} - \gamma_{z2}) \\ \gamma_{z1} = \frac{\vec{k}_1 \cdot \vec{e}_z}{|\vec{k}_1|} = \cos(\theta_1) \quad \gamma_{z2} = \frac{\vec{k}_2 \cdot \vec{e}_z}{|\vec{k}_2|} = \cos(\theta_2). \quad (\text{A.7})$$



The reflection coefficient  $r_N$  depends on the wavelength via the  $\delta = \frac{\lambda}{\lambda_0}$  parameter, where  $\lambda_0$  is the Bragg wavelength defined by  $\lambda_0 = 4 L_1 n_1 = 4 L_2 n_2$ , and  $\lambda$  is the wavelength to be considered. The angular dependence is held in the coefficients  $\gamma_{zi}$  which appear in the calculation of  $r_N$  with  $i$  being an index running over the different dielectrics which make the structure. Since there are two different angles  $\theta_1$  and  $\theta_2$  in the structure, it is convenient to define an observation angle  $\theta_0$  and an observation index  $n_0$ , in such a way that we express all the angles with respect to  $\theta_0$  and  $n_0$ . We use the Snell's law for that purpose:

$$\gamma_{zi} = \frac{1}{n_i} \sqrt{n_i^2 - n_0^2 + n_0^2 \cos^2(\theta_0)}. \quad (\text{A.8})$$

In what follows we will consider that  $n_i \geq n_0$ , then  $\gamma_{zi}$  will always be real for  $\theta_0 \in [0, \pi/2]$ . Using the relations given in section 2.1, we find that

$$r_N = \frac{m_{12} \Phi(N)}{\Phi(N+1) - m_{11} \Phi(N)} = \frac{|K_1| e^{i\chi_1}}{|K_2| e^{i\chi_2}} \quad (\text{A.9})$$

where

$$\Phi(N) = \zeta^N - \zeta^{-N}. \quad (\text{A.10})$$

It is possible to show that  $\zeta$  is purely real in the stopband, which means that we can always define the real number  $\psi$  as  $\zeta = e^\psi$ . We have then  $\Phi(N) = 2 \sinh(\psi N)$  real.

We want to calculate  $D_\theta^N$  and  $D_\delta^N$  with

$$D_\theta^N = \left. \frac{d\varphi_N}{d \cos \theta_0} \right|_{(\delta=1, \theta_0=0)} \quad (\text{A.11})$$

and

$$D_\delta^N = \left. \frac{d\varphi_N}{d\delta} \right|_{(\delta=1, \theta_0=0)}. \quad (\text{A.12})$$

We calculate that at the center of the stopband we have:

$$\begin{aligned} u(\delta=1, \theta_0=0) &= \pi \\ v(\delta=1, \theta_0=0) &= 0 \\ A(\delta=1, \theta_0=0) &= \frac{(n+1)^2}{4n} \\ B(\delta=1, \theta_0=0) &= \frac{(n-1)^2}{4n} \\ C(\delta=1, \theta_0=0) &= \frac{n^2-1}{4n}. \end{aligned} \quad (\text{A.13})$$

We introduce the variable  $x$  which designs either  $\cos(\theta_0)$  or  $\delta$ . It is simple to find that:

$$\left. \frac{d\varphi_N}{dx} \right|_{(\delta=1, \theta_0=0)} = \left[ \frac{d\chi_1}{dx} - \frac{d\chi_2}{dx} \right]_{(\delta=1, \theta_0=0)} \quad (\text{A.14})$$

$$= \left[ \frac{1}{1 + \tan(\chi_1)^2} \frac{d \tan(\chi_1)}{dx} - \frac{1}{1 + \tan(\chi_2)^2} \frac{d \tan(\chi_2)}{dx} \right]_{(\delta=1, \theta_0=0)}. \quad (\text{A.15})$$

After simple calculations we have,

$$\tan(\chi_1) = -\frac{\sin u + \sin v}{\cos u - \cos v} \quad (\text{A.16})$$

from which we get:

$$\left. \frac{1}{1 + \tan(\chi_1)^2} \frac{d \tan(\chi_1)}{dx} \right|_{(\delta=1, \theta_0=0)} = \begin{cases} \frac{\pi}{2} \delta \left( \frac{n_0}{n_2} \right)^2 & \text{if } x = \cos \theta_0 \\ \frac{\pi}{2} & \text{if } x = \delta. \end{cases} \quad (\text{A.17})$$

In the same way:

$$\tan(\chi_2) = -\frac{XY}{Z} \quad (\text{A.18})$$

where  $X = \tanh(\psi N)$ ,  $Y = A \sin(u) + B \sin(v)$  and  $Z = \sinh(\psi)$ .

We can easily check that  $Y(\delta = 1, \theta_0 = 0) = 0$ , then:

$$\left. \frac{1}{1 + \tan(\chi_2)^2} \frac{d \tan(\chi_2)}{dx} \right|_{(\delta=1, \theta_0=0)} = - \left[ \frac{X}{Z} \frac{dY}{dx} \right]_{(\delta=1, \theta_0=0)}. \quad (\text{A.19})$$

From equation (A.9), we can verify that

$$|r_N(\delta = 1, \theta_0 = 0)| \equiv r_N^0 = -2C \left[ \frac{X}{Z} \right]_{(\delta=1, \theta_0=0)} = \frac{n^{2N} - 1}{n^{2N} + 1}. \quad (\text{A.20})$$

After some long but not difficult manipulations we finally get:

$$\left. \frac{d\varphi_N}{d\delta} \right|_{(\delta=1, \theta_0=0)} = \frac{\pi}{2} \left[ \left( \frac{n+1}{n-1} \right) r_N^0 - 1 \right] \equiv D_\delta^N \quad (\text{A.21})$$

$$\left. \frac{d\varphi_N}{d \cos \theta_0} \right|_{(\delta=1, \theta_0=0)} = \frac{\pi}{2} \tilde{n}^2 \left[ \left( \frac{2n^2 - n + 1}{n - 1} \right) r_N^0 - 1 \right] \equiv D_\theta^N. \quad (\text{A.22})$$

If we consider the case where  $\delta$  can vary and where the angle is fixed to zero (normal incidence), then we have  $u = \pi\delta$  and  $v = 0$ . It is clear from previous relations that  $r_N$  depends on  $\delta$  via the terms  $e^{\pm iu}$ . This means that the properties of  $r_N$  are unchanged if we add a multiple of  $2\pi$  to  $u$ , then

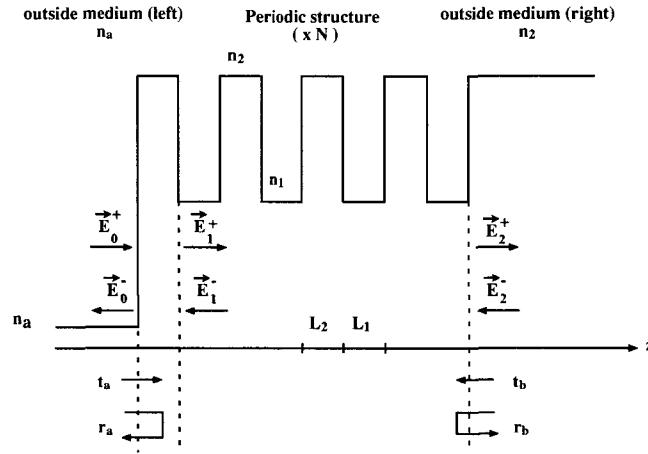


Figure A.3: Asymmetrical Distributed Bragg Reflector: definitions.

$u = \pi \delta + 2 \pi p = \pi \bar{\delta}$  where  $\bar{\delta} = \delta + 2p$  and  $p$  is an integer. We see that  $r_N$  is periodic with respect to  $\delta$ , 2 being the period.

From the previous calculations it is rather easy to determine the properties of the structure given on figure A.3.

With the phasors definitions given on the figure A.3, we have the following matrix relations:

$$\begin{bmatrix} E_2^+ \\ E_2^- \end{bmatrix} = \begin{bmatrix} p_{11} & p_{12} \\ p_{21} & p_{22} \end{bmatrix} \begin{bmatrix} E_0^+ \\ E_0^- \end{bmatrix} \quad (\text{A.23})$$

and

$$\begin{bmatrix} E_2^+ \\ E_2^- \end{bmatrix} = \begin{bmatrix} r_{11}^N & r_{12}^N \\ r_{21}^N & r_{22}^N \end{bmatrix} \begin{bmatrix} E_1^+ \\ E_1^- \end{bmatrix}. \quad (\text{A.24})$$

Using the relations given previously for the symmetrical DBR, we have:

$$r_N = \frac{m_{12} \Phi(N)}{\Phi(N+1) - m_{11} \Phi(N)} = \frac{|K_1| e^{i\chi_1}}{|K_2| e^{i\chi_2}} = |r_N| e^{i(\chi_1 - \chi_2)} = |r_N| e^{i\varphi_N} \quad (\text{A.25})$$

$$t_N = \frac{\Phi(1)}{\Phi(N+1) - m_{11} \Phi(N)} e^{-i\gamma} = \frac{\Phi(1) r_N}{\Phi(N) m_{12}} e^{-i\gamma} \quad (\text{A.26})$$

where  $\gamma = \frac{\pi}{2} \gamma_{z2} \delta$  and  $\delta = \frac{\lambda}{\lambda_0}$ .

As we know that:

$$m_{12} = -2C \sin\left(\frac{\pi}{2} \delta \gamma_{z1}\right) e^{i\left(-\frac{\pi}{2} \delta \gamma_{z2} + \frac{\pi}{2}\right)} \quad (\text{A.27})$$

where  $C$  is real, we finally find that:

$$t_N = |t_N| e^{i(\varphi_N + \frac{\pi}{2})}. \quad (\text{A.28})$$

From this result we get that  $(r_N)^2 - (t_N)^2 = e^{2i\varphi_N}$ , which is used to finally find the expressions given below:

$$r_b = \frac{p_{12}}{p_{22}} = \frac{\alpha |r_N| - \beta e^{i(2\gamma + \varphi_N)}}{\alpha - \beta |r_N| e^{i(2\gamma + \varphi_N)}} e^{i\varphi_N} \quad (\text{A.29})$$

$$r_a = -\frac{p_{21}}{p_{22}} = \frac{\alpha |r_N| e^{i(2\gamma + \varphi_N)} - \beta}{\alpha - \beta |r_N| e^{i(2\gamma + \varphi_N)}} \quad (\text{A.30})$$

$$t_b = \frac{1}{p_{22}} = \frac{|t_N| e^{i(\gamma + \varphi_N + \frac{\pi}{2})}}{\alpha - \beta |r_N| e^{i(2\gamma + \varphi_N)}} e^{i\varphi_N} \quad (\text{A.31})$$

$$t_a = \frac{k_{za}}{k_{z2}} t_b. \quad (\text{A.32})$$

We can now calculate the first derivative of the reflection and transmission coefficients phases with respect to a parameter that we call  $x$ , which will correspond to either  $\delta$  or  $\cos(\theta_0)$ .

We set:

$$r_a = \frac{|\chi_a^1| e^{i\varphi_a^1}}{|\chi_a^2| e^{i\varphi_a^2}} = |r_a| e^{i\varphi_a} \quad (\text{A.33})$$

from which it is simple to calculate that:

$$\tan(\varphi_a^1) = \frac{\alpha |r_N| \sin(\Omega)}{\alpha |r_N| \cos(\Omega) - \beta} \quad (\text{A.34})$$

$$\tan(\varphi_a^2) = \frac{-\beta |r_N| \sin(\Omega)}{\alpha - \beta |r_N| \cos(\Omega)} \quad (\text{A.35})$$

with  $\Omega = 2\gamma + \varphi_N$ . Derivating the  $\tan$  function with respect to  $x$ , we have:

$$\frac{d\varphi_a}{dx} = \frac{1}{1 + (\tan \varphi_a)^2} \frac{d \tan(\varphi_a)}{dx} \quad (\text{A.36})$$

and

$$\frac{d \tan(\varphi_a)}{d x} = \frac{[1 + (\tan \varphi_a^1)^2] [1 + (\tan \varphi_a^2)^2]}{[1 + \tan(\varphi_a^1 \varphi_a^2)]^2} \frac{1}{1 + (\tan \varphi_a)^2} \left[ \frac{d \varphi_a^1}{d x} - \frac{d \varphi_a^2}{d x} \right]. \quad (\text{A.37})$$

Since  $\Omega(\delta = 1, \theta_0 = 0) = \pi$ , we have  $\tan(\varphi_a^1) = \tan(\varphi_a^2) = \tan(\varphi_a) = 0$  and it follows that:

$$\left. \frac{d \varphi_a}{d x} \right|_{(\delta=1, \theta_0=0)} = \left[ \frac{d \varphi_a^1}{d x} - \frac{d \varphi_a^2}{d x} \right]_{(\delta=1, \theta_0=0)}. \quad (\text{A.38})$$

After tedious but not difficult manipulations we finally get:

$$\left. \frac{d \varphi_a}{d x} \right|_{(\delta=1, \theta_0=0)} = \frac{(\alpha^2 - \beta^2) |r_N|}{[\alpha |r_N| + \beta] [\alpha + \beta |r_N|]} \left[ \frac{d \varphi_N}{d x} + 2 \frac{d \gamma}{d x} \right]_{(\delta=1, \theta_0=0)} \quad (\text{A.39})$$

and

$$\begin{aligned} \left. \frac{d \varphi_b}{d x} \right|_{(\delta=1, \theta_0=0)} &= \frac{2 \alpha \beta + (\alpha^2 + \beta^2) |r_N|}{[\alpha |r_N| + \beta] [\alpha + \beta |r_N|]} \left. \frac{d \varphi_N}{d x} \right|_{(\delta=1, \theta_0=0)} \\ &+ \frac{2 \alpha \beta [1 - |r_N|^2]}{[\alpha |r_N| + \beta] [\alpha + \beta |r_N|]} \left. \frac{d \gamma}{d x} \right|_{(\delta=1, \theta_0=0)}. \end{aligned} \quad (\text{A.40})$$

It is obvious from equations (A.29) and (A.30) that  $r_a$  and  $r_b$  are periodic with respect to  $\delta$  (at normal incidence),  $2p$  ( $p$  integer) being the period.



## Appendix B

# Material Parameters

Note that all the parameters which are given in this section were measured at a temperature of 300 K, and that  $(Al_xGa_{1-x})_{0.5}In_{0.5}P$  compounds were assumed to be in their disordered phase.

### B.1 Indices of refraction

The refractive indices of  $Al_xGa_{1-x}As$  and  $(Al_xGa_{1-x})_{0.5}In_{0.5}P$  compounds which were used in our numerical simulations are presented in this section. For  $Al_xGa_{1-x}As$  compounds, the experimental values given in reference [3] were used. Figure B.1 shows the real part of the index of refraction (left axis) and its imaginary part on the right axis. Analytical expressions based on a single oscillator model can be found in reference [5].

For  $(Al_xGa_{1-x})_{0.5}In_{0.5}P$  compounds, the experimental data of reference [110] were used. An analytical model is used in this reference to fit the experimental data. The absorption due to phonons is described by a single delta-shaped oscillator with the frequency of the TO phonon. The fundamental absorption edge is approximated by two oscillators at energies  $E_1$  and  $E_2$  and constant absorption between the bandgap  $E_g$  and  $E_1$ . The refractive index  $n(E)$  is then determined by applying the Kramers-Kronig relations:

$$n^2(E) - 1 = \frac{G_{TO}}{E_{TO}^2 - E^2} + \frac{A}{\pi} \ln \frac{E_1^2 - E^2}{E_g^2 - E^2} + \frac{G_1}{E_1^2 - E^2} + \frac{G_2}{E_2^2 - E^2} \quad (B.1)$$

where  $E$  is the energy in units of [eV] and:

$E_1(x) = 3.35 + 0.38x$ [eV]	Energetic position of oscillator 1
$E_2(x) = 5.20 + 0.35x$ [eV]	Energetic position of oscillator 2
$E_g(x) = 1.90 + 0.48x$ [eV]	Bandgap energy
$A(x) = 0.72 + 0.35x$	Dispersion relation
$G_{TO} = 4.4 \cdot 10^{-3}$ [eV <sup>2</sup> ]	Oscillator strength of the TO phonons
$G_1 = 34.7$ [eV <sup>2</sup> ]	Oscillator strength of oscillator at $E_1$
$G_2 = 140$ [eV <sup>2</sup> ]	Oscillator strength of oscillator at $E_2$
$E_{TO} = 40$ [meV]	Energetic position of the TO phonons.

Note that this description of  $n(E)$  is reasonable only below the band edge. The bandgap resonance was numerically smoothed out in figure B.2. Reference [150] presents simpler analytical expressions for this refractive index.

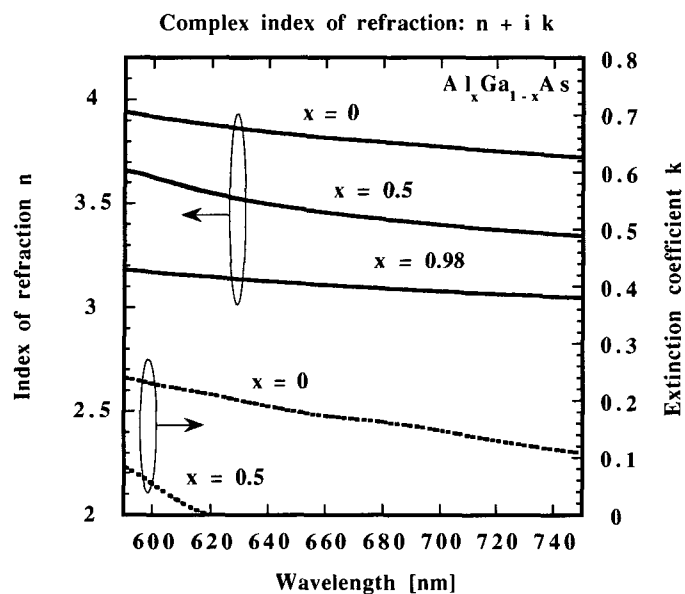


Figure B.1: Real (left axis) and imaginary (right axis) parts of complex indices of refraction for  $Al_xGa_{1-x}As$  compounds.

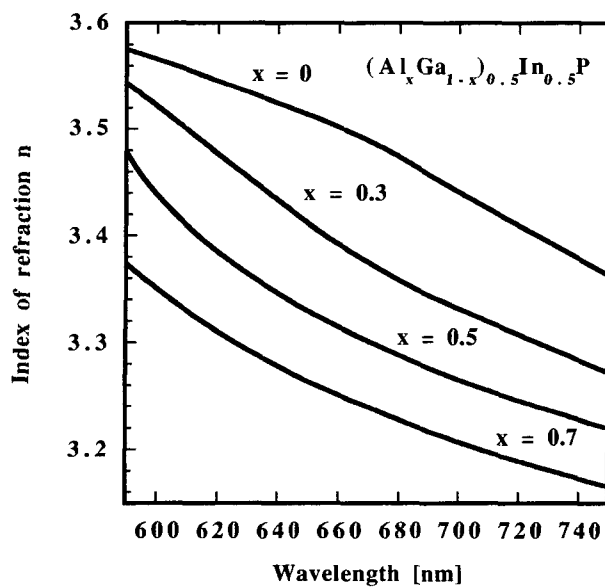


Figure B.2: Refractive indices of  $(Al_xGa_{1-x})_{0.5}In_{0.5}P$  compounds.



## B.2 Lattice constants

The lattice constants  $a$  of the binary III-V compounds are given in the table below [89]:

	GaP	InP	AlP	GaAs	AlAs
$a$ [nm]	0.5451	0.5869	0.5451	0.5653	0.5660

In ternary III-V solid solutions, the lattice constant of the crystal generally scales linearly with composition (Vegard's law), and this behavior can be reasonably assumed to occur also for the quaternary solutions [23].

The lattice constant  $a(x)$  of  $Ga_xIn_{1-x}P$  is then given by:

$$a(x) = a(InP) + x[a(GaP) - a(InP)] \quad (B.2)$$

showing that  $Ga_xIn_{1-x}P$  can be grown lattice matched on  $GaAs$  substrates for a composition  $x = 0.52$ . Applying Vegard's law to  $Al_xIn_{1-x}P$ , one can see that  $Al_{0.52}In_{0.48}P$  and  $Ga_{0.52}In_{0.48}P$  have about the same lattice constant. It follows that  $(Al_xGa_{1-x})_{0.52}In_{0.48}P$  alloys can be grown lattice matched to  $GaAs$  substrates at all aluminium contents ( $x = 0..1$ ), which makes this quaternary compound very appealing for large bandgap heterostructure devices. Note that  $Ga_xIn_{1-x}P$  quantum wells are grown tensile strained with respect to  $(Al_xGa_{1-x})_{0.52}In_{0.48}$  when  $x > 0.52$ , and compressively strained when  $x < 0.52$  [27].

## B.3 Bandgap energy and band discontinuity

The bandgap energy  $E_g(x)$  of the ternary and quaternary compounds used in this work are given on the table below and are displayed on figure B.3. All the energies given in this section are expressed in units of [eV].

Material	$E_g(x)$		Reference
$Al_xGa_{1-x}As$	$E_g^\Gamma(x) = 1.424 + 1.155x + 0.37x^2$ $E_g^X(x) = 1.9 + 0.124x + 0.144x^2$	$x < 0.43$ $x > 0.43$	[94]
$Ga_xIn_{1-x}P$	$E_g^\Gamma(x) = 1.351 + 1.429x + 0.786(x^2 - x)$ $E_g^X(x) = 2.311 - 0.052x + 0.207(x^2 - x)$	$x < 0.73$ $x > 0.73$	[112]
$(Al_xGa_{1-x})_{0.52}In_{0.48}$	$E_g^\Gamma(x) = 1.9 + 0.61x$ $E_g^X(x) = 2.204 + 0.085x$	$x < 0.58$ $x > 0.58$	[106]

The band offset between  $(Al_xGa_{1-x})_{0.5}In_{0.5}P$  and  $Ga_{0.5}In_{0.5}P$  is given by [106]:

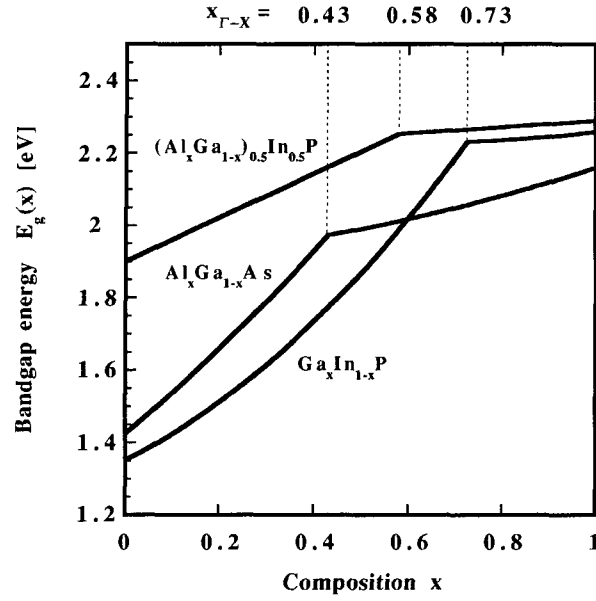


Figure B.3: Bandgap energies of  $(Al_xGa_{1-x})_{0.5}In_{0.5}P$  and  $Al_xGa_{1-x}As$  compounds.

$E_c^\Gamma((Al_xGa_{1-x})_{0.5}In_{0.5}P) - E_c^\Gamma(Ga_{0.5}In_{0.5}P)$	$0.547x - 0.157x^2$	$x < 0.58$
$E_c^X((Al_xGa_{1-x})_{0.5}In_{0.5}P) - E_c^X(Ga_{0.5}In_{0.5}P)$	$0.304 + 0.022x - 0.157x^2$	$x > 0.58$
$E_v((Al_xGa_{1-x})_{0.5}In_{0.5}P) - E_v(Ga_{0.5}In_{0.5}P)$	$-0.063x - 0.157x^2$	

The band offset between  $Ga_{0.5}In_{0.5}P$  and  $GaAs$  is given by [45]:

$E_c(Ga_{0.5}In_{0.5}P) - E_c(GaAs)$	0.12
$E_v(Ga_{0.5}In_{0.5}P) - E_v(GaAs)$	-0.37

The band offset between  $Al_xGa_{1-x}As$  and  $GaAs$  is given by [45]:

$E_c^\Gamma(Al_xGa_{1-x}As) - E_c^\Gamma(GaAs)$	$0.695x + 0.37x^2$	$x < 0.43$
$E_c^X(Al_xGa_{1-x}As) - E_c^X(GaAs)$	$0.476 - 0.336x + 0.14x^2$	$x > 0.43$
$E_v(Al_xGa_{1-x}As) - E_v(GaAs)$	$-0.46x$	

Composition dependence of conduction and valence band offsets in lattice-matched  $(Al_xGa_{1-x})_{0.5}In_{0.5}P/Ga_{0.5}In_{0.5}P$  heterostructures, compared to those in  $Al_xGa_{1-x}As/GaAs$  heterostructures is displayed on figure B.4.

Some more information concerning the characterization of  $(Al_xGa_{1-x})_{0.5}In_{0.5}P$  band structure can

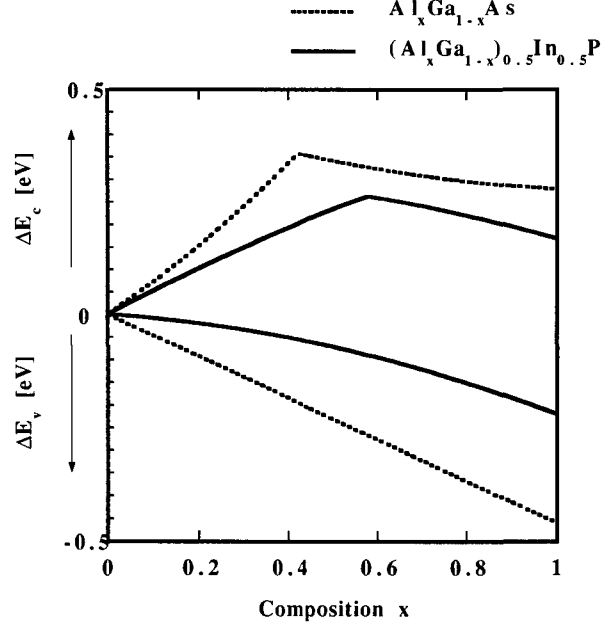


Figure B.4: Conduction and valence band offsets in  $(Al_xGa_{1-x})_{0.5}In_{0.5}P/Ga_{0.5}In_{0.5}P$  (solid line) and  $Al_xGa_{1-x}As/GaAs$  heterostructures (dotted line).

be found in the following references: [112], [119], [6], [4], [111], [34], [123], [69]. Discussion of interpolation techniques between binary, ternary and quaternary compounds is presented in [86]. For some more information concerning band-offset determination, the reader is referred to the references [78], [33], [125], [121], [45], [25], [95], [83], [163].

## B.4 Effective masses

Effective masses of  $Al_xGa_{1-x}As$  compounds given in reference [94] are presented below.

$Al_xGa_{1-x}As$		
Electrons	Effective mass of density of states	Conductivity effective mass
$\Gamma$ valley	$m_{\Gamma} = (0.063 + 0.083 x) m_0$	$m_{cc} = m_{\Gamma}$
L valley	$m_L = (0.56 + 0.1 x) m_0$	$m_{cc} = (0.11 + 0.03 x) m_0$
X valley	$m_X = (0.85 - 0.14 x) m_0$	$m_{cc} = 0.26 m_0$

$Al_xGa_{1-x}As$	
Holes	Effective mass
Heavy holes	$m_h = (0.51 + 0.25 x) m_0$
Light holes	$m_l = (0.082 + 0.068 x) m_0$
Split-off	$m_{so} = (0.15 + 0.09 x) m_0$

Effective masses for the density of state of  $(Al_xGa_{1-x})_{0.5}In_{0.5}P$  compounds are given in the table below.

	$Ga_{0.5}In_{0.5}P$ [95]	$(Al_{0.6}Ga_{0.4})_{0.5}In_{0.5}P$ [95]	$(Al_xGa_{1-x})_{0.5}In_{0.5}P$
Electrons	$0.105 m_0$	$0.11 m_0$	$(0.092 + 0.146 x) m_0$ [124]
Light holes	$0.14 m_0$	$0.15 m_0$	$(0.62 + 0.05 x) m_0$ [52]
Heavy holes	$0.48 m_0$	$0.51 m_0$	
Split-off	$0.226 m_0$	$0.244 m_0$	

# Bibliography

- [1] I. Abram, I. Robert, and R. Kuszelewicz. Spontaneous Emission Control in Semiconductor Microcavities with Metallic or Bragg Mirrors. *IEEE J. Quantum Electron.*, 34(1):71–76, 1998.
- [2] M. Abramowitz and I. A. Stegun. *Handbook of Mathematical functions*. Dover Publications, New York, 1972.
- [3] S. Adachi. *Properties of aluminium gallium arsenide*. INSPEC, London, 1993.
- [4] S. Adachi, S. Ozaki, M. Sato, and K. Ohtsuka. Electroreflectance Study of  $(Al_xGa_{1-x})_{0.5}In_{0.5}P$  Alloys. *Jpn. J. Appl. Phys.*, 35(2):537–542, 1996.
- [5] M. A. Afromowitz. Refractive Index of  $Ga_{1-x}Al_xAs$ . *Solid. State Commun.*, 15:59–63, 1974.
- [6] C. Alibert, G. Bordure, A. Laugier, and J. Chevallier. Electroreflectance and Band Structure of  $Ga_xIn_{1-x}P$  Alloys. *Phys. Rev. B*, 6(4):1301–1310, 1972.
- [7] Y. H. Aliyu, D. V. Morgan, H. Thomas, and S. W. Bland. AlGaInP LEDs using reactive thermally evaporated transparent conducting indium tin oxide (ITO). *Electron. Lett.*, 31(25):2210–2212, 1995.
- [8] D. I. Babic and S. W. Corzine. Analytic Expressions for the Reflection Delay, Penetration Depth, and Absorbance of Quarter-Wave Dielectric Mirrors. *IEEE J. Quantum Electron.*, 28(2):514–524, 1992.
- [9] R. Baets, P. Bienstman, and R. Bockstaele. Basics of dipole emission from a planar cavity. In H. Benisty, J. M. Gérard, R. Houdré, J. Rarity, and C. Weisbuch, editors, *Confined Photons Systems*, Lecture Notes in Physics, pages 38–79. Springer, Berlin, 1999.
- [10] G. Bastard. *Waves mechanics applied to semiconductor heterostructures*. Halsted Press, New York, 1988.
- [11] P. K. Basu. *Theory of optical processes in semiconductors*. Oxford Science Publications, Oxford, 1997.
- [12] H. Benisty, H. De Neve, and C. Weisbuch. Impact of Planar Microcavity Effects on Light Extraction - Part II: Selected Exact Simulations and Role of Photon Recycling. *IEEE J. Quantum Electron.*, 34(9):1632–1643, 1998.

- [13] H. Benisty, H. De Neve, and C. Weisbuch. Impact of Planar Microcavity Effects on Light Extraction - Part I: Basic Concepts and Analytical Trends. *IEEE J. Quantum Electron.*, 34(9):1612–1631, 1998.
- [14] H. Benisty, R. Stanley, and M. Mayer. Method of source terms for dipole emission modification in modes of arbitrary planar structures. *J. Opt. Soc. Amer. A*, 15(5):1192–1201, 1998.
- [15] H. H. Berger. Models for contacts to planar devices. *Solid-State Electronics*, 15:145–158, 1972.
- [16] G. Björk. On the Spontaneous Lifetime Change in an Ideal Planar Microcavity-Transition from a Mode Continuum to Quantized Modes. *IEEE J. Quantum Electron.*, 30(10):2314–2318, 1994.
- [17] G. Björk, S. Machida, Y. Yamamoto, and K. Igeta. Modification of spontaneous emission rate in planar dielectric microcavity structures. *Phys. Rev. A*, 44(1):669–681, 1991.
- [18] J. Blondelle, H. De Neve, P. Demeester, P. Van Daele, G. Borghs, and R. Baets. 16 % external quantum efficiency from planar microcavity LEDs at 940 nm by precise matching of cavity wavelength. *Electron. Lett.*, 31(15):1286–1288, 1995.
- [19] M. Born and E. Wolf. *Principles of Optics*. Pergamon Press, London, 1959.
- [20] J. A. Borsuk. Light intensity Profiles of Surface-Emitting InGaAsP LED's: Impact on Coupling to Optical Fibers. *IEEE Trans. Electron. Devices*, 30(4):296–303, 1983.
- [21] D. P. Bour, D. W. Treat, R. L. Thornton, R. S. Geels, and D. F. Welch. Drift Leakage Current in AlGaInP Quantum-Well Lasers. *IEEE J. Quantum Electron.*, 29(5):1337–1342, 1993.
- [22] J. F. Carlin, P. Royo, R. P. Stanley, R. Houdré, J. Spicher, U. Oesterle, and M. Illegems. Design and characterization of top-emitting microcavity light-emitting diodes. *Semiconduct. Sci. Technol.*, 15:145–153, 2000.
- [23] H. C. Casey and M. B. Panish. *Heterostructure lasers*. Academic Press, Orlando, 1978.
- [24] S. J. Chang and C. S. Chang. AlGaInP-GaInP Compressively Strained Multiquantum-Well Light-Emitting Diodes for Polymer Fiber Application. *IEEE Photon. Technol. Lett.*, 10(6):772–774, 1998.
- [25] J. Chen, J. R. Sites, I. L. Spain, M. J. Hafich, and G. Y. Robinson. Band offset of  $GaAs/In_{0.48}Ga_{0.52}P$  measured under hydrostatic pressure. *Appl. Phys. Lett.*, 58(7):744–746, 1991.
- [26] W. C. Chew. *Waves and Fields in Inhomogeneous Media*. IEEE Press Series on Electromagnetic Waves, New York, 1995.

- [27] W. W. Chow, K. D. Choquette, M. H. Crawford, K. L. Lear, and G. R. Hadley. Design, Fabrication, and Performance of Infrared and Visible Vertical-Cavity Surface-Emitting Lasers. *IEEE J. Quantum Electron.*, 33(10):1810–1823, 1997.
- [28] W. W. Chow and S. W. Koch. *Semiconductor-Laser Fundamentals*. Springer, Berlin, 1999.
- [29] L. A. Coldren and S. W. Corzine. *Diode Lasers and Photonic Integrated Circuits*. John Wiley & Sons, New York, 1995.
- [30] J. J. Coleman. Metalorganic Chemical Vapor Deposition for Optoelectronic Devices. *Proc. of the IEEE*, 85(11):1715–1729, 1997.
- [31] M. G. Craford. Commercial light emitting diode technology: Status, trends, and possible future performance. In J. Rarity and C. Weisbuch, editors, *Microcavities and Photonic Bandgaps*, pages 323–331. Kluwer Academic Publishers, Netherlands, 1996.
- [32] M. G. Craford and F. Steranka. Light-emitting diodes. In *Encyclopedia of Applied Physics*, pages 485–514. VCH Publishers, New York, 1994.
- [33] M. D. Dawson and G. Duggan. Band-offset determination for GaInP-AlGaInP structures with compressively strained quantum well active layers. *Appl. Phys. Lett.*, 64(7):892–894, 1994.
- [34] M. C. DeLong, D. J. Mowbray, R. A. Hogg, M. S. Skolnick, J. E. Williams, K. Meehan, S. R. Kurtz, J. M. Olson, R. P. Schneider, M. C. Wu, and M. Hopkinson. Band gap of completely disordered  $Ga_{0.52}In_{0.48}P$ . *Appl. Phys. Lett.*, 66(23):3185–3187, 1995.
- [35] D. G. Deppe and C. Lei. Spontaneous emission from a dipole in a semiconductor microcavity. *J. Appl. Phys.*, 70(7):3443–3448, 1991.
- [36] C. Dill, R. P. Stanley, U. Oesterle, and M. Ilegems. 16.8% external quantum efficiency from a planar led. In *Part of the SPIE Conference on Light-Emitting Diodes: Research, Manufacturing and Applications III*, pages 160–169, 1999.
- [37] C. Dill, R. P. Stanley, U. Oesterle, D. Ochoa, and M. Ilegems. Effect of detuning on the angular emission pattern of high-efficiency microcavity light-emitting diodes. *Appl. Phys. Lett.*, 73(26):3812–3814, 1998.
- [38] M.A. Dupertuis, B. Acklin, and M. Proctor. Generalized energy balance and reciprocity relations for thin-films optics. *J. Opt. Soc. Amer. A*, 11(13):1167–1174, 1994.
- [39] M.A. Dupertuis, M. Proctor, and B. Acklin. Generalization of complex Snell-Descartes and Fresnel laws. *J. Opt. Soc. Amer. A*, 11(13):1159–1166, 1994.
- [40] A. K. Dutta. Prospects of Highly Efficient AlGaInP Based Surface Emitting Type Ring-LED for 50 and 156 Mb/s POF Data Link Systems. *IEEE J. Lightwave Technol.*, 16(1):106–113, 1998.

- [41] A. K. Dutta, A. Suzuki, K. Kurihara, F. Miyasaka, H. Hotta, and K. Sugita. High-Brightness, AlGaInP-Based, Visible Light-Emitting Diode for Efficient Coupling with POF. *IEEE Photon. Technol. Lett.*, 7(10):1134–1136, 1995.
- [42] A. K. Dutta, K. Ueda, K. Hara, and K. Kobayashi. High Brightness and Reliable AlGaInP-Based Light-Emitting Diode for POF Data Links. *IEEE Photon. Technol. Lett.*, 9(12):1567–1569, 1997.
- [43] A. Fiore, Y. A. Akulova, J. Ko, E. R. Hegblom, and L. A. Coldren. Postgrowth Tuning of Semiconductor Vertical Cavities for Multiple-Wavelength Laser Arrays. *IEEE J. Quantum Electron.*, 35(4):616–623, 1999.
- [44] R. M. Fletcher, C. P. Kuo, T. D. Osentowski, K. H. Huang, M. C. Craford, and V. M. Robbins. The Growth and Properties of High Performance AlGaInP Emitters Using a Lattice Mismatched GaP Window Layer. *Journal of Electronic Materials*, 20(12):1125–1130, 1991.
- [45] S. Froyen, A. Zunger, and A. Mascarenhas. Polarization fields and band offsets in GaInP/GaAs and ordered/disordered GaInP superlattices. *Appl. Phys. Lett.*, 68(20):2852–2854, 1996.
- [46] F. Gardiol. *Electromagnétisme*. Presses Polytechniques et Universitaires Romandes, Lausanne, 1996.
- [47] N. F. Gardner, H. C. Chui, E. I. Chen, M. R. Krames, J. W. Huang, F. A. Kish, S. A. Stockman, C. P. Kocot, T. S. Tan, and N. Moll. 1.4x efficiency improvement in transparent-substrate  $(Al_xGa_{1-x})_{0.5}In_{0.5}P$  light-emitting diodes with thin ( $\leq 2000\text{\AA}$ ) active regions. *Appl. Phys. Lett.*, 74(15):2230–2232, 1999.
- [48] E. Greger. *Development of Vertical-Cavity Surface Emitting Lasers and Polarization Switches Based on Superlattice Ordered GaInP*. PhD dissertation, Friedrich-Alexander-Universität, Erlangen-Nürnberg, Institut für Technische Physik I, 1998.
- [49] B. W. Hakki. Carrier and gain spatial profiles in GaAs stripe geometry lasers. *J. Appl. Phys.*, 44(11):5021–5028, 1973.
- [50] B. W. Hakki. GaAs double heterostructure lasing behavior along the junction plane. *J. Appl. Phys.*, 46(1):292–302, 1975.
- [51] S. Hansmann. Transfer Matrix Analysis of the Spectral Properties of Complex Distributed Feedback Laser Structures. *IEEE J. Quantum Electron.*, 28(11):2589–2595, 1992.
- [52] G. I. Hatakoshi, K. Itaya, M. Ishikawa, M. Okajima, and Y. Uematsu. Short-Wavelength InGaAlP Visible Laser Diodes. *IEEE J. Quantum Electron.*, 27(6):1476–1482, 1991.
- [53] G. I. Hatakoshi, K. Nitta, K. Itaya, Y. Nishikawa, M. Ishikawa, and M. Okajima. High-Power InGaAlP Laser Diodes for High-Density Optical Recording. *Jpn. J. Appl. Phys.*, 31(1):501–507, 1992.



- [54] C. H. Henry and R. A. Logan. Nonradiative "large dark spots" in  $Al_xGa_{1-x}As - GaAs$  heterostructures. *J. Appl. Phys.*, 48(9):3962–3970, 1977.
- [55] C. H. Henry, R. A. Logan, and F. R. Meritt. The effect of surface recombination on current in  $Al_xGa_{1-x}As$  heterojunctions. *J. Appl. Phys.*, 49(6):3530–3542, 1978.
- [56] S. T. Ho, L. Wang, and S. Park. Spontaneous emission control and microcavity light emitters. In H. Benisty, J. M. Gérard, R. Houdré, J. Rarity, and C. Weisbuch, editors, *Confined Photons Systems*, Lecture Notes in Physics, pages 243–297. Springer, Berlin, 1999.
- [57] G. E. Höfler, D. A. Vanderwater, D. C. DeFever, F. A. Kish, M. D. Camras, F. M. Steranka, and I. H. Tan. Wafer bonding of 50-mm diameter GaP to AlGaInP-GaP light-emitting diode wafers. *Appl. Phys. Lett.*, 69(6):803–805, 1996.
- [58] R. T. Holm, S. W. McKnight, E. D. Palik, and W. Lukosz. Interference effects in luminescence studies of thin films. *Appl. Opt.*, 21(14):2512–2519, 1982.
- [59] R. H. Horng, D. S. Wu, S. C. Wei, C. Y. Tseng, M. F. Huang, K. H. Chang, P. H. Liu, and K. C. Lin. AlGaInP light-emitting diodes with mirror substrates fabricated by wafer bonding. *Appl. Phys. Lett.*, 75(20):3054–3056, 1999.
- [60] S. Y. Hu, E. R. Hegblom, and L. A. Coldren. Multiple-wavelength top-emitting vertical-cavity photonic integrated emitter arrays for direct-coupled wavelength-division multiplexing applications. *Electron. Lett.*, 34(2):189–190, 1998.
- [61] K. H. Huang, J. G. Yu, C. P. Kuo, R. M. Fletcher, T. D. Osentowski, L. J. Stinson, M. G. Craford, and A. S. Liao. Twofold efficiency improvement in high performance AlGaInP light-emitting diodes in the 555–620 nm spectral region using a thick GaP window layer. *Appl. Phys. Lett.*, 61(9):1045–1047, 1992.
- [62] Z. Huang, C. C. Lin, and D. G. Deppe. Spontaneous Lifetime and Quantum Efficiency in Light Emitting Diodes Affected by a Close Metal Mirror. *IEEE J. Quantum Electron.*, 29(12):2940–2949, 1993.
- [63] D. L. Huffaker and D. G. Deppe. Intracavity Contacts for Low-Threshold Oxide-Confined Vertical-Cavity Surface-Emitting Lasers. *IEEE Photon. Technol. Lett.*, 11(8):934–936, 1999.
- [64] D. L. Huffaker, C. Lei, D. G. Deppe, C. J. Pinzone, J. G. Neff, and R. D. Dupuis. Controlled spontaneous emission in room-temperature semiconductor microcavities. *Appl. Phys. Lett.*, 60(26):3203–3205, 1992.
- [65] D. L. Huffaker, C. C. Lin, J. Shin, and D. G. Deppe. Resonant cavity light emitting diode with an  $Al_xO_y/GaAs$  reflector. *Appl. Phys. Lett.*, 66(23):3096–3098, 1995.

- [66] D. L. Huffaker, J. Shin, and D. G. Deppe. Low threshold half-wave vertical-cavity lasers. *Electron. Lett.*, 30(23):1946–1947, 1994.
- [67] N. E. Hunt, E. F. Schubert, R. F. Kopf, D. L. Sivco, A. Y. Cho, and G. J. Zydzik. Increased fiber communications bandwidth from a resonant cavity light emitting diode emitting at  $\lambda=940$  nm. *Appl. Phys. Lett.*, 63(19):2600–2602, 1993.
- [68] M. Ishikawa, H. Shiozawa, K. Itaya, G. I. Hatakoshi, and Y. Uematsu. Temperature Dependence of the Threshold Current for InGaAlP Visible Laser Diodes. *IEEE J. Quantum Electron.*, 27(1):23–28, 1991.
- [69] Y. Ishitani, S. Minagawa, and T. Tanaka. Temperature dependence of the band-gap energy of disordered GaInP. *J. Appl. Phys.*, 75(10):5326–5331, 1994.
- [70] M. Jalonen, J. Köngas, M. Toivonen, P. Savolainen, A. Salokatve, and M. Pessa. Monolithic Super-Bright Red Resonant Cavity Light-Emitting Diode Grown by Solid Source Molecular Beam Epitaxy. *IEEE Photon. Technol. Lett.*, 10(7):923–925, 1998.
- [71] M. Jalonen, M. Toivonen, J. Köngas, A. Salokatve, and M. Pessa. Oxide-confined resonant cavity red light-emitting diode grown by solid source molecular beam epitaxy. *Electron. Lett.*, 33(23):1989–1990, 1997.
- [72] J. D. Joannopoulos. An introduction to photonic crystals. In H. Benisty, J. M. Gérard, R. Houdré, J. Rarity, and C. Weisbuch, editors, *Confined Photons Systems*, Lecture Notes in Physics, pages 150–172. Springer, Berlin, 1999.
- [73] J. D. Joannopoulos, R. D. Meade, and J. N. Winn. *Photonic Crystals*. Princeton University Press, Princeton, 1995.
- [74] W. B. Joyce. Current-crowded carrier confinement in double-heterostructure lasers. *J. Appl. Phys.*, 51(5):2394–2401, 1980.
- [75] W. B. Joyce. Carrier transport in double-heterostructure active layers. *J. Appl. Phys.*, 53(11):7235–7239, 1982.
- [76] W. B. Joyce and S. H. Wemple. Steady-State Junction-Current Distributions in Thin Resistive Films on Semiconductor Junctions. *J. Appl. Phys.*, 41(9):3818–3830, 1970.
- [77] R. S. Kern. Progress and status of visible light emitting diode technology. In *Part of the SPIE Conference on Light-Emitting Diodes: Research, Manufacturing and Applications III*, pages 16–27, 1999.
- [78] K. S. Kim, Y. H. Cho, B. D. Choe, W. G. Jeong, and H. Lim. Determination of Al mole fraction for null conduction band offset in  $In_{0.5}Ga_{0.5}P/Al_xGa_{1-x}As$  heterojunction by photoluminescence measurement. *Appl. Phys. Lett.*, 67(12):1718–1720, 1995.

- [79] F.A. Kish, F. M. Steranka, D. C. DeFevere, D. A. Vanderwater, K. G. Park, C. P. Kuo, T. D. Osentowski, M. J. Peanasky, J. G. Yu, R. M. Fletcher, D. A. Steigerwald, and M. G. Craford. Very high-efficiency semiconductor wafer-bonded transparent-substrate  $(Al_xGa_{1-x})_{0.5}In_{0.5}P$  light-emitting diodes. *Appl. Phys. Lett.*, 64(21):2839–2841, 1994.
- [80] Z. Knittel. *Optics of thin films*. Wiley, New York, 1976.
- [81] C. Koeppen, R.F. Shi, W. D. Chen, and A. F. Garito. Properties of plastic optical fibers. *J. Opt. Soc. Amer. B*, 15(2):727–739, 1998.
- [82] J. A. Kong. Theorems of Bianisotropic Media. *Proceedings of the IEEE*, 60(9):1036–1046, 1972.
- [83] O. P. Kowalski, J. W. Cockburn, D. J. Mowbray, M. S. Skolnick, R. Teissier, and M. Hopkinson. GaInP-AlGaInP band offsets determined from hydrostatic pressure measurements. *Appl. Phys. Lett.*, 66(5):619–621, 1995.
- [84] M. R. Krames, M. Ochiai-Holcomb, G.E. Höfler, C. Carter-Coman, E. I. Chen, I. H. Tan, P. Gril-lot, N. F. Gardner, H. C. Chui, J. W. Huang, S. A. Stockman, F. A. Kish, M. G. Craford, T. S. Tan, C. P. Kocot, M. Hueschen, J. Posselt, B. Loh, G. Sasser, and D. Collins. High-power truncated-inverted-pyramid  $(Al_xGa_{1-x})_{0.5}In_{0.5}P/GaP$  light-emitting diodes exhibiting  $\geq 50\%$  external quantum efficiency. *Appl. Phys. Lett.*, 75(16):2365–2367, 1999.
- [85] H. Kressel and J. K. Butler. *Semiconductor Lasers and Heterojunctions LEDs*. Academic Press, New York, 1977.
- [86] M. P. C. Krijn. Heterojunction band offsets and effective masses in III-V quaternary alloys. *Semiconduct. Sci. Technol.*, 6(1):27–31, 1991.
- [87] R. E. Kunz and W. Lukosz. Changes in fluorescence lifetimes induced by variable optical environments. *Phys. Rev. B*, 21(10):4814–4828, 1980.
- [88] C. P. Kuo, R. M. Fletcher, T. D. Osentowski, M. C. Lardizabal, and M. G. Craford. High performance AlGaInP visible light-emitting diodes. *Appl. Phys. Lett.*, 57(27):2937–2939, 1990.
- [89] Landolt-Börnstein. *Zahlenwerte und Funktionen aus Naturwissenschaft und Technik 17a*. Springer Verlag, Berlin, 1982.
- [90] M. C. Larson and J. S. Harris. Wide and continuous wavelength tuning in a vertical-cavity surface-emitting laser using a micromachined deformable-membrane mirror. *Appl. Phys. Lett.*, 68(7):891–893, 1996.
- [91] S. J. Lee. Design Rules for High-Brightness Light-Emitting Diodes Grown on GaAs Substrate. *Jpn. J. Appl. Phys.*, 1(2):509–516, 1998.

- [92] S. J. Lee and S. W. Song. Efficiency improvement in light-emitting diodes based on geometrically deformed chips. In *Part of the SPIE Conference on Light-Emitting Diodes: Research, Manufacturing and Applications III*, pages 237–249, 1999.
- [93] H. A. McLeod. *Thin film optical filters*. Adam Hilger, London, 1969.
- [94] M. Levinshstein, S. Rumyantsev, and M. Shur. Ternary and quaternary iii-v compounds. In M. Levinshstein, S. Rumyantsev, and M. Shur, editors, *Semiconductor parameters*, Handbook series on semiconductor parameters, pages 1–36. World Scientific, Singapore, 1999.
- [95] C. T. H. F. Liedenbaum, A. Valster, A. L. G. J. Severens, and G. W. 't Hooft. Determination of the GaInP/AlGaInP band offset. *Appl. Phys. Lett.*, 57(25):2698–2700, 1990.
- [96] J. F. Lin, M. C. Wu, M. J. Jou, C. M. Chang, B. J. Lee, and Y. T. Tsai. Highly reliable operation of indium tin oxide AlGaInP orange light-emitting diodes. *Electron. Lett.*, 30(21):1793–1794, 1994.
- [97] J. A. Lott, R. P. Schneider, G. A. Vawter, J. C. Zolper, and K. J. Malloy. Visible (660nm) resonant cavity light-emitting diodes. *Electron. Lett.*, 29(4):328–329, 1993.
- [98] J. A. Lott, R. P. Schneider, J. C. Zolper, and K. J. Malloy. AlGaInP Visible Resonant Cavity Light-Emitting Diodes. *IEEE Photon. Technol. Lett.*, 5(6):631–633, 1993.
- [99] W. Lukosz. Light emission by magnetic and electric dipoles close to a plane interface. III Radiation patterns of dipoles with arbitrary orientation. *J. Opt. Soc. Amer. A*, 69(11):1495–1502, 1979.
- [100] W. Lukosz. Theory of optical-environment-dependent spontaneous-emission rates for emitters in thin layers. *Phys. Rev. B*, 22(6):3030–3038, 1980.
- [101] W. Lukosz. Light emission by multipole sources in thin layers. I. Radiation patterns of electric and magnetic dipoles. *J. Opt. Soc. Amer. A*, 71(6):744–754, 1981.
- [102] W. Lukosz and R. E. Kunz. Light emission by magnetic and electric dipoles close to a plane interface. I Total radiated power. *J. Opt. Soc. Amer. A*, 67(12):1607–1615, 1977.
- [103] W. Lukosz and R. E. Kunz. Light emission by magnetic and electric dipoles close to a plane interface. II Radiation patterns of perpendicular oriented dipoles. *J. Opt. Soc. Amer. A*, 67(12):1615–1619, 1977.
- [104] W. Lukosz and R. E. Kunz. New method for determining refractive index and thickness of fluorescent thin films. *Opt. Commun.*, 31(3):251–256, 1979.
- [105] W. Lukosz and M. Meier. Lifetimes and radiation patterns of luminescent centers close to a thin metal film. *Opt. Lett.*, 6(5):251–253, 1981.

- [106] A. T. Meney, A. D. Prins, A. F. Phillips, J. L. Sly, E. P. O'Reilly, D. J. Dunstan, A. R. Adams, and A. Valster. Determination of the Band Structure of Disordered AlGaInP and its Influence on Visible-Laser Characteristics. *IEEE J. Select. Topics Quantum Electron.*, 1(2):697–706, 1995.
- [107] D. V. Morgan, I. M. Al-Ofi, and Y. H. Aliyu. Indium tin oxide spreading layers for AlGaInP visible LEDs. *Semiconduct. Sci. Technol.*, 15(1):67–72, 2000.
- [108] A. P. Morison, J. D. Lambkin, C. J. van der Poel, and A. Valster. Evaluation of Multiquantum Barriers in Bulk Double Heterostructure Visible Laser Diodes. *IEEE Photon. Technol. Lett.*, 8(7):849–851, 1996.
- [109] M. Moser, K. H. Gulden, J. Epler, and H. P. Schweizer. High performance deep red AlAs/AlGaAs top emitting VCSELs grown by MOVPE at high growth rates. *J. Cryst. Growth*, 170:404–407, 1997.
- [110] M. Moser, R. Winterhoff, C. Geng, I. Queisser, F. Scholz, and A. Dörnen. Refractive index of  $(Al_xGa_{1-x})_{0.5}In_{0.5}P$  grown by metalorganic vapor phase epitaxy. *Appl. Phys. Lett.*, 64(2):235–237, 1994.
- [111] J. S. Nelson, E. D. Jones, S. M. Myers, D. M. Follstaedt, H. P. Hjalmarson, J. E. Schirber, R. P. Schneider, J. E. Fouquet, V. M. Robbins, and K. W. Carey. Compositional dependence of the luminescence of  $In_{0.49}(Al_yGa_{1-y})_{0.51}P$  alloys near the direct-indirect band-gap crossover. *Phys. Rev. B*, 53(23):15893–15901, 1996.
- [112] R. J. Nelson and N. Holonyak. Exciton absorption, photoluminescence and band structure of N-free and N-doped  $In_{1-x}Ga_xP$ . *J. Phys. Chem. Solids*, 37(1):629–637, 1976.
- [113] H. De Neve, J. Blondelle, R. Baets, P. Demeester, P. Van Daele, and G. Borghs. High Efficiency Planar Microcavity LED's: Comparison of Design and Experiment. *IEEE Photon. Technol. Lett.*, 7(3):287–289, 1995.
- [114] H. De Neve, J. Blondelle, P. Van Daele, P. Demeester, and R. Baets. Recycling of guided mode light emission in planar microcavity light emitting diodes. *Appl. Phys. Lett.*, 70(7):799–801, 1997.
- [115] A. Neyer, B. Wittmann, and M. Jöhnck. Plastic-Optical-Fiber-Based Parallel Optical Interconnects. *IEEE J. Select. Topics Quantum Electron.*, 5(2):193–200, 1999.
- [116] K. A. Neyts. Simulation of light emission from thin-film microcavities. *J. Opt. Soc. Amer. A*, 15(4):962–971, 1998.
- [117] D. Ochoa. *Optoelectronic applications of photonic bandgap structures*. PhD dissertation, Ecole Polytechnique Fédérale de Lausanne, Department of Physics, 2000.

- [118] D. Ochoa, R. Houdré, R. P. Stanley, C. Dill, U. Oesterle, and M. Ilegems. Device simultaneous determination of the source and cavity parameters of a microcavity light-emitting diode. *J. Appl. Phys.*, 85(5):2994–2996, 1999.
- [119] A. Onton, M. R. Lorentz, and W. Reuter. Electronic Structure and Luminescence Processes in  $In_{1-x}Ga_xP$  alloys. *J. Appl. Phys.*, 42(9):3420–3432, 1971.
- [120] J. I. Pankove. *Optical Processes in Semiconductors*. Dover Publications, New York, 1971.
- [121] S. H. Park, M. Markarian, P. K. L. Yu, and P. M. Asbeck. Conduction Band Offset of Strained InGaP by Quantum Well Capacitance-Voltage Profiling. *Journal of Electronic Materials*, 24(10):1381–1386, 1995.
- [122] N. Peyghambarian, S. W. Koch, and A. Mysyrowicz. *Introduction to Semiconductor Optics*. Prentice Hall, New Jersey, 1993.
- [123] G. D. Pitt, M. K. R. Vyas, and A. W. Mabbitt. The conduction band structure of the  $In_{1-x}Ga_xP$  alloys system. *Solid. State Commun.*, 14(1):621–625, 1974.
- [124] P. Raisch, R. Winterhoff, W. Wagner, M. Kessler, H. Schweizer, T. Riedl, R. Wirth, A. Hangleiter, and F. Scholz. Investigation on the performance of multiquantum barriers in short wavelength (630 nm) AlGaInP laser diodes. *Appl. Phys. Lett.*, 74(15):2158–2160, 1999.
- [125] M. A. Rao, E. J. Caine, H. Kroemer, S. I. Long, and D. I. Babic. Determination of valence and conduction-band discontinuities at the (Ga,In)P/GaAs heterojunction by C-V profiling. *J. Appl. Phys.*, 61(2):643–649, 1987.
- [126] T. J. Rogers, D. G. Deppe, and B. G. Streetman. Effect of an AlAs/GaAs mirror on the spontaneous emission of an InGaAs-GaAs quantum well. *Appl. Phys. Lett.*, 57(18):1858–1860, 1990.
- [127] P. Royo, R. P. Stanley, R. Houdré, M. Ilegems, M. Moser, R. Hövel, H. P. Schweizer, and K. H. Gulden. AlGaInP-based microcavity light emitting diodes: controlled on-wafer detuning and measurement of the internal quantum efficiency. *Appl. Phys. Lett.*, 75(26):4052–4054, 1999.
- [128] T. Rozzi and M. Mongiardo. *Open electromagnetic waveguides*. The Institution of Electrical Engineers, London, 1997.
- [129] T. E. Sale. *Vertical Cavity Surface Emitting Lasers*. John Wiley & Sons, New York, 1995.
- [130] B. E. A. Saleh and M. C. Teich. *Fundamentals of Photonics*. John Wiley & Sons, New York, 1991.
- [131] V. Savona. Linear optical properties of semiconductors microcavities with embedded quantum wells. In H. Benisty, J. M. Gérard, R. Houdré, J. Rarity, and C. Weisbuch, editors, *Confined Photons Systems*, Lecture Notes in Physics, pages 173–242. Springer, Berlin, 1999.

- [132] W. Schmid, F. Eberhard, M. Schauler, M. Grabherr, R. King, M. Miller, E. Deichsel, G. Stareev, U. Martin, R. Jäger, J. Joos, R. Michalzik, and K. J. Ebeling. Infrared light-emitting diodes with lateral outcoupling taper for high extraction efficiency. In *Part of the SPIE Conference on Light-Emitting Diodes: Research, Manufacturing and Applications III*, pages 198–205, 1999.
- [133] R. P. Schneider and J. A. Lott. Cavity design for improved electrical injection in InAlGaP/AlGaAs visible (639-661 nm) vertical-cavity surface-emitting laser diodes. *Appl. Phys. Lett.*, 63(7):917–919, 1993.
- [134] R. P. Schneider, J. A. Lott, M. Hagerott Craford, and K. D. Choquette. Epitaxial Design and Performance of AlGaInP Red (650-690 nm) VCSELs. *International Journal of High Speed Electronics and Systems*, 5(4):625–666, 1994.
- [135] I. Schnitzer and E. Yablonovitch. 30 % external quantum efficiency from surface textured, thin-film light-emitting diodes. *Appl. Phys. Lett.*, 63(16):2174–2176, 1993.
- [136] I. Schnitzer, E. Yablonovitch, C. Caneau, and T. J. Gmitter. Ultrahigh spontaneous emission quantum efficiency, 99.7 % internally and 72 % externally, from AlGaAs/GaAs/AlGaAs double heterostructures. *Appl. Phys. Lett.*, 62(2):131–133, 1993.
- [137] E. F. Schubert, N. E. J. Hunt, R. J. Malik, M. Micovic, and D. L. Miller. Temperature and Modulation Characteristics of Resonant-Cavity Light-Emitting Diodes. *IEEE J. Lightwave Technol.*, 14(7):1721–1728, 1996.
- [138] E. F. Schubert, Y. H. Wang, A. Y. Cho, L. W. Tu, and G. J. Zydzik. Resonant cavity light-emitting diode. *Appl. Phys. Lett.*, 60(8):921–923, 1992.
- [139] J. W. Scott. *Design, Fabrication and Characterization of High-Speed Intra-Cavity Contacted Vertical-Cavity Lasers*. PhD dissertation, University of California Santa Barbara, Department of Electrical and Computer Engineering, 1995.
- [140] J. W. Scott, R. S. Geels, S. W. Corzine, and L. A. Coldren. Modeling Temperature Effects and Spatial Hole Burning to Optimize Vertical-Cavity Surface-Emitting Laser Performance. *IEEE J. Quantum Electron.*, 29(5):1295–1307, 1993.
- [141] G. S. Smith. *An introduction to classical electromagnetic radiation*. Cambridge University Press, Cambridge, 1997.
- [142] P. M. Snowton and P. Blood. Threshold current temperature dependence of GaInP/(Al<sub>y</sub>Ga<sub>1-y</sub>) 670 nm quantum well lasers. *Appl. Phys. Lett.*, 67(9):1265–1267, 1995.
- [143] R. P. Stanley. -. in preparation.
- [144] R. P. Stanley. -. private communication.

- [145] R. P. Stanley, R. Houdré, U. Oesterle, M. Illegems, and C. Weisbuch. Impurity modes in one-dimensional periodic systems: The transition from photonic band gaps to microcavities. *Phys. Rev. A*, 48(3):2246–2250, 1993.
- [146] K. Streubel, U. Helin, V. Oskarsson, E. Bäcklin, and Å. Johansson. High Brightness Visible (660 nm) Resonant-Cavity Light-Emitting Diode. *IEEE Photon. Technol. Lett.*, 10(12):1685–1687, 1998.
- [147] H. Sugawara, M. Ishikawa, and G. I. Hatakoshi. High-Efficiency InGaAlP/GaAs Visible Light-Emitting Diodes. *Appl. Phys. Lett.*, 58(10):1010–1012, 1991.
- [148] H. Sugawara, K. Itaya, M. Ishikawa, and G. I. Hatakoshi. High-Efficiency InGaAlP Visible Light-Emitting Diodes. *Jpn. J. Appl. Phys.*, 1(8):2446–2451, 1992.
- [149] T. Takagi, F. Koyama, and K. Iga. Potential Barrier Height Analysis of AlGaInP Multi-Quantum Barrier (MQB). *Jpn. J. Appl. Phys.*, 29(11):L1977–L1980, 1990.
- [150] H. Tanaka, Y. Kawamura, and H. Asahi. Refractive indices of  $In_{0.49}Ga_{0.51-x}Al_xP$  lattice matched to GaAs. *J. Appl. Phys.*, 59(3):985–986, 1986.
- [151] D. A. Vanderwater, I. H. Tan, G. E. Höfler, D. C. Defever, and F. A. Kish. High-Brightness AlGaInP Light Emitting Diodes. *Proc. of the IEEE*, 85(11):1752–1764, 1997.
- [152] A. M. Vredenberg, N. E. J. Hunt, E. F. Schubert, D. C. Jacobson, J. M. Poate, and G. J. Zydzik. Controlled Atomic Spontaneous Emission from  $Er^{3+}$  in a Transparent  $Si/SiO_2$  Microcavity. *Phys. Rev. Lett.*, 71(4):517–520, 1993.
- [153] J. J. Wierer, D. A. Kellogg, and N. Holonyak. Tunnel contact junction native-oxide aperture and mirror vertical-cavity surface-emitting lasers and resonant-cavity light-emitting diodes. *Appl. Phys. Lett.*, 74(7):926–928, 1999.
- [154] R. Williams. *Modern GaAs Processing Methods*. Artech House, New York, 1990.
- [155] R. H. Windisch, P. Heremans, A. Knobloch, P. Kiesel, G. H. Döler, B. Dutta, and G. Borghs. Light-emitting diodes with 31% external quantum efficiency by outcoupling of lateral waveguide modes. *Appl. Phys. Lett.*, 74(16):2256–2258, 1999.
- [156] R. H. Windisch, A. Knobloch, J. Potemans, B. Dutta, G. H. Döler, G. Borghs, and P. L. Heremans. Light-Emitting Diodes with 17% External Quantum efficiency at 622 Mb/s for High-Bandwidth Parallel Short-Distance Optical Interconnects. *IEEE J. Select. Topics Quantum Electron.*, 5(2):166–171, 1999.
- [157] T. Wipiejewski, M. G. Peters, E. R. Hegblom, and L. A. Coldren. Vertical-Cavity Surface-Emitting Laser Diodes with Post-Growth Wavelength Adjustment. *IEEE Photon. Technol. Lett.*, 7(7):727–729, 1995.



- [158] R. Wirth, A. Moritz, C. Geng, F. Scholz, and A. Hangleiter. Birefringence in ordered (Al)GaInP. *Phys. Rev. B*, 55(3):1730–1740, 1997.
- [159] S. A. Wood, C. H. Molloy, P. M. Smowton, P. Blood, D. J. Somerford, and C. C. Button. Electron transport in AlGaInP quantum well lasers. *Appl. Phys. Lett.*, 75(12):1748–1750, 1999.
- [160] S. A. Wood, P. M. Smowton, C. H. Molloy, P. Blood, D. J. Somerford, and C. C. Button. Direct monitoring of thermally activated leakage current in AlGaInP laser diodes. *Appl. Phys. Lett.*, 74(17):2540–2542, 1999.
- [161] E. Yablonovitch. Inhibited Spontaneous Emission in Solid-State Physics and Electronics. *Phys. Rev. Lett.*, 58(20):2059–2062, 1987.
- [162] E. Yablonovitch, T. J. Gmitter, and R. Bhat. Inhibited and Enhanced Spontaneous Emission from Optically Thin AlGaAs/GaAs Double Heterostructures. *Phys. Rev. Lett.*, 61(22):2546–2549, 1988.
- [163] H. K. Yow, P. A. Houston, and M. Hopkinson. Conduction band discontinuities in  $Ga_{0.5}In_{0.5}P - Al_xGa_{0.5-x}In_{0.5}P$  heterojunctions measured by internal photoemission. *Appl. Phys. Lett.*, 66(21):2852–2854, 1995.
- [164] P. S. Zory. *Quantum Well Lasers*. Academic Press, New York, 1993.



# Curriculum vitae

## ROYO Paul

Nationality	French
Date of birth	November 3, 1971
Place of origin	France
Civil status	Single

## EDUCATION

1989	- Baccalauréat français C (Scientific high school diploma)
1989-1994	- Study at the Department of Electrical Engineering , Ecole Polytechnique Fédérale de Lausanne (EPFL) 1015 Lausanne, Switzerland
1993	Practical training at the Swiss Federal Office of Metrology in Bern
1994-1995	- Diploma work under the direction of Prof. F. Gardiol, Diploma thesis: "Etude de guides d'ondes optiques intégrés à coeur chiral par la méthode des éléments finis."
1995	Practical training at the Blackett Laboratory, Imperial College of Science Technology and Medicine, London
1995-1996	Military service in France
1996-1998	- Doctoral thesis work in the Optoelectronic group of the Centre Suisse d'Electronique et de Microtechnique (CSEM) in Zurich and in the Department of Physics of EPFL under the direction of Prof. M. Illegems
1998-2000	

## PUBLICATIONS

- P. Royo, R. P. Stanley, R. Houdré, M. Ilegems, M. Moser, R. Hövel, H. P. Schweizer, K. H. Gulden, "AlGaInP-based microcavity light emitting diodes: controlled on-wafer detuning and measurement of the internal quantum efficiency", *Applied Physics Letters*, **75**(1999) 4052-4054.
- J.F. Carlin, P. Royo, M. Ilegems, B. Gerard, X. Marcadet, J. Nagle, "High-efficiency top-emitting microcavity LEDs on GaAs and GaAs/Si substrates", *Journal of Crystal Growth*, **201/202**(1999) 994-998.
- J.F. Carlin, P. Royo, R. P. Stanley, R. Houdré, J. Spicher, U. Oesterle and M. Ilegems, "Design and characterization of top-emitting microcavity light emitting diodes", *Semicond. Sci. Technol.*, **15**(2000) 145-154.
- P. Royo, J. F. Carlin, J. Spicher, R. Stanley, R. Houdré, V. Bardinal, U. Oesterle, M. Ilegems, "High efficiency top-emitting microcavity light-emitting diodes", *Part of the SPIE Conference on Light-Emitting Diodes: Research, Manufacturing and Applications III, San Jos, California., SPIE Vol. 3621*(1999) 151.
- P. Royo, M. Ilegems, M. Moser, R. Hövel, H. P. Schweizer, K. H. Gulden, "Controlled growth variation for the detuning of AlGaInP-based microcavity light emitting diodes", *Proceedings of the IPRM'99 Conference in Davos, ISBN 0-7803-5562-8*(1999) 111.
- P. Royo, R. P. Stanley, M. Ilegems, K. Streubel, K. H. Gulden, "Deconvolution of the intrinsic spontaneous spectrum of vertical cavity surface emitting devices", *submitted*
- P. Royo, R. P. Stanley, M. Ilegems, K. Streubel, K. H. Gulden, "On-wafer determination of the intrinsic spontaneous spectrum of vertical cavity surface emitting devices", *submitted*
- P. Royo, R. P. Stanley, M. Ilegems, M. Moser, "Coupling of impurity modes in one-dimensional periodic systems", *submitted*
- P. Royo, R. P. Stanley, M. Ilegems, K. H. Gulden, "Microcavity Light-Emitting Diodes: analytic analysis of the extraction efficiency and design rules", *in preparation*
- P. Royo, R. P. Stanley, M. Ilegems, K. Streubel, K. H. Gulden, "Influence of the contact design on the emission properties of red top-emission Microcavity Light-Emitting Diodes", *in preparation*

- P. Royo, R. P. Stanley, M. Ilegems, K. Streubel, K. H. Gulden, "Factors determining the external quantum efficiency of AlGaInP Microcavity Light-Emitting Diodes", *in preparation*

## CONFERENCES AND SUMMER SCHOOLS

- P. Royo, R. Stanley, R. Houdré, M. Ilegems, E. Greger, H. P. Schweizer, M. Moser, K. H. Gulden, "Visible microcavity light-emitting diodes", *QED Phenomena and Applications of Microcavities and Photonics Crystals*, Institut d'Etudes Scientifiques de Cargèse, Corse, France, August 3rd-15th 1998, poster presentation.
- P. Royo, R. Stanley, R. Houdré, M. Ilegems, E. Greger, H. P. Schweizer, M. Moser, K. H. Gulden, "Visible microcavity light-emitting diodes", *Summer School and European Optical Society Topical Meeting on Semiconductor Microcavity Light Emitters*, Centro Stefano Franscini, Monte Verita, Ascona, Switzerland, September 20th-25th 1998, poster presentation.
- P. Royo, J. F. Carlin, J. Spicher, R. Stanley, R. Houdré, V. Bardinal, U. Oesterle, M. Ilegems, "High efficiency top-emitting microcavity light-emitting diodes", *Part of the SPIE Conference on Light-Emitting Diodes: Research, Manufacturing and Applications III*, San José, California, USA, January 23rd-29th 1999, oral presentation.
- P. Royo, M. Ilegems, M. Moser, R. Hövel, H. P. Schweizer, K. H. Gulden, "Controlled growth variation for the detuning of AlGaInP-based microcavity light emitting diodes", *Indium Phosphide and Related Materials IPRM'99 Conference*, Davos, Switzerland, May 16th-20th 1999, poster presentation.
- P. Royo, R. Stanley, M. Ilegems, K. Streubel, K. H. Gulden "Factors determining the external quantum efficiency of AlGaInP Microcavity Light-Emitting Diodes", *27th International Symposium on Compound Semiconductors*, Monterey, California, USA, October 2nd-5th 2000, oral presentation.
- P. Royo, R. Stanley, M. Ilegems, K. Streubel, K. H. Gulden "Study of the external quantum efficiency of red MCLEDs", *European Optical Society Topical Meeting and Summer School on semiconductor microcavity photonics*, Centro Stefano Franscini, Monte Verita, Ascona, Switzerland, October 21th-25th 2000, poster presentation.



# Remerciements

Je remercie chaleureusement le Professeur Ilegems qui a dirigé ce travail de thèse, m'a apporté de nombreux conseils et encouragements et m'a laissé beaucoup de liberté pour l'organisation de mon temps entre les laboratoires de Lausanne et de Zurich.

La partie pratique de ce travail de thèse a en grande partie été effectuée au CSEM-Zurich où j'ai séjourné de façon continue pendant près de deux ans. Je remercie à ce propos les Docteurs Hanswilly Lehmann et Karlheinz Gulden de m'y avoir accueilli et d'avoir de leur côté facilité l'organisation de cette collaboration.

La partie zurichoise de ce travail a été directement supervisée par le Docteur Michael Moser que je remercie pour sa totale disponibilité et les nombreuses choses qu'il m'a apprises de façon amicale.

Ma reconnaissance va également aux Docteurs Ross Stanley et Romuald Houdré qui ont encadré mon travail à Lausanne. Merci à Romuald pour avoir guidé mes premiers pas de thésard et à Ross pour sa très grande disponibilité et ses conseils.

Je remercie par ailleurs Jacques Spicher, Nicolas Leiser, Paola Pellandini, Andrea Fiore et Rolando Ferrini qui ont partagé avec bonne humeur mon bureau (à Lausanne), ainsi que Eric Greger, Marcel Brunner et Sven Eitel (à Zurich). Je n'oublie pas non plus les autres membres du groupe: Jean-François Carlin, Daniel Ochoa, Christian Dill, Véronique Bardinal, Ursula Oesterle, Mathias Beck et David Leuenberger.

Mes remerciements vont aussi aux membres du CSEM-Zurich, en particulier à Rainer Hövel et Hanspeter Schweizer pour l'épitaxie, Daniel Jeggle et Bruno Graf pour leur aide en salle blanche, Arthur Vonlanthen pour le bonding des diodes et aux autres membres du groupe, Stefan Gehrsitz, Hanspeter Gauggel, Hanspeter Zappe et Fabrice Monti Di Sopra.

Merci aussi à Fabienne Bobard du Centre Interdépartemental de Microscopie Electronique (CIME) de l'EPFL pour le temps qu'elle a passé sur les mesures TEM.

Une partie de mon travail ayant été conduite dans le cadre du projet européen ESPRIT-SMILED, je tiens finalement à remercier les membres des groupes partenaires, en particulier de Mitel Semiconductor (Klaus Streubel et Rickard Marcks von Württemberg), de l'Ecole Polytechnique de Paris (Claude Weisbuch et Henri Benisty), de l'IMEC (Université de Gent) et de ORC (Université de Tempere).